Simulation and Prediction of Wakes and Wake Interaction in Wind Farms

Andersen, Søren Juhl

Publication date:
2014

Document Version
Peer reviewed version

DTU Wind Energy

Simulation and Prediction of Wakes and Wake Interaction in Wind Farms

Department of Wind Energy Report 2013

Søren Juhl Andersen

DTU Wind Energy PhD-0021

September 2013

DTU Vindenergi
Institut for Vindenergi

Preface

This dissertation is submitted in partial fulfillment of the requirements for the PhD degree from the Technical University of Denmark. The dissertation is based on research work performed from June 2010 to September 2013 at the Department of Wind Energy, Fluid Mechanics Section.

The present work has been carried out with the support of Vattenfall, the Danish Council for Strategic Research for the project 'Center for Computational Wind Turbine Aerodynamics and Atmospheric Turbulence'(COMWIND) (grant 2104-09-067216/DSF)[1], and the Nordic Consortium on Optimization and Control of Wind Farms [2], which has provided valuable access to the National Supercomputer Centre in Sweden(NSC). Finally, the proprietary data for Vestas' NM80 turbine has been used.

I would like to express my gratitude and thanks to my supervisors Jens Nørkær Sørensen, Wen Zhong Shen, and Robert Flemming Mikkelsen for their guidance, support, and fruitful discussions. I would also like to extend my thanks to all my colleagues at the Department of Wind Energy for an inspiring and friendly working environment, which give rise to many rewarding and challenging discussions.

Finally, I would like to express my sincere thanks and love to my friends and families around the world for their love and support.

Technical University of Denmark

Søren Juhl Andersen

Copenhagen, September, 2013

[1] http://www.comwind.mek.dtu.dk/Partners.aspx
[2] http://picard.hgo.se/~nordwind/

Abstract

The highly turbulent wake and the wake interaction of merging wakes between multiple wind turbines are modelled using Large Eddy Simulation(LES) in a general Navier-Stokes solver. The Actuator Line(AL) technique is employed to model the wind turbines, and the aeroelastic computations are fully coupled with the flow solver. The numerical simulations include the study of the far wake behind a single turbine, three idealised cases of infinitely long rows of turbines and finally three infinite wind farm scenarios with different spacings. The flow characteristics between the turbines, turbine performance, and principal turbulent quantities are examined for the different scenarios. The study focuses on the large coherent structures and movements of the wake behind and between wind turbines. The large coherent structures are analysed using Proper Orthogonal Decomposition(POD). POD constitutes the basis for two proposed dynamic wake models of the turbulent wake deep inside large wind farms. The first model is based on a direct reconstruction using POD, while the other model(REDOMO) is based on an additional reduction by only including the most dominant frequencies. The flow fields derived from the two wake models are assessed and verified by comparing turbine performance and loads to those derived from the flow extracted from the full numerical simulations. The most comprehensive model yields excellent agreement for small and intermediate turbine spacing, while the simpler version is unable to resolve the complex dynamics due to severe temporal filtering. The models have difficulties capturing the more extreme and spurious events for larger turbine spacings. The performance is also compared to stochastically generated Mann turbulence, which gives better results for larger spacings. The comparison also reveals how much information should be retained by the POD models to add more value than simply applying homogeneous turbulence as inflow.

Resumé

Det komplekse og turbulente kølvand bag vindmøller og i særdeleshed vekselsvirkninger i kølvandet mellem mange vindmøller er simuleret ved hjælp af Large Eddy Simulation(LES) implementeret i en generel Navier-Stokes løser. Actuator Linje metoden bruges til at simulere vindmøllerne, og de aeroelastiske beregninger er fuldt koblet med Navier-Stokes løseren. Der er foretaget tre forskellige typer numeriske beregninger for at studere: kølvandet bag en enkelt vindmølle, tre idealiserede scenarier med uendelige rækker af vindmøller og slutteligt tre uendelige vindmøllerparker med variende afstand mellem møllerne. Strømningerne mellem møllerne beskrives, møllernes ydeevne og de primære turbulente størrelser undersøges i de forskellige scenarier. Undersøgelsen fokuserer på de store sammenhængende strukturer og disses bevægelser i strømningsfeltet bag og mellem vindmøllerne. De store sammenhængende strukturer analyseres ved hjælp af Proper Orthogonal Decomposition(POD). POD udgør også fundamentet for to dynamiske modeller, der beskriver de turbulente strømninger dybt inde i store vindmølleparker. Den ene model er baseret på en direkte genskabelse af strømningsfeltet via POD, mens den anden model(REDOMO) er baseret på en yderligere reducering ved kun at medtage de mest dominerende frekvenser. De to modellers strømningsfelter undersøges og veriferes ved at sammenligne produktion og belastninger med de tilsvarende for det fulde strømningsfelt. Den mest omfattende model giver glimrende resultater for små og mellemstore afstande, mens den simplere model er ude af stand til at beskrive den komplekse dynamik på grund af den tidsmæssige filtrering. Modellerne har problemer med at beskrive dynamikken for store afstande på grund af mere ekstreme og pludselige fluktuationer. Endelig sammenlignes med stokastisk genereret turbulens, der giver bedre resultater for store afstande. Sammenligningen afslører også hvor meget information modellerne skal inkludere for at opnå bedre resultater end ved blot at anvende homogen turbulens.

Nomenclature

α	Local angle of attack.
α_{NOJ}	Entrainment constant for N. O. Jensen wake model.
α_{PBL}	Shape parameter for prescribed boundary layer.
α_{SF}	Entrainment constant for Frandsen wake model.
β	Constant for SGS model.
$\beta_{k,m}^{(1,2)}$	REDOMO parameters.
ΔT_{win}	Temporal window for statistics.
ΔVol	Volume of a cell.
Δy	Lateral increment for iteration to determine wake centre.
Δz	Vertical increment for iteration to determine wake centre.
Δ_{PBL}	Transition height between parabolic and power law profile in prescribed boundary layer.
$\dot{m}$	Mass flux.
ϵ	Smearing parameter.
η_ϵ	Regularization kernel.
γ	Local pitch angle.
$\hat{R}$	Cross-correlation.
κ	Kurtosis.
λ	POD eigenvalues.
λ_{TS}	Tip-speed ratio.
$\mathbf{\Lambda}$	Diagonal matrix containing POD eigenvalues.
$\overline{\mathbf{V}}$	Filtered velocity field.
$\widehat{\mathbf{u}}$	POD reconstruction.
$\widetilde{\mathbf{u}}$	REDOMO reconstruction.

$\mathbf{A}$	Matrix containing the temporal eigenfunctions.
$\mathbf{e_D}$	Unit vector parallel to the drag coefficient.
$\mathbf{e_L}$	Unit vector parallel to the lift coefficient.
$\mathbf{f}_{mf}$	Body forces imposed to keep mass flux constant.
$\mathbf{f}_{pbl}$	Body forces applied to obtain prescribed boundary layer.
$\mathbf{f}_{turb}$	Body forces for introducing atmospheric turbulence.
$\mathbf{f}_{WT}$	Body forces used in the actuator line method.
$\mathbf{G}$	Matrix of orthonormal eigenvectors.
$\mathbf{S}$	Domain surface.
$\mathbf{v}'$	Sub-grid scale velocity field.
$\mathcal{P}$	Production of turbulent kinetic energy.
$\mathcal{R}$	Radial distance for cross-correlation.
ν	Eddy viscosity.
ν_{SGS}	SGS eddy viscosity.
Ω	Rotor speed.
$\overline{\Delta}$	Filter cut-off length.
ϕ	Flow angle.
ϕ_0	Initial mass flux.
ϕ_k	POD modes.
ρ	Density of air.
σ	Standard deviation.
τ_{ij}	Reynolds stresses.
$\tilde{\Delta}$	Test filter size.
ξ_j	Deviation in mass flux.
$\zeta(z)$	Vertical distribution function for high altitude turbulence.
a	Induction factor.
A_R	Rotor area.
B	Number of turbine blades.
c_1	Shape parameter for prescribed boundary layer.
c_2	Shape parameter for prescribed boundary layer.

C_D	Drag coefficient.
C_L	Lift coefficient.
C_m	Constant for SGS model.
C_P	Power coefficient.
C_T	Thrust coefficient.
f	Frequency.
F_x	Axial force.
F_θ	Tangetial force.
$f_{k,m}$	Dominant frequencies used for REDOMO.
$f_{WT}, 1P$	Rotational frequency of the wind turbine.
H_{hub}	Hub height.
j_{rot}	Blade resolution.
K	Number of POD modes.
k, m	Index for POD mode and dominant frequency.
K_d	PID controller coefficient for derivative gain.
K_i	PID controller coefficient for integral gain.
K_p	PID controller coefficient for proportional gain.
L_{eq}	Equivalent load.
M	Number of frequencies used in REDOMO.
m	Material parameter for equivalent load calculation.
M_E	Edgewise moment.
M_F	Flapwise moment.
M_T	Tilt moment.
M_Y	Yaw moment.
M_{HG}	Number of frequencies used in REDOMO by including high gradient frequencies.
N	Number of slices, time steps.
N_{eq}	Number of equivalent load cycles.
$N_{RF,i}$	Number of load cycles with amplitude RF_i.
P	Power.
p	Pressure.

q_c^2	Kinetic energy in SGS model.
R	Radius of turbine.
r	Radial coordinate.
$R_{i,j}, \mathbf{R}$	Two-point velocity correlation tensor.
Re	Reynolds number.
RF_i	Amplitude of equivalent load.
S	Turbine spacing.
s	Skewness.
St	Strouhal number.
T	Thrust.
T_E	Integral length scale.
T_T	Turnaround time.
U	Streamwise velocity.
U_0	Initial streamwise velocity.
u_0	Mean velocity subtracted in POD.
U_{hub}	Streamwise velocity at hub height.
U_{pbl}	Velocity profiles in prescribed boundary layer.
V	Lateral velocity.
V_0	Initial lateral velocity.
V_x	Axial velocity, same as U.
V_θ	Tangential velocity.
V_{rel}	Relative velocity at blade section.
W	Vertical velocity.
W_0	Initial vertical velocity.
X	Streamwise coordinate.
Y	Lateral coordinate.
Y_C	Lateral wake centre coordinate.
Z	Vertical coordinate.
Z_C	Vertical wake centre coordinate.
AL	Actuator line.

CFD Computational Fluid Dynamics.

DWM Dynamic Wake Meandering.

HAT High altitude turbulence.

LES Large Eddy Simulation.

LSMR Iterative least squares solver.

NS Navier-Stokes.

PBL Prescribed boundary layer.

PDF Probability density function.

PID Proportional-Integral-Derivative(controller).

POD Proper Orthogonal Decompositon.

PSD Power Spectral Density.

REDOMO Reduced Order Model.

RMS Root-mean-square.

SGS Sub-grid scale.

TKE Turbulent Kinetic Energy.

List of Tables

List of Figures

Contents

Chapter 1

Introduction

Humanity has harnessed the power of the wind for thousands of years initially through sails and wind mills. By the end of the 19th century pioneers such as Poul la Cour employed wind turbines for generating electricity. The development of industrial sized wind turbines accelerated with the emerging energy crisis in the 1970's, particular in countries such as USA, Sweden, Germany, and Denmark. In 1980, the world's first onshore wind farm with 20 turbines was installed in Crotched Mountain, NH, USA, and followed in 1991 by the first offshore wind farm consisting of 11 turbines at Vindeby, Denmark. Other notable offshore wind farms include Horns Rev I, Denmark, which was installed in 2002 with 80 Vestas V80-2.0 MW turbines and produces approximately 2% of the annual electricity consumption in Denmark. As of 2013, the first phase of the London Array is the largest operating wind farm consisting of 175 wind turbines with a total capacity of 630MW. In 2012 a total of approximately $5GW$ is installed offshore according to the "Deep Water" report [7].

In 2008, the EU adopted a baseline target that at least 20% of the total energy consumption must be supplied by renewable energy sources by 2020[1]. In 2012, Denmark set out even higher aims that 35% of the total energy consumption should come from renewables by 2020, and that the entire Danish energy supply should be derived from renewables by 2050. Wind power is currently the most developed renewable technology and is expected to deliver the lion's share in the transition from fossil based energy production to renewables. As such, Denmark aims to cover 50% of the total Danish electricity consumption by wind power by 2020. Amongst a number of necessary initiatives in the Danish policy plan[2] are the installment of $1,500MW$ offshore and an expected net increase in installed onshore capacity of $500MW$. The recent "Deep Water" report [7] states that a total of $40GW$ and as much as $140GW$ could be installed offshore by 2020 and 2030, respectively. Globally, there are large wind farms under development, and several prospects with capacity of $1,000 + MW$ are under development, particular around the British Isles. Triton Knoll Offshore Wind Farm was given the final consent in July 2013 with a planned capacity

[1] Directive 2009/28/EC of the European Parliament and of the Council, April 23rd, 2009: `http://eur-lex.europa.eu/LexUriServ/LexUriServ.do?uri=Oj:L:2009:140:0016:0062:en:PDF`

[2] Danish Energy Policy 2012: `http://www.ens.dk/politik/dansk-klima-energipolitik/politiske-aftaler-pa-energiomradet/energiaftalen-22-marts-2012`

of $1,200MW$ and up to 288 turbines. It is the biggest offshore wind farm development approved in the world[3]. Such wind farms will be instrumental in reaching the objectives laid out in adopted policies around the world aimed at making green and renewable energy deliver a larger portion of the world's total energy consumption. Large wind farms on this scale also provide new challenges in terms of optimizing power production and decreasing the overall cost of energy, as large scale wind farm power production is still in its infancy. These challenges leads to an ever increasing demand for improved engineering methods and tools. The present work sets out to provide new insights aimed at addresssing the challenges related to wake modelling inside large wind farms, such as optimizing turbine design and wind farm layout.

Challenges Related to Large Wind Farms

Large wind farms are usually organised in a systematic pattern of rows and columns, e.g. the layout of Horns Rev is an 8×10 array with spacings of $14R$ and $20R$. The array configuration and the directional variability of the wind means that all turbines will experience wake situations, where the turbine is more or less aligned with one or more upstream turbines and their wake(s). A wind turbine operating in the wake of one or more wind turbines yields significantly less power, e.g. Barthelmie et al. [13] reported reductions of more than 40% for certain wind directions at Horns Rev. Furthermore, the turbine is also subject to greater loadings due to increased turbulence levels, which subsequently leads to increased fatique loads. However, the increased turbulence also facilitates an increased turbulent mixing, which entrains energy from the surrounding atmosphere leading to a faster wake recovery.

An important part of the highly turbulent flow is the large coherent structures. Kelley et al. [32] investigated the structural impact of large coherent structures, and showed the potential detrimental impact on different turbine components as loads are transferred from the low frequencies to high frequencies through the structure. Kelley et al. distinguished between large coherent structures of the same magnitude as the turbine or smaller and even larger convective structures. The convective structures are often denoted wake meandering, as Larsen et al. [33], [34] associated this meandering with the large scale atmospheric turbulence. Medici and Alfredsson [45] related meandering to a wake instability analogous to the vortex shedding behind a bluff body. The large scales enhance the turbulent mixing, but the large scales are also responsible for exerting higher and particular differential loads on the turbine due to the partial wake alignment originating from the large movements of the turbulent wake. The extraction of energy balanced with the increased turbulent mixing means the flow deep inside a large wind farm tends asymptoticly towards an equilibrium wake or infinite wind farm state. Despite tending towards such an equilibrium state, the highly turbulent flow is very complex and the understanding of this asymptotic scenario is of great interest because it is directly related to the prediction of power production and loads.

Reliable power and load predictions are hence very intricate and yet essential for optimizing the design of both the individual wind turbine and the layout of wind farms. Furthermore, the variability in wind power production also

[3]RenewableUK press release July 11th, 2013: `http://www.renewableuk.com/en/news/press-releases.cfm/2013-07-11world-s-biggest-offshore-wind-farm-gets-go-ahead`

introduce challenges in both short and long term predictions. The short term prediction is related to optimizing the overall farm performance through farm control, while the longer term predictions are essential for the integration of wind power into the existing electrical grid. Despite significant advances in measuring instanteneous wake velocities using lidar, see Bingöl et al. [15] and Trujillo et al. [71], deriving empirical knowledge from measuring campaigns are still both expensive and difficult, because measurements contain large uncertainties due to the complex and everchanging inflow conditions. On the other hand, numerical simulations have all the relevant properties described, but detailed numerical simulations are very time consuming, so simpler engineering models are still utilized for optimization purposes.

Previous Work

Several engineering wake models exist, also called kinematic models, and are widely used due to their simplicity and computational speed. Generally, these models are based on simple single wake calculations and often assumes self-similar velocity profiles in the far wake. The models use different assumptions to superpose merging wakes in order to describe the overall wake interaction inside wind farms. However, "the superposition assumption could be seriously in error"(Ainslie [3]). These methods are based on steady state considerations, and are developed with the aim of predicting mean quantities, e.g. the mean velocity for predicting average power production. Therefore, the models exclude the details of the dynamic wake interaction and turbulence properties needed to assess the instanteneous turbine performance and loadings. Notable models include the models by N. O. Jensen [28] and Frandsen et al. [20]. Jensen assumed the wake behind a wind turbine to be analogous to a negative jet with a linear wake expansion and operating at Betz' optimum(induction factor $a = \frac{1}{3}$), and derived an explicit expression for the asymptotic wind speed. Frandsen et al. [20] developed a wake model based on momentum analysis over a control volume. Frandsen's model includes three distinct regimes, the first regime of multiple inline wake interaction, the second regime where the wake expansion is limited due to the ground and adjacent rows of turbines and their wake, and hence the combined wake can only expand vertically. Finally, the third regime models the equilibrium or infinite scenario, where the flow internally in the wind farm is in balance with the boundary layer created over the wind farm. The Frandsen solution yields a linear expansion of the wake area, i.e. $D \propto \sqrt{x}$. Several of these engineering models are capable of giving good agreement with some experiments, particular in terms of overall farm efficiency. However, the results are not consistent, not even for the same wake model. Barthelmie et al. [12] showed an average absolute error of 15% in determining the wind velocity at hub height using six different wake models. Furthermore, the models does generally not include the dynamics of the wake, which prevent a proper prediction of the turbine loads.

Frandsen [22] proposed a model for assessing fatique loads on rotors using the effective turbulence intensity as the governing parameter, arguing that the various changes in turbulence properties are usually correlated with the standard deviation of wind speed fluctuations. The effective turbulence intensity is hence taken as a design variable, and not as a physical quantity. The model has shown improved accuracy compared to the existing engineering models, al-

beit still occassionally resulting in large discrepancies between the predicted and measured results. The models still lack a complete calibration and verification before they can be applied to all situations, particular inside large wind farms. Barthelmie et al. [12] compared six different wake models with measurements from Vindeby wind farm, and concluded: "the spread of the wake model predictions is considerable even for these relative simple offshore single wake cases". A thorough overview of different wake models are given by Sanderse [55] and Schepers [59].

The analytical models have also been combined with models describing the so-called meandering or large scale motions of the wake governed by the large atmospheric scales, first introduced by Ainslie [2] and [3]. The Dynamic Wake Meandering(DWM) model by Larsen et al. [33] and [34] is based on this hypothesis. The DWM model is state-of-the art in applied wake modelling and combines the effects of quasi-steady wake deficits, wake turbulence and a stochastic model of the wake meandering, which transports the quasi-steady wake deficit downstream as a passive tracer. The DWM model has been shown to yield good agreement with experimental data measured behind a single turbine using lidar, e.g. Bingöl et al. [15] and Trujillo et al. [71], and the DWM model has provided good agreement with both measured power production and loads for free wake situations and the fifth turbine in a wake situation at the Dutch wind farm Egmond aan Zee, see Larsen et al. [35]. However, the DWM model is based on the filtered output from stochasticly determined turbulence. Stochastic turbulence models, such as Mann [42] and [43] or Veers [72], require deterministic parameters. Solari and Piccardo [61] and Saranyasoontorn and Manuel [58] examined the variability in parameters based on field measurements. Saranyasoontorn and Manuel concluded that the large variability of deterministic parameters generally gave rise to insignificant variability in the turbine load statistics, except a few load cases, e.g. yaw loads, which needs to be considered when determining design loads for wind turbines. Frandsen and Madsen [21] investigated the influence of ambient turbulence in large wind farms and found the internal turbulence to be dominated by the inherent turbulence stemming from the turbines and the ambient atmospheric turbulence to be less relevant. Barthelmie et al. [12] also concluded their model comparison stating "the need for more and better-quality measurements and further model evaluation, particularly for the multiple wake cases".

The dynamic and structural loads on a wind turbine are usually modelled using aeroelastic codes such as HAWC2 or Flex5. HAWC2 is a multi-body approach and developed at Risø National Laboratory, see Larsen et al. [37]. Flex5 employs a modal approach for determining the response and loads, and was developed at the Technical University of Denmark by Stig Øye, see Øye [52].

Wakes and wake interaction in wind farms have been modelled and studied numerically using Computational Fluid Dynamics(CDF), where the rotor is modelled in various ways. Previously, the turbines have been simulated merely as roughness elements, but state-of-the-art today is using the Actuator Disc or Actuator Line methods. These methods couple the Navier-Stokes equations with body forces to include the effect of the wind turbines on the flow without having to fully resolve the boundary layers over the rotating blades. The Navier-Stokes based Actuator Disc method was first introduced by Sørensen and Myken [62] to simulate axisymmetric flows around wind turbines. The Actu-

ator Line technique was later introduced as an extension to full 3-dimensional flows by Sørensen and Shen [63]. Both methods have been used extensively for wake studies on single and multiple wind turbines in wind farms. The so-called Fuga wake model, see Ott et al. [51], is based on a linearised version of the Navier-Stokes equations combined with Actuator Disc and implemented in WAsP(Wind Atlas Analysis and Application Program, Mann et al. [44]) using a number of look-up tables, which ensure high computational speed. Troldborg [68] and Ivanell [27] amongst other have used full CFD simulations and the Actuator Disc and Actuator Line methods. These latter numerical studies also employed Large Eddy Simulation(LES), which simulate the large eddies and model the small eddies through a sub-grid scale model. Other recent studies have investigated large wind farms within the atmospheric boundary layer, e.g. Lu and Porté-Agel [39] and Calaf et al. [16]. The simulations have provided valuable insights into wake dynamics, but run times are long and thus unsuitable for engineering applications as testing and optimizing different wind farm layouts require numerous runs.

Present Work

The present work aims to contribute additional knowledge on wakes and wake interaction deep within large wind farms. Gaining more knowledge on the complex wake interaction is an crucial part of the continued optimizing of wind turbine design and wind farm layouts in order to improve the overall efficiency and lower the cost of energy. The work includes the analyses of numerous simulations, from the study of the wake behind a single turbine (Chapter 3) via idealised cases of infinite rows of wind turbines (Chapter 4) before investigating cases of infinite wind farms operating in an atmospheric boundary layer(Chapter 5). This natural progression is chosen in order to isolate and investigate the individual effects leading to the highly complex wake dynamics deep inside large wind farms operating in the atmospheric boundary layer. The analyses of these simulations set out to investigate the key components of the turbulent wake interaction with the aim of constructing a new dynamic wake model describing the complex inflow experienced by wind turbines operating in large wind farms. The wake models are constructed and validated in Chapter 6. Preliminary results have been reported in Andersen et al. [5] and [6].

The tradeoff between capturing the complex dynamics of the flow and the need for short computational times remain a pending issue in developing dynamic wake models applicable to wind turbine design and wind farm optimization. Sanderse [55] listed three criterias which any successful wake model should fulfill:

1. Performance and Efficiency: The wake model must enable the engineer to calculate the rotor performance and overall park efficiency, which requires a good prediction of the time-averaged wake velocity profile.

2. Dynamic Load and Power Prediction: Reliable prediction of the dynamic loads experienced by the turbine and the fluctuations in power production are key for design optimization, and both are related to the turbulent fluctuations in the wake.

3. Large Turbulent Structures: The wake model must include the prediction of large scale turbulent structures(meandering).

The proposed wake models are derived from detailed CFD computations using Actuator Line and LES to simulate the turbulent wake interaction deep inside large wind farms. Therefore, the underlying assumption throughout this analysis is that the numerical simulations model the fundamental physics correctly. Proper Orthogonal Decomposition(POD) is employed to extract and identify the dominant turbulent structures, which will eventually form the basis for two proposed wake models. POD is also known as or closely related to Principal Component Analysis(PCA), Karhunen-Loève Transform(KLT), EigenValue Decomposition(EVD), and Singular Value Decomposition(SVD). The application of POD determines a set of optimal and orthogonal components with decreasing variance, which can be used for data compression, e.g. for image compression. POD is considered the most efficient linear decomposition, e.g. more efficient than a Fourier decomposition, because it determines an optimal set of modes, which maximize the kinetic energy content. In the field of fluid dynamics, POD has proven very useful in examining and detecting large coherent turbulent structures, as first proposed by Lumley [40]. Pioneering work have been conducted by Aubry et al. [10] as well as Sirovich [60], who developed the so-called snapshot POD. POD have traditionally been applied extensively to experimental data, e.g. Citriniti and George [17] and Johansson and George [30]. In recent years POD has also become increasingly popular as an analysis tool for CFD data with the advent of powerful supercomputers, which enables handling of the huge data sets generated by CFD, e.g. Noack et al. [50].

The two proposed wake models are comprised of a truncated reconstruction of the turbulent flow based on POD. As such the models are low-dimensional models or reduced order models, which is a well-known approach from other fluid dynamic areas. Examples of low-dimensional models include the wake behind a cylinder, see Noack et al. [50], flow around an airfoil by Stankiewicz et al. [66], and cavity driven flow by Jørgensen et al. [31]. Such low-dimensional models are often employed for flow control, see Noack et al. [49], because low-dimensional models capture the dynamics and are computational efficient enough to enable the fast adoption by actuators to anticipate highly dynamic changes in the flow.

Initial application of POD in the field of wind turbines have been done by Spitler et al. [65], Lindberg et al. [38], Saranyasoontorn and Manuel [56] and [58], and Troldborg [68]. Lindberg et al. and Spitler et al. applied POD to measurements in the atmospheric boundary layer and validated the promising potential of applying POD for optimal flow representation as opposed to Fourier decomposition. Saranyasoontorn and Manuel [56] created a compelling low-dimensional model for the turbulent inflow for wind turbines by applying POD on turbulence generated using a Kaimal spectral model. The model was verified by examining the turbine response and loads, which showed very good agreement.

The present work aims to create a wake model, which describe and capture the highly dynamic and turbulent inflow based on detailed turbulence modelling of the flow deep inside large wind farms. The wake models aspire to capture the necessary dynamics in order to address all three criterias satisfactorily within one dynamic model and be computational efficient enough to settle the aforementioned tradeoff between the fast and simple kinematic models and the expensive and detailed CFD computations.

Since the two proposed models are derived directly from the simulated physics, the verification process is essentially a matter of determining the min-

imum number of fundamental components needed to reconstruct a flow, which results in matching any given parameter, e.g. power production or load. Eventually, the models could be verified against actual wind farm data to validate the simulated physics.

Chapter 2

Methodology

This chapter presents the background and theory for the general flow solver EllipSys3D and the implemented LES model and Actuator Line(AL) method. The approaches for introducing turbulence into the domain, modelling an atmospheric boundary layer as well as ensuring a constant mass flux are also presented. Furthermore, it outlines the methodology used in the following analysis, which includes determining statistical convergence of the flow before performing a Proper Orthogonal Decomposition(POD). POD forms the basis for the REDuced Order MOdel(REDOMO), which again will be verified by comparing time series and equivalent loads.

2.1 Flow Solver

The numerical simulations are performed using the 3D flow solver EllipSys3D, which has been developed as a collaboration between DTU(Michelsen [46]) and the former Risø(Sørensen [64]). This code solves the discretised incompressible Navier-Stokes equations in general curvilinear coordinates using a block structured finite volume approach. EllipSys3D is formulated in primitive variables (pressure-velocity) in a collocated grid arrangement. In the present work, the pressure correction equation is solved using the PISO algorithm and pressure decoupling is avoided using the Rhie/Chow interpolation technique. The convective terms are discretised using a hybrid scheme combining the third order QUICK scheme and the fourth order CDS scheme. This technique was employed as a compromise to limit unphysical numerical wiggles related to a pure fourth order scheme as well as numerical diffusion due to the upwind biasing nature of the QUICK scheme.

Large Eddy Simulation applies a low-pass filter on the Navier-Stokes equations, which results in a filtered velocity field. The scales resolved by the grid are simulated directly by the filtered Navier-Stokes equations whereas scales below the grid scale is modelled through a sub-grid scale(SGS) model, which provides the turbulence closure. Therefore, the velocity($\mathbf{V}$) is decomposed into a sum of the filtered velocity($\overline{\mathbf{V}}$) containing the large scales and the small scales($\mathbf{v}'$) calculated using a sub-grid scale(SGS) model:

$$\mathbf{V} = \overline{\mathbf{V}} + \mathbf{v}' \tag{2.1}$$

The resemblance to Reynolds decomposition is evident, but the Reynolds decomposition is filtered in time, whereas LES is a spatial filtering, and generally $\overline{\mathbf{v}'} \neq 0$. Further details of spatial filtering and SGS model are given in Section 2.1.1.

The flow field is thus approximated by solving the filtered 3D incompressible Navier-Stokes equations for $\overline{\mathbf{V}}$:

$$\frac{\partial \overline{\mathbf{V}}}{\partial t} + \overline{\mathbf{V}} \cdot \nabla \overline{\mathbf{V}} = -\frac{1}{\rho}\nabla \overline{p} + \nabla[(\nu + \nu_{SGS})\nabla \overline{\mathbf{V}}] + \frac{1}{\rho}\mathbf{f}_{WT} + \frac{1}{\rho}\mathbf{f}_{turb} + \frac{1}{\rho}\mathbf{f}_{pbl} + \frac{1}{\rho}\mathbf{f}_{mf}. \quad (2.2)$$

$$\nabla \overline{\mathbf{V}} = 0. \quad (2.3)$$

where ρ denotes density, p is pressure, and ν is eddy viscosity. A number of actuators or body forces($\mathbf{f}_{WT}$, $\mathbf{f}_{turb}$) $\mathbf{f}_{pbl}$ and $\mathbf{f}_{mf}$ are explicitly applied in the simulations to model the effect of the wind turbine, atmospheric turbulence, atmospheric boundary layer, and to account for any loss in mass flux. The individual body forces are described in detail in Section 2.1.2, 2.1.3, 2.1.4 and 2.1.5, respectively. The flow solver is implemented in a normalised form, i.e. the velocity components ($\overline{\mathbf{V}} = (U, V, W)$) are scaled by the freestream velocity U_0. U, V, and W will be used interchangeable with $\frac{U}{U_0}$, $\frac{V}{U_0}$, and $\frac{W}{U_0}$ for the streamwise, lateral, and vertical velocity component.

2.1.1 Large Eddy Simulation

The two key components of LES are the spatial filtering and modelling the SGS viscosity through a SGS model, and the current implementation is based on the mixed scale model by Ta Phuoc et al. [67].

The SGS viscosity is determined by:

$$\nu_{SGS}(\beta)(\mathbf{x}, f) = \rho C_m |\nabla \times \overline{\mathbf{V}}(\mathbf{x}, t)|^{\beta} \left(q_c^2\right)^{\frac{1-\beta}{2}} (\mathbf{x}, t) \overline{\Delta}^{1+\beta} \quad (2.4)$$

where ρ is the density of air, $\overline{\mathbf{V}}$ is the filtered velocity, $\overline{\Delta}$ is the filter cut-off length, which is set equal to $(\Delta Vol)^{1/3}$, where ΔVol is the volume of a given cell. $\mathbf{x} = (X, Y, Z)$ denotes the streamwise, lateral, and vertical direction. C_m and β are constants set to 0.01 and 0.5.

The kinetic energy q_c^2 is evaluated as:

$$q_c^2(\mathbf{x}, t) = \frac{1}{2}\left(\overline{\mathbf{V}} - \tilde{\overline{\mathbf{V}}}\right)\left(\overline{\mathbf{V}} - \tilde{\overline{\mathbf{V}}}\right) \quad (2.5)$$

where $\overline{\mathbf{V}} - \tilde{\overline{\mathbf{V}}}$ represents the high frequency part of the resolved velocity field found by subtracting the velocity resolved using a second filter $\tilde{\overline{\mathbf{V}}}$, referred to as the test filter. The test filter is twice the size of the actual filter ($\tilde{\Delta} = 2\overline{\Delta}$),

and the discrete implementation for calculating $\widetilde{\overline{\mathbf{V}}}$ for the kinetic energy is:

$$\begin{aligned}
\widetilde{\overline{\mathbf{V}}} = & \frac{1}{8} \cdot \overline{\mathbf{V}}(i,j,k) \\
& + \frac{1}{16}\big(\overline{\mathbf{V}}(i+1,j,k) + \overline{\mathbf{V}}(i-1,j,k) + \overline{\mathbf{V}}(i,j+1,k) \\
& \qquad + \overline{\mathbf{V}}(i,j-1,k) + \overline{\mathbf{V}}(i,j,k+1) + \overline{\mathbf{V}}(i,j,k-1)\big) \\
& + \frac{1}{32}\big(\overline{\mathbf{V}}(i-1,j-1,k) + \overline{\mathbf{V}}(i-1,j+1,k) + \overline{\mathbf{V}}(i+1,j-1,k) \\
& \qquad + \overline{\mathbf{V}}(i+1,j+1,k) + \overline{\mathbf{V}}(i-1,j,k-1) + \overline{\mathbf{V}}(i-1,j,k+1) \\
& \qquad + \overline{\mathbf{V}}(i+1,j,k-1) + \overline{\mathbf{V}}(i+1,j,k+1) + \overline{\mathbf{V}}(i,j-1,k-1) \\
& \qquad + \overline{\mathbf{V}}(i,j-1,k+1) + \overline{\mathbf{V}}(i,j+1,k-1) + \overline{\mathbf{V}}(i,j+1,k+1)\big) \\
& + \frac{1}{64}\big(\overline{\mathbf{V}}(i-1,j-1,k-1) + \overline{\mathbf{V}}(i-1,j-1,k+1) \\
& \qquad + \overline{\mathbf{V}}(i-1,j+1,k-1) + \overline{\mathbf{V}}(i+1,j-1,k-1) \\
& \qquad + \overline{\mathbf{V}}(i-1,j+1,k+1) + \overline{\mathbf{V}}(i+1,j-1,k+1) \\
& \qquad + \overline{\mathbf{V}}(i+1,j+1,k-1) + \overline{\mathbf{V}}(i+1,j+1,k+1)\big)
\end{aligned} \tag{2.6}$$

The mixed scale model has been chosen because of its simplicity and because it accounts for the dissipation of energy at the same time as it ensures the interaction between the smallest resolved scales and the largest unresolved scales. For a general overview of different models, see Sagaut [54].

2.1.2 Turbine Modelling

The influence of the wind turbine is simulated using the Actuator Line(AL) technique. AL applies body forces distributed along rotating lines representing the blades of the wind turbine, see Sørensen and Shen [63] for details. AL was implemented in EllipSys3D by Mikkelsen [47]. The body forces imposed in the NS equations are calculated using Flex5, a full aeroelastic code for calculating deflections and loads on wind turbines, see Øye [52]. The aerodynamic loads are calculated using a blade element approach, which takes the dynamic influence of the induced velocities from the wake into account. This effect on the local inflow conditions are important to get realistic predictions of the response of changing the pitch angle, which forms the basis for the design of the control system for a pitch regulated wind turbine.

Figure 2.1 shows the local velocities and forces acting on a cross-sectional airfoil segment. The local velocity triangle relative to the rotating airfoil segment is determined from the velocity triangle, where $V_x(=U)$ and V_θ are the velocities in the axial and tangential directions, respectively, and the relative velocity at the blade section is given as:

$$V_{rel} = \sqrt{V_x^2 + (\Omega r + V_\theta)^2} \tag{2.7}$$

The flow angle is given as $\phi = tan^{-1}\left(\frac{V_x}{\Omega r + V_\theta}\right)$, where Ω denotes the rotor speed. This gives the local angle of attack as $\alpha = \phi - \gamma$, with γ denoting the local pitch angle. Lift and drag forces are found from:

$$\mathbf{f}_{2D} = (\mathbf{L}, \mathbf{D}) = \frac{1}{2}\rho V_{rel} c B (C_L \mathbf{e}_L, C_D \mathbf{e}_D) \tag{2.8}$$

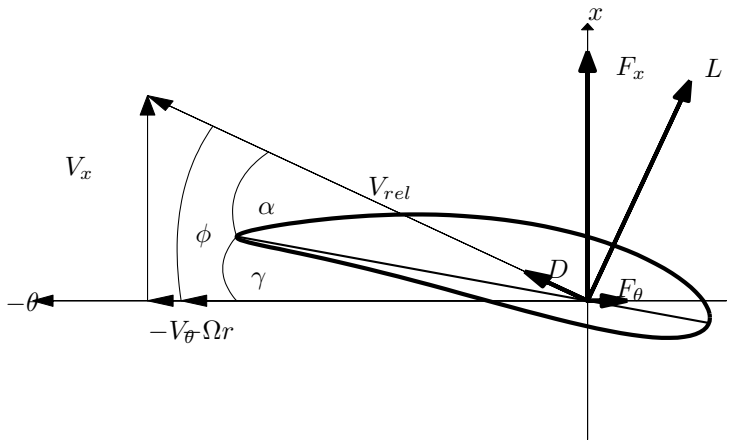

Figure 2.1: Velocity triangle showing velocity and force vectors used in the Actuator Line method.

where $C_L(\alpha, Re)$ and $C_D(\alpha, Re)$ are lift and drag coefficients as function of angle of attack(α) and Reynolds number(Re), given as tabulated data. The Reynolds number is based on chord length and relative velocity. $\mathbf{e_L}$ and $\mathbf{e_D}$ are unit vectors parallel to lift and drag and B is the number of blades. Projection gives the axial and tangential forces, F_x and F_θ. The body forces are numerically smeared across a few cells to avoid singularities. The smearing is Gaussian distributed by applying a convolution to the local load $\mathbf{f}_{2D}$ using a regularization kernel(η_ϵ) as follows:

$$\mathbf{f_{WT}}(\mathbf{x}) = \sum_{i=1}^{B=3} \int_0^R \mathbf{f}_{2D}(r)\eta_\epsilon(\|\mathbf{x} - r\mathbf{e}_i\|)dr. \quad \eta_\epsilon = \frac{1}{\epsilon^3\pi^{3/2}} exp[-(r/\epsilon)^2] \quad (2.9)$$

Here, $r = \|\mathbf{x} - r\mathbf{e}_i\|$, where $\|\ \|$ is the euclidean norm, i.e. the distance between the grid point and the force points on the $i'th$ actuator line denoted by the unit vector $\mathbf{e}_i$.

The advantage of representing the individual blades by line-distributed loads is that much fewer grid points are needed to model the influence of the blades, as compared to resolving and simulating the actual geometry of the blades. The actuator line model allows for detailed studies of the dynamics of the different wake structures, such as the tip and root vortices, using a reasonably low number of grid points. Furthermore, the model benefits from being applicable with simple structured grids and therefore issues connected to grid generation do not occur. The drawback of the method is that it relies on the quality of tabulated airfoil data.

Airfoil data corresponding to an upscaled verion of the NM80 turbine is used in the present work. The NM80 turbine is proprietary to Vestas Wind Systems A/S, so certain details of the turbine and performance are excluded, but reference is made to the DAN-AERO MW Experiments, see Madsen et al. [1]. The 2D airfoil data is corrected to account for 3D effects, see e.g. Hansen et al. [26] for a generic description of how to correct for 3D effects. NM80 is a three bladed horizontal axis wind turbine with a radius $R = 40m$ and rated to

$2.75MW$ at a hub velocity of $U_{hub} = 14m/s$. This is upscaled from the original NM80 rated at $2.00MW$. The simulations exclude the effect of the tower. Zahle and Sørensen [73] assessed the influence of the tower to reduce thrust and torque by $1 - 2\%$, but this effect is excluded in the present simulations.

A general controller is implemented for the turbine which is a combination of a variable speed P-controller for the generator for wind speeds below rated($U_{hub} < 14m/s$) and a PI-pitch angle controller for higher wind speeds, see Larsen and Hanson [36] or Hansen et al. [25] for a general description of such a controller. The variable speed controller sets the power setpoint based on the lowpass filtered generator speed, which basically means that the power production is related to wind speed as $P \propto U^3$. The PI-pitch angle controller keeps a constant power production by changing the global blade pitch. The controller is tested using a sweep or step curve, where the inflow velocity is incrementally increased and subsequently decreased, as given in Figure 2.2.

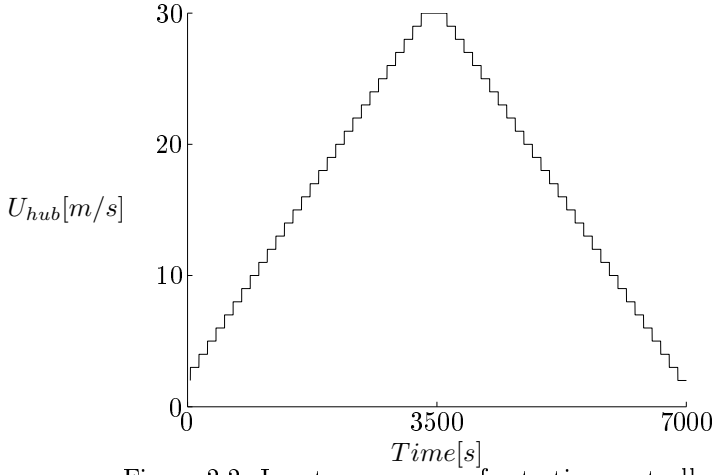

Figure 2.2: Input sweep curve for testing controller.

The resulting pitch, generator speed, C_T, and power curves as function of U_{hub} for the NM80 turbine is shown in Figure 2.3, where the rated speed is marked by vertical lines. The generator speed is increased with increasing wind speed, and as the power increases to rated, the generator speed and power is kept constant by changing the pitch. The C_T-curve is plotted with a generic expression for determing C_T given by Frandsen [19] as:

$$C_T \approx \frac{7}{U_{hub}} \tag{2.10}$$

The generic expression is a good approximation for $U_{hub} \in [8 - 13]m/s$. The power curve is plotted with constant C_P-curve($P \propto U^3$) for comparison, which is also a good approximation.

The implemented controller essentially means that the rotor is not constantly loaded, and as such it operates like a real turbine. Therefore, the aeroelastic code and flow solver are fully coupled.

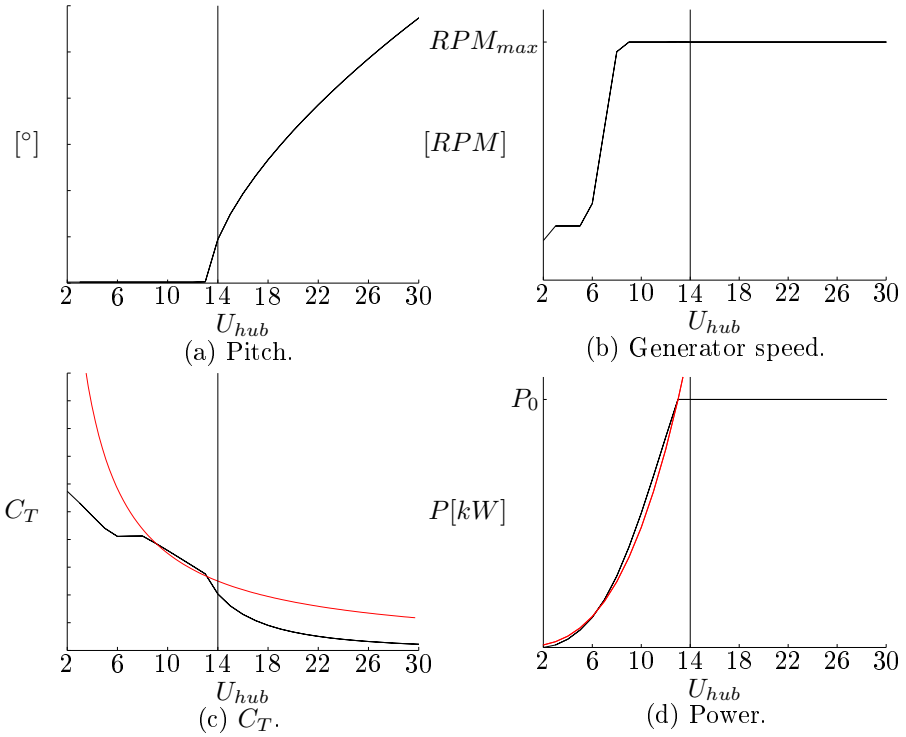

(a) Pitch. (b) Generator speed. (c) C_T. (d) Power.

Figure 2.3: Pitch, generator speed, C_T, and power curve for the NM80 turbine. Legend: ——: Mean values. - - - : Max and min values. ——: (c) $C_T = \frac{7}{U_{hub}}$. (d) $P \propto U_{hub}^3$

2.1.3 Introducing and Modelling Atmospheric Turbulence

The atmospheric turbulence is introduced into the flow by imposing small body force fluctions($\mathbf{f}_{turb}$) into the flow. These body forces corresponds to turbulent fluctuations generated by the so-called Mann model, see Mann [42] and [43] for details. The Mann turbulence employs a spectral tensor derived from a linearization of the incompressible Navier-Stokes equations. It generates a 3D field of all three velocity components following Taylor's frozen turbulence hypothesis, i.e. linking time and space. The second order statistics (variance, cross-spectra etc.) are matched to those occuring in a neutral atmosphere and the generated turbulence is homogenous, anisotrophic and stationary.

The body forces are introduced into the flow (see Equation 2.2) in a plane upstream the turbines. This approach is usually used to decrease the total number of mesh points, because a coarser grid can be used upstream the turbulence plane as opposed to the alternative of imposing the turbulent fluctuations at the inlet boundary, which then requires a finely resolved mesh to transfer the turbulent structures correctly downstream. All meshes for the present simulations have equidistantly distributed grid points in the streamwise direction, so it is not a major concern. For a validation of the method, reference is made to Gilling et al. [23]. The magnitude of the body forces are calculated as:

$$\mathbf{f}_{fluc} = \dot{m}\mathbf{u} + \rho\epsilon\frac{d\mathbf{u}}{dt} \tag{2.11}$$

where $\dot{m}$ is the mass flux and ϵ is a parameter, which controls the concentration of the body forces or smearing. Similar to the body forces for the turbine blades, the body forces for the atmospheric turbulence is smeared in the domain to avoid singularities. However, the body forces for the atmospheric turbulence is smeared perpendicular to plane using a 1D Gaussian convolution(as opposed to 3D in the AL method):

$$\mathbf{f}_{turb}(x) = \mathbf{f}_{fluc} \otimes \eta_\epsilon \qquad \eta_\epsilon(x) = \frac{1}{\epsilon\sqrt{\pi}} exp\left[-\left(\frac{x - x_d}{\epsilon}\right)^2\right] \tag{2.12}$$

Here $x - x_d$ is the normalised distance between the point in question and the turbulence plane. Usually, the articifial Mann turbulence is generated on a coarser mesh than the mesh used for the CFD computations. Therefore, the body forces are interpolated both spatially and temporally before being applied in the domain.

One simulation is performed by adding atmospheric turbulence at high altitudes. This special case is modelled to mimic the case of a fully developed wind farm, and to investigate whether large scale turbulent structures from the atmospheric boundary layer can penetrate the boundary layer formed by the wind turbines. A more or less arbitrary vertical distribution function($\zeta(z)$) is applied to ease the transition between the applied turbulence in the atmospheric boundary layer and the boundary layer formed over the wind turbines. The vertical distribution is taken as:

$$\zeta(z) = \frac{1}{2}\left(1 + \tanh\left(\frac{1}{10}z\right)\right) \tag{2.13}$$

The applied profile is shown in Figure 2.4. It should be emphasized that it is a scaling factor applied to a given turbulence intensity, e.g. 10%, and as such the

plotted scale is grossly exaggerated. The profile effectively alters the turbulent statics, but the investigation of adding turbulence at high altitudes is more a qualitative investigation of the overall mixing processes and the ability for high altitude turbulence to penetrate into the wind farm and the detailed statistics of the applied turbulence is of less importance.

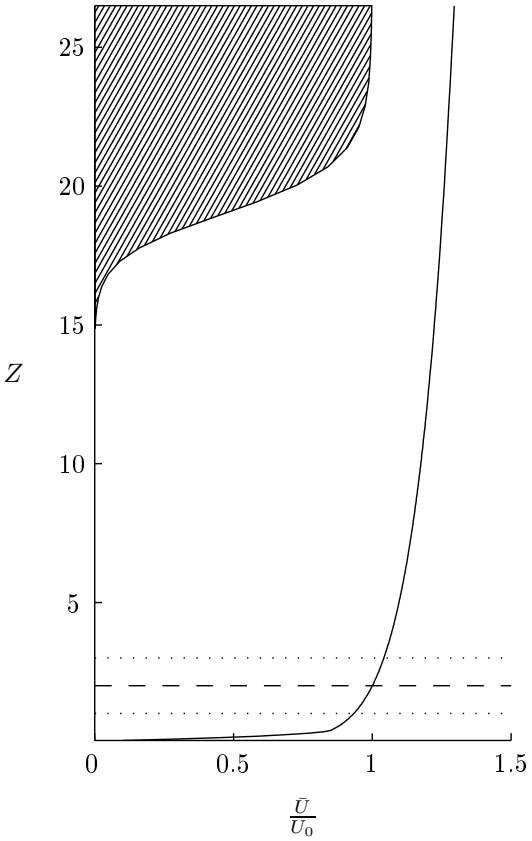

Figure 2.4: Vertical shape factor applied to the high altitude turbulence and the prescribed boundary layer.

2.1.4 Prescribed Boundary Layer

The atmospheric boundary layer is usually modelled in one of two ways.

The flow can be modelled as it develops freely into an atmospheric boundary layer due to various effects, e.g. roughness through a non-slip boundary condition and heat transfer, which in turn gives rise to various boundary layers, i.e. unstable(ground hotter than the air), neutral or stable(ground colder than the air). The freely developing boundary layer is often solved using LES models, see for instance Lu and Porté-Agel [39]. This approach usually demands a precursor simulation, where the flow converge towards a given boundary layer profile. Alternatively, a very large domain can be utilized. A domain large enough for the flow to converge before the region of interest, e.g. in the present case wind turbines.

An alternative method is a more engineering approach of modelling the atmospheric boundary layer by applying internal body forces as described by Mikkelsen et al. [48]. This approach is based on a simple 1D momentum fit and is employed in the present simulations. The advantage of this approach is a much shorter precursor simulation is needed, which determines the body forces necessary to maintain any desired arbitrary boundary layer profile, henceforth also denoted prescribed boundary layer(PBL). It is important to emphasize that the determined body forces are maintained constant throughout the simulations, hence acting similar to a constant pressure gradient. Details of the method have been investigated by Troldborg et al. [70], who also examined the effective magnitude of the imposed body forces. The imposed body forces were shown to be inversely proportional to the Reynolds number and hence the impact of the body forces on the wake development was deemed insignificant by Troldborg et al. A slip boundary condition is imposed at the ground, since a non-slip condition would counter-act the prescribed boundary layer. The present implementation stipulates the prescribed boundary layer as a combination of a parabolic and a power law profile. The combined profile is governed by:

$$U_{pbl}(z) = \begin{cases} U_0 \cdot (c_2 z^2 + c_1 z) & z \leq \Delta_{PBL} \\ U_0 \cdot \left(\frac{z}{H_{hub}}\right)^{\alpha_{PBL}} & z > \Delta_{PBL} \end{cases}$$

where Δ_{PBL} determines the height, where the profile shift from the parabolic to power law profile. H_{hub} is the hub height, c_1, c_2, and α_{PBL} are shape parameters. c_1 and c_2 are calculated to ensure a smooth transition between the parabolic and the power law expression using the following expressions:

$$c_1 = \frac{U_{hub}}{H_{hub}} \cdot (2 - \alpha_{PBL}) \cdot \left(\frac{\Delta_{PBL}}{H_{hub}}\right)^{(\alpha_{PBL}-1)} \tag{2.14}$$

$$c_2 = \frac{U_{hub}}{H_{hub}} \cdot \frac{1}{\Delta_{hub}} \cdot (\alpha_{PBL} - 1) \cdot \left(\frac{\Delta_{PBL}}{H_{hub}}\right)^{(\alpha_{PBL}-1)} \tag{2.15}$$

The prescribed boundary layer is scaled to have a velocity of unity at hub height, U_{hub}. The boundary layer is also considered neutral as no thermal effects are included in the simulations. The prescribed boundary layer is included in the simulations presented in Section 5 and the boundary layer is shown in Figure 2.4.

2.1.5 Ensuring Constant Mass Flux

The majority of the simulations employ cyclic boundary conditions and very long run times, which would usually lead to a decrease in mass flux as the turbine extracts energy from the flow. Therefore, the mass flux is continously corrected to account for the energy extracted by the turbines by applying small body forces ($\mathbf{f}_{mf}$) distributed evenly throughout the domain. These body forces essentially also corresponds to a pressure gradient, although varying in time as opposed to the body forces governing the prescribed boundary layer. The correction is only applied in conjuction with cyclic boundary conditions and is calculated using a Proportional-Integral-Derivative(PID) controller to correct for the error or loss of mass flux. The error or deviation (ξ_j) for a given time

step j is defined as the difference between the initial mass flux (ϕ_0) and the mass flux at time $j(\phi_j)$:

$$\xi_j = \phi_0 - \phi_j = \int_{\mathbf{S}} \rho \mathbf{u}_0 d\mathbf{S} - \int_{\mathbf{S}} \rho \mathbf{u}_j d\mathbf{S} \tag{2.16}$$

where $\mathbf{S}$ is the surface of the domain. The PID controller integrates over the previous 20 time steps, so the correcting body force at time j is given as

$$\mathbf{f}_{mf,j} = K_p \xi_j + K_i \int_{t=j-19}^{t=j} \xi(t) dt + K_d \frac{d\xi_j}{dt} \tag{2.17}$$

The coefficients K_p, K_i, and K_d of the PID controller has been set to 2, 1, and 1 respectively. This ensures that the mass flux is kept constant during the simulation time.

2.2 Analysis Methodology

The majority of the analyses focus on examining data extracted in vertical slices, often immediately ($1R$) in front of the first turbine, i.e. the incoming flow as seen by the turbine. The mean velocities, root mean square(RMS) values of the turbulent fluctuations, Reynolds stresses, and the Turbulent Kinetic Energy production terms are collectively denominated the turbulent quantities in the following. Slices of data are extracted approximately every $0.1s$.

Standard definitions (see Pope [53]) are used to calculate Reynolds stresses, Turbulent Kinetic Energy (TKE), and TKE production although density, ρ, and viscosity, ν are excluded. The Reynolds stresses are calculated as:

$$\tau_{ij} \equiv \overline{u_i' u_j'} \tag{2.18}$$

where $u_i' = U_i - \overline{U}$ is the fluctuating part and $\overline{U}$ denotes the time average of the streamwise velocity(U) for $i = 1$. Similarly for the lateral velocity(V) for $i = 2$ and vertical velocity(W) for $i = 3$. TKE is half the trace of the Reynolds stress tensor:

$$TKE \equiv \frac{1}{2} \overline{u_i' u_i'} \tag{2.19}$$

The production of TKE is calculated as:

$$\mathcal{P} \equiv -\overline{u_i' u_i'} \frac{\partial \overline{U}}{\partial X_j} \tag{2.20}$$

As previously mentioned, all velocities have been normalised by U_0. Therefore, the turbulent quantities are dimensionless. The turbulent quantities form the basis for determining when the turbulent flow has converged towards a random stationary process, defined as a window and period where the spatial RMS values of these turbulent quantities do not change (significantly) over time. This analysis is performed in Section 4.5.

The two point cross-correlations are calculated to investigate the coherent structures in the flow. The two point cross-correlation over time of two time series $u_1(t)$ and $u_2(t)$ are calculated as:

$$\hat{R}(\tau) = \frac{\sum_i^N [(u_1(t_i) - \overline{u}_1)(u_2(t_i - \tau) - \overline{u}_2)]}{\sqrt{\sum_i^N (u_1(t_i) - \overline{u}_1)^2} \sqrt{\sum_i^N (u_2(t_i - \tau) - \overline{u}_2)^2}} \tag{2.21}$$

where τ is the range of possible delays within the time series($t \in [0;T]$) for $i = 1, 2, \ldots, N$. The two point cross-correlation can also be calculated spatially by substituting time with radial position(r):

$$\hat{R}(r) = \frac{\sum_i^N [(u_1(r_i) - \langle u_1 \rangle_r)(u_2(r_i - \mathcal{R}) - \langle u_2 \rangle_r)]}{\sqrt{\sum_i^N (u_1(r_i) - \langle u_1 \rangle_r)^2} \sqrt{\sum_i^N (u_2(r_i - (R)) - \langle u_2 \rangle_r)^2}} \tag{2.22}$$

where $\langle \rangle_r$ is the radial average and $\mathcal{R}$ is the radial distance. The integral length scale is define by:

$$T_E = \int_0^T \hat{R}(r) d\mathcal{R} \tag{2.23}$$

which yields a length scale for the coherent structures.

2.3 Proper Orthogonal Decomposition

POD is a statistical method yielding an optimal linear subspace, optimal in terms of the variance of the energy content, i.e. it ensures that the sorted modes contain the most energetic states. As such, POD requires fewer modes than a Fourier or other transformations to reconstruct a turbulent field, Spitler et al. [65]. POD was first introduced as an analysis tool for turbulence studies by Lumley [40], and POD has since proved a valuable method for examining coherent structures in turbulent flows. The starting point for the decomposition is a hermetian symmetric two-point velocity correlation tensor based on the fluctuations:

$$R_{i,j}(\mathbf{x}, \mathbf{x}', t, t') = \overline{u_i(\mathbf{x}, t), u_j^*(\mathbf{x}', t')} \tag{2.24}$$

where u_j^* is the complex conjugate. Subsequently, the integral eigenvalue equation of Fredholm type is solved:

$$\int R_{i,j}(\mathbf{x}, \mathbf{x}', t, t') \mathbf{g}_j(\mathbf{x}', t') = \lambda \mathbf{g}_j(\mathbf{x}', t') \tag{2.25}$$

The solution yields an optimal subspace given as a set of real eigenvalues λ:

$$\lambda_1 \geq \lambda_2 \geq \lambda_3 \geq ... \geq \lambda_N \tag{2.26}$$

and orthogonal eigenfunctions containing the temporal variations for the individual modes. For additional details, see the seminal work by Sirovich [60], Aubry et al. [10], one of the examples mentioned in the Introduction or the general overview given by Berkooz et al. [14].

A brief overview of the practical implementation of POD is given in the following, adapted from Jørgensen et al. [31]. The three velocity components are extracted as vertical planes perpendicular to the main flow direction and POD is applied to all three velocity components, as opposed to Saranyasoontorn and Manuel [56], who only applied POD to the streamwise direction. POD is only applied in the equidistant grid region, as there should otherwise be added a spatial weighting matrix. The normalised velocity components ($\mathbf{u} = (U, V, W)$) of each of the N extracted slices are organised in vectors $\mathbf{u_i}$, which constitute a matrix defined as:

$$\mathbf{U} = [\mathbf{u_1'} \ldots \mathbf{u_N'}] \tag{2.27}$$

It is common to subtract the mean value $\mathbf{u_0}$, because it essentially reduces the number of dimensions by one. Therefore, $\mathbf{u'_j}$ is defined as:

$$\mathbf{u'_j} = \mathbf{u_j} - \frac{1}{N}\sum_{i=1}^{N} \mathbf{u_i} = \mathbf{u_j} - \mathbf{u_0} \tag{2.28}$$

The $N \times N$ auto-covariance matrix is then given as:

$$\mathbf{R} = \mathbf{U^T U} \tag{2.29}$$

Defining an eigenvalue matrix with $\lambda_1 \geq \lambda_2 \geq \ldots \lambda_{N-1} > 0$:

$$\mathbf{\Lambda} = \begin{pmatrix} \lambda_1 & & \mathbf{0} \\ & \ddots & \\ \mathbf{0} & & \lambda_{N-1} \end{pmatrix}$$

and matrix of orthonormal eigenvectors:

$$\mathbf{G} = [\mathbf{g_1} \ldots \mathbf{g_{N-1}}] \tag{2.30}$$

yields an eigenvalue problem of the form (equivalent to Equation 2.25 on integral form):

$$\mathbf{RG} = \mathbf{G\Lambda} \tag{2.31}$$

The basis vectors or POD modes can be written as:

$$\phi_k = \frac{\mathbf{U g_j}}{\|\mathbf{U g_j}\|} \tag{2.32}$$

These are spatial modes, which contain information on the coherent structures. POD can be considered an energy filter, which reveal the large spatial turbulent structures. It is important to note that some of these individual structures or POD modes might not be physical structures in the sense that they are visible or measurable to an observer, but merely a result of the mathematical operations lumping the energy content into an optimal set of modes.

The original vectors $\mathbf{u'_j}$ containing the velocity components of slice $\mathbf{j}$ can be reconstructed from:

$$\mathbf{u'_j} = \sum_{k=1}^{N-1} \phi_k a_{kj} \tag{2.33}$$

where a_{kj} are the elements of $\mathbf{A} = \mathbf{\Phi^T U}$. $\mathbf{A}$ contains the temporal eigenfunctions, which determines the development of the spatial POD modes, as described by Aubry [9], who referred to it as the biorthogonal decomposition, when examining the temporal eigenfunctions.

Since the eigenvalues or POD modes are sorted in terms of variance(equivalent to turbulent kinetic energy), it is possible to approximate the flowfield by truncating the reconstruction by only including the first K POD modes:

$$\mathbf{u_j} \approx \widehat{\mathbf{u}}_\mathbf{j} = \mathbf{u_0} + \sum_{k=1}^{K} \phi_k a_{kj} \tag{2.34}$$

where $\widehat{\mathbf{u}}$ is the POD truncated reconstruction of $\mathbf{u}$.

2.4 Reduced Order Model

Effectively, POD lumps energy together in spatial modes. An additional truncation of the temporal eigenfunctions attempts to lump the energy from the corresponding spectrums onto a few key frequencies. Truncating both the spatial and temporal modes enables an additional reduction in the reconstruction of the flow through a Reduced Order Model ($\widetilde{\mathbf{u}}$). $\mathbf{A}$ contains the temporal development of the POD modes, and since the flow has approached a random stationary process the eigenfunctions are composed of Fourier modes. The dominant frequencies of the temporal eigenfunctions can be identified through spectral analysis and choosing an optimal combination of these dominant frequencies($f_{k,m}$) makes it possible to reconstruct the flow field:

$$\mathbf{u_j} \approx \widehat{\mathbf{u}}_\mathbf{j} \approx \widetilde{\mathbf{u}}_\mathbf{j} = \mathbf{u_0} + \beta \sum_{k=1}^{K} \phi_k \widetilde{a}_{kj} \tag{2.35}$$

$$= \mathbf{u_0} + \sum_{k=1}^{K} \phi_k \sum_{m=1}^{M} (\beta_{k,m}^{(1)} cos(2\pi f_{k,m} t_j) - \beta_{k,m}^{(2)} sin(2\pi f_{k,m} t_j)) \tag{2.36}$$

Here, k denote the POD mode and m denote the dominant frequency number for a given POD mode. The coefficients $\beta_{k,m}$ are determined by optimising the reconstruction by solving a least square problem $||b - Ax||^2$ to obtain x. In the present implementation, b is the full flow solution($\mathbf{u_j}$), $A = \sum_{k=1}^{K} \phi_k \widetilde{a}_{kj}$, and $\beta^{(1,2)}$ are the solutions to the least squares problem, i.e. minimizing $||\mathbf{U} - \widetilde{\mathbf{U}}||^2$. The enormous size of the least squares problem requires an iterative method and the LSMR algorithm by Fong and Saunders [18] is utilized. The LSMR method[1] is based on a Golub-Kahan bidiagonalization of the matrix A, which is theoretically spares. The LSMR was tested on smaller problems with full matrices and gave identical results to solving the least squares problem with a Single Value Decomposition and is hence employed for the larger least squares problem.

2.5 Verification of Wake Models

The full flow simulated using EllipSys3D is assumed to resemble the true flow, which occurs in large wind farms. The proposed wake models are based on a number of key spatial and temporal modes derived from this flow. The reconstruction in terms of energy variance is naturally a direct measure of how good the reconstruction of the flow is. However, the wake models are only the mean to achieve the overall aim of eventually constructing a more dynamical and physical correct wake model for optimizing turbine performance, design, and wind farm layout. Therefore, the true measure of the quality of any wake model is to investigate the turbine performance and response compared to the actual inflow obtained either by measurements or CFD. As for the CFD computations, the turbine is modelled using the aeroelastic code Flex5 (Øye [52]). An aeroelastic computation yields a whole range of structural loads and performance parameters. The verification will focus on the velocity at hub height, power

[1] LSMR: `http://www.stanford.edu/group/SOL/software/lsmr.html`

production, flap- and edgewise moments, and yaw and tilt moments. These principal parameters will be compared for four different inflow cases:

1. **Full Inflow:** The full inflow extracted $1R$ upstream the wind turbine from the CFD simulations, which forms the basis for the POD and REDOMO reconstruction.

2. **POD:** Energy truncation of the full inflow, reconstructed using Equation 2.34.

3. **REDOMO:** Energy and temporal truncation of the full inflow, reconstructed using Equation 2.35.

4. **Mann Turbulence:** Stochastically generated turbulence using Manns turbulence, see Section 2.1.3.

The resulting response of the different inflows will be compared directly through time series, spectral and higher order statistical analyses, and in terms of equivalent loads in Section 6.

2.5.1 Equivalent Loads

Equivalent loads is the standard method for assessing wind turbine loads, and the method is outlined in "Recommended Practices for Wind Turbine Testing and Evaluation: 3. Fatigue Loads", IEA [41]. The equivalent loads method is based on the so-called rainflow counting, which is one of several cycle counting methods, which essentially reduce a dynamic loading or response signal to a histogram of full and half cycles within different load ranges. The equivalent load is derived from the histogram to give a single load value equivalent of a load situation of N_{eq} cycles with constant amplitude. Thereby, enabling the direct comparison of the severity of different load cases. The equivalent load is determine by:

$$L_{eq} = \left(\sum_{i}^{N} \frac{N_{RF,i} \cdot RF_i^m}{N_{eq}} \right)^{\frac{1}{m}} \tag{2.37}$$

where $N_{RF,i}$ is the number of cycles with amplitude RF_i in the i^{th} loading range, and N_{eq} is the equivalent number of cycles. N is the total number of cycles and m is a material parameter. The MATLAB implementation by Adam Nieslony[2] has been utilized, which is in accordance with the "Standard practices for cycle counting in fatigue analysis" [8].

2.6 Summary

The general flow solver EllipSys3D has been presented along with a brief overview of the implemented LES model and general description of the Actuator Line technique. The background for generating and adding atmospheric turbulence, modelling an atmospheric boundary layer, and ensuring constant mass flux have also been described. The analysis methodology is outlined with particular focus

[2]Rainflow Counting Algorithm: `http://www.mathworks.se/matlabcentral/fileexchange/3026-rainflow-counting-algorithm`

on POD and the approach for constructing a reduced order model. The theoretical background outlined in the preceding will be referenced throughout this dissertation as more complexity is included in the simulations and analyses.

Chapter 3

Single Far Wake

This chapter presents results investigating the far wake behind a single turbine. Two different cases are presented with different tip-speed ratios, which essentially governs the downstream wake development. The differences are examined as a fundamental background study before the subsequent analyses of the wake interaction within an infinitely long row of wind turbines and an infinitely large wind farm. As such this chapter serves as a brief introduction to the main analyses in the following chapters.

The flow characteristics and mean quantities are examined as function of distance behind the turbine. The large scale motions of the wake are investigated through a centre of mass approach and finally, POD is applied to the flow to build the understanding of the core methodology applied in the present work.

3.1 Setup

Domain

Two idealised simulations with uniform inflow have been run on the same grid. The grid is Cartesian and consists of 216 blocks of 40^3 mesh points, a total of $13.8 \cdot 10^6$ mesh points. The domain size is $48R \times 20R \times 20R$ in X, Y, Z, respectively, where X is the streamwise, Y the lateral and Z the vertical direction. The size of the domain is chosen to avoid numerical blockage by adhering to a blockage ratio of 0.8% which is less than 3% as recommended by Baetke et al. [11]. The rotor is positioned at $(X, Y, Z) = (8, 0, 0)$, which makes it possible to study the wake development up to $40R$ downstream. The grid is equidistant for $\pm 3R$ around the wind turbine and stretched towards the boundaries to optimise the resolution in the vicinity of the turbine. Figure 3.1 shows the cross-sectional grid distribution, where the rotor and the equidistant region are marked by thick lines.

The blade resolution is $j_{rot} = 16$, which corresponds to a discretization of $2.5m$. This is a rather coarse mesh when applying actuator line. The grid resolution will be discussed in further details in Section 4.2 with reference to Troldborg [68], who concluded that a coarse grid only gives rise to minor differences in the far wake, which is the primary focus of the present study. Furthermore, the current simulations demand very long run times and a coarser grid must be employed due to limitations in available computational ressources.

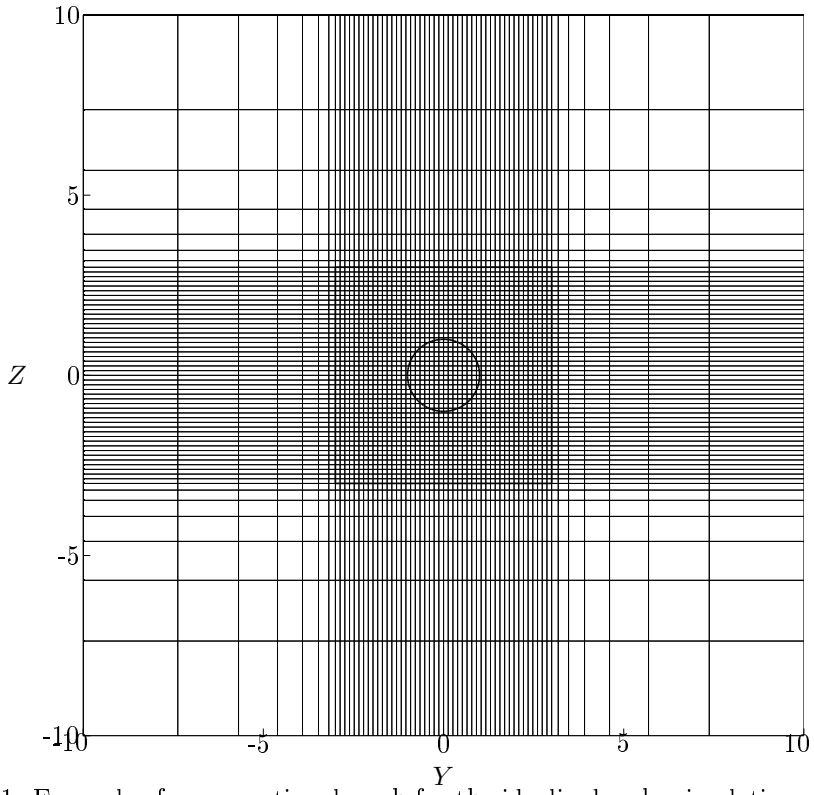

Figure 3.1: Example of cross-sectional mesh for the idealised wake simulations. The equidistant region and the rotor coverage are marked by thicker lines.

Boundary Conditions

A Dirichlet boundary condition of constant and uniform velocity (U_0) is enforced on the inlet boundary with no lateral or vertical velocity components, i.e. $V_0 = W_0 = 0$. Cyclic boundary conditions (sometimes referred to as periodic) link the lateral boundaries and the vertical boundaries. Therefore, the wake could potentially interact with wakes originating from virtual turbines on all sides. However, the large cross-sectional area of the domain(due to the blockage criteria) effectively prevents this. A convective boundary condition is applied to the outlet boundary.

Inflow Conditions and Turbine Performance

Two different simulations are run to investigate the influence of different tip-speed ratios. Different tip-speed ratios give rise to different thrust coefficients(C_T) which essentially govern the wake development. C_T is found as:

$$C_T = \frac{T}{\frac{1}{2}\rho U_0 A_R}$$

where T is the thrust on the turbine and A_R is the rotor area. The two tip-speed ratios given by $\lambda_{TS} = \frac{\omega R}{U}$ are set to 11.42 and 7.78 with a constant $\omega = 1.8055s^{-1}$. The turbine is forced to operate at different tip-speed ratios, since the high tip-speed ratio is outside the usual operational regime for the NM80 turbine. This means that the controller described in Section 2.1.2 is not applied for these simulations, although the turbine is essentially operating according to the controller for tip-speed ratio of 7.78. Since the rotational speed is forced, the turbine is considered stiff and constantly loaded, i.e. the simulations presented in this chapter do not include full aeroelastic coupling with the Navier-Stokes solver. The tip-speed ratios give rise to C_T-values of $C_{T,\lambda_{TS}=11.42} = 0.86$ and $C_{T,\lambda_{TS}=7.78} = 0.75$, respectively.

Both simulations include the application of Mann turbulence with 0.1% turbulence intensity for all three velocity components. The turbulence is applied in a vertical plane of $\pm 3R$ at $4R$ upstream the rotor. The small amount of turbulence is essentially applied to ensure that the computations are triggered into the turbulent regime.

The simulations have been run for a total time of $2,369s$ for $C_T = 0.86$ and $4,850s$ for $C_T = 0.75$.

3.2 Wake and Flow Characteristics

Figure 3.2 shows instanteneous vorticity at hub height for the two simulations, where the rotor is marked by a full line. The resolution is not large enough to resolve the individual tip vortices in the near wake, so the tip vorticity is smeared into a continuous vorticity sheet. The effects of the higher λ and C_T are visible in two distinct ways. First, the higher C_T stems from a higher force acting on the blades, see Figure 3.3. The larger radial force(F_X) distribution yields a larger axial interference factor(a), which locally exceeds the Betz' optimum of $a = \frac{1}{3}$. Second, the higher loading and thrust yields a lower wake velocity, i.e. a higher relative difference between the internal wake velocity and

the external freestream. The resulting shear layer is hence stronger, which instigates the wake to break down quicker. For $\lambda_{TS} = 11.42$ the vorticity sheet changes to a Kelvin-Helmholtz instability before the wake break down around $9R$ downstream, while the Kelvin-Helmholtz instability and wake breakdown occurs around $15R$ downstream for $\lambda_{TS} = 7.78$. Troldborg [68] reported similar results. It is important to note, that Troldborg used the Tjæreborg turbine as opposed to the present simulations with the NM80 turbine. The blade of the Tjæreborg turbine ends very abruptly, while the NM80 has a smooth transition to the tip. The Tjæreborg turbine therefore yields more pronounced tip vortices.

Troldborg [68] investigated the wake development up to $19.8R$ downstream, while the present simulations extend the downstream wake region to $40R$. The extended wake region reveal how the far wake eventually resembles a von Karman vortex street, particularly for $\lambda_{TS} = 11.42$. The large scale motions are investigated in details in Section 3.4.

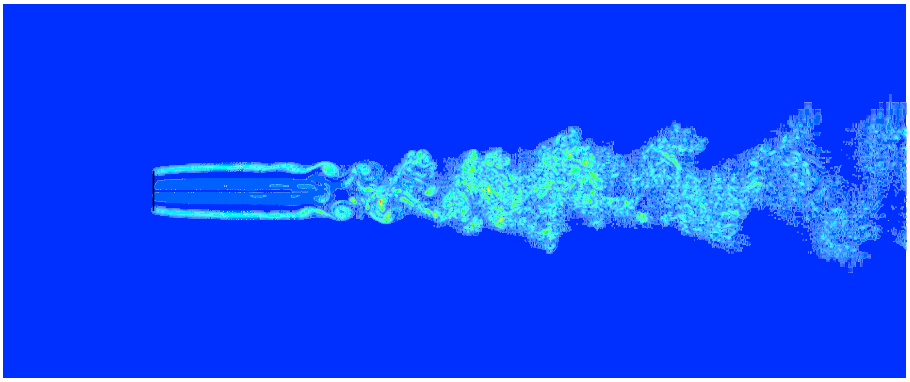

(a) $\lambda_{TS} = 11.42$ and $C_T = 0.86$

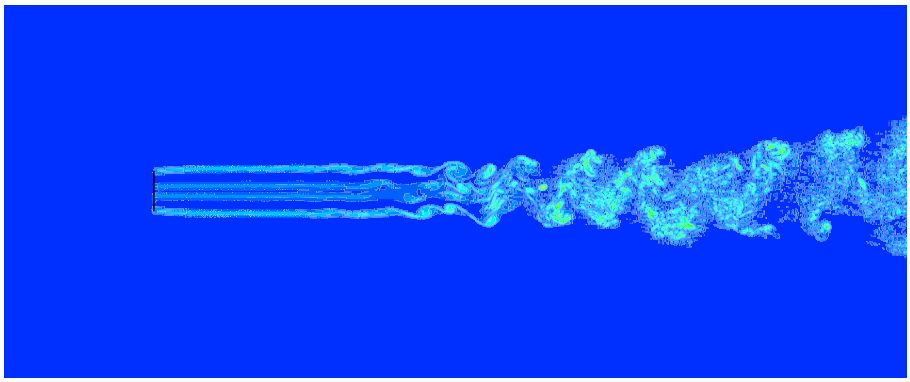

(b) $\lambda_{TS} = 7.78$ and $C_T = 0.75$

Figure 3.2: Horizontal slice through hub height showing instanteneous vorticity plots for the wake behind a single turbine. Bright areas indicate high vorticity.

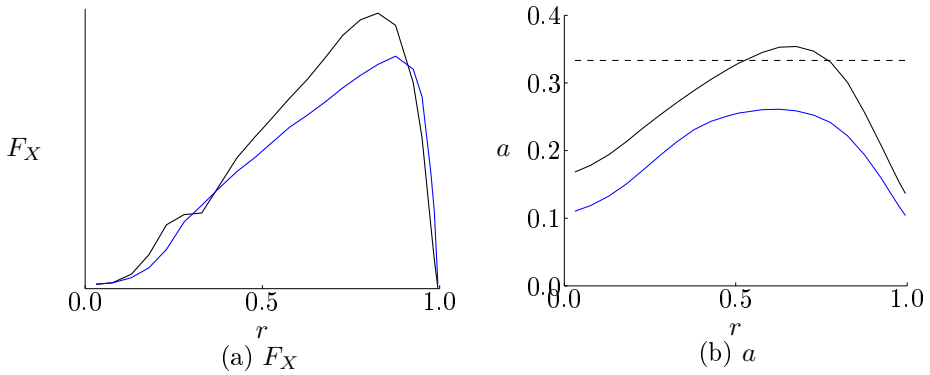

(a) F_X (b) a

Figure 3.3: Radial distribution of the axial force and interference factor for two different tip-speed ratios. Note, the Y-scale for the force distribution is excluded for proprietary reasons. Legend: —— : $\lambda_{TS} = 11.42$ and $C_T = 0.86$. —— : $\lambda_{TS} = 7.78$ and $C_T = 0.75$.- - - : Betz' optimum $a = \frac{1}{3}$.

3.3 Spatial Development

The three velocity components are extracted in the far wake from $8R$ to $38R$ downstream the turbine for every $2R$. The statistical convergence of the mean and turbulent quantities are examined in the last plane extracted at $38R$ downstream to ensure that all the flow statistics have converged. The details of such a convergence analysis is not shown here, but instead elaborated in Section 4.5. The following analysis is conducted using a temporal window covering the last $1,500s = 25mins$ of the simulations.

Figure 3.4 depicts the azimuthally averaged ($\langle\rangle_\theta$) axial velocity profiles and the development downstream for both simulations from $8R$ to $20R$ downstream. The initial wake deficit is approximately 0.7 at $8R$ downstream, and the high C_T leads to a slightly higher wake deficit($1 - \frac{U}{U_0}$). The influence of the two tip vortices on the mean velocity profile have disappeared $12R$ downstream for $\lambda_{TS} = 11.42$, while the tip vortices are distinguishable up to $16R$ downstream for $\lambda_{TS} = 7.78$. Beyond this, the wake is smeared and approach a Gaussian shaped bell curve, where the wake deficit of the normally loaded rotor eventually supersedes that of the highly loaded rotor, i.e. the wake behind the highly loaded turbine recovers faster.

Figure 3.5 shows the azimuthally averaged profiles of the RMS values of the axial velocity fluctuations and the downstream development for both simulations from $8R$ to $20R$ downstream. The turbulence level is clearly much higher behind the highly loaded rotor, initially more than two times higher, which assists in the faster wake recovery further downstream. The wake behind the normally loaded rotor initially includes very little turbulence, before it reaches comparable levels around $18R$ downstream. The remnants of the tip vortices are discernible up to $14R$ for the highly loaded case and beyond $20R$ for $\lambda_{TS} = 7.78$. The latter case also reveals distinct regions of elevated turbulence levels around the root.

Despite the initial differences in the wake, the results also show that the streamwise velocity and fluctuations eventually resemble each other further downstream as the wake becomes more turbulent.

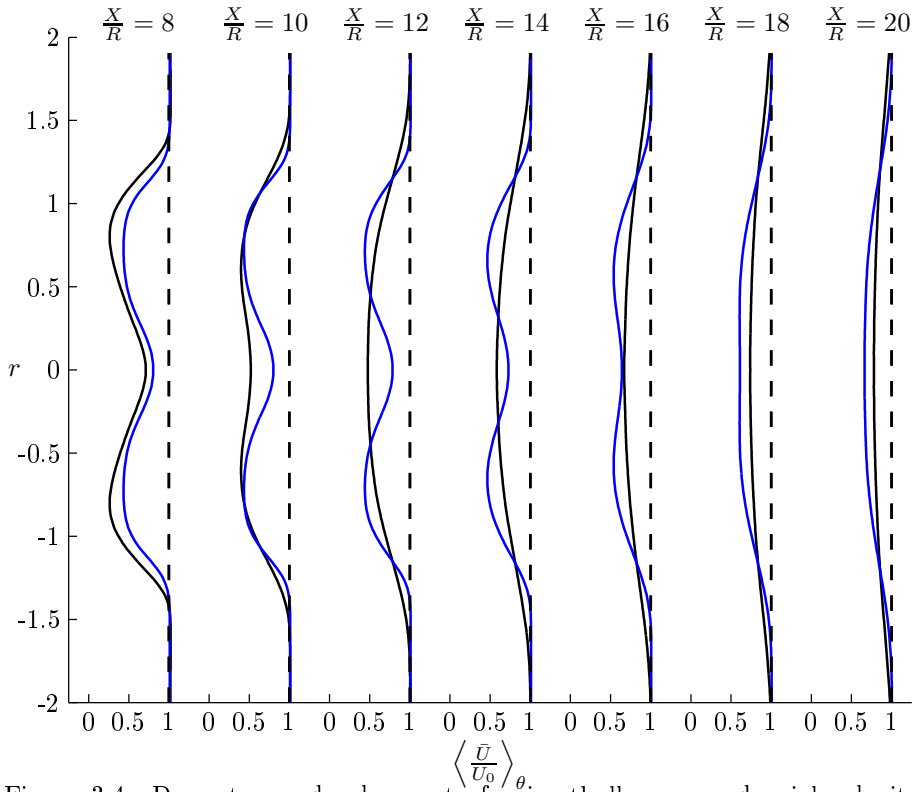

Figure 3.4: Downstream development of azimuthally averaged axial velocity $\langle \frac{\bar{U}}{U_0} \rangle_\theta$. Legend: —— : $\lambda_{TS} = 11.42$ and $C_T = 0.86$ —— : $\lambda_{TS} = 7.78$ and $C_T = 0.75$

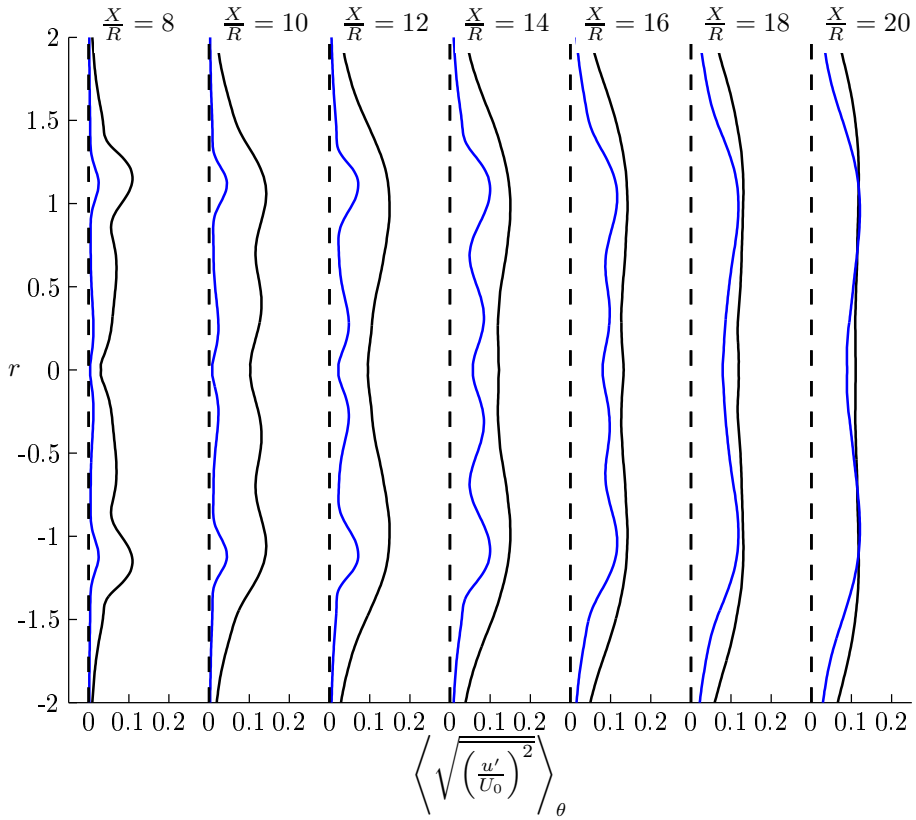

Figure 3.5: Downstream development of azimuthally averaged axial velocity fluctuations $\langle \sqrt{\overline{\overline{\left(\frac{u'}{U_0}\right)^2}}} \rangle_\theta$. Legend: —— : $\lambda_{TS} = 11.42$ and $C_T = 0.86$ —— : $\lambda_{TS} = 7.78$ and $C_T = 0.75$

3.4 Large Scale Motions

Figure 3.2 shows how the wake eventually resembles a von Karman vortex street, where vortex shedding occurs with a very distinct pattern and a corresponding Strouhal frequency, $St = \frac{fD}{U_0}$. These large scale motions are investigated by identifying a wake centre(Y_C, Z_C) using a centre of mass analogy on the wake deficit $(1 - \frac{U}{U_0})$. The wake centre is found in an iterative manner, where the coordinate is updated as $Y_C = Y_C + \Delta y$ untill $\Delta y < 10^{-3}R$ and similarly for Z_C. Δy and Δz are the incremental changes in the iteration determined by:

$$\Delta y = \frac{\int (y - Y_C)(1 - \frac{U}{U_0})^m dA}{\int (1 - \frac{U}{U_0})^m dA}, \qquad \Delta z = \frac{\int (z - Z_C)(1 - \frac{U}{U_0})^m dA}{\int (1 - \frac{U}{U_0})^m dA} \tag{3.1}$$

where dA is the cross sectional area and $m = 3$. Different values of m were tested, and $m = 3$ appeared to give more consistent results. Figure 3.6 illustrates the instanteneous wake deficit and the computed wake centre. The wake centre is not a clearly defined point in the turbulent wake, but the centre of mass yields a simple estimate and it is assumed that the wake centre follows and captures the large scale motions of the wake. Large scale motions of the wake behind wind turbines are often referred to as wake meandering, see Larsen et al. [34], who related meandering to the large turbulent scales in the atmosphere.

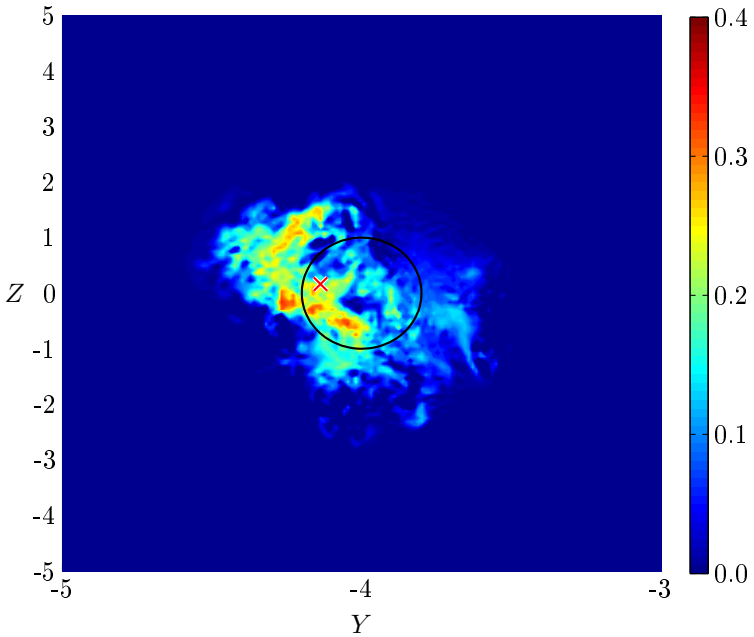

Figure 3.6: Instanteneous wake deficit $38R$ behind a highly loaded rotor.
Legend: —— : Rotor extend. × : Wake centre.

The wake centre coordinates extracted $38R$ downstream of the rotors are depicted in Figure 3.7, which shows how the wake centre moves substantial distances from the rotor centre with a maximum of $1.6R$ for both cases. The wake centre for $\lambda_{TS} = 7.78$ clearly moves much more rapidly over time.

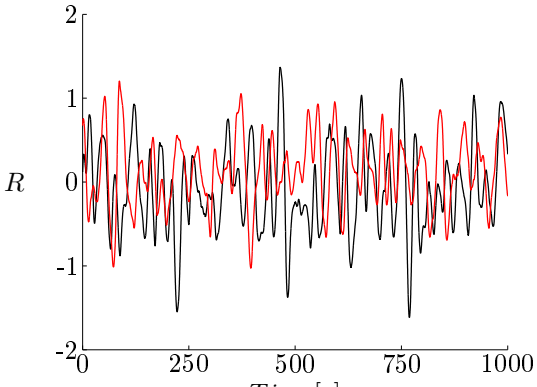

(a) $\lambda_{TS} = 11.42$ and $C_T = 0.86$

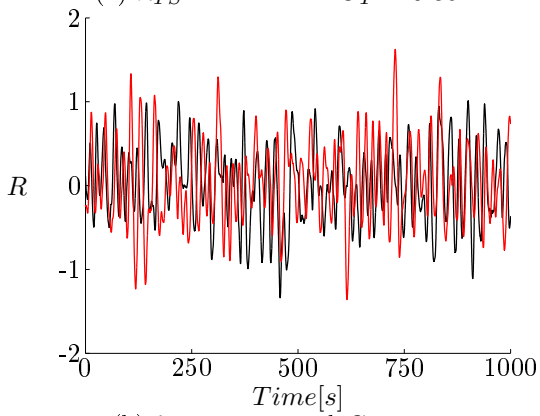

(b) $\lambda_{TS} = 7.78$ and $C_T = 0.75$

Figure 3.7: Wake centre coordinates, (Y_C, Z_C), extracted $38R$ downstream the rotor. Legend: —— : Y_C —— : Z_C

The RMS and maximum values for the wake centre coordinates as function of downstream distance are given in Figure 3.8. The RMS values of the large scale motions increase with downstream distance for both simulations before stabilising around $0.5R$. Furthermore, the large scale motions are initiated before the wake breakdown and the graphs suggest that the breakdown occurs once the RMS value reach approximately $0.15R$ for both simulations. The lateral motions(Y_C) are larger than the vertical(Z_C), although there should be no predominant directions in the simulations in the absence of gravity and sheer. However, a minor bug was detected in the implementation of the Mann Turbulence described in Section 2.1.3, which gave rise to a minor increase in the lateral turbulence for these simulations. However, the overall influence of this discrepancy was not deemed significant enough to recompute the full simulations. The applied turbulence intensity predominantly serves to trigger the wake instability, and therefore the results are still presented. Troldborg [68] assessed meandering $14R$ downstream using a similar approach and reported a standard deviations of only $(Y_C, Z_C) = 0.07 - 0.08R$ for $\lambda_{TS} = 11.78$, which is significantly lower than the standard deviation of $0.30-0.35$ for the present case with $\lambda_{TS} = 11.42$. The difference is mainly attributed to the difference in grid configuration and the imposed turbulence, which triggers the wake break down.

It is also obvious from Figure 3.7 that the wake centre motion is dominated by certain frequencies, and the frequency of the wake centre motion is noticably higher for the normally loaded rotor wake. Figure 3.9 shows the normalised Power Spectral Density(PSD) as function of distance and Strouhal number $St = \frac{fD}{U_0}$. Several dominant Strouhal numbers are visible. For $\lambda_{TS} = 11.42$, the dominant frequency is $St_{\lambda_{TS}=11.42,P1} = 0.33$ for the lateral motion and $St_{\lambda_{TS}=11.42,P1} = 0.27$ for the vertical. For $\lambda_{TS} = 7.78$, $St_{\lambda_{TS}=7.78,P1} = 0.35$ for the lateral and $St_{\lambda_{TS}=7.78,P1} = 0.46$ for the vertical motion of the wake centre. The subsequent dominant frequencies are $St_{\lambda_{TS}=11.42,P2} = 0.35$ and $St_{\lambda_{TS}=11.42,P3} = 0.17$ for Y_C, and $St_{\lambda_{TS}=11.42,P2} = 0.33$ for Z_C. The PSD for $\lambda_{TS} = 7.78$ yields multiple peak frequencies spanning $St \in [0.12 - 0.48]$, which prevents a clear interpretation. The vortex shedding behind a cylinder gives rise to a Strouhal shedding frequency of 0.2, which is not predominant in any of the spectrums, although $St = 0.17$ is present in the spectrums of the lateral motion for $\lambda_{TS} = 11.42$. Medici and Alfredsson [45] referenced personal communication with G. Schepers and reported a Strouhal number of approximately 0.3 as the dominant low-frequency peak in velocity spectrums measured at Alsvik wind farm for wind speeds up to $9m/s$. Medici and Alfredsson [45] also measured a Strouhal number of 0.12 behind a model turbine for $\lambda_{TS} > 4.5$. Several of the peak frequencies appear rather high, particular for $\lambda_{TS} = 7.78$. It could be attributed to the determined wake centre being a poor representative of the large scales. However, it is noteworthy that the dominant frequencies are preserved throughout the wake, as the amplitude naturally increases in accordance with the increase in the large scale motions seen in Figure 3.8. Medici and Alfredsson directly related low-frequency motions to the so-called meandering. Meandering or large scale motions behind wind turbines have been assumed to originate directly from the atmospheric turbulence by Larsen et al. [33], [34], which is one of the fundamental hypothesis behind the Dynamic Wake Meandering(DWM) model. However, the atmospheric turbulence is practically absent in both the experiments by Medici and Alfredsson and these simulations. The present results reveal several dominant frequencies, indicating that the wake behind an

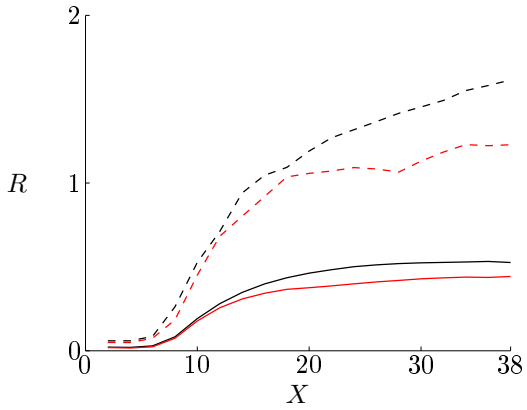

(a) $\lambda_{TS} = 11.42$ and $C_T = 0.86$

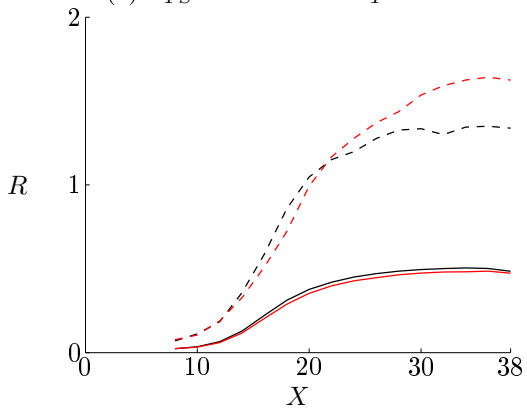

(b) $\lambda_{TS} = 7.78$ and $C_T = 0.75$

Figure 3.8: RMS and maximum values of the wake centre coordinates, (Y_C, Z_C). Legend: ——: RMS values for Y_C. ——: RMS values for Z_C.- - - : Max values for Y_C.- - - : Max values for Z_C.

operating wind turbine is more complex than the wake behind a cylinder, which gives one dominant Strouhal number. The results also suggest that PSD of the wake centre movements might not give a suitable representation of the large scale structures in terms of vortex shedding, which would disenable a frequency comparison between the wake centre PSD and PSD of the velocity. The wake centre and the corresponding frequencies are investigated in further details in Section 4.7.

The large turbulent structures are also captured by applying Proper Orthogonal Decomposition to slices of the three velocity components extracted from the CFD simulations.

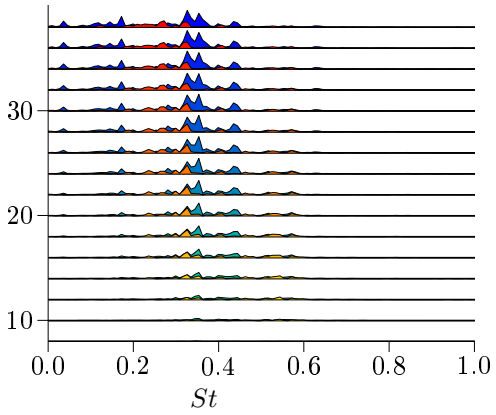

(a) $\lambda_{TS} = 11.42$ and $C_T = 0.86$

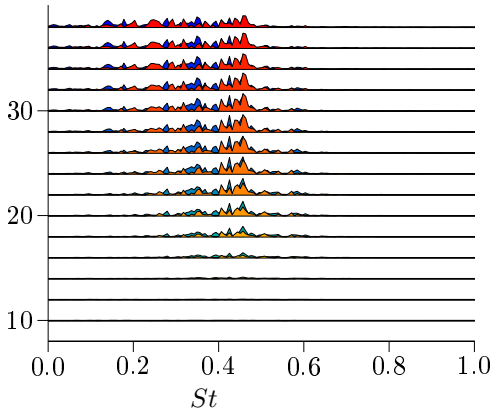

(b) $\lambda_{TS} = 7.78$ and $C_T = 0.75$

Figure 3.9: Power spectral density for wake centre coordinates as function of distance and Strouhal frequency. Y_C is given in blue, Z_C is given in red.

3.5 Proper Orthogonal Decomposition

The theoretical background for applying the Proper Orthogonal Decomposition(POD) is given in Section 2.3. POD is applied to the velocity components extracted in vertical slices for every $2R$ behind the turbine for the period of $1,500s$.

POD convergence

The convergence of the POD coefficients is investigated $38R$ behind the turbine by including various numbers of slices within the $1,500s$, i.e. examining how many of the total $14,911$ slices are needed. Figure 3.10 shows the convergence for the first 100 POD modes for the simulation with $\lambda_{TS} = 7.78$ and $C_T = 0.75$. Clearly, the POD coefficients quickly converge and there is no discernible difference for $f < 10$, which corresponds to $\Delta t \approx 1.0s$ and $N > 1,492$. The convergence of the POD coefficients shows that no(or very little) additional information is gained in terms of the large structures by including more slices.

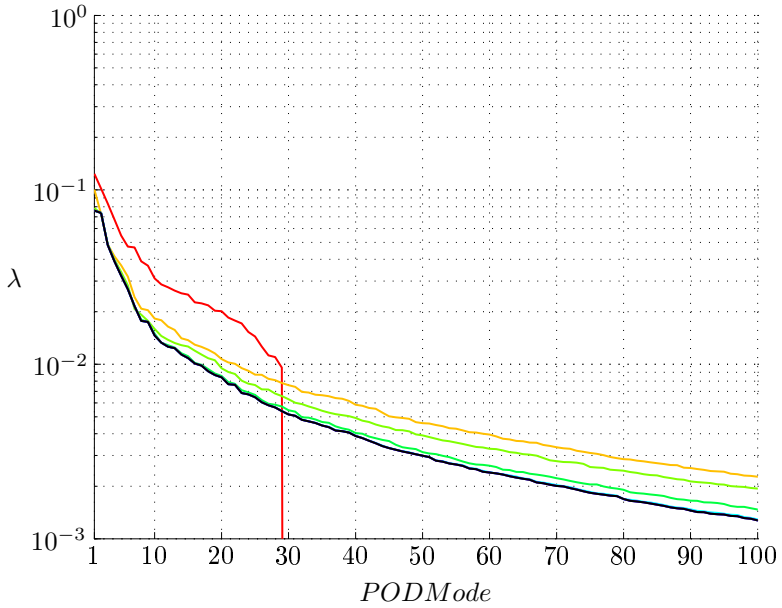

Figure 3.10: Convergence of POD coefficients for various number of slices at $38R$ behind the turbine for $\lambda_{TS} = 7.78$. Legend: ——: $N_{f=500} = 30$, $\Delta t \approx 50s$. ——: $N_{f=100} = 150$, $\Delta t \approx 10s$. ——: $N_{f=50} = 299$, $\Delta t \approx 5s$. ——: $N_{f=20} = 476$, $\Delta t \approx 2s$. ——: $N_{f=10} = 1,492$, $\Delta t \approx 1s$. ——: $N_{f=5} = 2,983$, $\Delta t \approx 0.5s$. ——: $N_{f=2} = 7,456$, $\Delta t \approx 0.2s$. ——: $N_{f=1} = 14,911$, $\Delta t \approx 0.1s$.

Figure 3.11 gives the cumulative coefficients at $38R$ behind the turbine for both simulations. The cumulative coefficients show the total amount of turbulent kinetic energy captured by a given number of POD modes, meaning that the first 10 POD modes contain 37% and 38% of the turbulent kinetic energy and the first 100 POD modes contain 71% and 73% for $\lambda_{TS} = 7.78$ and $\lambda_{TS} = 11.42$, respectively. The larger energy content of the first POD modes is an indication that there are larger coherent structures in the wake behind a turbine. However, the energy contained by each of the higher modes quickly decrease, which shows that the turbulent kinetic energy is spread over a large range of scales despite the presence of larger scales. These spatial structures are examined in the following.

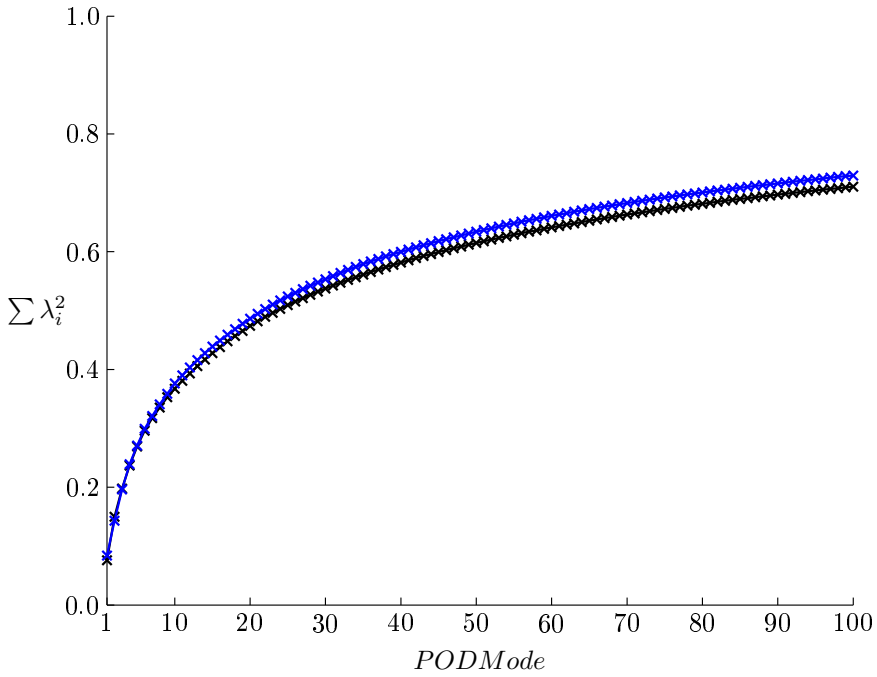

Figure 3.11: Cumulative POD coefficients for $38R$ behind the turbine.
Legend: ——: $\lambda_{TS} = 11.42$ and $C_T = 0.86$. ——: $\lambda_{TS} = 7.78$ and $C_T = 0.75$.

Spatial POD modes

The corresponding first ten spatial POD modes for the two simulations are plotted in Figures 3.12 and 3.13. The red and blue areas show the large coherent structures as positive and negative regions. It is important to keep in mind how the blue and red regions maintain their pattern, but pulsate between positive and negative according to the corresponding temporal eigenfunction. These ten POD modes account for 37% and 38% of the total turbulent kinetic energy for $\lambda_{TS} = 11.42$ and $\lambda_{TS} = 7.78$, respectively. The first POD mode shows clear dipole structure for both simulations and this structure is clearly associated with the lateral movement of the wake, particular for $\lambda_{TS} = 11.42$. The first POD mode is paired to the third and second POD mode for $\lambda_{TS} = 11.42$ and $\lambda_{TS} = 7.78$, respectively, which show a similar, but orthogonal, dipole structure. The pairing between the first and the third POD mode for $\lambda_{TS} = 11.42$, as opposed to the first and second, is a result of the vertical movements being less dominant for this case, as previously seen in Figure 3.8. Therefore, the energy content of the second POD modes exceeds the third governing the vertical movement. The inplane circulation also has two distinct circulation cells. The next pair of POD modes portrait distinct quadrupole distributions in both the streamwise velocity mode and the inplane circulation with four clear circulation cells. Hexapole structures are found in POD modes eight and nine for $\lambda_{TS} = 11.42$ and POD mode eight for $\lambda_{TS} = 7.78$. The fifth and sixth POD modes yield a central region, which fluctuates back and forth in time.

Figure 3.14 gives the spatial evolution of a few descriptive POD modes. Only the streamwise component is shown for clarity. The first POD mode

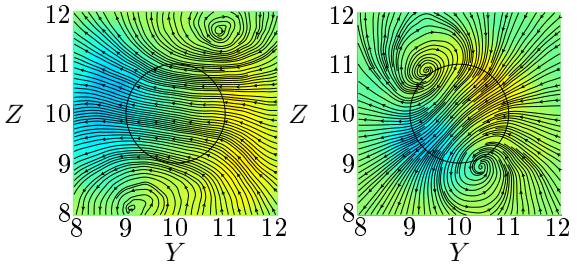

(a) POD mode 1.

(b) POD mode 1.

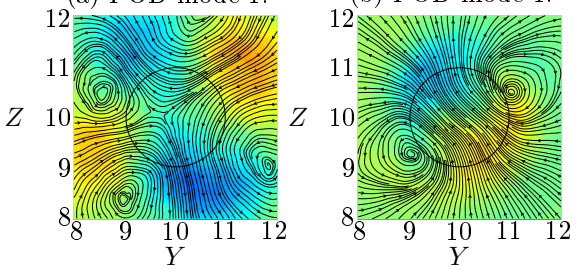

(c) POD mode 2.

(d) POD mode 2.

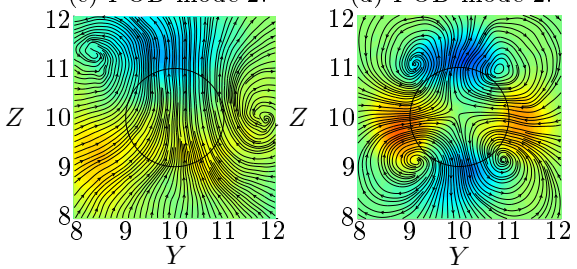

(e) POD mode 3.

(f) POD mode 3.

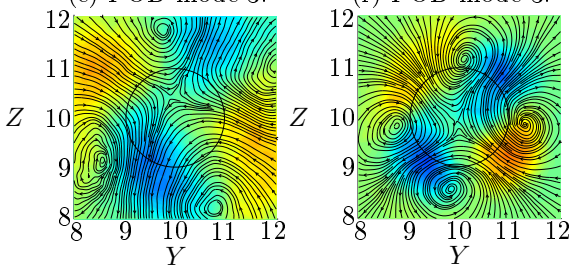

(g) POD mode 4.

(h) POD mode 4.

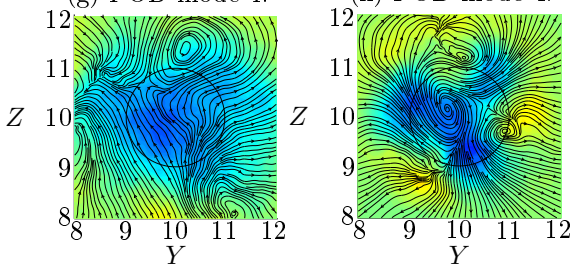

(i) POD mode 5.

(j) POD mode 5.

Figure 3.12: Spatial POD modes for $38R$ behind the turbine. Right column shows POD modes for $\lambda_{TS} = 11.42$ and $C_T = 0.86$. Left column shows POD modes for $\lambda_{TS} = 7.78$ and $C_T = 0.75$.

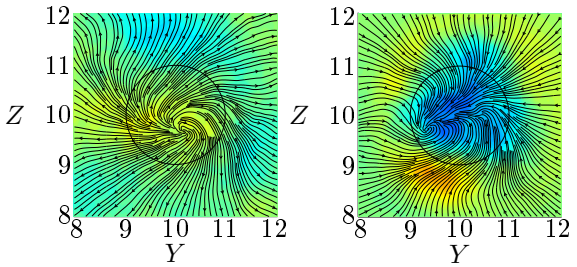

(a) POD mode 6. (b) POD mode 6.

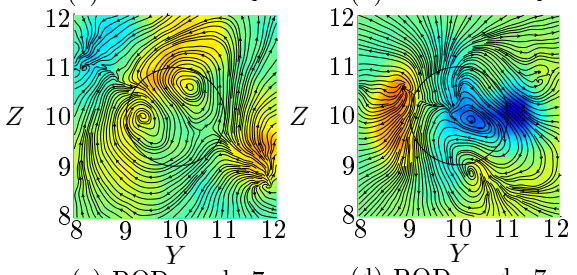

(c) POD mode 7 (d) POD mode 7.

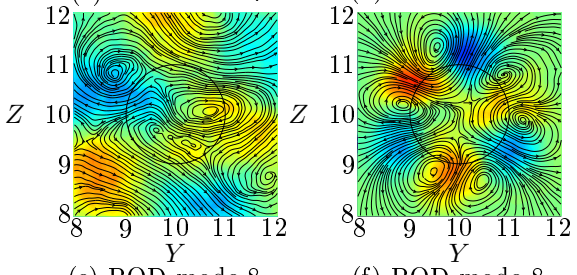

(e) POD mode 8. (f) POD mode 8.

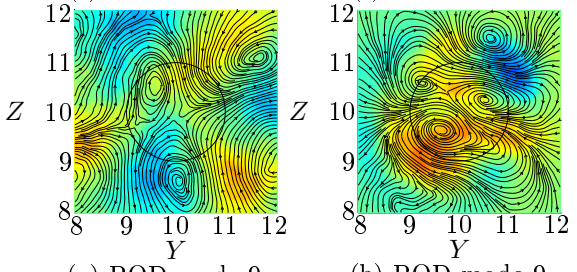

(g) POD mode 9. (h) POD mode 9.

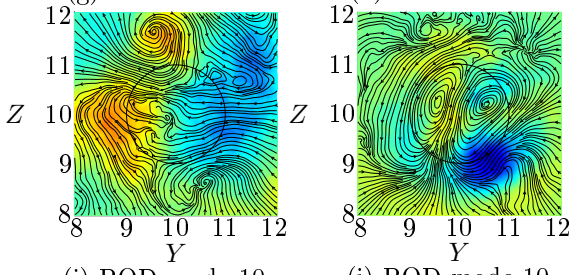

(i) POD mode 10. (j) POD mode 10.

Figure 3.13: Spatial POD modes for $38R$ behind the turbine. Right column shows POD modes for $\lambda_{TS} = 11.42$ and $C_T = 0.86$. Left column shows POD modes for $\lambda_{TS} = 7.78$ and $C_T = 0.75$.

maintains two dominant regions throughout the domain, althought it changes from very distinct around the tips to less distinct regions of bigger extend, a natural progression due to the turbulent mixing occuring with distance. The remnants of the tip vorticies are hence clearly captured by the first mode for the early and intermediate distances. The third POD mode initially yields four distinct regions along the rotor radius, which turns into a single dominant annular region before returning to four distinct regions. These changes does not necessarily infer that the actual POD mode changes shape or spatial distribution as the plot progresses downstream through the wake. It is more likely due to a redistribution of the turbulent kinetic energy between the different large scale structures, e.g. dipolar, quadrupole patterns. The redistribution of energy was reported by Johansson and George [30] for POD modes of the axisymmetric wake behind a disk. This is also evident for the sixth POD mode, which initially portraits an annular ring which eventually changes into a clear central region. The eighth POD mode initially contains a very dynamic description of the root vorticies as it captures five positive and five negative regions between $6R$ and $16R$ behind the turbine, before it turns to a hexapole pattern in the very far wake.

Some of the spatial POD modes can be directly related to the large scale physics, e.g. the dipole structures govern the larger wake motions also described by the wake centre movements. Therefore, POD modes yield insight into the dynamics of the turbulence flow, but it also enable an optimal reconstruction of the flow, optimal in terms of energy variance. These features of POD are the backbone of the present work.

3.6 Summary

The wake behind a single turbine was studied as a brief introduction to the core subject of wakes and wake interaction in wind farms. Two different cases were presented with different tip-speed ratios, which highlighted the effect of tip-speed and the thrust coefficient on the wake development. Key features of the flow characteristics have been described and the change in the basic statistics examined far into the wake. Despite differences in the near and intermediate wake, the results also showed how the differences diminish in the far wake as the wake breaks down. The simulations showed how large turbulent structures are inherent to the turbulent wake behind a turbine and not only an artifact of atmospheric turbulence. POD was applied and the initial insights into the methodology and the analysis of the spatial POD modes were presented as it paves the way for the proposed wake models derived in Chapter 6.

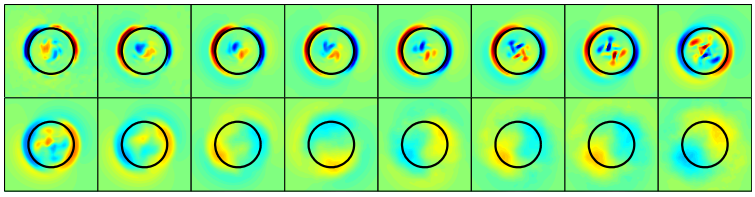

(a) POD mode 1 for $\lambda_{TS} = 7.78$ and $C_T = 0.75$

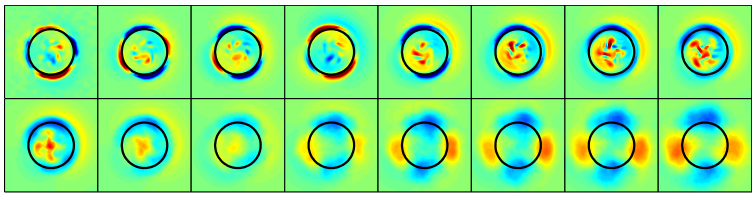

(b) POD mode 3 for $\lambda_{TS} = 7.78$ and $C_T = 0.75$

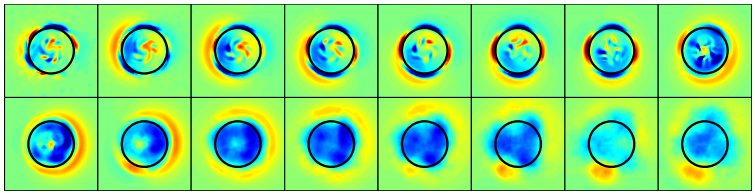

(c) POD mode 6 for $\lambda_{TS} = 7.78$ and $C_T = 0.75$

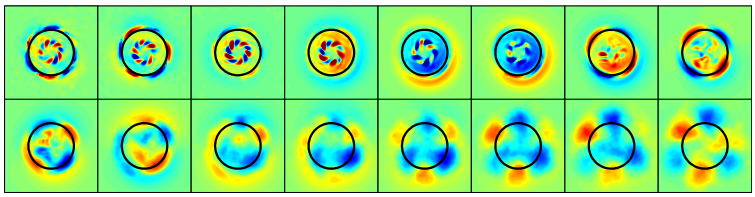

(c) POD mode 8 for $\lambda_{TS} = 7.78$ and $C_T = 0.75$

Figure 3.14: Spatial development of selected POD modes. Increments of $2R$ from top left corner starting at $8R$ behind turbine ending in lower right corner at $38R$ behind the turbine.

Chapter 4

Infinitely Long Row of Wind Turbines

This chapter investigates the wake interaction deep inside an idealised case of an infinitely long row of wind turbines. The simulations are considered idealised, because the initial inflow is uniform, i.e. excluding any shear and ground effects, and cyclic boundary conditions are applied in the streamwise direction to simulate an infinitely long row of turbines. This enables the study of the inherent turbulence. This inherent turbulence is sometimes referred to as mechanical turbulence, stemming directly from the presence of the turbine, as opposed to atmospheric turbulence. The investigation includes a minor grid study, but focus is on the infinitely long row of turbines. Three cases with spacings $12R$, $16R$, and $20R$ are examined. The chapter explores the turbine performance and the statistical convergence of the turbulent quantities. The converged results are compared with analytical models. The large scales are investigated in detail and the hypotheses behind the Dynamic Wake Meandering model tested. The potential effects of applying cyclic boundary conditions are examined through spectral and cross-correlation analysis, which reveal insights into the larger turbulent scales. The large coherent structures arise as a result of applying POD, and these structures are discussed.

4.1 Setup

Domain

The wake interaction is examined in three idealised cases of an infinitely long row of turbines with three different streamwise spacings S of $12R$, $16R$, and $20R$. The grids are equidistant in the streamwise direction, which is necessary to maintain and model the turbulence correctly as it is transferred using the cyclic boundary conditions. The grids are non-equidistant in the transverse and vertical directions with a higher resolution in an equidistant region for $\pm 3R$ around the turbine, equivalent to the cross section in Figure 3.1 with $20R \times 20R$ in the lateral and vertical direction, again yielding a blockage ration of 0.8%. The domain lengths are $36R$, $48R$, and $40R$ for spacings of $12R$, $16R$, and $20R$, respectively, which places 3, 3 and 2 turbines in each domain. The

S	Dimensions	Turbines	Cells	j_{rot}	T_T	Total Time
	$X \times Y \times Z[R]$		10^6		$[s]$	$[s]$
$12R$	$36 \times 20 \times 20$	3	17.9	20	96	$7,511$
$16R$	$48 \times 20 \times 20$	3	24.6	22	128	$3,691$
$20R$	$40 \times 20 \times 20$	2	24.6	22	107	$4,872$

Table 4.1: Overview of domain setup for idealised cases.

domain lengths are chosen to include several turbines to limit the introduction of additional frequencies due to the finite size of the domain, i.e. ensuring that the dominant domain length is in the flow direction(see Section 4.7). This means that the domain length in the streamwise direction should be approximately two times larger than the lateral and vertical dimensions. Hence, only 2 turbines are included for spacing of $20R$ and 3 turbines for the other spacings. Introducing several turbines ensures that turbulent length scales of up to at least $36R = 1,440m$, $48R = 1,920m$, and $40R = 1,600m$ may appear in the computations. The turnaround time is defined as the time it takes for the free stream wind to pass through the entire domain. With a rotor radius of $R = 40m$ and three turbines with a spacing of $16R$, the turnaround time is $T_{T,16R} = \frac{3 \cdot 16 \cdot 40m}{15m/s} \approx 128s$. Table 4.1 summarise the domain setup including the total number of point, the rotor resolution, turnaround time, and total simulation time.

Boundary Conditions

The infinitely long row of turbines comes from applying cyclic boundary conditions in the flow direction, i.e. coupling the inflow with the outflow. Far field Dirichlet boundary conditions ($U = constant$) are applied on the transverse and vertical boundaries, i.e. making it a single row of wind turbines, not an infinite wind farm in the transverse and vertical directions.

Inflow Conditions and Turbine Performance

The initial inflow is uniform inflow of $U_0 = 15m/s$, which is above rated speed for the wind turbine. Uniform inflow means that no atmospheric boundary layer and no ambient turbulence is added, i.e. the body forces $\mathbf{f}_{turb}$ and $\mathbf{f}_{pbl}$ in Equation 2.2 are nil. Thereby, making it possible to study the turbulence inherent to the wind turbines themselves. Furthermore, the simulations are idealised by excluding ground, gravitational and temperature effects on the flow.

4.2 Grid Study

A minor grid study have been conducted for three different grid resolutions, where the rotor blade is resolved using 11, 16, and 25 cells. The grids are as described in the previous section with cyclic boundary conditions applied in the flow direction and a total domain size of $36R \times 20R \times 20R$ in X, Y, Z, except only one turbine is included in the domain, i.e. the simulations essentially examine spacings of $36R$, which is only used for the grid study. The grid study is denoted only minor as only $1,300s$ are simulated, whereas the simulations

presented afterwards demand significantly longer run times to converge statistically, see Section 4.5 for details on the statistical convergence. The mere nature of the simulations with long run times combined with the limitations imposed by available computational ressources, makes it unfeasible at the present stage to conduct a more detailed grid study with longer run times and for a number of different grid resolutions. Furthermore, the focus of the present study is on the turbulent far wake, and Troldborg [68] have previously investigated blade resolutions of $j_{rot} = 30$ and $j_{rot} = 40$. Troldborg concluded that only minor differences appear in the near wake and the tip vortice region, while the differences are even smaller in the far wake. Hence, a coarse grid was deemed sufficient by Troldborg. Therefore, this minor grid study merely sets out to verify that the far wake statitics of the three different grids are in accordance with each other.

Figure 4.1 depicts the incoming streamwise velocity at hub height for the three different grid resolutions. There are very large fluctuations in the streamwise velocity, where it plummets to only 33% of the freestream velocity around $t = 300s$ in the coarse configuration. Afterwards, the velocity at hub height peaks several times at the freestream velocity. Despite the large fluctuations, the incoming flow also reach a sort of equilibrium after $t > 700s$, where the velocity fluctuates around a given mean inflow velocity. The mean streamwise velocity for $t \in [700 - 1,300]s$ are $11.89m/s$, $11.75m/s$, and $12.44m/s$ for j_{rot} of 11, 16, and 25, respectively. Similarly, the standard deviations are $0.79m/s$, $0.87m/s$, and $0.84m/s$. The mean values and standard deviations offer no clear dependance on grid resolution, but all yield same order of magnitude results for all grid resolutions.

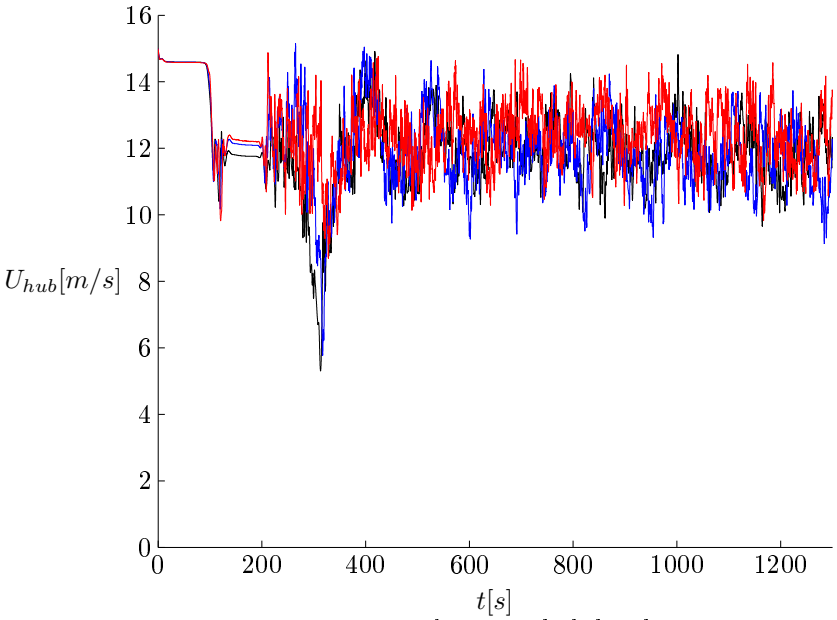

Figure 4.1: Incoming streamwise velocity at hub height as experienced by the turbine for three different grid resolutions. Legend: —— : $j_{rot} = 11$ —— : $j_{rot} = 16$ —— : $j_{rot} = 25$

The influence of the grid resolution on the far wake is shown in Figure 4.2, which shows the azimuthally averaged profiles of streamwise velocity and RMS

values of the streamwise velocity fluctuations for all three grid configurations. The averaged streamwise velocities are comparable for all three grid resolutions, although the wake deficit is less for the high resolution and its shape is less Gaussian with an almost constant velocity within the rotor area. The fluctuations show a similar pattern, where all three are very similar with elevated turbulent regions for $1R < r < 2R$, originating from the tip vortices and moved outwards due to the wake expansion. The coarse and fine resolution give slightly lower turbulence intensity within the rotor area compared to the medium resolution.

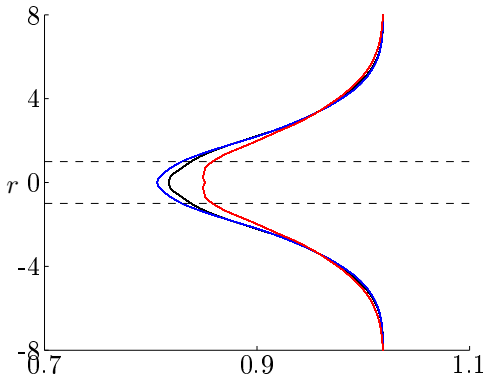

(a) $\langle \frac{U_x}{U_0} \rangle_\theta$

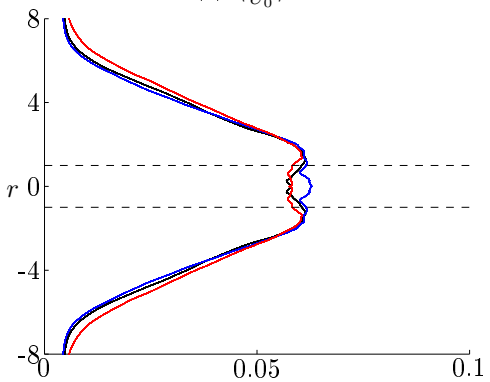

(b) $\langle \sqrt{\overline{\left(\frac{u'}{U_0}\right)^2}} \rangle_\theta$

Figure 4.2: Azimuthally averaged profiles of streamwise velocity and RMS values of streamwise velocity fluctuations for three different grid resolutions.
Legend: —— : $j_{rot} = 11$. —— : $j_{rot} = 16$. —— : $j_{rot} = 25$.
- - - : Rotor extend $\pm 1R$.

It is important to investigate the resolution of the resolved turbulent scales in grid studies for LES models, as opposed to e.g. RANS studies, which yields averaged results and the mean quantities should show a clear grid dependance, i.e. opposite to that noted for Figure 4.1. Therefore, the TKE spectrums at $1R$ upstream the turbine for the three grid resolutions are shown in Figure 4.3. It is evident how the three spectrums are comparable with the same low frequency peaks and same general shape. As expected the higher resolution yields higher TKE for the high frequencies, since the small scales are better resolved.

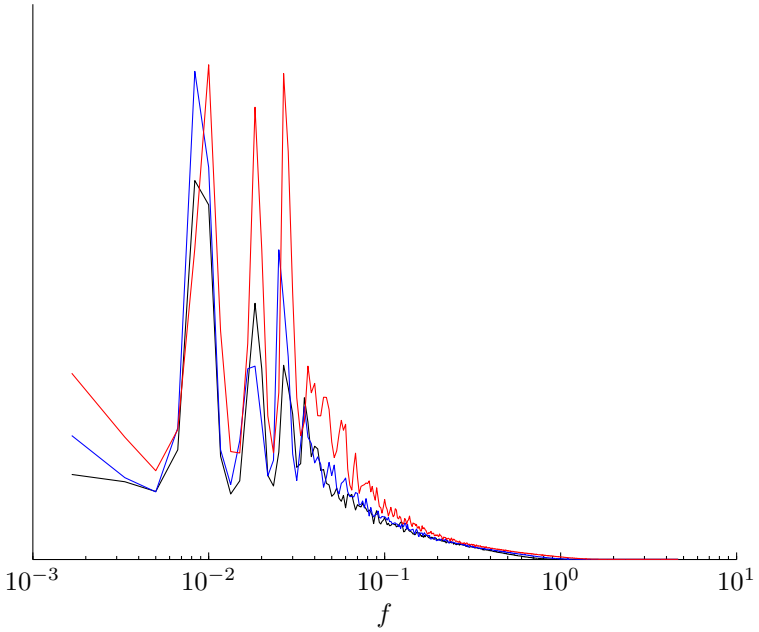

Figure 4.3: Mean TKE spectrums for three different grid resolutions. Legend: —— : $j_{rot} = 11$. —— : $j_{rot} = 16$. —— : $j_{rot} = 25$.

The minor grid study reveal only minor difference between the three examined grid resolutions in terms of the inflow velocity experienced by the turbine as well as the azimuthally averaged profiles in the far wake. Furthermore, the TKE spectrums of the three different grid resolution show only minor discrepancies, particular at high frequencies, which is to be expected. Therefore, in the following grid resolutions corresponding to $j_{rot} = 20 - 22$ are deemed sufficient and will be applied. The chosen resolution is also based on the limitation due to the computational cost of each simulation, as each of the presented simulations on average took 2-3 month of computing time on 100+ processors.

4.3 Wake and Flow Characteristics

Figure 4.4 shows the vorticity deep inside an infinite row of wind turbines with $S = 16R$. The three turbines in the domain are marked. Clearly, the flow is less symmetric and much more complex compared to the vorticity behind a single turbine as depicted in Figure 3.2. However, large scale structures are still present in the highly turbulent flow, e.g. between the first and second turbine where the wake shows large lateral movements.

The very dynamic flow is also illustrated in Figure 4.5, which shows three instantaneous plots of the streamwise velocity extracted $1R$ upstream the first turbine in the domain. The flow is highly complex with small and large scales stemming from the interaction between numerous wakes. The first subplot shows a half wake situation, where the lower part of the turbine is exerted by the wake, while the upper part is experiencing close to freestream conditions. This clearly gives rise to differentiated loads on the rotating blades and turbine.

The second subplot shows a scenario, where the entire rotor experience close to freestream conditions. Wake reminiscents are present, but less coherent and the wake centre is mixed by higher velocity areas. The rotor is exerted by a wake as a streak through the centre of the rotor area in the third image. Remnants of a second wake are present to the left of the rotor. The large scale motions will alternate the wake position and therefore the remnants of multiple wakes can be present at once without the wakes having merged. At other times the combined effect of the wakes will almost disintegrate as in the second subplot, where the coherent wake structures have been broken up and the turbine is exerted by a high and very even velocity distribution. The highly dynamic nature of the flow is emphasised by all three situations occuring within only $166s$, and the turbine has to adopt to all scenarios.

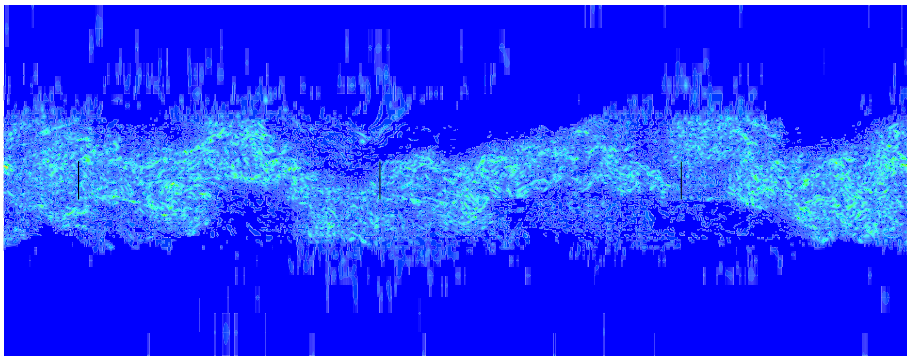

Figure 4.4: Horizontal slice through hub height showing instanteneous vorticity plots deep inside an infinite row of wind turbines. Three turbines (full line) are included in the domain. Bright areas indicate high vorticity.

4.4 Turbine Performance History

The turbulence inherent to the wind turbines deep inside a wind farm is naturally related to the performance of the wind turbine. Figure 4.6 shows the streamwise velocity at hub height, tip speed, and pitch as function of time for the second case with spacing of $16R$. The velocity is extracted $1R$ upstream of the first rotor. It is worth noticing the strong initial decrease from unity to $\frac{U_{hub}}{U_0} \approx 0.3$ in the early stages, i.e. when the flow goes through the first wind turbines. The incoming wind velocity eventually recovers from the initial large decrease and fluctuates around an almost constant level at $\frac{U_{hub}}{U_0} \approx 0.76$. The velocity at hub height fluctuates quite significantly, but the controller ensures that the change in tip speed is limitied to $\Omega \cdot R \approx 71 - 73m/s$, where $\Omega \approx 1.80rad/s$ is the rotational speed. The effect of the PI-pitch angle controller is visualised through the local pitch angle(γ), which is regulated when the incoming wind speed approach the rated wind speed and otherwise kept constant at 0.1° the majority of the time.

The velocity fluctuations naturally gives rise to fluctuations in the power production, which is depicted in Figure 4.7 along with the thrust. The power

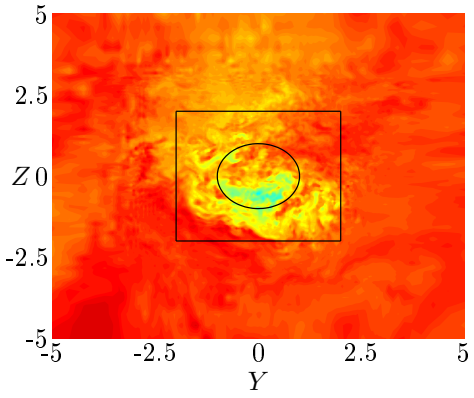

(a) $t = 3,488s$

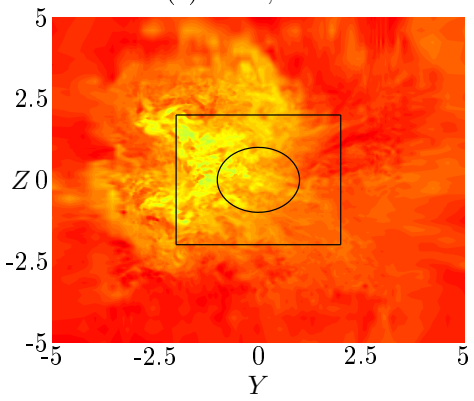

(b) $t = 3,632s$

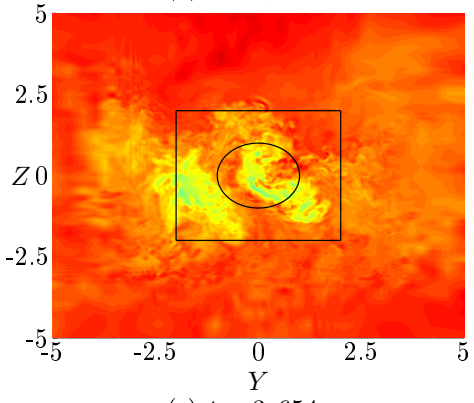

(c) $t = 3,654s$

Figure 4.5: Instantaneous streamwise velocity extracted $1R$ upstream the first turbine with $S = 16R$.

Spacing	$\overline{\frac{U_{hub}}{U_0}}$	$\sigma(\frac{U_{hub}}{U_0})$	$\sigma((\frac{U_{hub}}{U_0})^3)$	$\overline{\Omega R}$	$\overline{\frac{P}{P_0}}$	$\sigma(\frac{P}{P_0})$	$\overline{T}[kN]$
$12R$	0.74	0.11	0.18	72.4	0.87	0.11	272
$16R$	0.76	$9.5 \cdot 10^{-2}$	0.17	72.3	0.86	0.11	270
$20R$	0.78	$8.3 \cdot 10^{-2}$	0.15	72.4	0.89	$8.5 \cdot 10^{-2}$	273

Table 4.2: Mean and standard deviation of the velocity at hub height, standard deviation of the velocity at hub height cubed, mean tip speed, mean normalised power, standard deviation of normalised power and mean thrust of the last $1,500s$ for the three idealised simulations with spacings $12R$, $16R$, and $20R$.

production also fluctuates significantly, and frequently reach the rated power for short periods. The average power production is for all cases above 85%. Standard deviation on the normalised velocity is $\sigma(\frac{U_{hub}}{U_0}) = 9.5 \cdot 10^{-2}$ and normalised power production is $\sigma(\frac{P}{P_0}) = 0.11$. It appears as if the standard deviation for the power production is higher than for the velocity. However, the standard deviations of the power should be compared to $\sigma((\frac{U_{hub}}{U_0})^3) = 0.17$ since the incoming wind is generally below rated power where $P \propto U^3$, see Figure 2.3. The controller also ensures that the otherwises violent fluctuations in the streamwise velocity result in less violent fatique loads on the generator and turbine. The thrust of the turbine shows how the aeroelastic code and the flow solver are fully coupled, as the thrust takes on values from $200kN$ to $300kN$. The actual thrust is given, as opposed to a thrust coefficient(C_T), since there is no unambiguous reference velocity deep inside a wind farm. However, as the wind turbine operates below rated power, the controller ensures operation close to $P \propto U^3$.

The mean and standard deviation of the velocity at hub height, tip speed, power, and thrust of the last $1,500s$ for the three simulations are summarised in Table 4.2. The reasons for averaging over the last $1,500s$ will be elaborated in Section 4.5. The effect of increasing the turbine spacing is clearly seen in the mean and standard deviation of the velocity, which increase and decrease respectively for increasing spacing. This is to be expected as a larger spacing yields a better wake recovery. However, the mean normalised power production also reveal that it is not directly related to an increase in power production, which is basically constant for all three spacings with a marginally larger power production for $12R$ and $20R$ spacing than $16R$ over the $1,500s$. The increased power production for $12R$ is related to the higher standard deviation, i.e. higher degree of change in the velocity at hub height, whereas the increase for $S = 20R$ is due to the increased wake recovery. However, the increase in standard deviation indicates that the loads would be higher for lower spacing. The loads on the turbine will be examined in more detail in Section 6.3. The tip-speed and thrust are practically constant for the three different spacings due to the controller. The variability of the inflow combined with the full aeroelastic coupling with the flow solver results in a highly complex flow. The flow is eventually the combined effect of merging numerous wakes, where the instantaneous wake depends on the thrust and load distribution as described in Chapter 3 for single wakes behind differently loaded rotors. The increased turbulence levels assists in merging the wakes to form an average wake situation as experienced by the turbine, which is examined in details in the following.

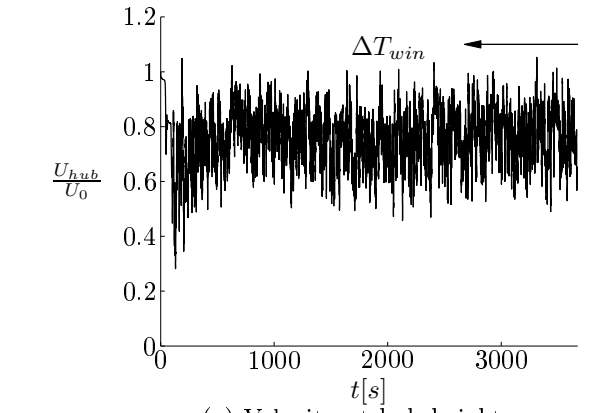

(a) Velocity at hub height.

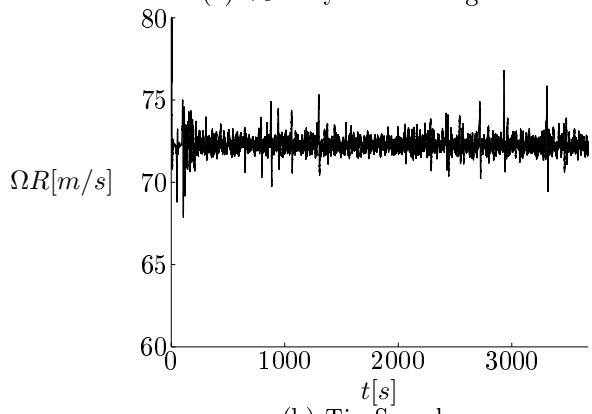

(b) Tip Speed.

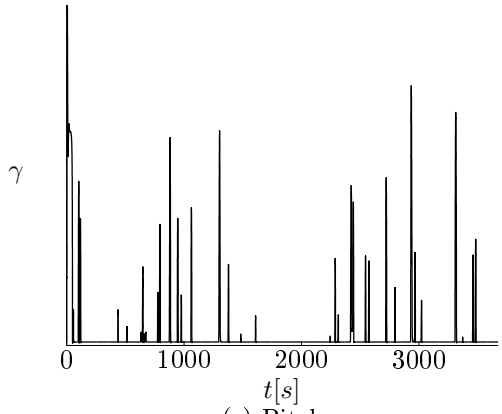

(c) Pitch.

Figure 4.6: Velocity at hub height, tip-speed, and pitch as experienced by the first turbine in the domain with $S = 16R$.

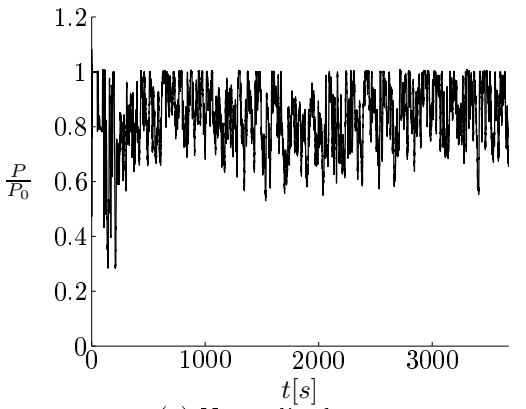

(a) Normalised power.

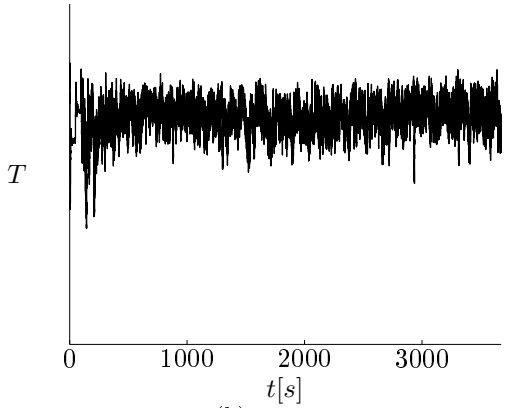

(b) Thrust.

Figure 4.7: Normalised power and thrust as experienced by the first turbine in the domain with separation of $16R$.

4.5 Convergence of Mean and Turbulent Quantities

The previous section initiated the investigation of the dynamic inflow with large fluctuations as experienced by the turbines. Despite the highly dynamic inflow, the statistics will eventually converge to the infinite wind farm scenario, where there is an overall balance between the energy extracted by the turbines and the energy fed into the wake from the surrounding freestream, i.e. to the wake recovery. Figure 4.6 indicated how the flow between the turbines approaches an equilibrium with large fluctuations. Ideally, the flow should approach a random stationary process in order to apply POD, see Section 4.8. The turbulent quantities should converge statistically to approach such a random stationary process. The three velocity components are extracted $1R$ upstream the first turbine in the domain, simular to the streamwise velocity shown in Figure 4.5. The statistical convergence of the mean and turbulent quantities are examined to ensure that the total simulation time is long enough for all dominant flow statistics to converge. The flow is assumed to have converged statistically, when the spatial RMS values of the normalised mean and turbulent quantities within $\pm 2R$ of hub height have reached an approximately constant level, i.e. taking the RMS of the quantities located within the box marked on Figure 4.5. Therefore, each simulation is examined for a range a temporal windows (ΔT_{win}) starting from the end of the simulations to determine a sufficiently large ΔT_{win} to achieve this statistical convergence. ΔT_{win} is indicated in Figure 4.6.

Figure 4.8 shows the mean velocities and RMS values of the velocity fluctuations as function of ΔT_{win} for $S = 16R$. Clearly, the streamwise velocity dominates the flow with only small lateral and vertical components. The minor discrepancy from zero is related to the swirl or rotation of the wake. It is worth noting that the values of the mean streamwise velocity ratio here is significantly larger than the 0.76 reported in Table 4.2, because it is averaged for $\pm 2R$, i.e. the averaging includes the surrounding high velocity areas. The streamwise fluctuations are approximately 20% larger than the inplane fluctuation. Generally, the mean streamwise velocity is at an approximate constant level for all ΔT_{win}. Similarly, streamwise velocity fluctuations are approximately $\sqrt{\overline{u'^2}} \approx 0.10$.

Similarly, Figure 4.9 shows the convergence for the inplane Reynolds stresses and Turbulent Kinetic Energy(TKE) production. The broken lines show the mean value and the dotted lines the $\pm 10\%$ of the mean of the RMS values. The diagonal Reynolds stresses ($\tau_{i,j}, i = j$) dominate the flow, with the streamwise almost twice the size of the inplane stresses. The Reynolds stresses portrait a similar convergence as the velocity fluctuations, as expected. The off-diagonal Reynolds stresses are smaller than the diagonal stresses. The TKE production is dominated by the components related to the streamwise velocity derivatives, which reaches an approximate constant level when applying a window of more than $21min$, marked by a vertical black line. The terms related to the diagonal Reynolds stresses are about 50% less in magnitude. The remaining two terms($\tau_{yz}\frac{dV}{dZ}$ and $\tau_{zy}\frac{dW}{dY}$) also reach a constant, but much smaller level, for a window of approximately $21min$. A second vertical black line marks the larges applicable window, ΔT_{win}.

Similar analyses have been done for all simulations in this section, which is summarised in Table 4.3. The table also gives the maximum and minimum

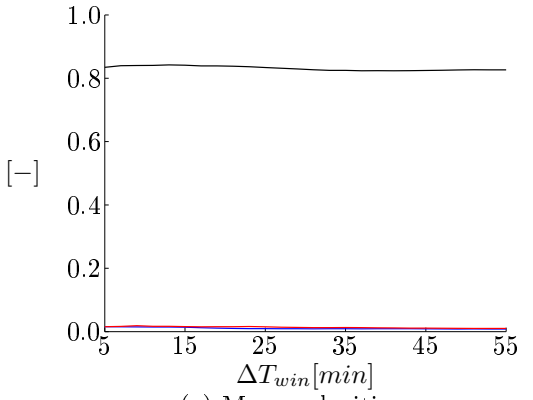

(a) Mean velocities.

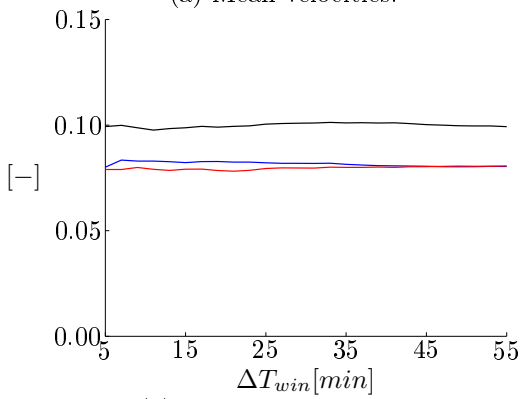

(b) Turbulent fluctuations.

Figure 4.8: Spatial RMS values of mean velocities and turbulent fluctuations within $\pm 2R$ for $16R$. Notice, quantities are dimensionless. Legend: ——: $\sqrt{\overline{U}^2}$ and $\sqrt{\overline{u'^2}}$. ——: $\sqrt{\overline{V}^2}$ and $\sqrt{\overline{v'^2}}$. ——: $\sqrt{\overline{W}^2}$ and $\sqrt{\overline{w'^2}}$.

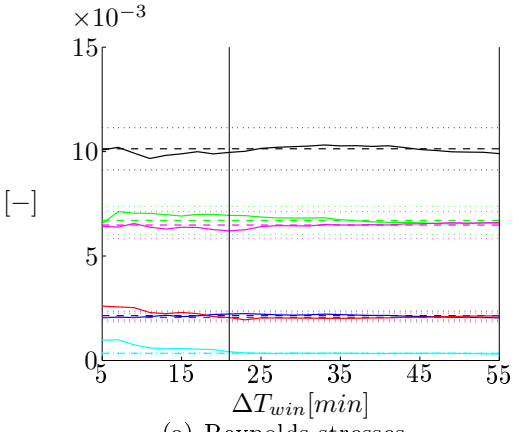

(a) Reynolds stresses.

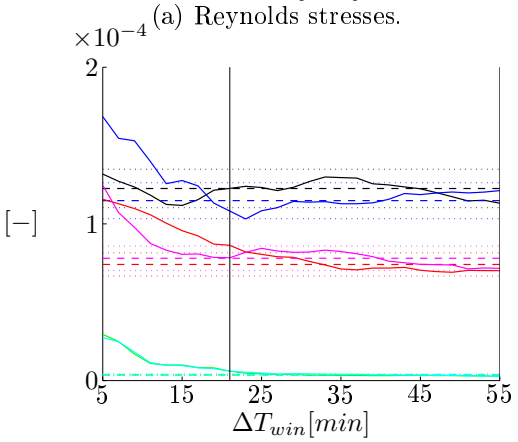

(b) TKE Production.

Figure 4.9: Spatial RMS values of Reynolds stresses and TKE production within $\pm 2R$ for $16R$. Notice, quantities are dimensionless. Legend: —— : τ_{yy} and $\tau_{xy}\frac{dU}{dY}$. —— : τ_{yz} and $\tau_{xz}\frac{dU}{dZ}$. —— : τ_{yx} and $\tau_{yy}\frac{dV}{dY}$. —— : τ_{zz} and $\tau_{yz}\frac{dV}{dZ}$. —— : τ_{zx} and $\tau_{zy}\frac{dW}{dY}$. —— : τ_{xx} and $\tau_{zz}\frac{dW}{dZ}$.

windows as well as the converged levels for reference. The table reveal several trends for the turbulent quantities. The increased wake recovery and decrease in turbulence intensity for increasing turbine spacing is clear again. This effectively means that both Reynolds stresses and TKE production terms are approximately twice as big for $S = 12R$ compared to $S = 20R$.

A maximum window is given in Table 4.3 for the statistical analysis, because the averaging window can be too large, i.e. the statistics starts to include the transient from the initial startup. The same analysis have been done for the simulations presented in Section 3 and Section 5, and a temporal window of $25min$ is deemed adequately converged for all simulations and the following results are all based on a window of $\Delta T_{win} = 1,500s = 25min$ periods unless clearly stated.

Figure 4.10 shows the mean streamwise velocity for $16R$, which show a clear wake deficit larger than $1R$. The large spread is related to the large scale motions of the wake, which is investigated in detail in Section 4.7. The mean inplane streamlines are also shown, which show a minor clockwise rotation and an general outflow, which is caused by the divergent flow around the turbine. The rotation is clockwise, because the plot shows the incoming wake velocity as seen from the downstream turbine. The wake rotates counter-clockwise if seen from the previous turbine.

Figure 4.11 gives the three velocity fluctuations. The highest fluctuations are found around the rotor edge, but it is somewhat smeared compared to a clear annular distribution seen behind a single turbine, e.g. Figure 3.5. The lateral and veritical fluctuations are concentrated within the rotor area.

Figure 4.12 shows the Reynolds stresses. The diagonal Reynolds stresses(τ_{xx}, τ_{yy}, and τ_{zz}) dominate the overall Reynolds stresses, and reveal similar patterns as those for the fluctuations in Figure 4.11. There is a clear symmetry in the two off- diagonal Reynolds stresses involving the streamwise fluctuations(τ_{xy} and τ_{xz}), which shows how momentum is transferred from the surroundings into the wake centre. The symmetry of τ_{xy} and τ_{xz} are also due to the cartesian nature of the current plots. The last Reynolds stress(τ_{yz}) in the plane is smaller and more evenly distributed.

The inplane TKE production terms are shown in Figure 4.13. The significant TKE sources stems from the streamwise velocity gradient($\frac{dU}{dY}$ and $\frac{dU}{dZ}$) immediately outside the rotor area, i.e. turbulence is generated in the shear layer. The TKE sinks are related to the inplane diagonal Reynolds stresses, $-\tau_{yy}\frac{dV}{dY}$ and $-\tau_{zz}\frac{dW}{dZ}$, and concentrated within the rotor area. The two remaining terms are smaller and less distinct. The total inplane TKE production is portraited in Figure 4.14, where the inner sinks and outer sources are clearly visible. $S = 12R$ and $S = 20R$ yield similar results, but are left out for brevity, as the difference in level is summarised in Table 4.3.

The converged flow statistics corresponds to the asymptotic scenario of an infinitely long row of turbines.

4.6 Comparison with Analytical Models

As the flow statistics have converged, the internal flow in the infinite row of turbines have approached the infinite farm scenario. Kinematic wake models such as the N. O. Jensen [28] and Frandsen et al. [20] gives explicit expressions

Quantity	**12R**	**16R**	**20R**
$\Delta T_{win}[s]$	$[1,380-4,860]$	$[1,260-3,300]$	$[1,020-4,860]$
$RMS(\overline{U})$	0.83	0.83	0.85
$RMS(\overline{V})$	$8.0 \cdot 10^{-3}$	$9.0 \cdot 10^{-3}$	$9.7 \cdot 10^{-3}$
$RMS(\overline{W})$	$8.9 \cdot 10^{-3}$	$12 \cdot 10^{-3}$	$14 \cdot 10^{-3}$
$RMS(\sqrt{\overline{u'^2}})$	0.12	0.10	$8.9 \cdot 10^{-2}$
$RMS(\sqrt{\overline{v'^2}})$	$9.1 \cdot 10^{-2}$	$8.1 \cdot 10^{-2}$	$7.0 \cdot 10^{-2}$
$RMS(\sqrt{\overline{w'^2}})$	$9.1 \cdot 10^{-2}$	$8.0 \cdot 10^{-2}$	$6.9 \cdot 10^{-2}$
$RMS(\tau_{xx})$	$14 \cdot 10^{-3}$	$10 \cdot 10^{-3}$	$7.9 \cdot 10^{-3}$
$RMS(\tau_{yy})$	$8.4 \cdot 10^{-3}$	$6.7 \cdot 10^{-3}$	$5.1 \cdot 10^{-3}$
$RMS(\tau_{zz})$	$8.5 \cdot 10^{-3}$	$6.5 \cdot 10^{-3}$	$4.9 \cdot 10^{-3}$
$RMS(\tau_{xy})$	$3.1 \cdot 10^{-3}$	$2.1 \cdot 10^{-3}$	$1.7 \cdot 10^{-3}$
$RMS(\tau_{xz})$	$3.1 \cdot 10^{-3}$	$2.1 \cdot 10^{-3}$	$1.5 \cdot 10^{-3}$
$RMS(\tau_{yz})$	$7.0 \cdot 10^{-4}$	$3.4 \cdot 10^{-4}$	$2.6 \cdot 10^{-4}$
$RMS(\tau_{xy}\frac{d\overline{U}}{dY})$	$2.1 \cdot 10^{-4}$	$1.2 \cdot 10^{-4}$	$9.3 \cdot 10^{-5}$
$RMS(\tau_{xz}\frac{d\overline{U}}{dZ})$	$2.2 \cdot 10^{-4}$	$1.1 \cdot 10^{-4}$	$7.0 \cdot 10^{-5}$
$RMS(\tau_{yy}\frac{d\overline{V}}{dY})$	$8.4 \cdot 10^{-5}$	$7.4 \cdot 10^{-5}$	$5.3 \cdot 10^{-5}$
$RMS(\tau_{yz}\frac{d\overline{V}}{dZ})$	$8.1 \cdot 10^{-6}$	$3.6 \cdot 10^{-6}$	$2.4 \cdot 10^{-6}$
$RMS(\tau_{zy}\frac{d\overline{W}}{dY})$	$7.0 \cdot 10^{-6}$	$3.9 \cdot 10^{-6}$	$2.9 \cdot 10^{-6}$
$RMS(\tau_{zz}\frac{d\overline{W}}{dZ})$	$8.2 \cdot 10^{-5}$	$7.8 \cdot 10^{-5}$	$6.0 \cdot 10^{-5}$
$RMS(\mathcal{P})$	$3.2 \cdot 10^{-4}$	$1.9 \cdot 10^{-4}$	$1.4 \cdot 10^{-4}$

Table 4.3: Spatial RMS values of the converged turbulent quantities within the limits of the temporal window ΔT_{win} for $12R$, $16R$, and $20R$. Notice, quantities are dimensionless.

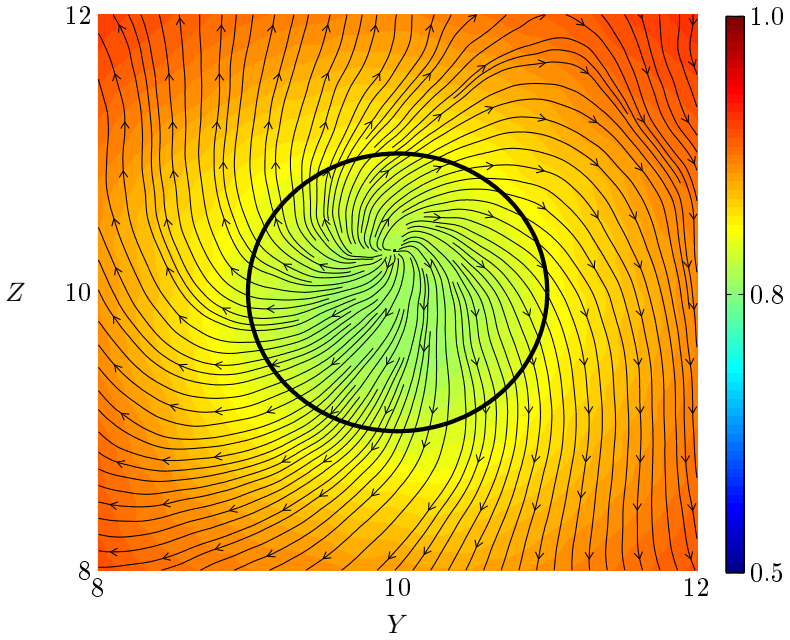

Figure 4.10: Mean streamwise velocity and mean inplane streamlines at $1R$ upstream the first rotor with $S = 16R$. Notice, quantities are dimensionless.

for the asymptotic mean wind velocity inside an infinitely long row of wind turbines. The kinematic models are assessed and fitted to the CFD data given in Figure 4.6, Table 4.2, and Table 4.3 in the following.

N. O. Jensen Model

N. O. Jensen gives the following expression:

$$\frac{U_{NOJ}}{U_0} = 1 - \frac{\frac{2}{3} \cdot k}{1 - \frac{1}{3} \cdot k}, \quad \text{where} \quad k = \left(\frac{R}{R + \alpha_{NOJ} \cdot S} \right)^2 \tag{4.1}$$

R is the rotor radius, $S = \frac{X}{R}$ is the turbine spacing, and α_{NOJ} is an entrainment constant governing the wake expansion, which is assumed to be linear. The original article by Jensen gives $\alpha_{NOJ} = 0.1$, while others recommend values of $\alpha_{NOJ} = 0.05$ for offshore, e.g. Barthelmie et al. [12].

The parameter α_{NOJ} is determined by fitting the Jensen model to the asymptotic wind velocity at hub height in a least squares sense, which yields $\alpha_{NOJ} = 0.0501$, indicating that the recommended value by Barthelmie et al. [12] is sufficient and hence will be used in the following.

Frandsen Model

Frandsen's control volume analysis yields the following expression for the asymptotic relative velocity value:

$$\frac{U_{SF}}{U_0} = \frac{\alpha_{SF}}{\alpha_{SF} + \frac{1}{2} \frac{C_T}{\frac{1}{2} S}} \tag{4.2}$$

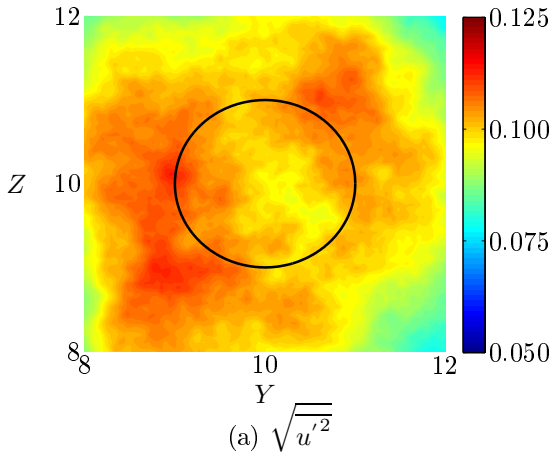

(a) $\sqrt{\overline{u'^2}}$

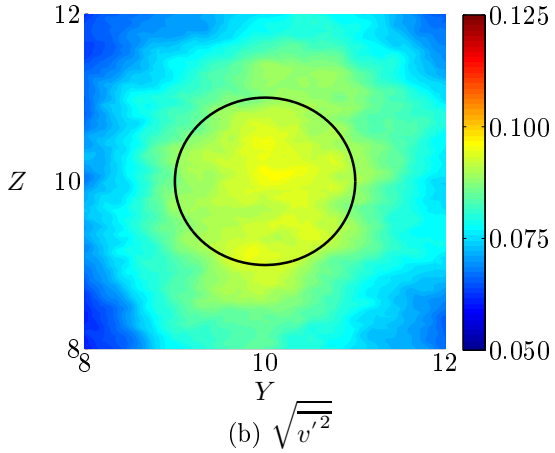

(b) $\sqrt{\overline{v'^2}}$

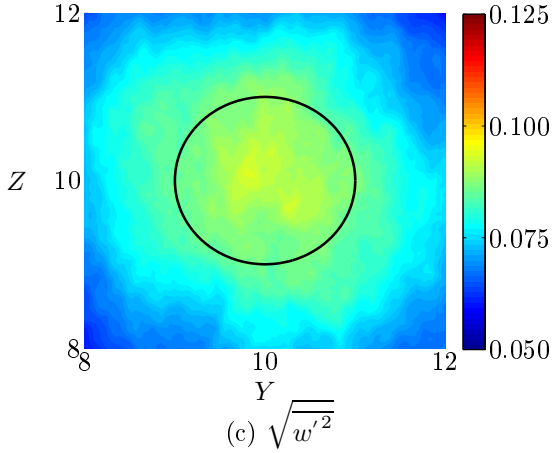

(c) $\sqrt{\overline{w'^2}}$

Figure 4.11: Velocity fluctuations $1R$ upstream the first rotor with $S = 16R$. Notice, quantities are dimensionless.

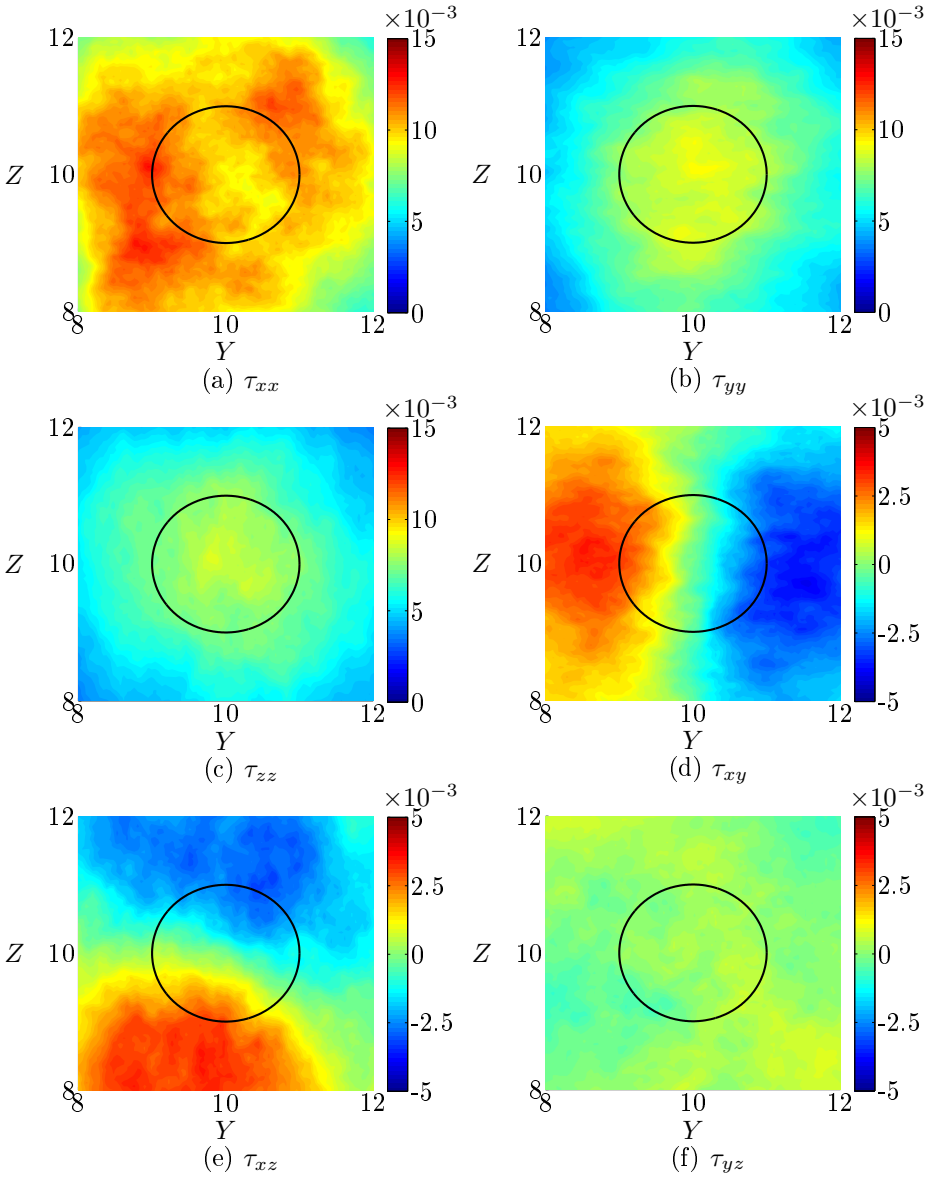

Figure 4.12: Reynolds stresses $1R$ upstream the rotor with $S = 16R$. Notice, quantities are dimensionless.

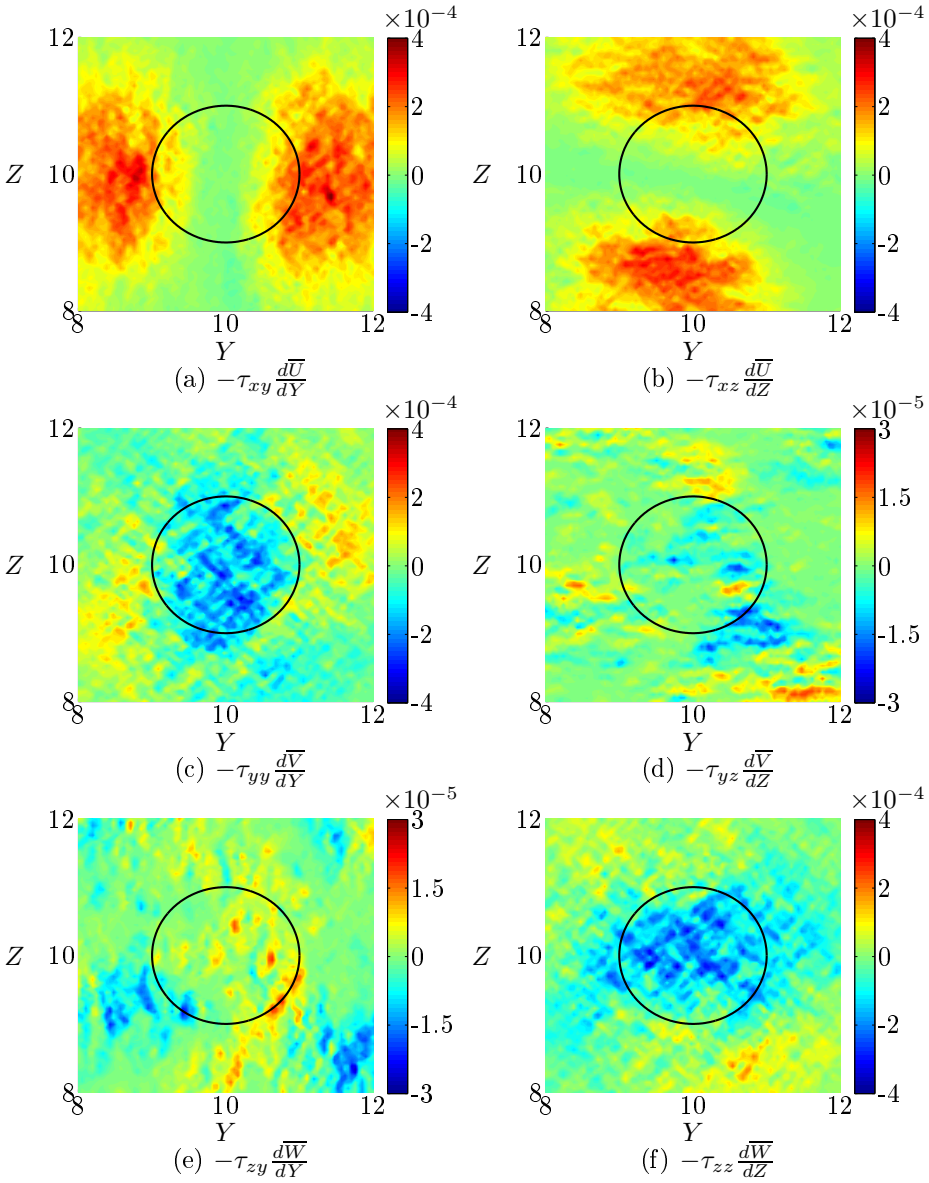

Figure 4.13: TKE production $1R$ upstream the rotor with $S = 16R$. Notice, quantities are dimensionless.

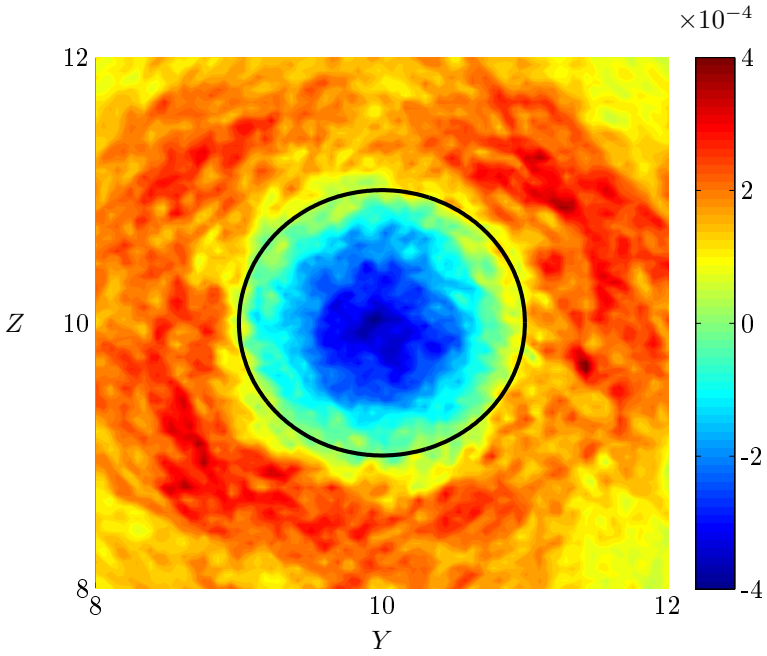

Figure 4.14: Total inplane TKE production $1R$ upstream the rotor of spacing $16R$. Notice, TKE production is dimensionless.

where $\frac{1}{2}S = \frac{X}{D}$ is the non-dimensional turbine spacing in terms of diameters, α_{SF} is a constant, different from α_{NOJ}, which should be determined experimentally. Alternatively, α_{SF} could be determined from the expression above if $\frac{U_{SF}}{U_0}$ is known:

$$\alpha_{SF} = \frac{1}{2}\frac{C_T}{S}\frac{\frac{U_{SF}}{U_0}}{1-\frac{U_{SF}}{U_0}} \tag{4.3}$$

However, C_T is still a parameter, and it is not trivial to determine C_T internally in the wind farm, since there is no obvious choice of reference velocity. Frandsen [19] suggest calculating C_T as

$$C_T = \frac{3.5(2 \cdot U_{hub} - 3.5)}{U_{hub}^2} \approx \frac{7}{U_{hub}} \tag{4.4}$$

which has since been adopted into the IEC standard [4] as a generic approximation for C_T. The latter expression yields a good agreement with the C_T curve for the present NM80 turbine and is applied to determine α_{SF}, as seen in Figure 2.3. Decreasing the turbine spacing leads to increasing C_T, which again yields increasing α_{SF}. Frandsen et al. [20] and Barthelmie et al. [12] set $\alpha_{SF} = \mathcal{O}(10 \cdot \alpha_{NOJ})$ for small C_T and large spacings. However, the present results suggests that increasing turbine spacing leads to a decrease in α_{SF} and $\alpha_{SF}\mathcal{O}(2 - 3\alpha_{NOJ})$. The fitted α_{SF} are depicted in Figure 4.15 for the generic C_T and C_T for the NM80 turbine.

Figure 4.15 shows the asymptotic mean wind speed at hub height in the infinite wind farm case for the simulations and the two kinematic models with the abovementioned parameters. The results using the Frandsen model with

both recommended value($\alpha_{SF} = 0.5$) and fitted values as function of C_T are shown. Clearly, the Frandsen model using the recommended values overpredicts the wake recovery by roughly 20%, which is surprisingly far from the target value. However, the N. O. Jensen and the fitted Frandsen model give a good fit, particular at the intermediate spacings, while the velocity is underpredicted for short spacing and overpredicted for large spacings. The recommended value for the Frandsen model are 3-4 times bigger than the actually fitted. These models are expected to give a reasonable agreement for the idealised cases excluding shear and ground effects, since they are based on momentum considerations. The parameters and predicted values are summarised in Table 4.4, which also gives the difference from CFD results. Generally, the difference is within ±5% for the mean wind speed deep inside a wind farm.

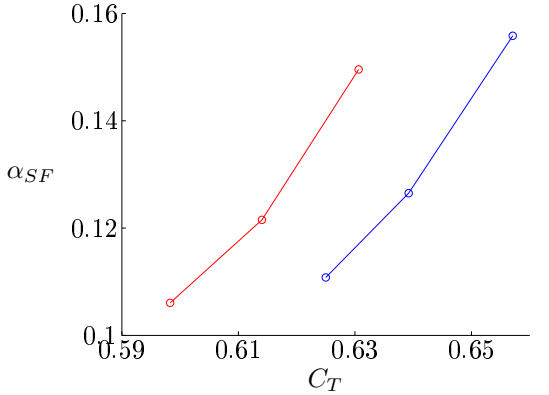

(a) $\alpha_{SF}(C_T)$.

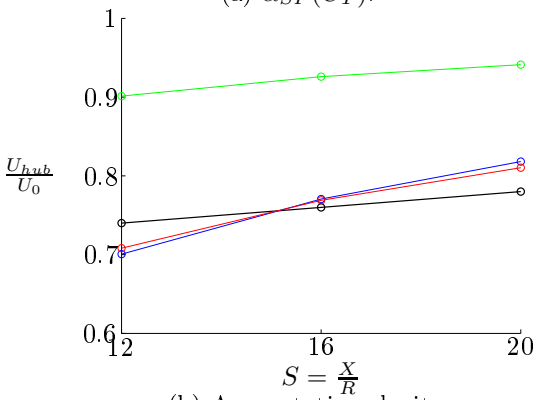

(b) Asymptotic velocity.

Figure 4.15: Fit for $\alpha_{SF}(C_T)$ using C_T-values for NM80 turbine and generic expression and comparison of asymptotic mean velocity at hub height from CFD and kinematic models. Legend: —— : CFD. —— : (a) NM80 C_T. (b) N.O. Jensen model. —— : Frandsen model using generic C_T and $\alpha_{SF} = 0.5$. —— : (a) Generic C_T. (b) Frandsen model using generic C_T and fitted $\alpha_{SF} = f(C_T)$.

Quantity	12R	16R	20R
$\frac{\overline{U_{hub}}}{U_0}$	0.74	0.76	0.78
C_T	0.63	0.61	0.60
α_{NOJ}	0.05	0.05	0.05
$\frac{U_{NOJ}}{U_0}$	0.70	0.77	0.82
$Difference$	-5.3%	$+1.4\%$	$+4.9\%$
$\alpha_{SF,rec}$	0.5	0.5	0.5
$\frac{U_{SF,rec}}{U_0}$	0.90	0.93	0.94
$Difference$	$+22\%$	$+22\%$	$+21\%$
$\alpha_{SF,fit}$	0.15	0.12	0.11
$\frac{U_{SF,fit}}{U_0}$	0.71	0.77	0.81
$Difference$	-4.3%	$+1.2\%$	$+3.9\%$

Table 4.4: Summary of comparison of asymptotic hub height velocities from CFD results and the kinematic models by N. O. Jensen and Frandsen with spacings $12R$, $16R$, and $20R$. Positive difference indicates that the kinematic wake model overpredicts the asymptotic velocity at hub height.

4.7 Large Scale Motions

The large scale motions are again calculated using the centre of mass approach described in Section 3.4. The wake centre movement for $S = 16R$ is presented in Figure 4.17. The large scale motions or meandering are initiated after approximately $100s$, and continue to grow in magnitude to about $1R$ over the next $600s$. This self-induced meandering is initiated after $76s$ and $116s$ for $S = 12R$ and $S = 20R$, respectively. For all cases, the time corresponds to initiating self-induced meandering in the third wake, i.e. the initial uniform flow has passed through three turbines. The large scale movements remain constant around $\pm 1R$ with a few extreme deviations of up to $1.5R$. The standard deviations of the lateral and vertical directions are $0.43R$ and $0.46R$, respectively. The corresponding values for $12R$ are $0.49R$ and $0.51R$, and $0.37R$ and $0.42R$ for $S = 20R$. The large scale motions appears to increase for smaller spacings between the turbines. The large scale motions are significantly increased compared to the RMS values behind a single turbine for $S = 12R$ and $S = 16R$, shown in Figure 3.8. However, the difference is only minor for $S = 20R$, where the corresponding RMS values $20R$ behind a single turbine are $0.38R$ and $0.35R$ for the lateral and vertical movements. This indicates that the large scales are less dependent on the turbine arrangement for large spacings as the wake break down occurs before reaching the next turbine. There appears to be a minor bias towards larger meandering in the vertical, although there once again should be no preferred direction in the present setup, but the deviation is assumed insignificant as it does not give rise to any significant bias in the turbulent quantites

presented in Section 4.5.

Figure 4.16 depicts the inplane trajectory of the wake centre, which shows that not only is the flow complex, but so are the large scale motions. The location of the wake centre changes and it alternates between moving clock- and counterclockwise.

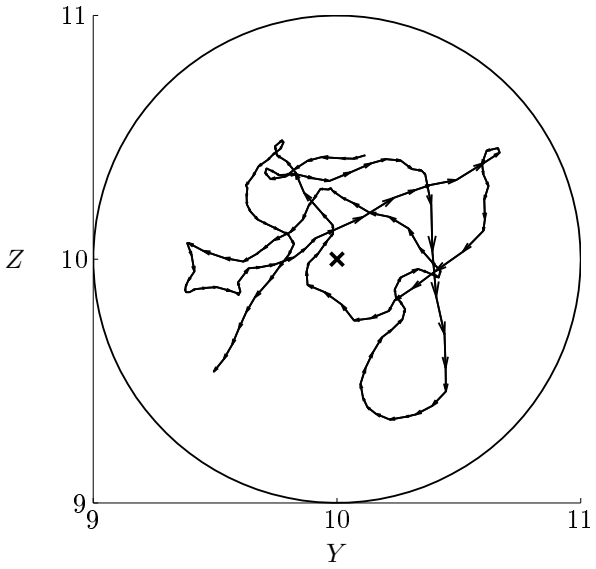

Figure 4.16: Inplane wake centre coordinates $1R$ upstream the rotor of spacing $16R$ for $t \in [2,695 - 2,865s]$.

One of the fundamental hypotheses of the Dynamic Wake Meandering(DWM) model is that the large scales are driven directly by the large scales in the atmospheric turbulence. Lu and Porté-Agel [39] have also reported a direct link between the large scales and the atmospheric turbulence. However, the present simulations exclude the presence of atmospheric turbulence, yet low frequent structures arise, similar to the low frequencies found in the wake behind a single turbine in Section 3.4.

The other basic assumption in the DWM model is that the wake is translated downstream as a passive tracer by low frequent structures. This hypothesis is tested by computing the Power Spectral Density(PSD) of TKE within $\pm 2R$ in both the fixed frame of reference and a moving frame of reference relative to the wake centre motion. The data has been interpolated to a polar grid and the latter is corrected for the location of the wake centre and the inplane displacement of the wake, i.e. correcting V and W by the lateral and vertical velocity of the wake centre motion. The two spectrums for the three simulations are presented in Figure 4.18, where the spectrums are normalised by the integral of the spectrum. First, the PSD in the fixed frame of reference show clear peaks at low frequency for all three cases. However, dominant peaks still persist in the moving frame of reference, and although the energy is redistributed in the spectrum, the same peak frequencies are present in both reference frames. If the hypothesis is correct, the low frequent peaks should be removed by accurately determining the centre of the wake. The question naturally arise if the wake centre is determined accurately as the detection of the wake centre is not trivial.

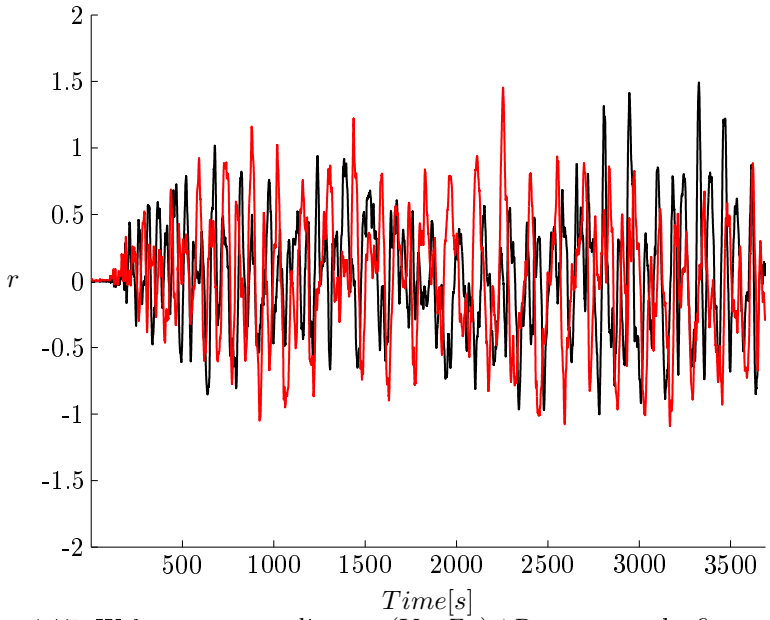

Figure 4.17: Wake centre coordinates, (Y_C, Z_C) $1R$ upstream the first rotor with $S = 16R$. Legend: —— : Y_C —— : Z_C

The centre of mass approach is a simple approach, and tests indicated that $m = 3$ generally gave more consistent results than $m = 1$, see Equation 3.1. Trujillo et al. [71] discuss the drawbacks of the centre of mass approach behind a single turbine, and conclude that it is not robust because low speed regions due to turbulence outside the immediate wake affect the position of the wake centre. Therefore, Trujillo et al. suggest fitting a bivariate Gaussian shape to the wake deficit. However, such an assumption is not robust either, particular when multiple wakes interacts. The assumption of a generic shape inevitably raises two distinct questions when interpreting Figure 4.5. Which is the correct wake centre and how appropriate is such a Gaussian fit is in the case of multiple wakes, where the shape of the wake deficit clearly morphs continuously between various complex shapes and remnants of numerous past wakes are present.

Therefore, the current results suggests that the highly complex wake dynamics deep within a wind farm can not be modelled as a collective entity overlaid with the large scale motions of the atmospheric turbulence. The results also suggest that such an assumption is only valid for the first few turbines, but does not hold in the interior of a wind farm where the self-induced meandering prevails. This is in part due to the instanteneous lack of axisymmetry in Figure 4.5. There are no apparent traces of general symmetries, axial or azimuthal, which would allow such a transformation to a moving frame of reference. Rather, the wake deficit constantly changes shape and occassionally also rotational direction as examplified in Figure 4.16.

Figure 4.17 and the subsequent analysis showed how the large scale motions are initiated before a full turnaround have been completed, i.e. some self-induced meandering is inherent to the turbines. Medici and Alfredsson [45] experimentally examined the turbulent wake behind a rotor and found shedding similar to the vortex shedding behind a bluff body. Medici and Alfredsson

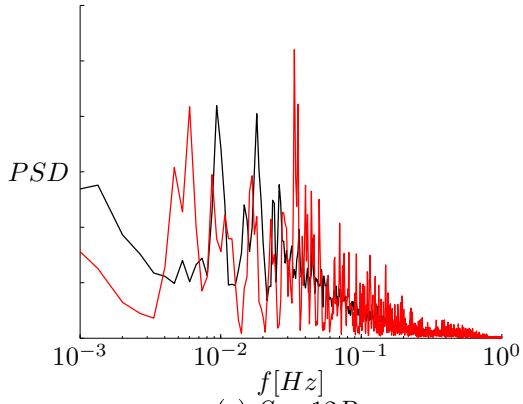

(a) $S = 12R$

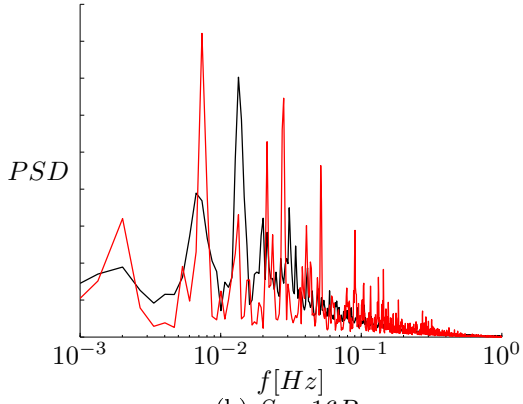

(b) $S = 16R$

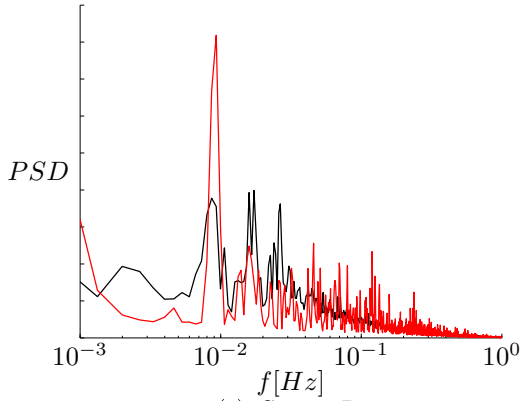

(c) $S = 20R$

Figure 4.18: Power Spectral Density in fixed frame of reference and in moving frame of reference. The PSD have been scaled by the integral of the spectrum. Legend: —— : Fixed frame of reference. —— : Moving frame of reference.

reported $St = 0.12$ for tip-speed ratios above 4.5. Therefore, Figure 4.19 portraits the TKE spectrums for the three idealised cases as well as the spectrums computed $12R$, $16R$, and $20R$ behind the single turbine reported in Chapter 3. The spectrums are plotted versus Strouhal number:

$$St = \frac{fL}{U_{in}} \tag{4.5}$$

where U_{in} is the inflow velocity in the single wake case and $\overline{U}_{hub}$ in the infinitely long row scenarios. Large scales are evident in both spectrums for all three cases, and occassionally the peaks coincide directly, e.g. peak frequency $St_{P,1} \approx 0.07$ for $12R$ and $St_{P,1} \approx 0.1$ and $St_{P,2} \approx 0.14$ for $16R$. The spectrums for $20R$ are less comparable, since there is a larger number of peak frequencies at relative high Strouhal numbers behind a single turbine. The peak frequencies are located at low frequencies, but there are evidently also secondary peak frequencies present in the vicinity of $St = 0.2$ for all the three idealised cases. The corresponding frequencies are $St = 0.19$ for $S = 12R$, $St = 0.22$ for $S = 16R$, and $St = 0.18$ and $St = 0.20$ for $20R$. Furthermore, it is noteworthy that the rotational frequency of the wind turbine ($1P = f_{WT} = 0.29Hz$) is no longer present in any of the spectrums, as also reported by Lu and Porté-Agel [39]. This shows how the spacings are large enough to consider the wake inflow as far wake.

The three PSD spectrums from Figure 4.18 are presented again in Figure 4.20, both as a function of frequency and as function of an equivalent Strouhal number based on the domain length, i.e.

$$St_{L_x} = \frac{fL_x}{U_{hub}} \tag{4.6}$$

where L_x is the domain length in the streamwise direction, see Table 4.1. Scaling with the domain length clearly shifts the low peak frequencies to coincide, which suggest that the large scales could be introduced due to the domain length and the cyclic boundary conditions. These large scales might also be introduced due to the spacing between the individual turbines, which is inevitably connected to the total domain length. The domains have been increased to contain several turbines to limit any such domain effect and the cross-correlations are calculated to further investigate any domain effects. Figure 4.21 shows the two point temporal cross-correlation for $S = 16R$. The cross-correlations are calculated between time series extracted at various cross-sections in the domains at $(Y, Z) = (10R, 10R)$. The reference time serie, which yields the auto-correlation, is extracted $1R$ upstream the first turbine in the domain. Obviously, the correlation is large ($\hat{R} \approx 0.8$) between $1R$ and $2R$ upstream the first turbine, while it decreases to $\hat{R} = 0.25 - 0.35$ for correlations with time series extracted between the first and second turbine. The cyclic nature ensures comparable correlations between the reference point and time series extracted between the second and third turbine with a difference in time lag. The time lag between the maximum correlations upstream the first, second, and third turbine is roughly $50s$, corresponding to a propagation speed of $12.3m/s$, which is larger than the average streamwise velocity of $0.76 \cdot 15m/s = 11.4m/s$. It is also pronounced how the correlation quickly dimish and does not persist over multiple turnaround periods. In fact, the second highest auto-correlation is 0.18, i.e. secondary peaks

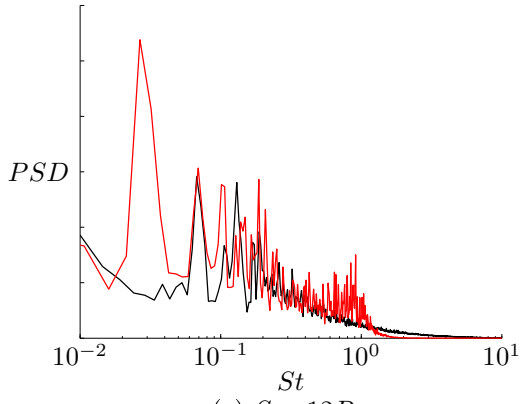

(a) $S = 12R$.

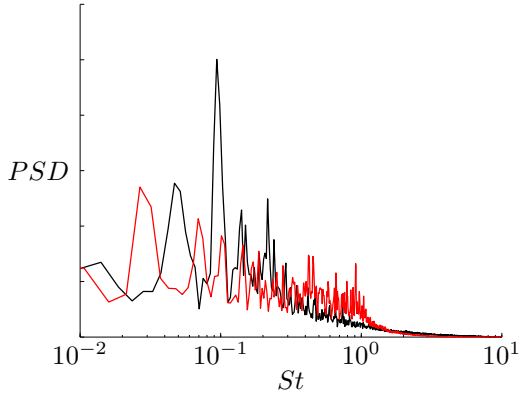

(b) $S = 16R$.

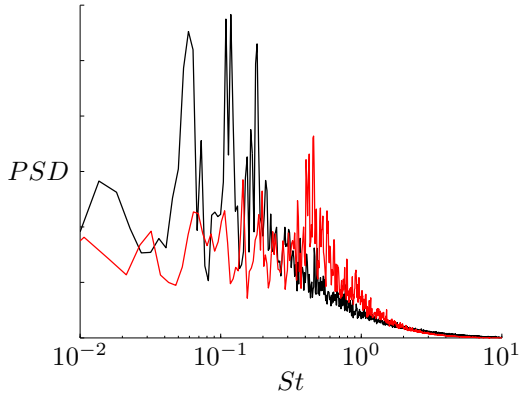

(c) $S = 20R$.

Figure 4.19: PSD in infinitely long rows of turbines compared to PSD in the wake behind a single turbine. The PSD have been scaled by the integral of the curve. Legend: —— : Infinite row of turbines. —— : Single wake.

for the thicker black line. This level yields the largest possible correlation due to the cyclic boundary conditions. However, the actual correlation is presumably lower. The cross-correlation includes an inherent minimum correlation due to resemblance in the turbulent structures of the merged wakes which is maintained by each passing of the turbines. This is not a domain effect, but an effect of the wake similarities. This is investigated further by plotting the maximum cross-correlation for each distance and for all three spacings as function of the distance between the two points considered, see Figure 4.22. The vertical lines indicate the location of the turbines in the domain. The cross-correlation as function of distance behind a single turbine is plotted for reference. The open circles for larger spacings indicate that the cross-correlation has crossed zero. The cross-correlation between the turbines are only $0.27-0.37$ for all three cases. However, the maximum correlation due to the cyclic boundaries can not exceed the minimum cross-correlation. Comparatively, the correlation behind a single turbine decrease linearly to the constant level of $\hat{R} \approx 0.1$ for distances above $10R$, indicating that the wake maintains a certain degree of correlation even far into the wake. The difference between $\hat{R} \approx 0.1$ and $\hat{R} \approx 0.18$ could be caused by the cyclic boundary conditions, but the cross-correlations also increase for time series extracted in similar positions, e.g. $1R$ upstream a turbine. This implies that the majority of the correlation stems from the large structures inherent to the wake, not the domain. It is furthermore conjectured that the turbines assist in breaking up the large domain scales, so applying cyclic boundaries does not introduce dominant large scales provided there are multiple turbines in the domain.

The inplane radial cross-correlation($\hat{R}_r$) is also computed as function of radius, see Figure 4.23. The radial cross-correlations are averaged azimuthally and temporally. Several locations are plotted, and the cross-correlations clearly coincide with only minor differences between the locations in the domain. The computed integral length scale(T_E) are marked along the axis. The integral length scale is approximately $1.0 - 1.1R$ for all simulations, which is a measure of the length scale of the inplane turbulent structures. The spatial extend of $1R$ can visually be seen in Figure 4.5.

In summary, low frequent motions are inherent to the wake interaction deep inside an infinitely long row of wind turbines. The low frequent motions could potentially arise due to the unphysical effect originating from the cyclic boundaries, but cross-correlations indicate this effect to be less than dominant. However, even larger domains are needed to formally exclude such potential domain effect. The turnaround time should be an order of magnitude larger than the physical periods in question, which would require domains $\mathcal{O}(10)$ times larger than the present domains. Domains of that magnitude are beyond the scope of the present work as it would require tremendous computational ressources. Ideally, simulations should be run with numerous turbines(10+) with cyclic boundary conditions and with standard inflow-outflow conditions. This would enable the identification of the origin of the meandering and it would assist in determining when the infinite wind farm is obtained, i.e. after how many turbines. Despite this formal uncertainty, it is conjectured that the origin of the meandering is dominated by physical effects in the present simulations and the examination of the large coherent structures is continued by applying POD.

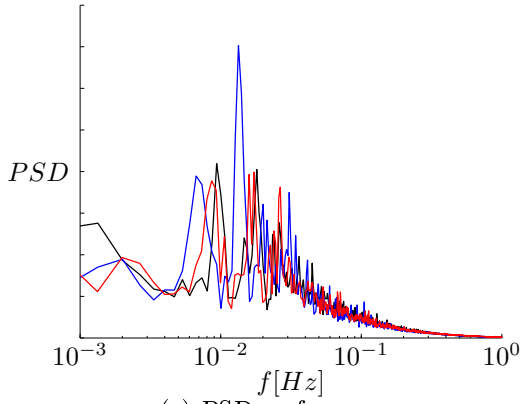

(a) PSD vs frequency.

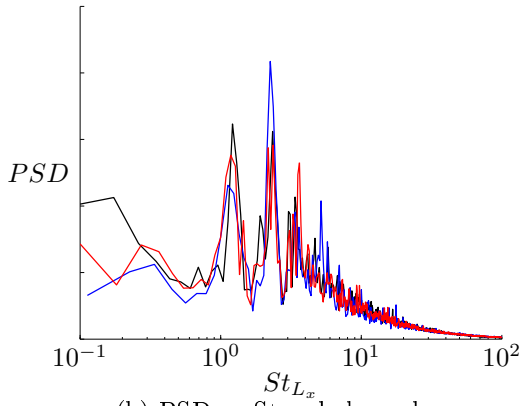

(b) PSD vs Strouhal number.

Figure 4.20: PSD vs frequency and an equivalent Strouhal number based on domain length. Legend: ——: $S = 12R$. ——: $S = 16R$. ——: $S = 20R$.

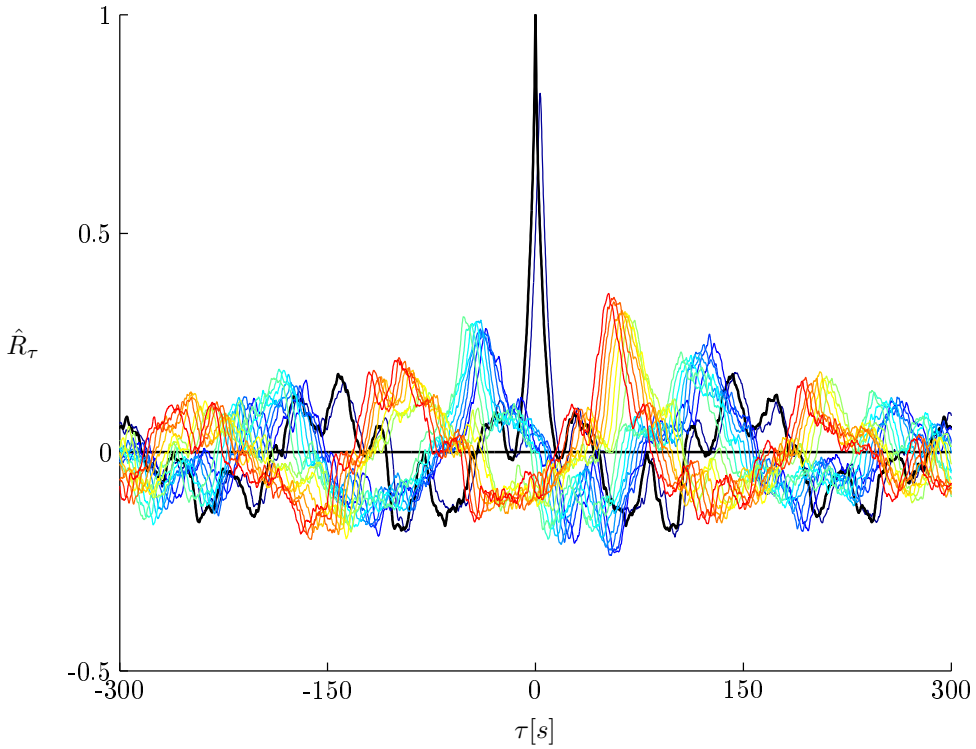

Figure 4.21: Cross-correlation for $S = 16R$ vs. time lag. Cross-correlation between different points are shown. The black line denotes the auto-correlation for the reference point $1R$ upstream of the first turbine.

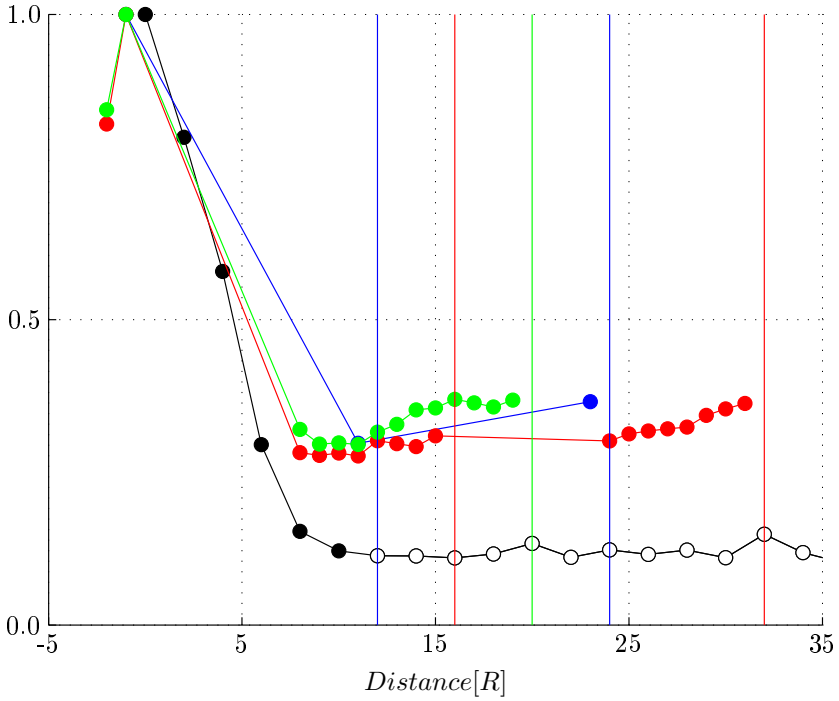

Figure 4.22: Maximum cross-correlation vs. distance between points for $S = 12R$, $S = 16R$, $S = 20R$. Cross-correlation in the wake behind a single turbine is included for reference. Legend: —— : Wake behind a single turbine. Open circles indicate that the cross-correlation has crossed 0. —— : $S = 12R$. —— : $S = 16R$. —— : $S = 20R$.

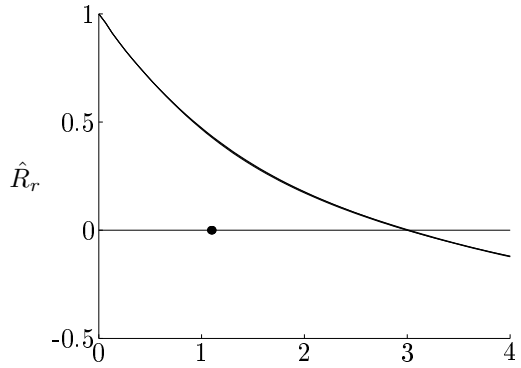

(a) $S = 12R$.

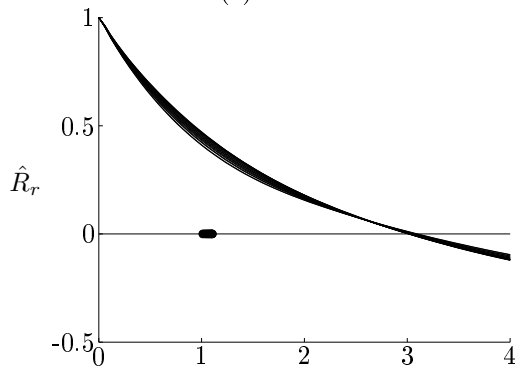

(b) $S = 16R$.

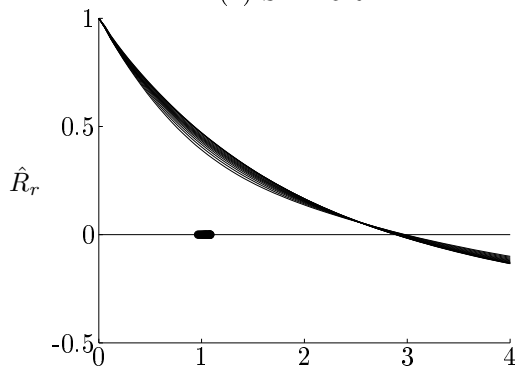

(c) $S = 20R$.

Figure 4.23: Spatial cross-correlation vs radius for various locations for the three scenarios of infinitely long rows of turbines.

4.8 Proper Orthogonal Decomposition

POD is applied to all three simulations for slices extracted in the last $1,500s$ within $\pm 1R$.

POD convergence

The convergence of the POD coefficients have been investigated by using various number of slices within the $1,500s$, similar to the analysis presented in Section 3.5. The convergence shows similar tendencies, and a loading frequency of $f = 5$ is sufficient for all simulations, meaning that POD is applied to a total of $2,796$ slices for these three cases.

Another measure of the POD convergence is to examine how well the temporal eigenfunctions are resolved by including different numbers of slices. Figure 4.24 shows $400s$ of the first temporal eigenfunction for $f = 1$, $f = 5$, and $f = 50$. Clearly, $f = 50$ is coarse, while there is virtually no difference between $f = 1$ and $f = 5$. Furthermore, the signal is not simply noise, but there are distinct frequencies present in the temporal signal. The spectrums of the first temporal eigenfunction for the three different number of slices are given in Figure 4.25, and all capture the low frequent fluctuations. The distinct frequencies are a key component of the later construction of a reduced order model in Chapter 6.

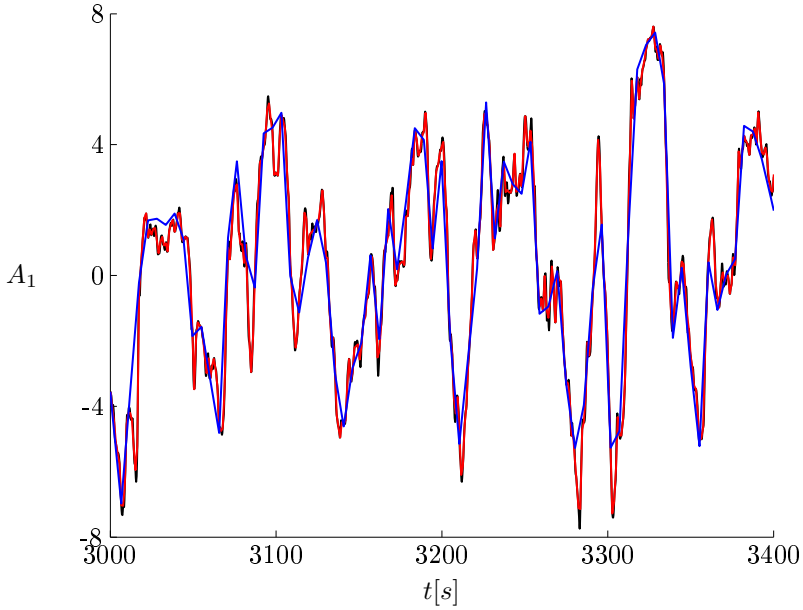

Figure 4.24: Convergence of the first POD temporal eigenfunctions for various number of slices with spacing $16R$. Legend: —— : $N_{f=50} = 280$, $\Delta t \approx 5s$. —— : $N_{f=5} = 2,796$, $\Delta t \approx 0.5s$. —— : $N_{f=1} = 13,978$, $\Delta t \approx 0.1s$.

The cumulative POD coefficients for the three simulations are shown in Figure 4.26. The POD coefficients are very similar for all spacings, and the coefficients tend towards an isotrophic distribution for POD modes larger than 30 as the slope becomes more constant, i.e. the remaining turbulent kinetic energy is spread over a large number of modes. The first POD mode contains

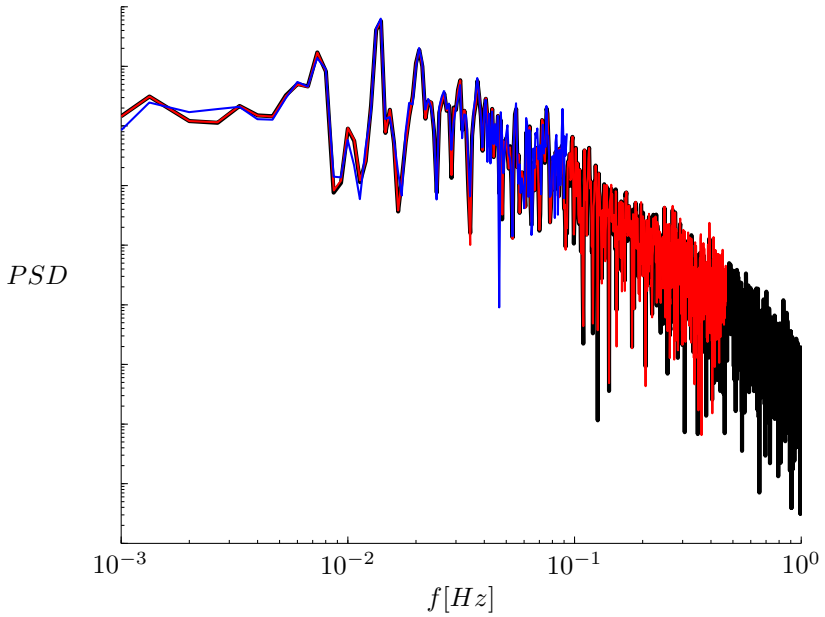

Figure 4.25: Convergence of the first POD temporal eigenfunction for various number of slices with spacing $16R$. Legend: —— : $N_{f=50} = 280$, $\Delta t \approx 5s$. —— : $N_{f=5} = 2,796$, $\Delta t \approx 0.5s$. —— : $N_{f=1} = 13,978$, $\Delta t \approx 0.1s$.

between $18-21\%$ of the turbulent kinetic energy, while the first five POD modes capture just over 50%, and the first 100 POD modes out of a total of $2,796$ contain about $86-88\%$ of the turbulent kinetic energy. Table 4.5 summarises the cumulative coefficients, i.e. the amount of turbulent kinetic energy contained within those POD modes. It is remarkably how the cumulative energy content of the first POD modes is higher for the infinite row of turbines than for the wake behind a single turbine, as the flow appears much more complex. This suggest that large, energetic scales dominate the internal flow between wind turbines. Applying POD on the same slices within $\pm 2R$ yields approximately 80% of the energy on the first 100 POD modes. This indicates how the flow is more complex when decomposing larger areas, which yields different spatial structures, particular at higher POD modes. The spatial distribution of the POD modes are discussed in the following.

Spatial POD modes

The first 20 spatial POD modes for the three different spacings are plotted in Figure 4.27-4.30. The first POD modes showcase dipole structures and mode pairing between the first and second POD mode, which is also indicated in the POD coefficients. The inplane streamlines in the two first POD modes provide clear lateral and vertical cross-stream flow, which fluctuates back and forth according to the temporal eigenfunction shown in Figure 4.24. These two modes govern the largest scales of the wake as experienced by the oncoming turbine. POD mode 3 show a somewhat central region, which fluctuates back and forth. Important to remember again, that the negative and positive areas are simply out of phase, and change sign according to the temporal eigenfunctions. The

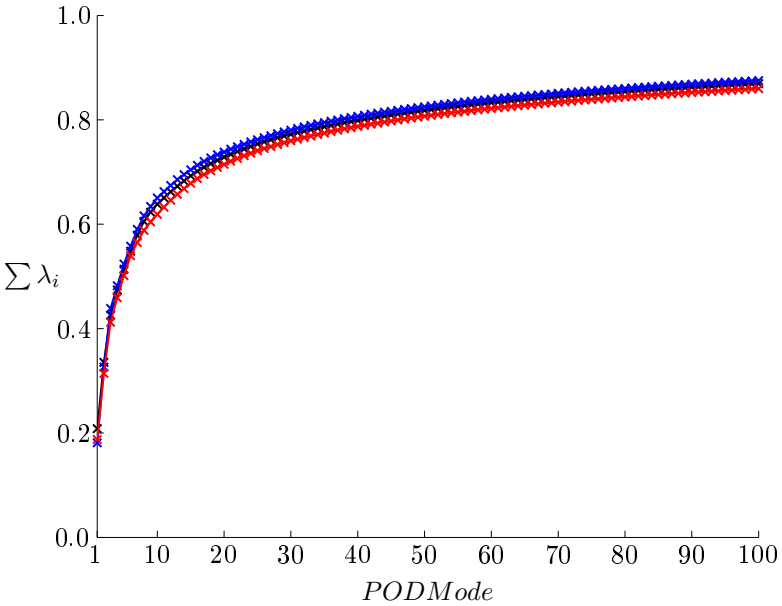

Figure 4.26: Cumulative POD coefficients. Legend: —— : $S = 12R$. —— : $S = 16R$. —— : $S = 20R$.

$\sum_{i=1}^{N} \lambda_\mathbf{i}$	**12R**	**16R**	**20R**
1	0.21	0.18	0.19
$1-2$	0.34	0.33	0.31
$1-3$	0.43	0.44	0.41
$1-4$	0.47	0.48	0.46
$1-5$	0.51	0.52	0.50
$1-6$	0.55	0.56	0.54
$1-7$	0.58	0.59	0.56
$1-8$	0.61	0.62	0.59
$1-9$	0.62	0.63	0.60
$1-10$	0.64	0.65	0.62
$1-20$	0.73	0.74	0.71
$1-50$	0.82	0.83	0.81
$1-100$	0.87	0.88	0.86

Table 4.5: Cumulative energy content of key POD modes for $12R$, $16R$, and $20R$.

inplane wake rotation is governed by POD modes 7 for $S = 12R$, 4 for $S = 16R$, and 4 and 5 for $S = 20R$. Interestingly, the modes $8 - 10$ are less exaggerated, i.e. the POD modes are more constant with only minor red/yellow and blue regions. Several higher POD modes portrait multiple inplane circulation cells, e.g. POD mode 10, 17, and 19 for $S = 16R$. Other notable modes include POD modes 11 and 14 for $S = 12R$, which show clear quadrupole and hexapole structures. The size of the large coherent structures in the first POD modes are $\mathcal{O}(1R)$ as also reported in the previous section based on the radial cross-correlation. Large coherent structures are visible in the higher POD modes although the complexity generally increase with increasing POD mode. The coherent structures are in several cases comparable for all three cases.

Saranyasoontorn and Manuel [56] constructed a low-dimensional model for the turbulent inflow to wind turbines based on applying POD to turbulence generated by a Kaimal spectral model of the atmospheric turbulence. POD modes 2 and 3 given by Saranyasoontorn and Manuel are directly comparable to the dipole structure of POD modes 1 and 2 in Figure 4.27. Other modes portrait similar resemblances, e.g. the central protusion in mode 3 resemble mode 5 by Saranyasoontorn and Manuel. Despite similarities, the POD modes by Saranyasoontorn and Manuel are more symmetric than those presented in Figures 4.27-4.30, which stems from the innate symmetry of reconstructing turbulence from a spectral model.

4.9 Summary

A minor grid study was reported in the chapter, but the focus was primarily on the examination of three idealised simulations of an infinitely long row of wind turbines with three different spacings of $12R$, $16R$, and $20R$. The simulations were considered idealised, since the effect of an atmospheric boundary layer was excluded and an initial uniform inflow was imposed before applying cyclic boundary conditions untill the flow had converged statistically. The complexity of the flow was visualised and described. The dynamic behaviour of the turbine was explored, which proved the influence of the controller. The key turbulent quantities in the incoming flow were investigated and shown to converge, when applying averaging windows of $25min$. The turbulent quantities portrait how the Reynolds stresses transfer momentum from the exterior into the rotor area and how the turbulent kinetic energy is generated in an annular shear layer around the rotor and extracted within the rotor area.

The mean asymptotic wind speed derived from the simulations have been compared to two kinematic models, and new model parameters given according to the best fit to the simulated data.

The large scales were examined and compared in a fixed and a moving frame of reference to test the basic hypotheses of the DWM model, where the wake meandering is directly related to the atmospheric turbulence which translate the wake downstream as an active tracer. The analysis highlighted the difficulties involved with simply translating the wake flow to a moving frame of reference, due to the difficulties involved with detecting an unambiguous wake centre as well as the lack of symmetry in the instanteneous wake. Furthermore, the analysis examined the spanwise and streamwise correlation, which showed that the cyclic boundary conditions can only account for a limited effect in terms of

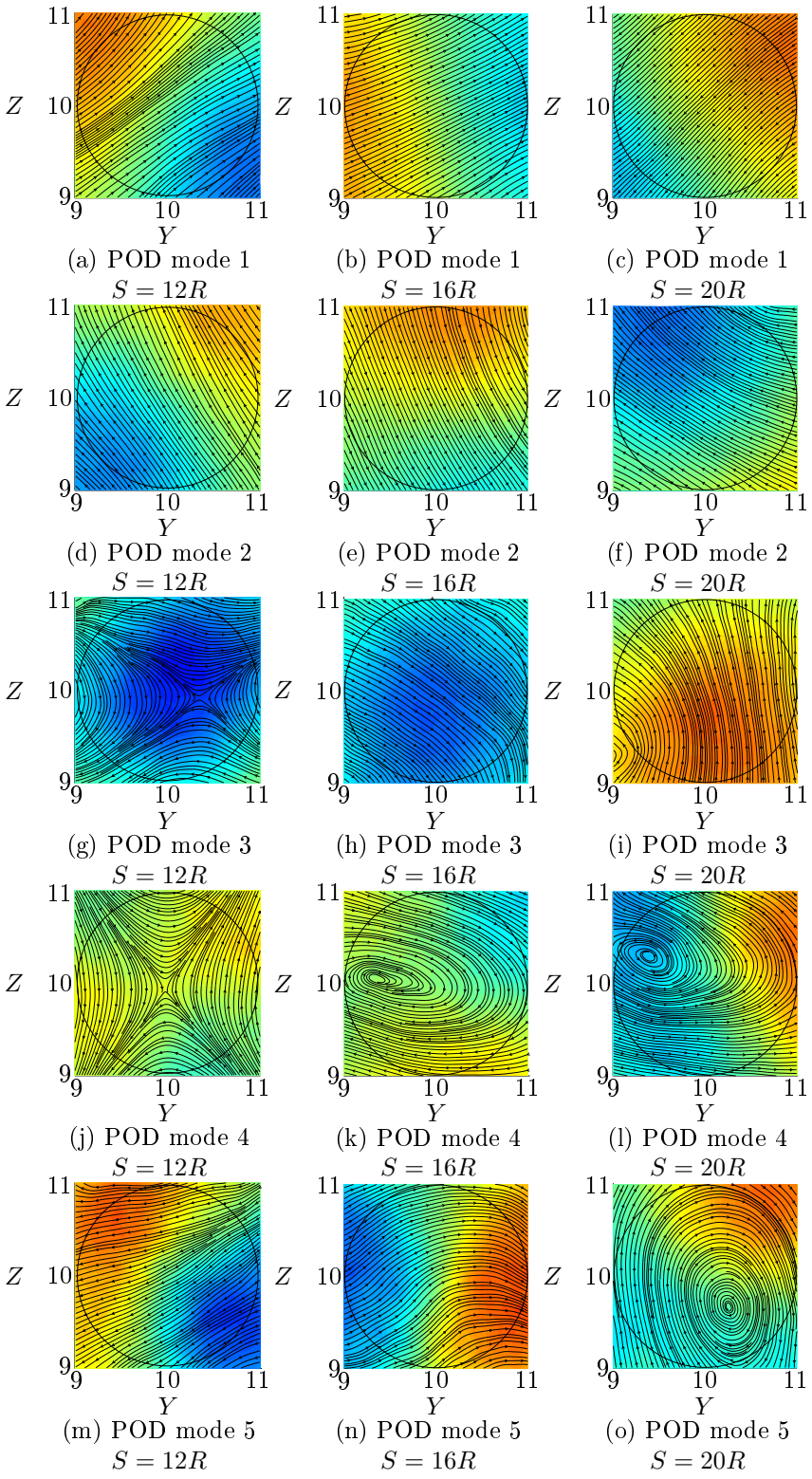

(a) POD mode 1 $S = 12R$ (b) POD mode 1 $S = 16R$ (c) POD mode 1 $S = 20R$

(d) POD mode 2 $S = 12R$ (e) POD mode 2 $S = 16R$ (f) POD mode 2 $S = 20R$

(g) POD mode 3 $S = 12R$ (h) POD mode 3 $S = 16R$ (i) POD mode 3 $S = 20R$

(j) POD mode 4 $S = 12R$ (k) POD mode 4 $S = 16R$ (l) POD mode 4 $S = 20R$

(m) POD mode 5 $S = 12R$ (n) POD mode 5 $S = 16R$ (o) POD mode 5 $S = 20R$

Figure 4.27: Spatial POD modes 1-5 for spacings $12R$, $16R$, and $20R$.

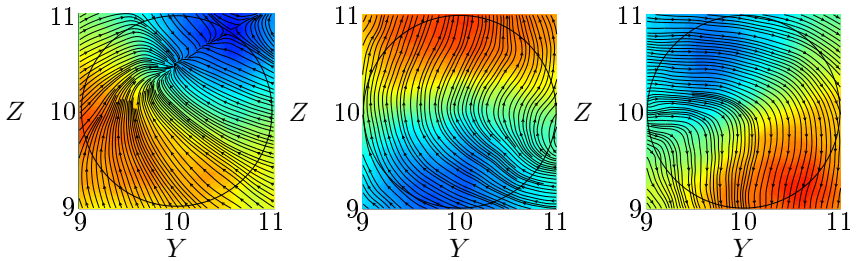

(a) POD mode 6 $S = 12R$ (b) POD mode 6 $S = 16R$ (c) POD mode 6 $S = 20R$

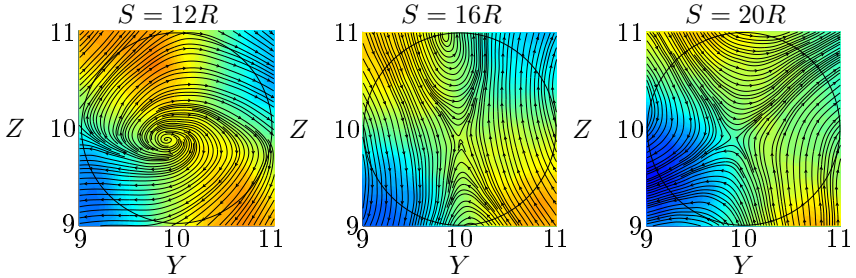

(d) POD mode 7 $S = 12R$ (e) POD mode 7 $S = 16R$ (f) POD mode 7 $S = 20R$

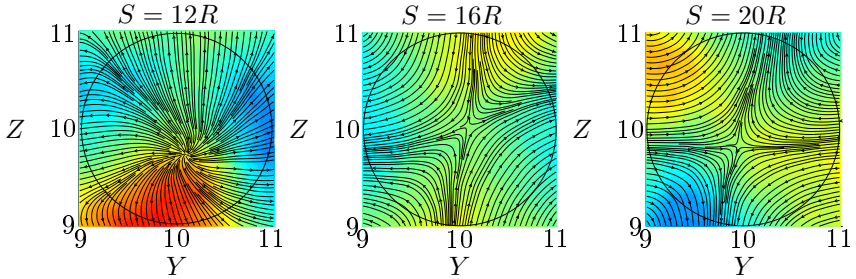

(g) POD mode 8 $S = 12R$ (h) POD mode 8 $S = 16R$ (i) POD mode 8 $S = 20R$

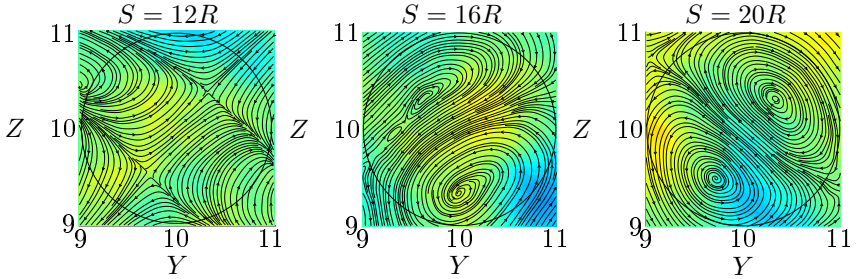

(j) POD mode 9 $S = 12R$ (k) POD mode 9 $S = 16R$ (l) POD mode 9 $S = 20R$

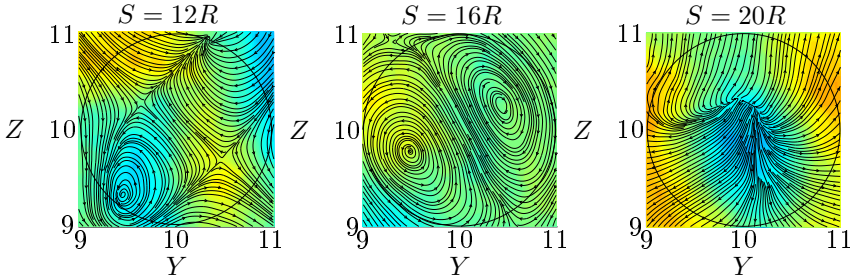

(m) POD mode 10 $S = 12R$ (n) POD mode 10 $S = 16R$ (o) POD mode 10 $S = 20R$

Figure 4.28: Spatial POD modes 6-10 for spacings $12R$, $16R$, and $20R$.

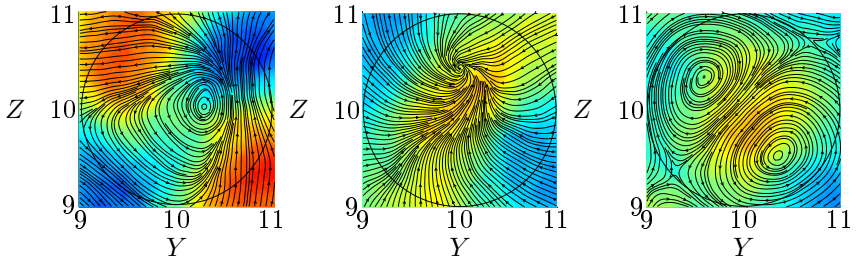

(a) POD mode 11 $S = 12R$ (b) POD mode 11 $S = 16R$ (c) POD mode 11 $S = 20R$

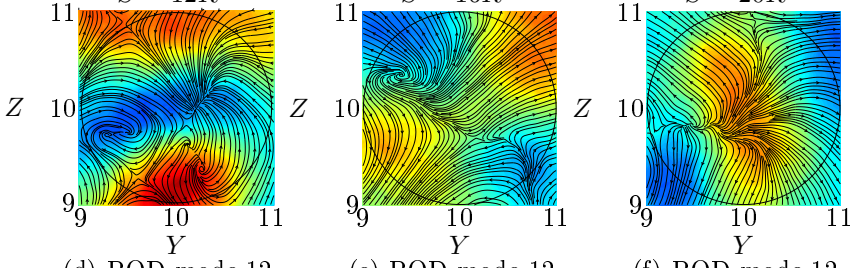

(d) POD mode 12 $S = 12R$ (e) POD mode 12 $S = 16R$ (f) POD mode 12 $S = 20R$

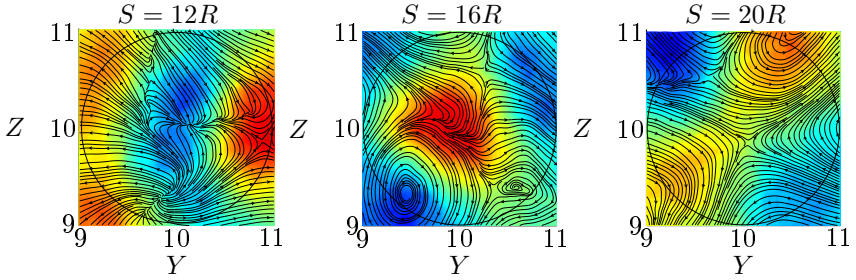

(g) POD mode 13 $S = 12R$ (h) POD mode 13 $S = 16R$ (i) POD mode 13 $S = 20R$

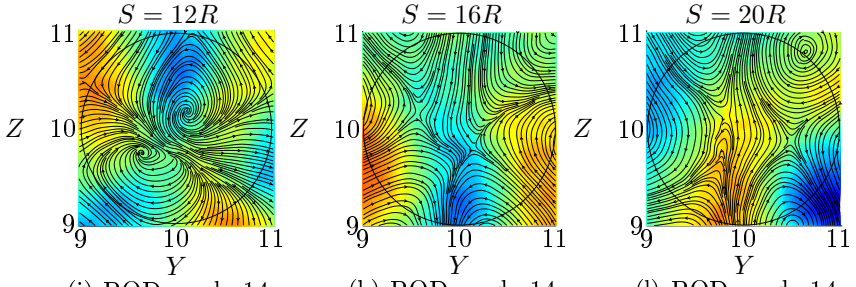

(j) POD mode 14 $S = 12R$ (k) POD mode 14 $S = 16R$ (l) POD mode 14 $S = 20R$

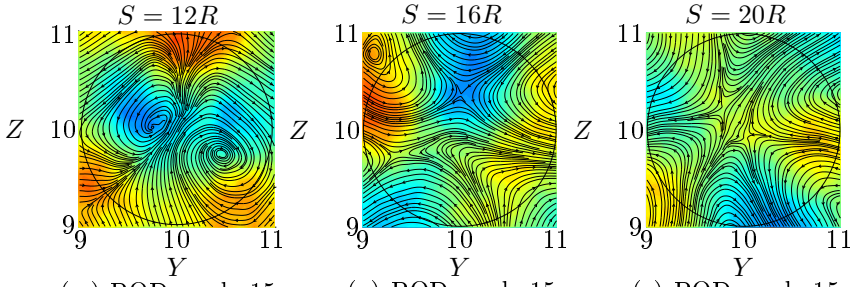

(m) POD mode 15 $S = 12R$ (n) POD mode 15 $S = 16R$ (o) POD mode 15 $S = 20R$

Figure 4.29: Spatial POD modes 11-15 for spacings $12R$, $16R$, and $20R$.

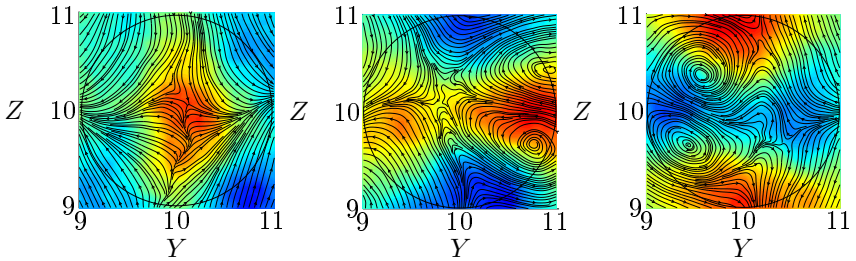

(a) POD mode 16 $S = 12R$ (b) POD mode 16 $S = 16R$ (c) POD mode 16 $S = 20R$

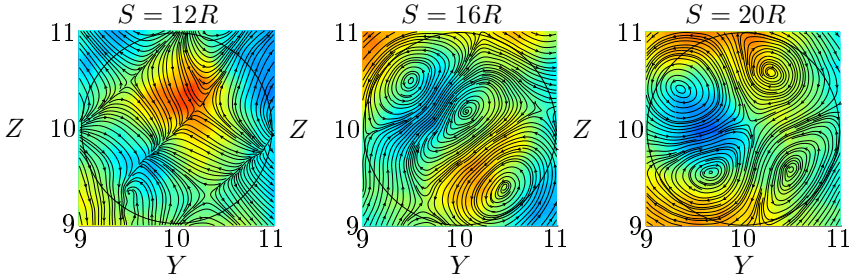

(d) POD mode 17 $S = 12R$ (e) POD mode 17 $S = 16R$ (f) POD mode 17 $S = 20R$

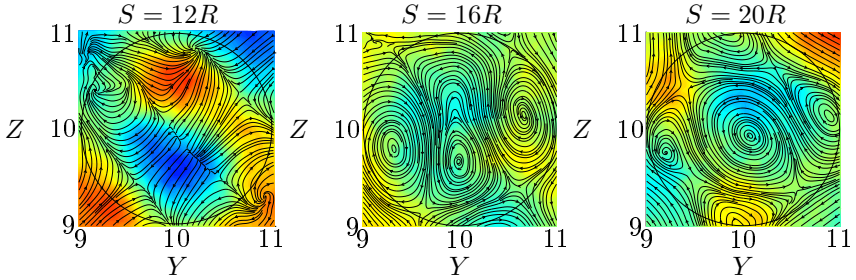

(g) POD mode 18 $S = 12R$ (h) POD mode 18 $S = 16R$ (i) POD mode 18 $S = 20R$

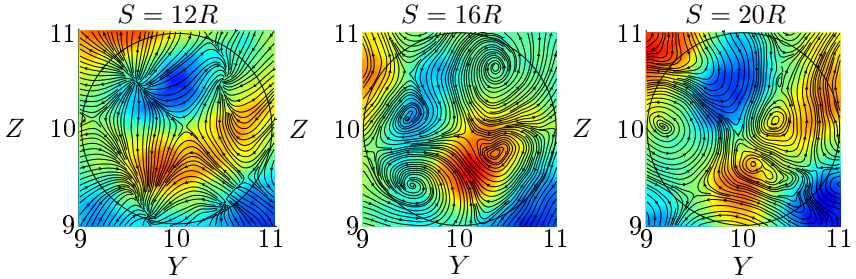

(j) POD mode 19 $S = 12R$ (k) POD mode 19 $S = 16R$ (l) POD mode 19 $S = 20R$

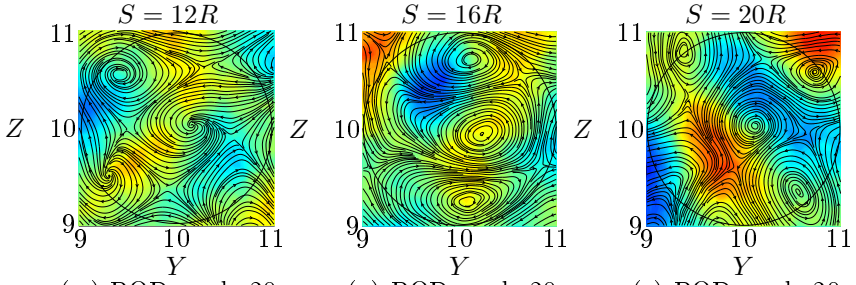

(m) POD mode 20 $S = 12R$ (n) POD mode 20 $S = 16R$ (o) POD mode 20 $S = 20R$

Figure 4.30: Spatial POD modes 16-20 for spacings $12R$, $16R$, and $20R$.

generating the large coherent structures.

Finally, POD was applied to slices extracted from the simulations, and the convergence of the temporal eigenfunctions investigated. The spatial POD modes reveal large coherent structures, which govern the large scale motions of the wake interactions deep inside an infinitely long row of turbines.

Chapter 5

Infinite Wind Farm with Atmospheric Boundary Layer

This chapter presents three different scenarios simulating infinite wind farms, where cyclic boundary conditions are applied both streamwise and laterally. The turbines are separated by $12R$, $16R$, and $20R$ in both directions for the three different scenarios. Furthermore, an atmospheric boundary layer is prescribed, which adds a vertical shear to the velocity profile. Therefore, the converged flow simulates the flow deep inside very large wind farms under neutral conditions, where the turbulence stems directly from the turbines.

Generally, no atmospheric turbulence is added, except in one additional simulation with spacing of $12R$. The two simulations with $S = 12R$ are comparable, except the latter includes the introduction of high altitude turbulence(HAT). The aim is a qualitative comparison of the effect of high altitude turbulence for the mixing and wake recovery deep inside a large wind farm.

The analysis examines the flow characteristics and turbine performance of turbines operating in a boundary layer. The flow behaviour in the interior of an infinite wind farm is investigated and related to the simulations presented in the previous chapter, where the effects of a boundary layer were excluded. POD is applied and POD modes are derived for the new wake model.

5.1 Setup

Domain

The wake interaction inside large wind farms is examined in three cases with three different streamwise and lateral spacings, namely $12R$, $16R$, and $20R$. The grids are equidistant in the streamwise and lateral direction, which is necessary to maintain and model the turbulence correctly as it is transferred using the cyclic boundary conditions. The two first grids are non-equidistant in the vertical directions, which is stretched towards the top to fulfil a blockage criteria of less than 1%. The third is equidistant in all directions. The domain height is $27R$, $20R$, and $20R$ and the domain lengths are $60R$, $48R$, and $40R$ for spacings of $12R$, $16R$, and $20R$, respectively. These lengths correspond to 5, 3 and 2 turbines in each domain. The domain lengths are chosen to include

Spacing	Dimensions	Turbines	Cells	j_{rot}	T_T	Total Time
	$X \times Y \times Z[R]$		10^6		$[s]$	$[s]$
$12R$	$60 \times 12 \times 27$	5	17.9	21	160	$4,024$
$12R + HAT$	$60 \times 12 \times 27$	5	17.9	22	160	$1,989$
$16R$	$48 \times 16 \times 20$	3	24.6	21	128	$2,682$
$20R$	$40 \times 20 \times 20$	2	24.6	20	107	$2,681$

Table 5.1: Overview of domain setup for infinite wind farm cases.

several turbines to limit the introduction of additional frequencies due to the finite size of the domain, i.e. ensuring that the dominant length scales are in the flow direction, see discussion in Section 4.7. Introducing several turbines means that turbulent length scales up to $60R = 2,400m$, $48R = 1,920m$, and $40R = 1,600m$ may appear in the computations. The rotors are placed in $(Y, Z) = (6R, 2R)$, $(Y, Z) = (8R, 2R)$, and $(Y, Z) = (10R, 2R)$, i.e. hub height is set to $2R$. The additional case with high altitude turbulence is comparable to the $S = 12R$ domain, but not identical since the simulations were run at different clusters with different optimum settings for the grid configuration. Table 5.1 summarises the domain setup including the total number of point, the rotor resolution, turnaround time, and total simulation time.

Boundary Conditions

Cyclic boundary conditions are imposed in the flow direction as well as on the lateral boundaries. Symmetry conditions are applied to both the top and bottom boundary condition, i.e. no cross flow and slip conditions.

Inflow Conditions and Turbine Performance

The current simulations include a prescribed boundary layer with $\Delta_{PBL} = 0.4$, $H_{hub} = 2R$, and $\alpha_{PBL} = 0.1$. The vertical velocity profile was shown in Figure 2.4 and Figure 5.1 shows a contour plot of the initial vertical velocity profile as experienced by the oncoming turbine. Johansen [29] reported power law coefficients in the range $\alpha_{PBL} \in [0.1 - 0.2]$. The prescribed boundary layer is scaled to have a velocity of unity at hub height, U_{hub}. The boundary layer is also considered neutral as no thermal effects are included in the simulations.

An additional case includes introduction of Mann turbulence at high altitude of approximately 10% turbulence intensity relative to the velocity at hub height, i.e. less at higher altitude. The Mann turbulence is introduced continuously during the simulation using body forces as described in Section 2.1.3. This approach have been used in several studies to introduce atmospheric turbulence upstream one or more turbines, see for instance Troldborg et al. [69]. However, this simulation aims to mimic the case of a fully developed boundary layer over a wind farm and to investigate whether large scale turbulent structures from the atmosphere can penetrate the boundary layer formed over the wind farm. Therefore, the turbulence is introduced above the boundary layer. The turbulence is introduced at $X = 6R$, which is directly above the first turbine and across the domain width from $Z = 15R$ upwards. This level is chosen in accordance with the height of the boundary layer, which eventually develops

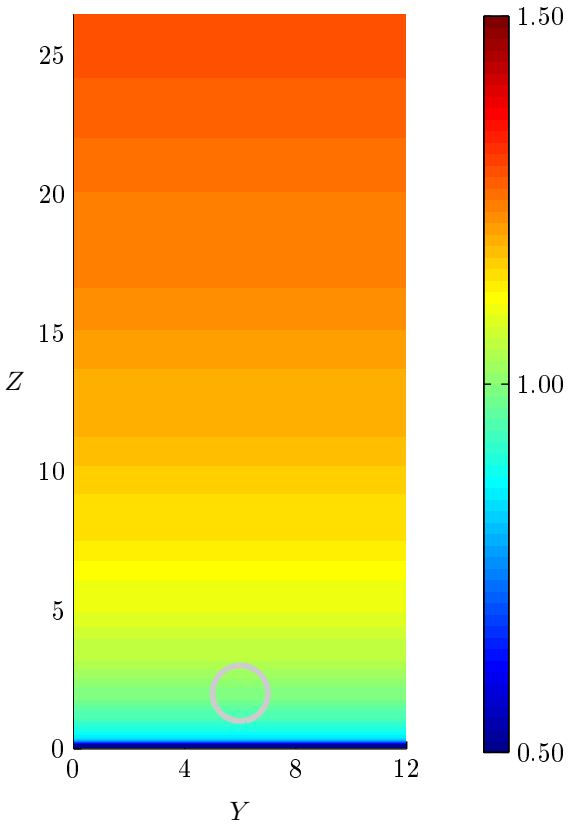

Figure 5.1: Prescribed boundary layer.

above the wind farm. The turbulence is imposed according to the vertical distribution given in Section 2.1.3.

The investigation of adding turbulence at high altitudes is more a qualitative investigation of the overall mixing process and the ability for high altitude turbulence to penetrate into the wind farm. The cyclic boundary conditions eventually means that this additional turbulence is added on top of turbulence generated by the wind farm, which should enhance mixing with the freestream flow above the boundary layer formed above the wind farm.

5.2 Wake and Flow Characteristics

Figure 5.2 shows instanteneous vorticity plots for a vertical and horizontal plane through the turbine centre. The top plot shows how vorticity is exchanged between the rows of turbines across the cyclic boundaries, but larger scales are still predominantly present in the immediate wake between the rotors. Similarly, the bottom plot shows large scales are mainly present in the lowest $3R$, with a few large scales extruding higher into the boundary layer. The vorticity is clearly limited to the lower part of the boundary layer.

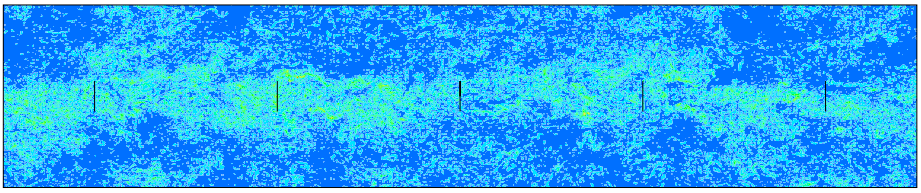

(a) XY-plane at $Z = 2R$.

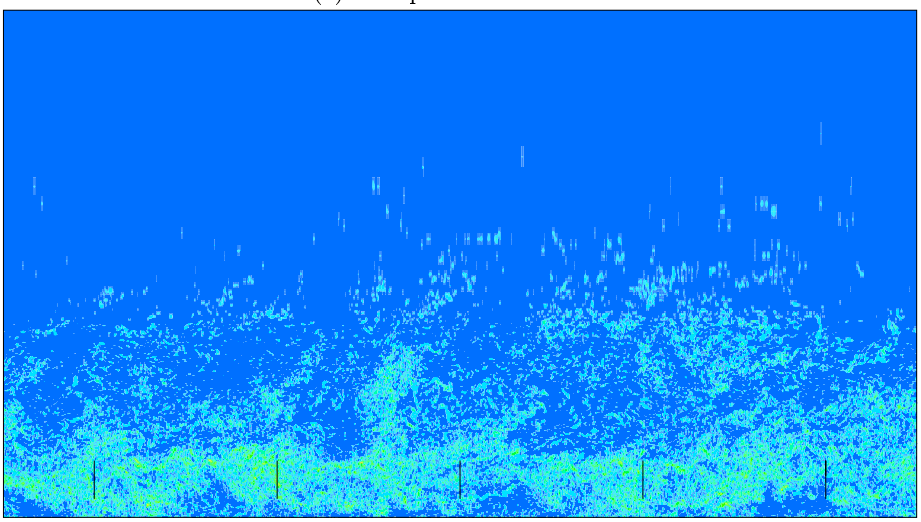

(b) XZ-plane at $Y = 6R$.

Figure 5.2: Instanteneous vorticity plot through the rotor centre for $S = 12R$. Total of five rotors are marked by solid lines. Bright areas indicate high vorticity.

Spacing	$\overline{\frac{U_{hub}}{U_0}}$	$\sigma(\frac{U_{hub}}{U_0})$	$\sigma((\frac{U_{hub}}{U_0})^3)$	$\overline{\Omega R}$	$\overline{\frac{P}{P_0}}$	$\sigma(\frac{P}{P_0})$	$\overline{T}[kN]$
$12R$	0.61	0.10	0.12	72.3	0.59	0.14	229
$16R$	0.73	0.10	0.17	72.3	0.80	0.12	263
$20R$	0.80	0.10	0.19	72.4	0.88	0.11	267

Table 5.2: Mean and standard deviation of the velocity at hub height, standard deviation of the velocity at hub height cubed, mean tip speed, mean normalised power, standard deviation of normalised power and mean thrust of the last $1,500s$ for the three infinite wind farm simulations with spacings $12R$, $16R$, and $20R$.

5.3 Turbine Performance History

The operational history of the turbines in terms of inflow velocity and power production for the three simulations is shown in Figure 5.3. The inflow velocities at hub height are comparable to Figure 4.6 although the PBL appears to stabilise the flow faster to avoid the large initial decrease. Clearly, larger spacing leads to larger velocities, hence power production, but less than for the idealised case. The above rated power peak for $S = 20R$ around $t \approx 1,000s$ is due to a simulation restart, where the turbine overshoots the rater power before it adjusts correctly to the flow. The basic turbine statistics are summarised in Table 5.2. The simulations of $S = 16R$ are almost identical with and without PBL(see Table 4.2) except the thrust is lower in the former case. The increase in velocity at hub height with increasing spacing is still clear, but much more pronounced with PBL. It suggests the vertical shear enhance the wake recovery for large turbine spacings($S > 16R$), while small turbine spacings confine the flow and hence the wake recovery. The mean inflow velocity is only 0.61 at hub height for $12R$, which is the reference velocity for the controller. Power production is up to 88% of rated for $S = 20R$. However, the power yield is lower than the idealised cases shown in Chapter 4, particular for $S = 12R$, where the presence of the PBL decreases the power yield from 87% to only 59%.

There is no apparent variation in inflow fluctuations(all 0.10), and the cubed standard deviation is increasing with increasing spacing, opposite to the results reported in Table 4.2. The standard deviation in power production is still increasing for decreasing spacing, but suprisingly the variation exceeds the variation of velocity fluctuations cubed for $S = 12R$. This suggests that the controller is struggling in this scenario. The turbulence intensity relative to mean velocity at hub height(as opposed to freestream) is 16.4%, 13.7%, and 12.5% for spacings $12R$, $16R$, and $20R$, respectively. This is a minor increase compared to 14.9%, 12.5%, and 10.6% without PBL.

Qualitative Comparison with High Altitude Turbulence

The turbine performance with $S = 12R$ is compared with the special case of adding additional atmospheric turbulence at high altitudes between $t \in [989s, 1,989s]$. The velocity at hub height and normalised power for the two cases are plotted in Figure 5.4, and initially the two simulations are identical before the addition of the turbulence alters the simulations. The figures also reveal how the addition of HAT at times gives rise to higher fluctuations, which

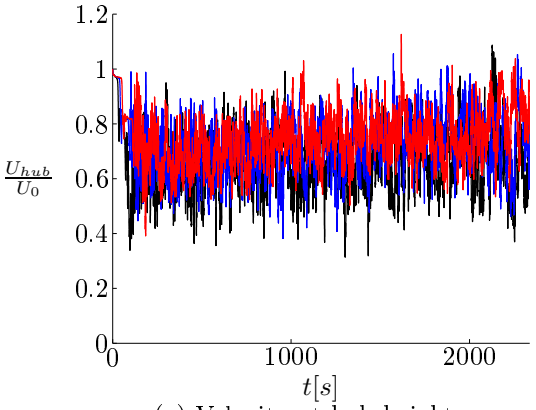

(a) Velocity at hub height.

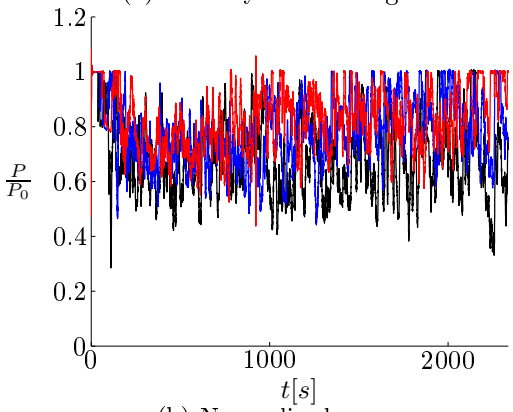

(b) Normalised power.

Figure 5.3: Normalised power and thrust in an infinite wind farm including PBL with spacings of $12R$, $16R$, $20R$. Legend: —— : $S = 12R$. —— : $S = 16R$. —— : $S = 20R$.

gives rise to a minor increase in the statistics of this period as presented in Table 5.3. The addition of HAT yields a power production of 0.71 as opposed to 0.66 for the examined period, which is also accompanied by an increase in fluctuations.

The comparison indicates that the additional turbulence does enhance the mixing process with overlaying boundary layer slightly. The effect is still minor relative to the added 10% turbulence intensity, which indicates the difficulties for atmospheric turbulence to penetrate the boundary layer formed over the wind turbines. Therefore, the additional mixing is assumed to be caused predominantly by the largest structures in the HAT, which can deliver large burst of energy into the interior of the wind farm. The internal turbulence is still dominanted by the turbulence added by the wind turbines, as also noted by Frandsen and Madsen [21].

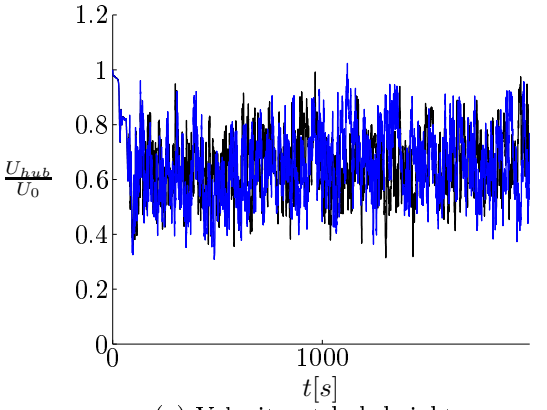

(a) Velocity at hub height.

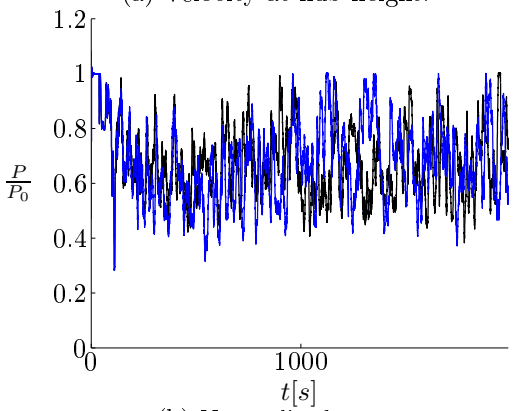

(b) Normalised power.

Figure 5.4: Normalised power and thrust in an infinite wind farm with spacings of $12R$ with and without high altitude turbulence(HAT).
Legend: —— : $S = 12R$. —— : $S = 12R$ with HAT.

Spacing	$\overline{\frac{U_{hub}}{U_0}}$	$\sigma(\frac{U_{hub}}{U_0})$	$\sigma((\frac{U_{hub}}{U_0})^3)$	$\overline{\Omega R}$	$\overline{\frac{P}{P_0}}$	$\sigma(\frac{P}{P_0})$	$\overline{T}[kN]$
$12R$	0.65	0.11	0.14	72.3	0.66	0.12	242
$12R + HAT$	0.67	0.12	0.17	72.3	0.71	0.14	249

Table 5.3: Mean and standard deviation of the velocity at hub height, standard deviation of the velocity at hub height cubed, mean tip speed, mean normalised power, standard deviation of normalised power and mean thrust of the $t \in [989s, 1,989s]$ for the infinite wind farm simulations with spacings $12R$ with and without HAT. Note, the difference in period changes the values compared to Table 5.2

.

5.4 Mean and Turbulent Quantities

The statistical convergence of the turbulent quantities are left out for brevity, but Section 4.5 describes the details of a similar analysis. The converged turbulent quantities are summarised in Table 5.4, similar to Table 4.3. The mean velocities show a similar trend to the velocity at hub height, although the application of PBL gives an increase in mean velocity for $S > 16R$ due to the shear in the vertical, which yields higher velocities above hub height. The mean lateral velocities are increased for all cases, while the vertical components are decreased except for $12R$. This indicates how the streamwise and lateral components are enhanced due to the vertical confinement near the ground. A similar trend is observed in the velocity fluctuations with equal or minor increases in the streamwise and lateral fluctuations, while the vertical fluctuations are equal or less compared to the idealised case without PBL. The Reynolds stresses and TKE production naturally follow the same trends.

Figure 5.5 depicts the mean streamwise velocity overlaid by the inplane average streamlines for all three simulations. The results have been duplicated two or three times in the lateral direction to improve the visualization of the inplane circulation and the vertical symmetry lines along the cyclic boundaries are marked. There are distinct wake deficits in the streamwise velocity around the wind turbines, and the wake deficit(blue colors) are both higher and extends over a larger area for $S = 12R$ while it is less pronounced for increased spacings, see the undisturbed PBL in Figure 5.1 with the same colorscaling for direct comparison. The wake deficits also extend in the vertical to approximately $10R$, $8R$, and $6R$ for the three cases, predominantly to the right of the turbine due to the wake rotation. This effect appears as lateral waves in the mean streamwise velocity. The level of the lateral waves indicate the boundary layer, which develops above the infinite wind farm. The waves also coincide with the inplane streamlines. There are two significant circulation cells for $12R$, a smaller to the left of the turbine and a larger cell to the right, which facilitates downwash of momentum from more than $20R$ vertically. This illustrates how the wake interaction is limited by the ground and merging wakes and can only expand upwards as described by Frandsen et al. [20]. The inflow to the rotor is from below, and the circulation in the immediate vicinity of the turbine for the three cases are given in Figure 5.6. The inplane streamlines for $16R$ and $20R$ are diverging around the turbine, similar to the divergent streamlines portraited in Figure 4.10, which excluded the effect of PBL. The inplane circulation cells

Quantity	**12R**	**16R**	**20R**
$\Delta T_{win}[s]$	$[1,260-3,540]$	$[1,500-2,100]$	$[1,140-1,500]$
$RMS(\overline{U})$	0.79	0.85	0.87
$RMS(\overline{V})$	$9.8 \cdot 10^{-3}$	$11 \cdot 10^{-3}$	$11 \cdot 10^{-3}$
$RMS(\overline{W})$	$12 \cdot 10^{-3}$	$6.7 \cdot 10^{-3}$	$9.2 \cdot 10^{-3}$
$RMS(\sqrt{\overline{u'^2}})$	0.12	0.10	$9.6 \cdot 10^{-2}$
$RMS(\sqrt{\overline{v'^2}})$	$9.2 \cdot 10^{-2}$	$8.7 \cdot 10^{-2}$	$8.1 \cdot 10^{-2}$
$RMS(\sqrt{\overline{w'^2}})$	$8.5 \cdot 10^{-2}$	$7.8 \cdot 10^{-2}$	$6.9 \cdot 10^{-2}$
$RMS(\tau_{xx})$	$14 \cdot 10^{-3}$	$10 \cdot 10^{-3}$	$9.3 \cdot 10^{-3}$
$RMS(\tau_{yy})$	$8.7 \cdot 10^{-3}$	$7.7 \cdot 10^{-3}$	$6.7 \cdot 10^{-3}$
$RMS(\tau_{zz})$	$7.4 \cdot 10^{-3}$	$6.1 \cdot 10^{-3}$	$4.8 \cdot 10^{-3}$
$RMS(\tau_{xy})$	$2.5 \cdot 10^{-3}$	$1.9 \cdot 10^{-3}$	$2.3 \cdot 10^{-3}$
$RMS(\tau_{xz})$	$3.2 \cdot 10^{-3}$	$2.7 \cdot 10^{-3}$	$1.8 \cdot 10^{-3}$
$RMS(\tau_{yz})$	$3.9 \cdot 10^{-4}$	$3.5 \cdot 10^{-4}$	$3.4 \cdot 10^{-4}$
$RMS(\tau_{xy}\frac{d\overline{U}}{dY})$	$1.5 \cdot 10^{-4}$	$7.6 \cdot 10^{-5}$	$8.9 \cdot 10^{-5}$
$RMS(\tau_{xz}\frac{d\overline{U}}{dZ})$	$2.6 \cdot 10^{-4}$	$2.2 \cdot 10^{-4}$	$1.1 \cdot 10^{-4}$
$RMS(\tau_{yy}\frac{d\overline{V}}{dY})$	$8.8 \cdot 10^{-5}$	$9.3 \cdot 10^{-5}$	$7.6 \cdot 10^{-5}$
$RMS(\tau_{yz}\frac{d\overline{V}}{dZ})$	$6.0 \cdot 10^{-6}$	$4.1 \cdot 10^{-6}$	$3.9 \cdot 10^{-6}$
$RMS(\tau_{zy}\frac{d\overline{W}}{dY})$	$5.5 \cdot 10^{-6}$	$3.5 \cdot 10^{-6}$	$3.6 \cdot 10^{-6}$
$RMS(\tau_{zz}\frac{d\overline{W}}{dZ})$	$9.0 \cdot 10^{-5}$	$7.1 \cdot 10^{-5}$	$6.2 \cdot 10^{-5}$
$RMS(\mathcal{P})$	$3.5 \cdot 10^{-4}$	$2.5 \cdot 10^{-4}$	$1.6 \cdot 10^{-4}$

Table 5.4: Mean RMS values of the converged turbulent quantities within $\pm 2R$ and the limits of the temporal window ΔT_{win} for $12R$, $16R$, and $20R$ with PBL. Notice, quantities are dimensionless.

are less pronounced for the larger spacings, and do not govern the momentum transfer into the incoming wake to the same degree. The circulation cells show how the large spacing is large enough to facilitate the transfer of new momentum into the wake from the surroundings as the wake recovers between the turbines. Contrary, the inflow appears confined by the small spacing and the inflow mainly occur from below, which significantly lowers the wake recovery, hence the average velocity seen by the turbine.

Figure 5.7 shows the lateral and vertical mean streamwise velocity and fluctuation profiles through the rotor center, i.e. $Z = 2R$ and $Y = 6R$, $Y = 8R$, and $Y = 10R$, respectively. The vertical velocity profiles show a clear wake deficit covering the rotor extend. The velocity is accelerated to be larger than the initial prescribed velocity above approximately $14R$ for $S = 12R$ and $S = 20R$, which is the rational behind applying HAT above $15R$. The horizontal velocity profiles reveal significant decreases in the streamwise velocity between the individual rows for $12R$ and $16R$, i.e. the turbines block and force the flow to go above the turbines, while $20R$ is unconfined and gives rise to a minor speedup between the rows, which again assist in the aforementioned mixing.

The fluctuation profiles are comparable, particular for $S = 16R$ and $S = 20R$, which are practically identical, while $S = 12R$ is slightly higher. The fluctuations decrease to approximately 5% above and between the turbines.

The remaining turbulent quantities are very similar to those presented in Chapter 4, although confined by the ground. For brevity, only the total TKE production is shown in Figure 5.8. The TKE sinks are still within the rotor area, while the sources are in the shear layer above the turbine. The TKE production beneath the turbine is virtually neutral for all three cases.

5.5 Proper Orthogonal Decomposition

POD is applied to the three simulations with PBL for the last $1,500s$ within $\pm 1R$ around the turbine. POD gives $2,796$ modes, but only the first 100 cumulative POD coefficients are summarised in Figure 5.9 and Table 5.5. The POD coefficients are very similar to those reported in Section 4.8 although the first POD modes contain slightly larger amounts of the turbulent kinetic energy. 50% of the variance is captured by the first five, four or even three POD modes for $S = 12R$, $S = 16R$, and $S = 20R$. The first 100 modes contain $87 - 89\%$ of the turbulent kinetic energy for all three cases, similar to those reported in Section 4.8.

Spatial POD modes

Figures 5.10-5.13 shows the first 20 POD modes of the streamwise velocity overlaid by the lateral and vertical streamlines for the three simulations. Several of the first POD modes shows dipole structures, very similar to those presented in Figure 4.27. Similarities in terms of patterns, which are occasionally rotated. The inplane wake rotation is captured in POD mode $4 - 5$ for all three simulations. Several of the other POD modes are comparable with and without PBL, e.g. quadrupole structures in mode 7 for $S = 16R$ and $S = 20R$. Deriving similar POD modes imply that the vertical shear is mainly captured by the mean velocity and that the turbulence inherent to the turbines are comparable,

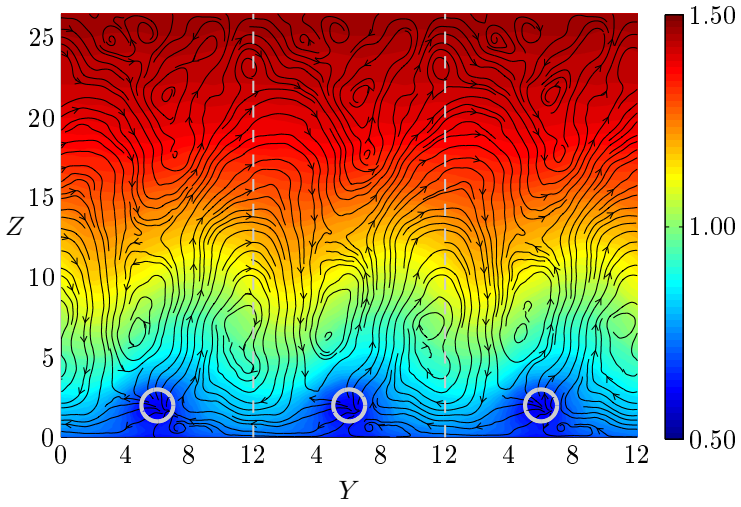

(a) $S = 12R$.

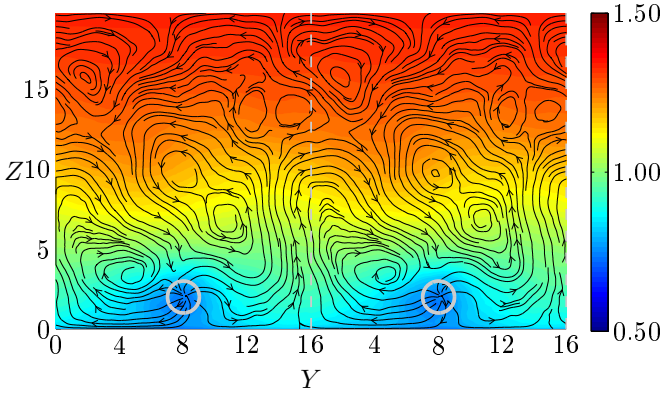

(b) $S = 16R$.

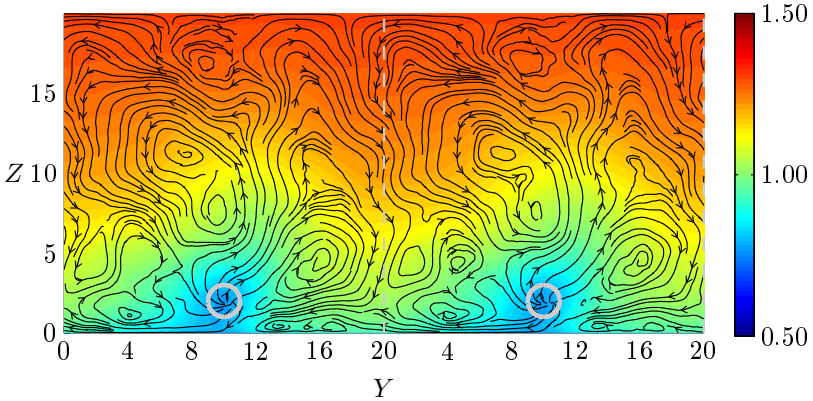

(c) $S = 20R$.

Figure 5.5: Mean streamwise velocity ($\frac{\bar{U}}{U_0}$) and streamlines for the average inplane circulation ($\frac{\bar{V}}{U_0}$ and $\frac{\bar{W}}{U_0}$). Results are duplicated two or three times in the lateral to giver better view of the inplane circulation. Broken lines denote the symmetry lines. The minor difference between the streamlines in the duplicated regions arise due to differences in the starting points of the streamlines, not difference in data.

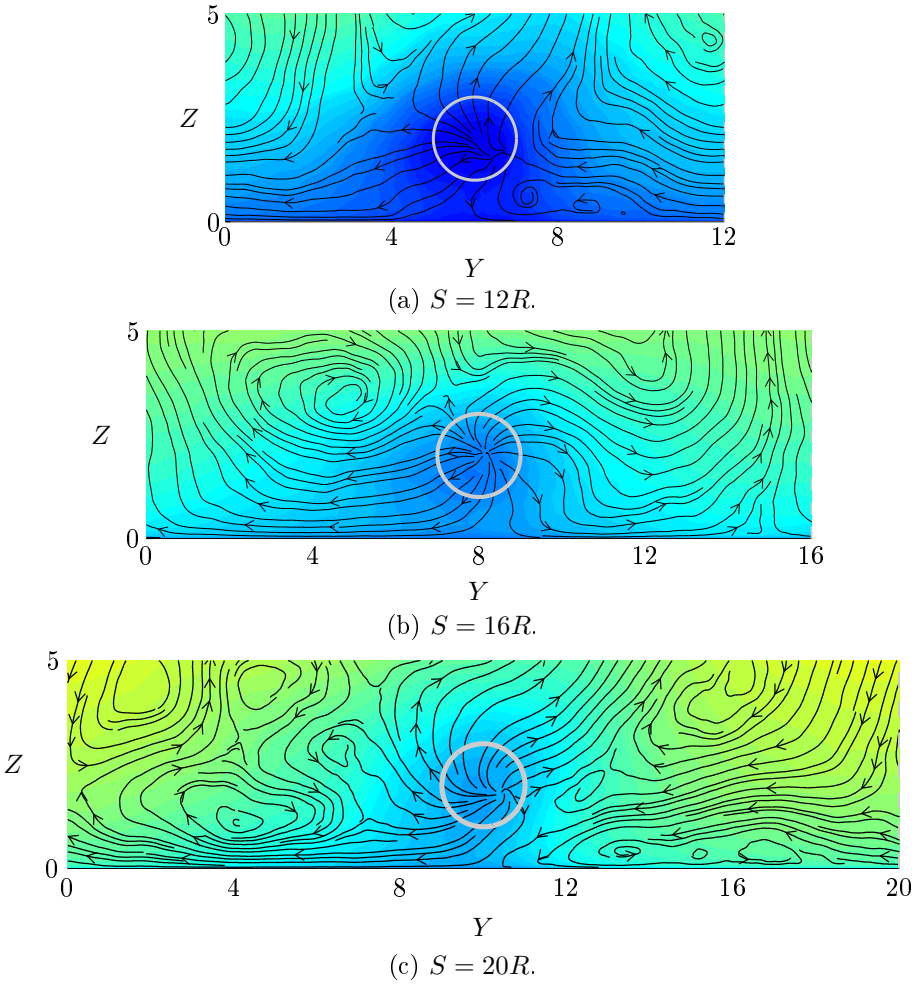

(a) $S = 12R$.

(b) $S = 16R$.

(c) $S = 20R$.

Figure 5.6: Detailed view of mean streamwise velocity ($\frac{\bar{U}}{U_0}$) and streamlines for the average inplane circulation ($\frac{\bar{V}}{U_0}$ and $\frac{\bar{W}}{U_0}$), see full view in Figure 5.5.

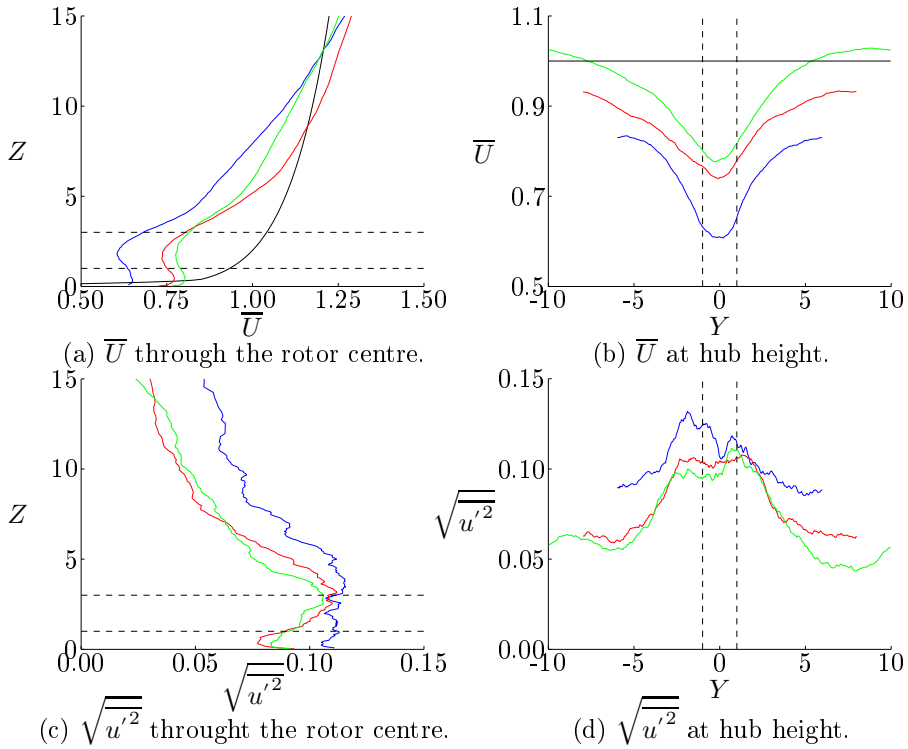

(a) $\overline{U}$ through the rotor centre.

(b) $\overline{U}$ at hub height.

(c) $\sqrt{\overline{u'^2}}$ throught the rotor centre.

(d) $\sqrt{\overline{u'^2}}$ at hub height.

Figure 5.7: Vertical and horizontal velocity and RMS profiles. Legend: —— : $S = 12R$. —— : $S = 16R$. —— : $S = 20R$. —— : Reference level from undisturbed PBL.- - - : Rotor extend.

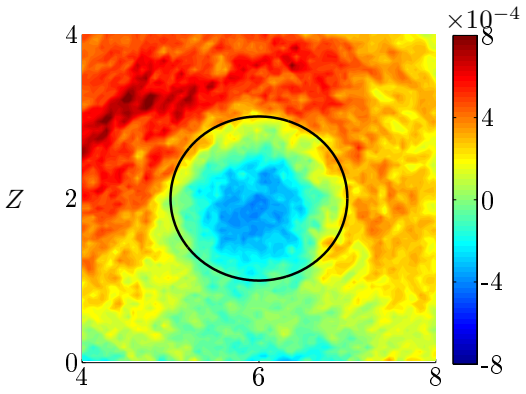

(a) $S = 12R$

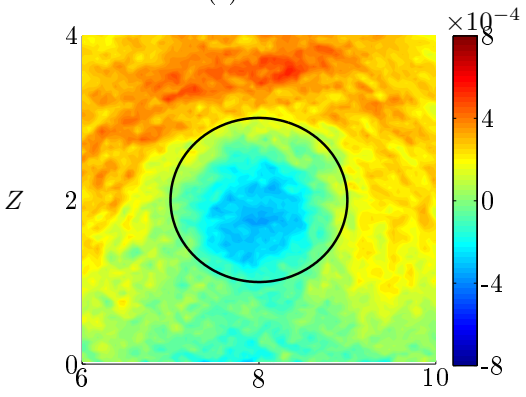

(b) $S = 16R$

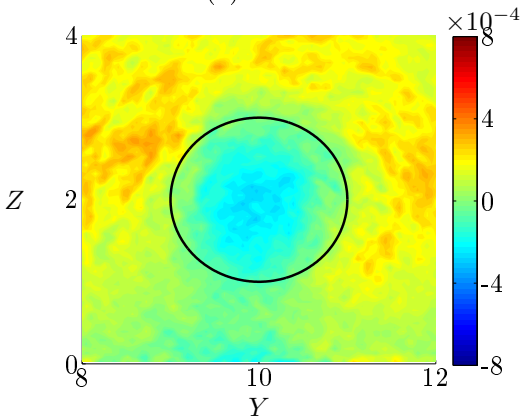

(c) $S = 20R$

Figure 5.8: TKE production in the lower PBL. Notice, TKE production levels are dimensionless.

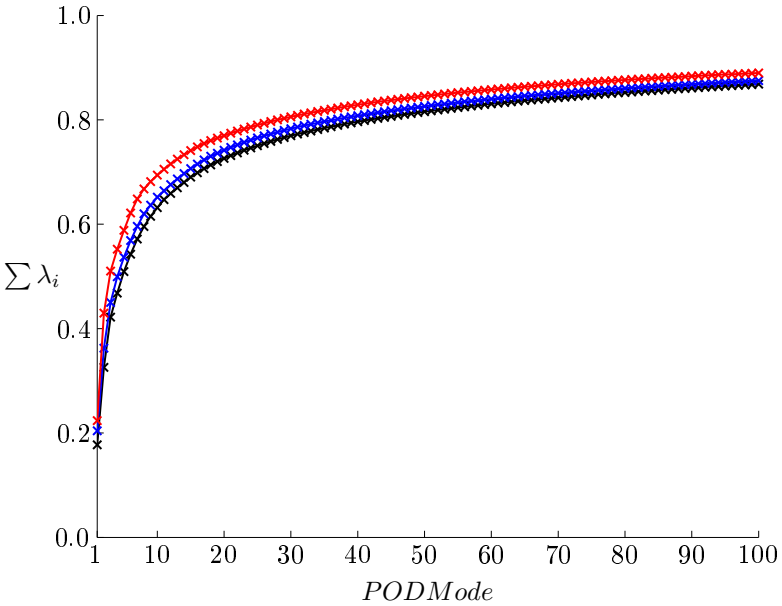

Figure 5.9: Cumulative POD coefficients with PBL. Legend: —— : $S = 12R$. —— : $S = 16R$. —— : $S = 20R$.

$\sum_{i=1}^{N} \lambda_\mathbf{i}$	**12R**	**16R**	**20R**
1	0.18	0.20	0.22
$1-2$	0.33	0.36	0.43
$1-3$	0.42	0.45	0.51
$1-4$	0.47	0.50	0.55
$1-5$	0.51	0.54	0.59
$1-6$	0.54	0.57	0.62
$1-7$	0.57	0.60	0.65
$1-8$	0.60	0.62	0.67
$1-9$	0.62	0.64	0.68
$1-10$	0.63	0.65	0.69
$1-20$	0.73	0.74	0.77
$1-50$	0.82	0.83	0.85
$1-100$	0.87	0.88	0.89

Table 5.5: Cumulative energy content of key POD modes for $12R$, $16R$, and $20R$ with PBL.

which in turn indicate that the ground only has minor influence on the dominant structures.

The similarities of the POD modes to the work of Saranyasoontorn and Manuel [56] were discussed in Section 4.8. Here, the dipole structures are present in the first POD modes, while the quadrupole structure of POD mode 3 by Saranyasoontorn and Manuel is present in mode 6 for $S = 12R$ and mode 7 for $S = 16R$ and $S = 20R$.

Saranyassontorn and Manuel [57] also examined an alternative sorting(as opposed to sorting purely by variance) to better account for yaw loads based on symmetry considerations. However, the present work deals with a three-bladed rotor as opposed to a two-bladed rotor in the case by Saranyassontorn and Manuel, and therefore symmetry is naturally broken and such considerations are of less importance. Furthermore, their input flow field was based on stochastic turbulence derived from a Kaimal spectrum, which naturally leads to symmetries in the flow.

Similar to the work of Saranyasoontorn and Manuel, the presented POD modes form the basis for constructing a new dynamic wake model in Chapter 6.

5.6 Summary

Three simulations of infinite wind farms with three different spacings were examined. The infinite wind farm situation is achieved by applying cyclic boundary conditions in the streamwise and lateral directions as well as imposing a prescribed boundary layer.

An additional simulation with atmospheric turbulence imposed at high altitudes was compared to the basic simulation with turbine spacings of $12R$. The qualitative comparison showed a minor increase in inflow velocity and power production due to the additional turbulence.

The presence of a boundary layer decrease the wake recovery for small turbine spacings, because the recirculation and turbulent mixing between the turbines are confined. Conversely, the inflow velocity is increased for large turbine spacings in the presence of a boundary layer, because the velocity between the turbine rows increase and enhance the turbulent mixing. The turbulence intensity in the rotor area is comparable to the three simulations presented in the previous chapter, which excluded the effect of an atmospheric bounday layer.

The large coherent structures were derived as POD modes and examined. The POD modes revealed remarkable resemblance with the POD modes derived in Chapter 4 implying the vertical shear is mainly captured by the mean velocity and the large turbulent scales inherent to the turbines are comparable. The investigated POD modes form the basis of the wake models described in Chapter 6.

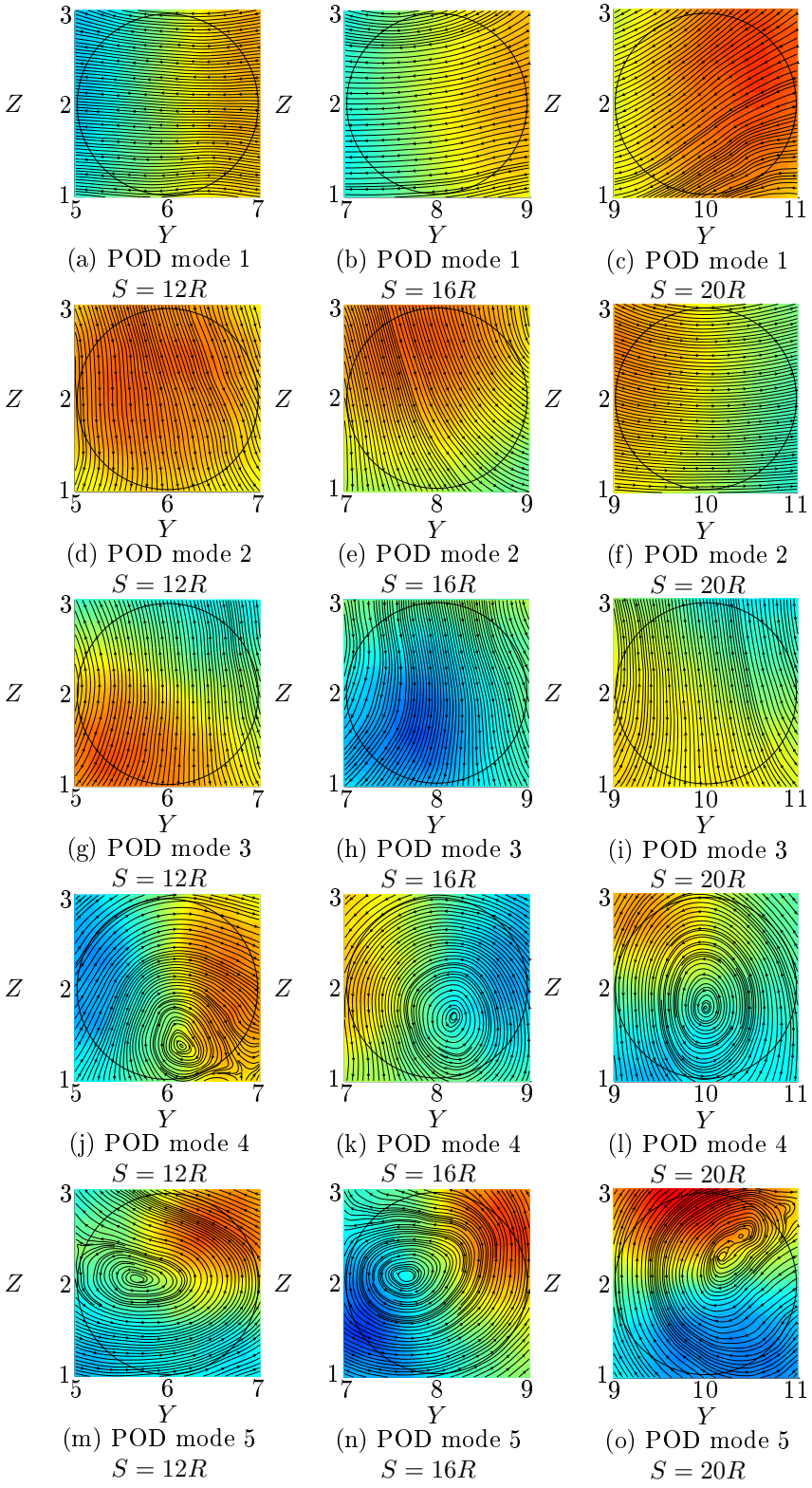

(a) POD mode 1 $S = 12R$ (b) POD mode 1 $S = 16R$ (c) POD mode 1 $S = 20R$

(d) POD mode 2 $S = 12R$ (e) POD mode 2 $S = 16R$ (f) POD mode 2 $S = 20R$

(g) POD mode 3 $S = 12R$ (h) POD mode 3 $S = 16R$ (i) POD mode 3 $S = 20R$

(j) POD mode 4 $S = 12R$ (k) POD mode 4 $S = 16R$ (l) POD mode 4 $S = 20R$

(m) POD mode 5 $S = 12R$ (n) POD mode 5 $S = 16R$ (o) POD mode 5 $S = 20R$

Figure 5.10: Spatial POD modes 1-5 for spacings $12R$, $16R$, and $20R$ with PBL.

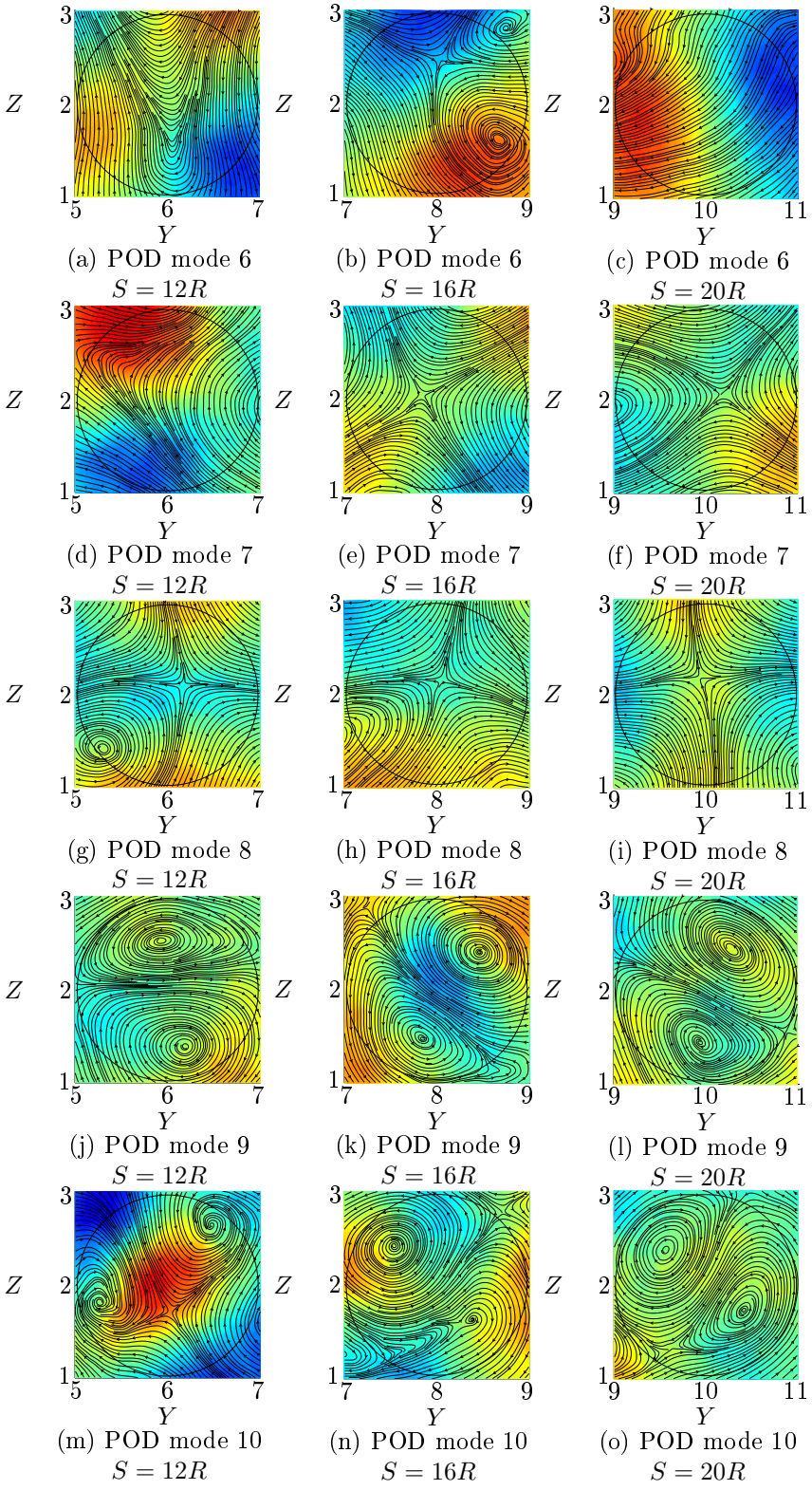

Figure 5.11: Spatial POD modes 6-10 for spacings $12R$, $16R$, and $20R$ with PBL.

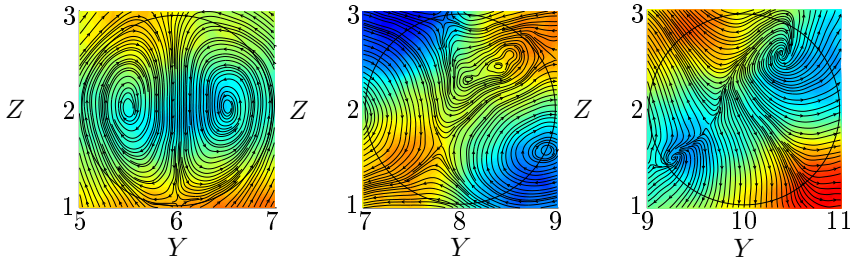

(a) POD mode 11 $S = 12R$ (b) POD mode 11 $S = 16R$ (c) POD mode 11 $S = 20R$

(d) POD mode 12 $S = 12R$ (e) POD mode 12 $S = 16R$ (f) POD mode 12 $S = 20R$

(g) POD mode 13 $S = 12R$ (h) POD mode 13 $S = 16R$ (i) POD mode 13 $S = 20R$

(j) POD mode 14 $S = 12R$ (k) POD mode 14 $S = 16R$ (l) POD mode 14 $S = 20R$

(m) POD mode 15 $S = 12R$ (n) POD mode 15 $S = 16R$ (o) POD mode 15 $S = 20R$

Figure 5.12: Spatial POD modes 11-15 for spacings $12R$, $16R$, and $20R$ with PBL.

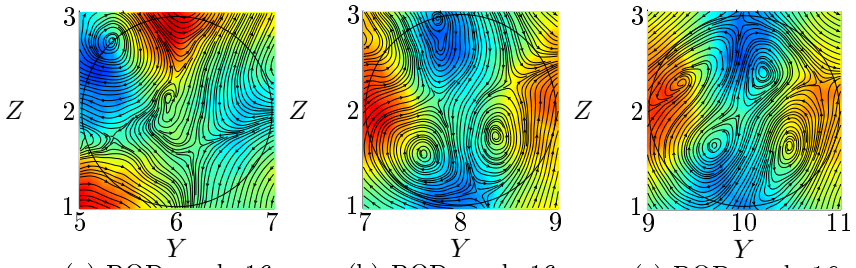

(a) POD mode 16 $S = 12R$ (b) POD mode 16 $S = 16R$ (c) POD mode 16 $S = 20R$

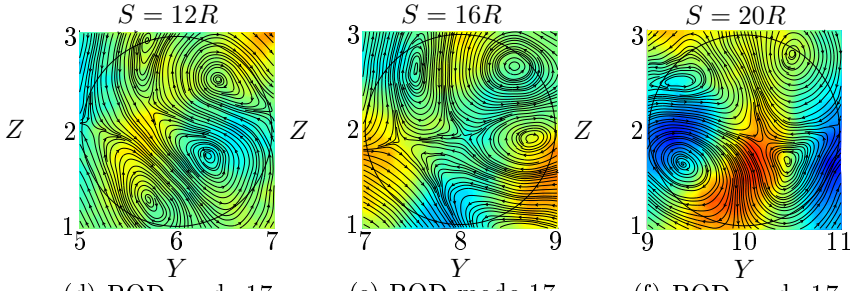

(d) POD mode 17 $S = 12R$ (e) POD mode 17 $S = 16R$ (f) POD mode 17 $S = 20R$

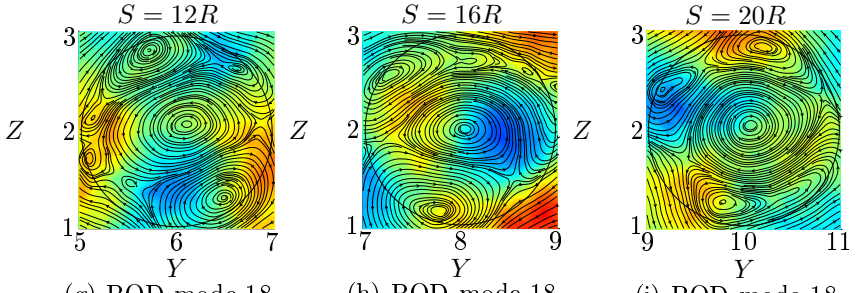

(g) POD mode 18 $S = 12R$ (h) POD mode 18 $S = 16R$ (i) POD mode 18 $S = 20R$

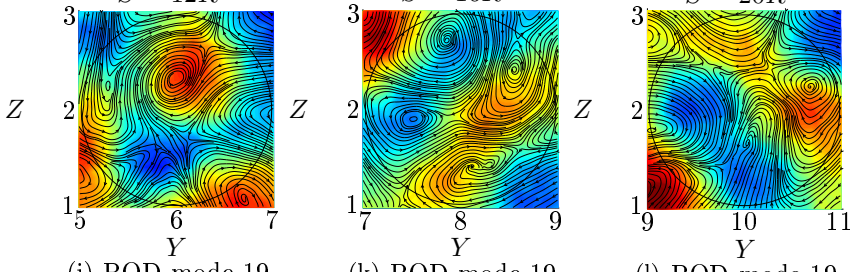

(j) POD mode 19 $S = 12R$ (k) POD mode 19 $S = 16R$ (l) POD mode 19 $S = 20R$

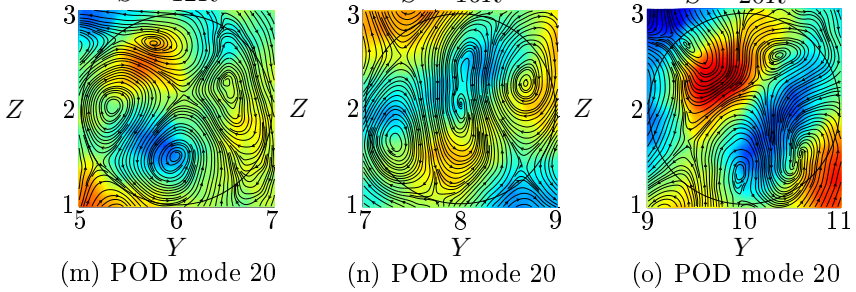

(m) POD mode 20 $S = 12R$ (n) POD mode 20 $S = 16R$ (o) POD mode 20 $S = 20R$

Figure 5.13: Spatial POD modes 16-20 for spacings $12R$, $16R$, and $20R$ with PBL.

Chapter 6

Wake Models

This chapter describes the construction of two wake models of the flow deep inside an infinite wind farm. Both are based on truncating the full flow field by only including a limited number of the spatial POD modes determined in the previous chapter. The POD modes constitute an optimal orthogonal basis for the reconstruction of the variance in the flow, i.e. the turbulent kinetic energy. The first model approach is in the following simply denoted POD, as it based on direct reconstruction of the flow with a limited number of POD modes. The second model includes an additional temporal truncation to give a further REDuced Order Model and hence abbreviated REDOMO(*Latin: to break, to tame*). The temporal truncation only includes the most dominant frequencies derived from the temporal eigenfunctions. Hence, REDOMO is directly based on POD. The reconstructed flow fields for the three infinite wind farm scenarios(excluding the HAT simulation) presented in Chapter 5 are investigated and compared to the full flow fields extracted from the CFD simulations.

The full and reconstructed flows fields are used as inflow conditions for full aeroelastic computations in Flex5 and the effectiveness of the wake models are assessed and verified by comparing the resulting power production and principal loads. The power production and loads are compared through time series, spectral analysis, statistics, and finally equivalent loads, described in Section 2.5.1. Notice, that the present computations corresponding to the full flow fields might differ from the turbine performance reported in the previous chapter. The turbine was previously fully coupled to the Navier-Stokes simulations and hence it responds to the entire flow field in the CFD computations, where the turbine in the following responds to the velocity components extracted from a plane $1R$ upstream the rotor. This generally gives rise to a minor increase in mean velocities as experienced by the turbine, but the differences are of minor importance as the aim is to verify the wake models against the full flow with the corresponding turbine performance and loads.

6.1 Reconstructing the flow using POD and REDOMO

The theoretical background and difference between the two proposed wake models are described in Sections 2.3 and 2.4, and the specific details are elaborated

in this section.

Figures 4.24 and 4.25 presented an example of a temporal eigenfunction and corresponding spectrum for the first POD mode. The POD model includes the full temporal eigenfunction in the reconstruction, while REDOMO truncates the reconstruction by determining the dominant frequencies and subsequently determine scaling parameters based on a linear least squares fit to the full flow.

Figures 6.1-6.3 presents two different spectrums of the temporal eigenfunctions for the first 20 POD modes for all three simulations, i.e. $S = 12R$, $S = 16R$, and $S = 20R$ with PBL. The blue shaded spectrums show spectrums of the eigenfunctions, while the red shaded spectrums show the spectrums of the corresponding gradients of the temporal eigenfunctions. Spitler et al. [65] outline the importance of the higher velocity gradients for assessing the turbine loads, and hence the effect is also examined here by inclusion in REDOMO. The spectrums are normalised by the amplitude of the peak frequency, which are marked by blue circles. The peak gradients are similarly marked by red circles. Clearly, the most energetic structures are located on the lower frequencies. Several of the peak frequencies are directly aligned for $S = 12R$ and $S = 16R$. The aligned peak frequencies reveal how mode pairing occasionally occur both spatially and temporally, e.g. modes 3 and 4 for $S = 12R$ have similar $f_{P,1} \approx 0.005Hz$. The peak frequencies are slightly more scattered for $S = 20R$, but still in the same range. The peak gradient frequencies are at higher frequencies and there is generally an increase in frequency for increasing POD mode. The spectrums also generally change from a single or a few peaks to numerous peaks for increasing POD mode. This shift indicates that the turbulence capture by the higher modes become more and more homogeneous. This trend towards more homogeneous turbulence was also revealed by the cumulative POD coefficient in Figure 5.9. The dominant frequencies are used in REDOMO by assuming that the energy can be lumped onto these frequencies by determining appropriate scaling parameters.

The scaling parameters $\beta_{k,m}$ are determined by minimizing $||\mathbf{u_j} - \widetilde{\mathbf{u}}_\mathbf{j}||^2$, as described in Section 2.4. The obtained $\beta_{k,m}$-values decrease rapidly with increasing POD mode, but the $\beta_{k,m}$-values are not shown for brevity.

In the following, M is the number of peak frequencies used in REDOMO for each POD mode. The special case of including the higher gradient frequencies is denoted with M_{HG}, which includes an equal number of peak and high gradient frequencies, e.g. $H_{HG} = 6$ corresponds to the three peak frequencies and the three highest gradient frequencies. Only a limited number of peak frequencies are used as REDOMO otherwise loose its appealing simplicity.

6.2 Reconstructed Flow Characteristics

Figure 6.4 shows three examples of the instanteneous velocity field extracted from the three CFD simulations. Figures 6.5 and 6.6 depict the corresponding reconstruction using POD and REDOMO, respectively. The efficiency of POD in reconstructing the turbulent flow is indisputable for $S = 12R$ and $S = 16R$. The general distribution with higher velocity in the top left corner and lower velocity in the lower right is captured using only a couple of POD modes, while adding more POD modes results in capturing the finer details. The reconstructed flow is very comparable to the full flow field using 20 POD modes,

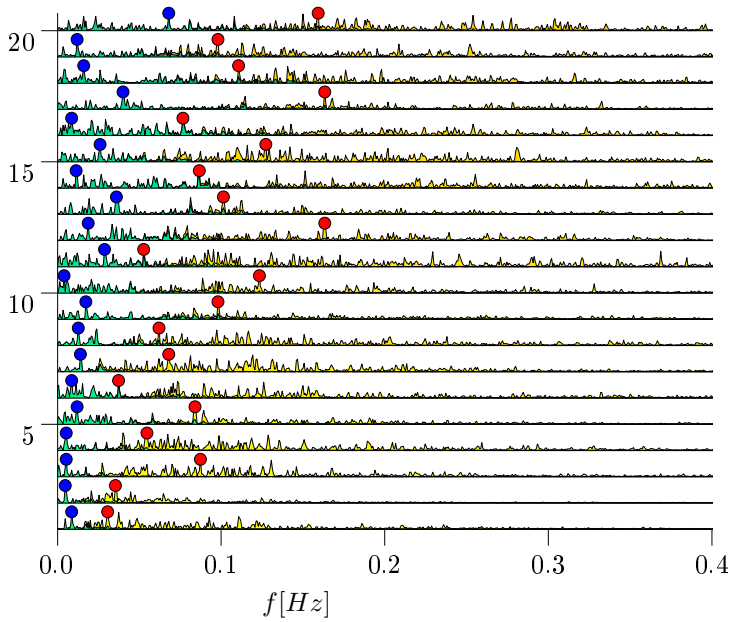

Figure 6.1: PSD for $S = 12R$ normalised by peak frequency. The most energy containing frequency is marked by a blue circle and the highest velocity gradient frequency is marked by a red circle.

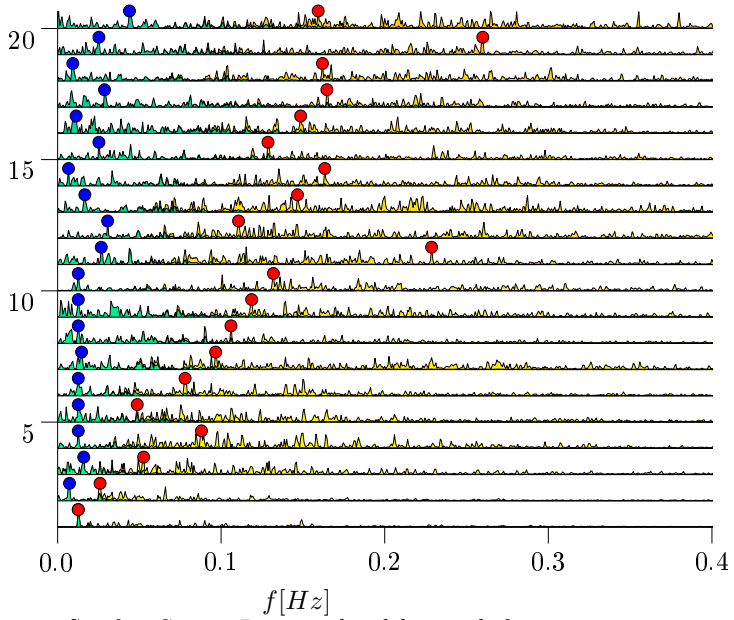

Figure 6.2: PSD for $S = 16R$ normalised by peak frequency. The most energy containing frequency is marked by a blue circle and the highest velocity gradient frequency is marked by a red circle.

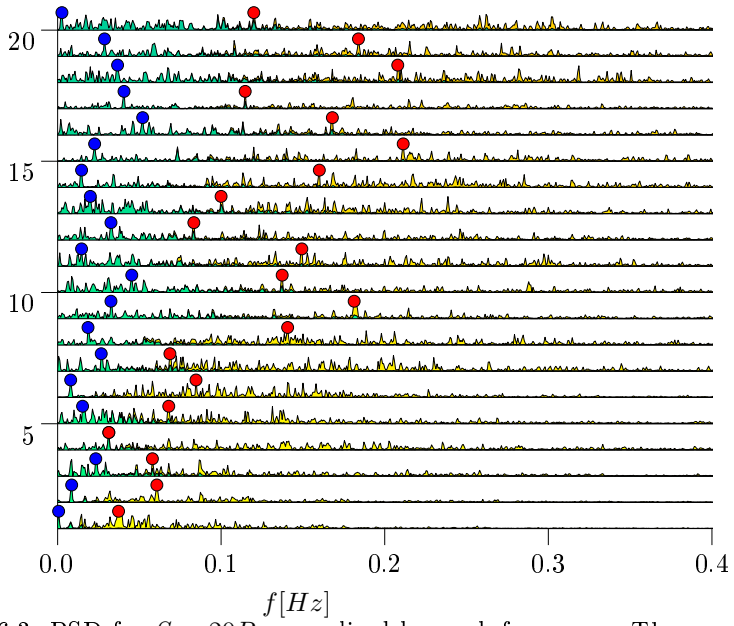

Figure 6.3: PSD for $S = 20R$ normalised by peak frequency. The most energy containing frequency is marked by a blue circle and the highest velocity gradient frequency is marked by a red circle.

and practically identical for 100 modes, even the inplane circulation. Similar agreement is achieved for $S = 12R$. The highest local peaks are not fully reconstructed, which shows the filtering effect of POD. The filtering effect is even more pronounced for the POD reconstruction of $S = 20R$. This example is included to show that there are instances, where the instanteneous reconstruction is less comparable. The reconstruction particularly fails to capture very high or very low velocities.

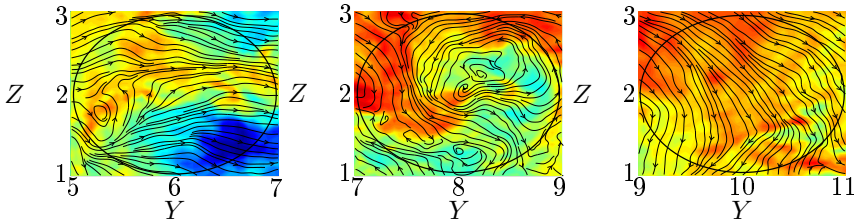

(a) Full flow for $S = 12R$

(b) Full flow for $S = 16R$

(c) Full flow for $S = 20R$

Figure 6.4: Instantaneous velocity extracted $1R$ upstream the first turbine for all three simulations with PBL.

Figure 6.6 only shows the REDOMO reconstruction for $S = 16R$, but for a range of spatial POD modes and frequencies. The left column shows the REDOMO flow field generating using only the most dominant frequency for each of the temporal POD eigenfunctions. Clearly, the instanteneous details of the flow are not sufficiently described. The high velocity areas are located in the upper plane, but on the right as opposed to the left in Figure 6.4. Only minor differ-

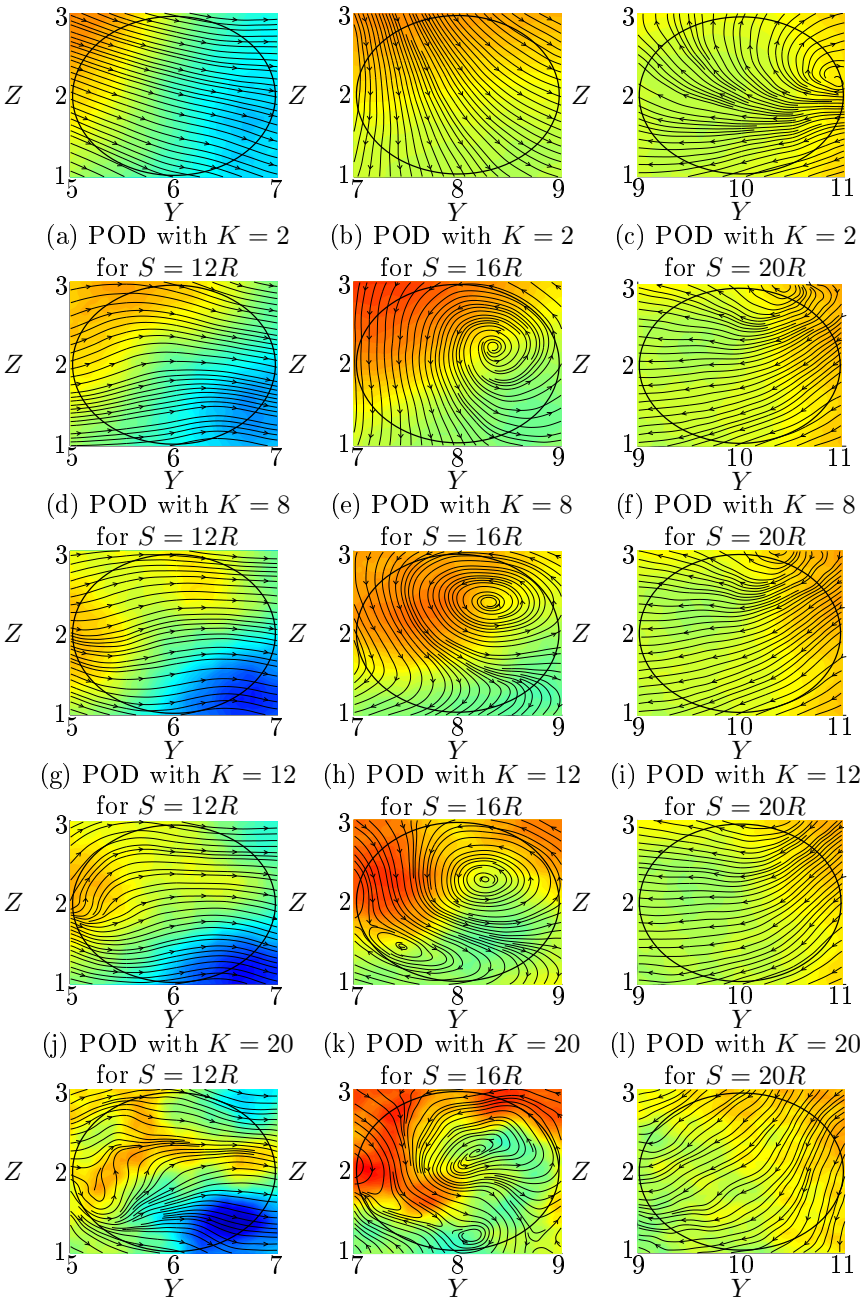

Figure 6.5: POD reconstructions of the instanteneous velocity in Figure 6.4 for various number of POD coefficients(K) for all three simulations with PBL.

ence are obtained by adding more POD modes. The middle column using three peak frequencies yield slightly better comparison, although the effect of adding more spatial POD modes is neglectible. The third column gives markedly better results by capturing the correct distribution for $K \geq 8$ by using the three peak frequencies and the three peak gradient frequencies. However, the reconstructed flow is still clearly filtered and does not reach the correct velocity levels. This indicates that the dynamic nature is predominantly captured by the temporal eigenfunctions, and that a temporal truncation is potentially problematic.

Figures 6.7-6.10 depicts the filtering effect on a more global scale in terms of the instanteneous turbulent kinetic energy for the full flow and the POD reconstruction for $S = 16R$ with $K = 2$, $K = 12$, and $K = 100$. The instanteneous TKE is computed using Equation 2.19 but omitting the temporal averaging. TKE is the most appropriate measure of the reconstructed flow field, since POD is based on optimising the variance, i.e. TKE. The spatial coordinates have been unfolded along the ordinate to give the variance with time along the abscissa. The contours are scaled equally in all figures to enable a direct comparison of the global patterns. The full flow field is very busy, yet there are clear evidence of large coherent structures as broad bands of elevated and lowered regions spanning the majority of the spatial extend. The following figures show how the inclusion of additional POD modes adds more and more TKE to the flow so the reconstructed flow field eventually capture the same patterns and resemble the full flow field, also on a global level. As such, there are only minor differences between the full flow field and the reconstructed flow field using the first 100 POD modes(88% of the TKE). Any minor difference arise in areas of very high or very low TKE.

The global TKE for REDOMO is not shown, since the filtering is so strong that it yields a very poorer comparison and reconstruction of the flow field. REDOMO results will still be presented, but focus is on the POD wake model in the following.

The figures show how POD can reconstruct the flow fields to any degree necessary. It is merely a matter of including more POD modes. Therefore, the most pertinent question is naturally how much information must be retained to adequately describe the flow field as experienced by the wind turbine.

6.3 Verification of Models

The question of how much information and complexity is needed is examined through numerous aeroelastic calculations using Flex5. The full flow field extracted from the CFD simulations as well as several reconstructed flow fields are used as input to Flex5. An additional reference case of stochastically generated Mann turbulence is included in the comparison when reasonable. The aeroelastic computations are conducted for $1,500s$ to keep in line with the previous analyses, which is two and a half times the standard period of $600s$ for aeroelastic computations. The resulting performance and loads on the turbine are examined as a verification of the proposed wake models. The verification focusses on the inflow velocity at hub height, power production, the local edge- and flapwise moment on the individual blades as well as yaw and tilting moments acting on the entire turbine. The investigated parameters are usually taken as a good measure of the turbine loads and performance, e.g. Hansen

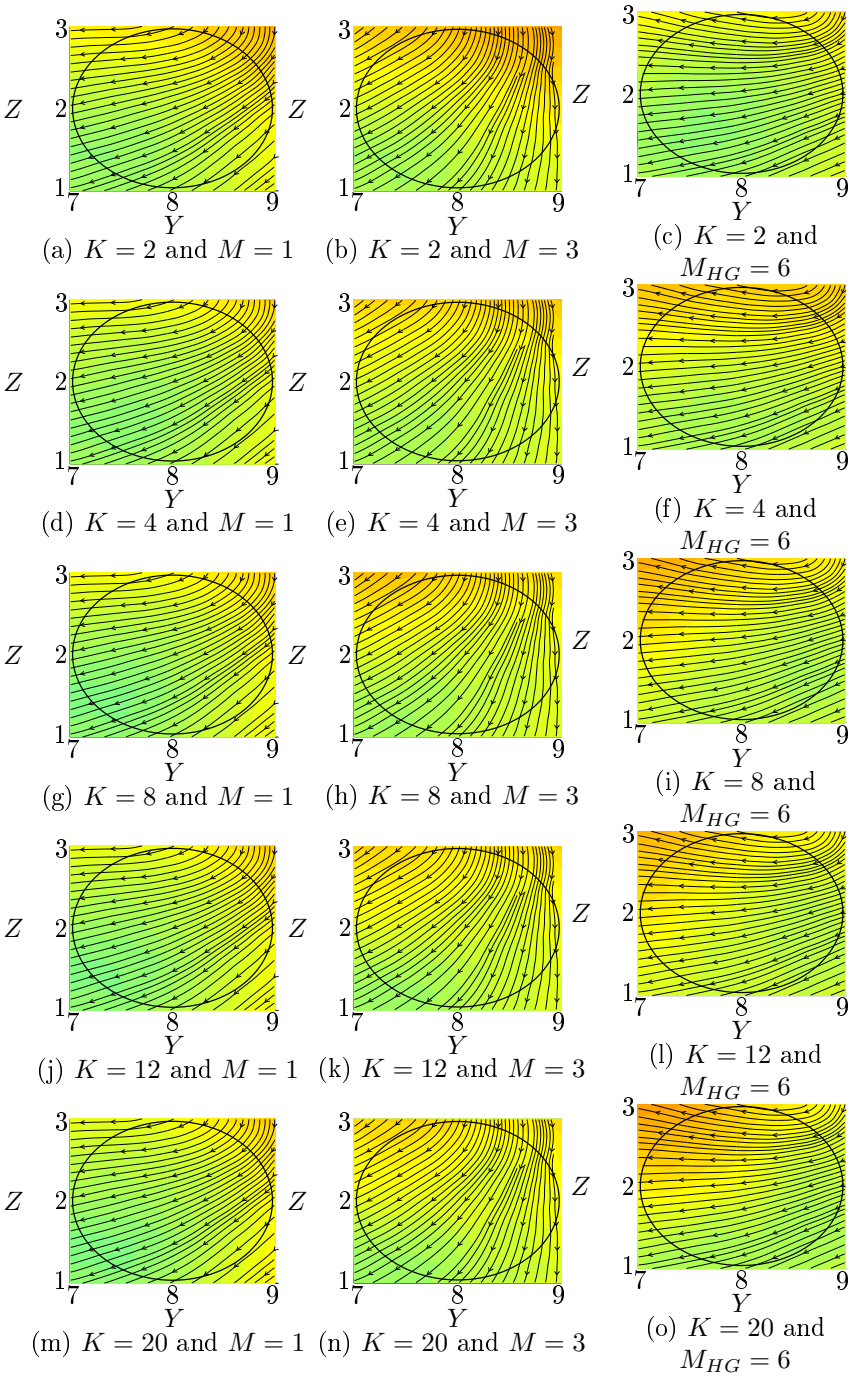

(a) $K = 2$ and $M = 1$ (b) $K = 2$ and $M = 3$ (c) $K = 2$ and $M_{HG} = 6$

(d) $K = 4$ and $M = 1$ (e) $K = 4$ and $M = 3$ (f) $K = 4$ and $M_{HG} = 6$

(g) $K = 8$ and $M = 1$ (h) $K = 8$ and $M = 3$ (i) $K = 8$ and $M_{HG} = 6$

(j) $K = 12$ and $M = 1$ (k) $K = 12$ and $M = 3$ (l) $K = 12$ and $M_{HG} = 6$

(m) $K = 20$ and $M = 1$ (n) $K = 20$ and $M = 3$ (o) $K = 20$ and $M_{HG} = 6$

Figure 6.6: REDOMO reconstructions of the instanteneous velocity in Figure 6.4 for various number of POD coefficients(K) and frequencies(M) for $S = 16R$.

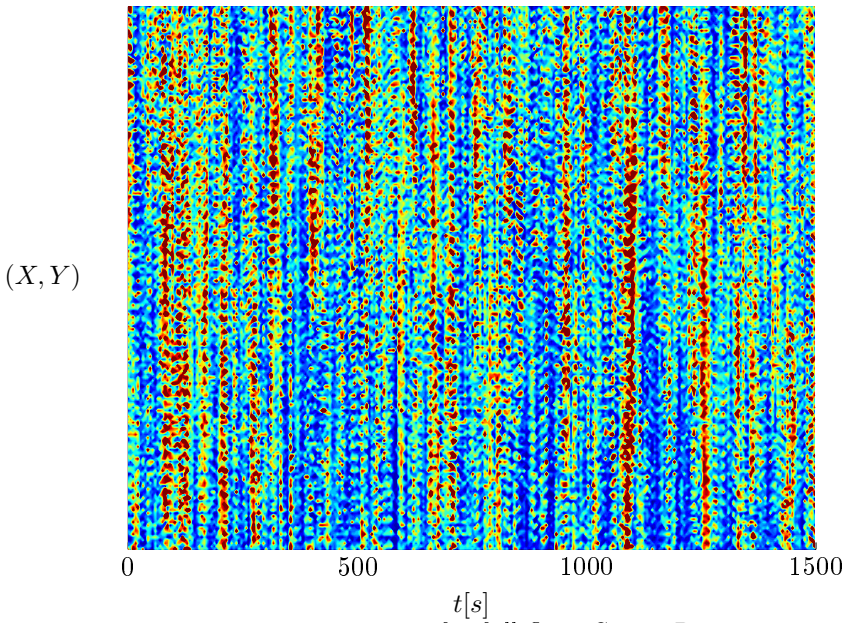

Figure 6.7: TKE for full flow, $S = 16R$.

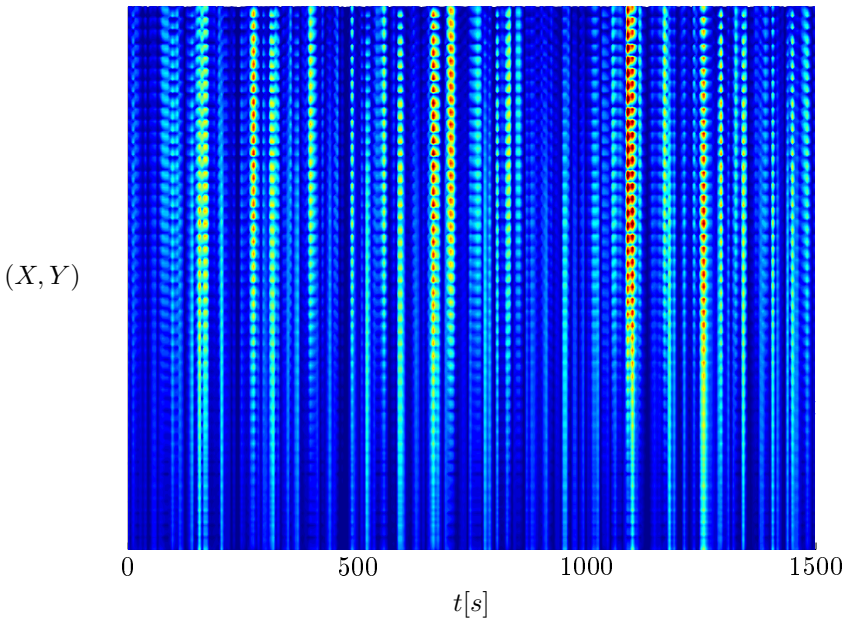

Figure 6.8: TKE for POD with $K = 2$, $S = 16R$.

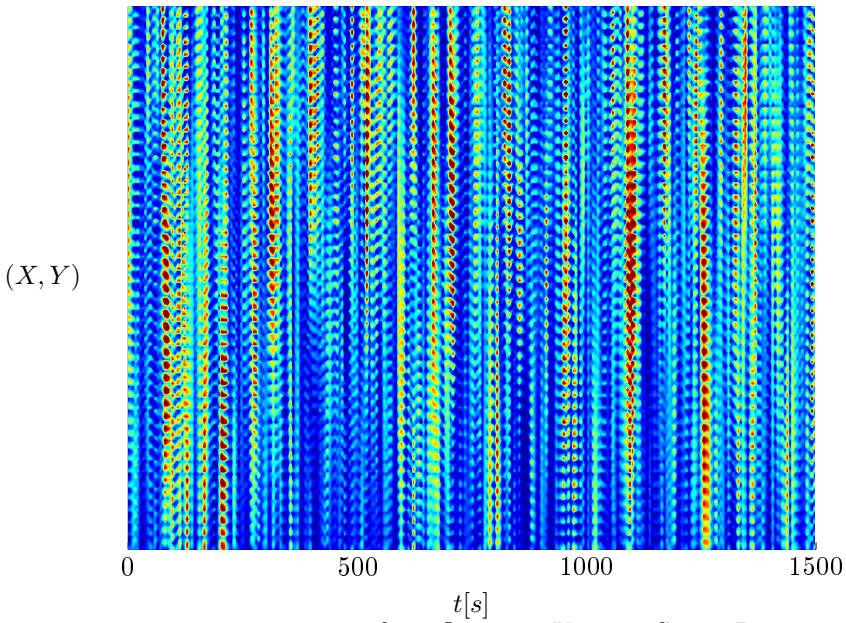

Figure 6.9: TKE for POD with $K = 12$, $S = 16R$.

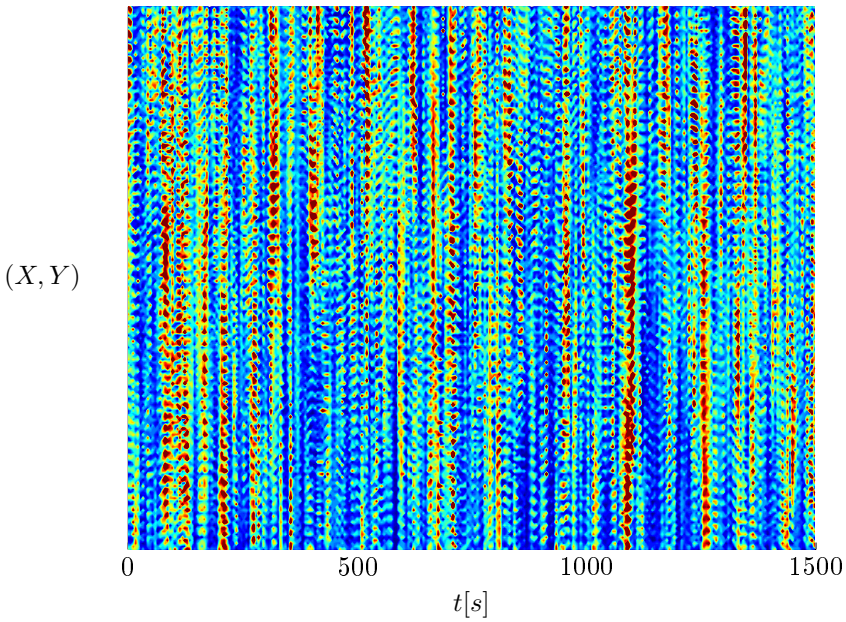

Figure 6.10: TKE for POD with $K = 100$, $S = 16R$.

Spacing	$\frac{\overline{U_{hub}}}{U_0}$	$\sigma(\frac{U}{U_0})$	$\sigma(\frac{V}{U_0})$	$\sigma(\frac{W}{U_0})$
$12R$	9.6	0.12	0.10	$9.2 \cdot 10^{-2}$
$16R$	11.5	0.10	$9.6 \cdot 10^{-2}$	$8.5 \cdot 10^{-2}$
$20R$	12.0	0.10	$8.8 \cdot 10^{-2}$	$7.5 \cdot 10^{-2}$

Table 6.1: Statistics for full flow and generated Mann turbulence.

[24]. The principal parameters are examined through direct comparison of time series, spectral and statistical analysis, and equivalent loads. The statistics are calculated for the entire period, although shorter time series are generally shown for clarity.

Additional flow fields of Mann turbulence(Section 2.1.3) are generated. Three turbulence boxes of $6.4R \times 6.4R \times 1,000R$ are generated. The size of the boxes are chosen to allow for inclusion of large scales and to obtain a resolution comparable to the numerical simulations, i.e. $20 - 22$ points per blade. Boxes of $2R \times 2R$ are extracted from the larger boxes as input to Flex5. The turbulence is generated based on the mean streamwise velocity of the full flow over the rotor area. The rotor hub height of $2R$ is used as input and roughness is neglected(sea state). The turbulence has finally been scaled to match the standard deviation of each of the velocity components in the full flow. Table 6.1 summarise the turbulent quantites for the generated Mann turbulence. The quantities differ slightly from those reported in Table 5.4, because the used values are calculated within $\pm 1R$.

6.3.1 Temporal Verification

The velocity at hub height is given in Figure 6.11 for all three simulations and for a variety of reconstructed flows and with the full flow as reference. The figure only shows a period of $300s$ to visualise the details. The POD reconstructions are given in the left pane. Reconstructing using only 2 POD modes gives a fairly good reconstruction for $S = 12R$, even captures the larger coherent structures around $t \approx 420s$, but struggles for larger spacings. POD yields excellent agreement with the full flow for $K \geq 12$ for $S = 12R$ and $16R$, but POD generally struggles with recreating the inflow velocity for $S = 20R$. This is somewhat surprising since the first POD coefficients where larger for $S = 20R$, see Figure 5.9 and Table 5.5. However, the time series gives insight into the underlying reasons for the poorer reconstruction. The large coherent structures are of noticeably shorter durations for the larger spacings, i.e. higher velocity gradients. High gradients are difficult to reconstruct since it resembles a discontinuity. Retaining such abrupt changes require larger number of modes, similar to Fourier transform of a jump discontinuity, which gives rise to the well-known Gibbs phenomenon. Therefore, the first POD coefficients for $S = 20R$ might contain more energy, but simultaneously demand more POD modes to capture the shorter and more extreme events, which may not contain large amounts of energy. The presence of more extreme events of shorter duration is validated by the smaller RMS values for the streamwise and lateral velocity fluctuations in Table 5.4. The shorter duration of these extreme events are presumed to be a direct artifact of the larger spacings, where the flow behind and between the turbines is less confined by the boundary layer over the wind

farm. This permits larger structures to penetrate the boundary layer more easily and add sudden bursts of energy to the flow inside the wind farm.

The REDOMO reconstructions are given in the right pane. The dynamics of the flow have clearly been filtered out and adding more spatial POD modes and the high gradient frequencies only yields minor improvements.

The power production is shown in Figure 6.12. The power production is reproduced very well by all POD reconstructions for $S = 12R$ and $S = 16R$, even for $K < 12$. The poorer reconstruction of the inflow velocity for $S = 20R$ affect the power production, and only minor improvements are made by adding more modes. The power production derived from REDOMO also gives a poor fit, but it is still capable of recreating some of the larger trends, e.g. $t \approx 400s$ for $S = 16R$.

Figure 6.13 shows the flapwise moment(M_F) acting on a turbine blade. The flapwise moment originates from the thrust and deflects the blades downwind. The figure tells the same story, where POD is very efficient at recreating the loads for the smaller and intermediate spacings. It also shows how POD for $S = 20R$ and REDOMO appear to capture the correct frequencies although with much smaller amplitudes.

The edgewise moments(M_E) are plotted in Figure 6.14 and stems from the tangential forces on the blades. All reconstructed flows gives very good agreement with the full flow situation, since this edgewise moments are dominated by gravity as the blades rotates.

The yaw moment(M_Y) attempts to turn the rotor around the tower axis and is depicted in Figure 6.15. The excellent reconstruction by POD is particular pronounced for the yaw moment for the smaller spacings, although a minimum number of POD modes is required as $K = 2$ is too few. The remaining reconstructions results in too small loads. Similar results are shown in Figure 6.16, which gives the tilting moment(M_T). The tilting moment bends the entire turbine back and forth, and the yaw and tilting moments are a direct measure of the large turbulent structures which will try to turn or overturn the turbine when in a partial wake situation.

6.3.2 Spectral Verification

The Power Spectral Density(PSD) are computed for the loads and compared to the full flow. The spectral analysis of the flapwise moments for all three spacing are given for a number of reconstructed flow fields and the reference Mann turbulence in Figure 6.17. The blade passing frequency $1P = 0.29Hz$ and its harmonics are present in all the spectrums, even spectrums derived from REDOMO. This indicates how even REDOMO resolves large structures, which are comparable to the actual structures in time, but not in magnitude. The peaks associated with the blade passing arise because the rotational time of the turbine is much lower than the passage time of the large coherent structures. Therefore, each blade passes through the coherent structures of high and low velocity and are exerted by high and low loads several times for each large coherent structure. Both wake models capture these peak frequencies, although REDOMO leads to smaller and very narrow peaks. Adding more POD modes enables the POD model to capture both peak width and levels of the spectrums correctly. So the comparison between higher POD models and the full flow is once again excellent. There are minor discrepancies at higher frequencies, which

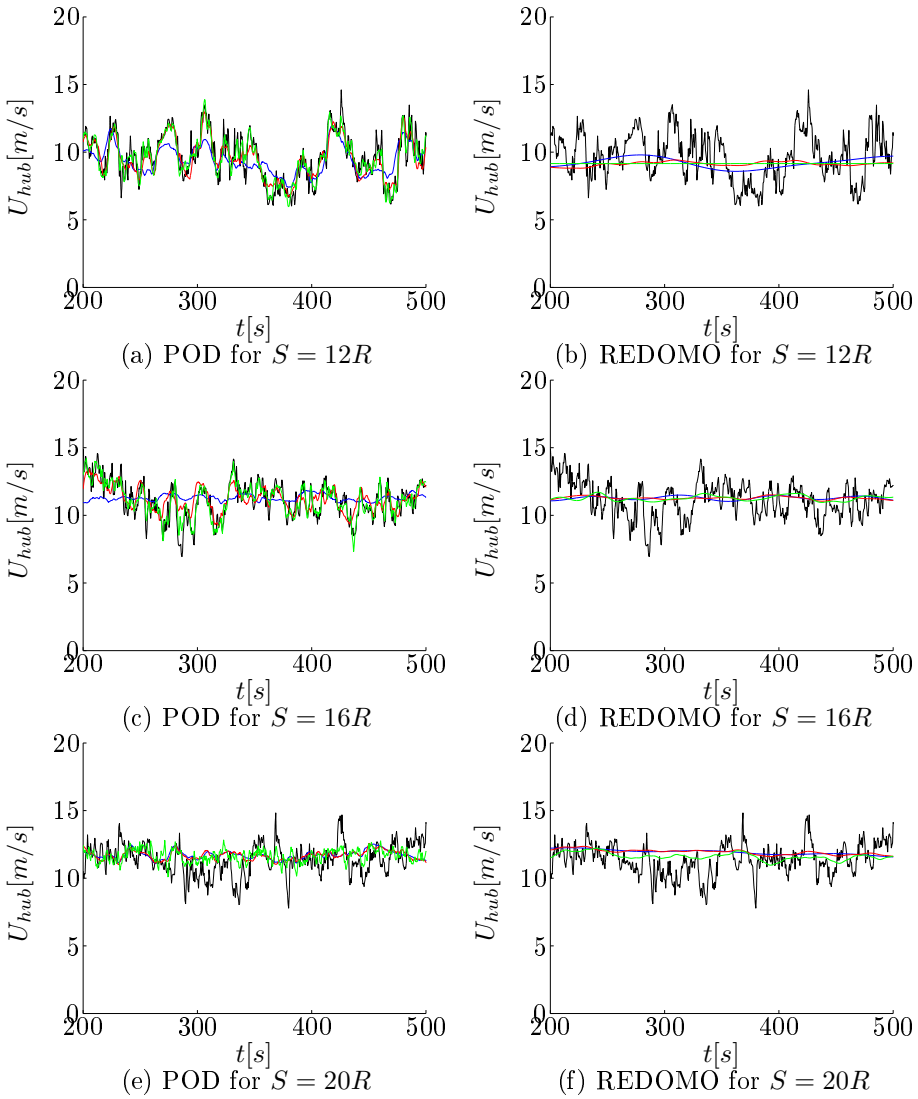

(a) POD for $S = 12R$ (b) REDOMO for $S = 12R$

(c) POD for $S = 16R$ (d) REDOMO for $S = 16R$

(e) POD for $S = 20R$ (f) REDOMO for $S = 20R$

Figure 6.11: Streamwise velocity at hub height for full and reconstructed flows. Legend: —— : Full flow. —— : POD: $K = 2$. REDOMO: $K = 2$ and $M = 1$. —— : POD: $K = 12$. REDOMO: $K = 20$ and $M = 1$. —— : POD: $K = 100$. REDOMO: $K = 20$ and $M_{HG} = 6$.

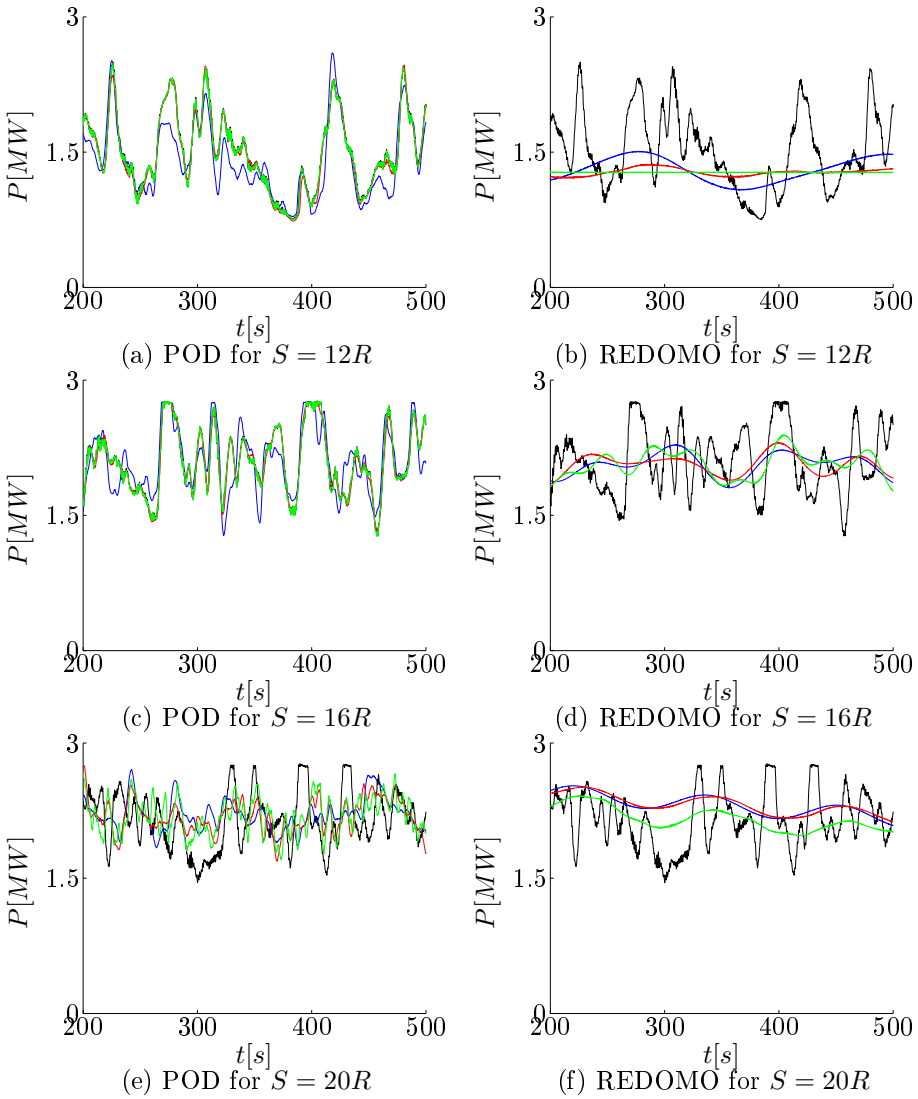

(a) POD for $S = 12R$ (b) REDOMO for $S = 12R$

(c) POD for $S = 16R$ (d) REDOMO for $S = 16R$

(e) POD for $S = 20R$ (f) REDOMO for $S = 20R$

Figure 6.12: Power production for full and reconstructed flows.
Legend: —— : Full flow. —— : POD: $K = 2$. REDOMO: $K = 2$ and $M = 1$.
—— : POD: $K = 12$. REDOMO: $K = 20$ and $M = 1$. —— : POD: $K = 100$.
REDOMO: $K = 20$ and $M_{HG} = 6$.

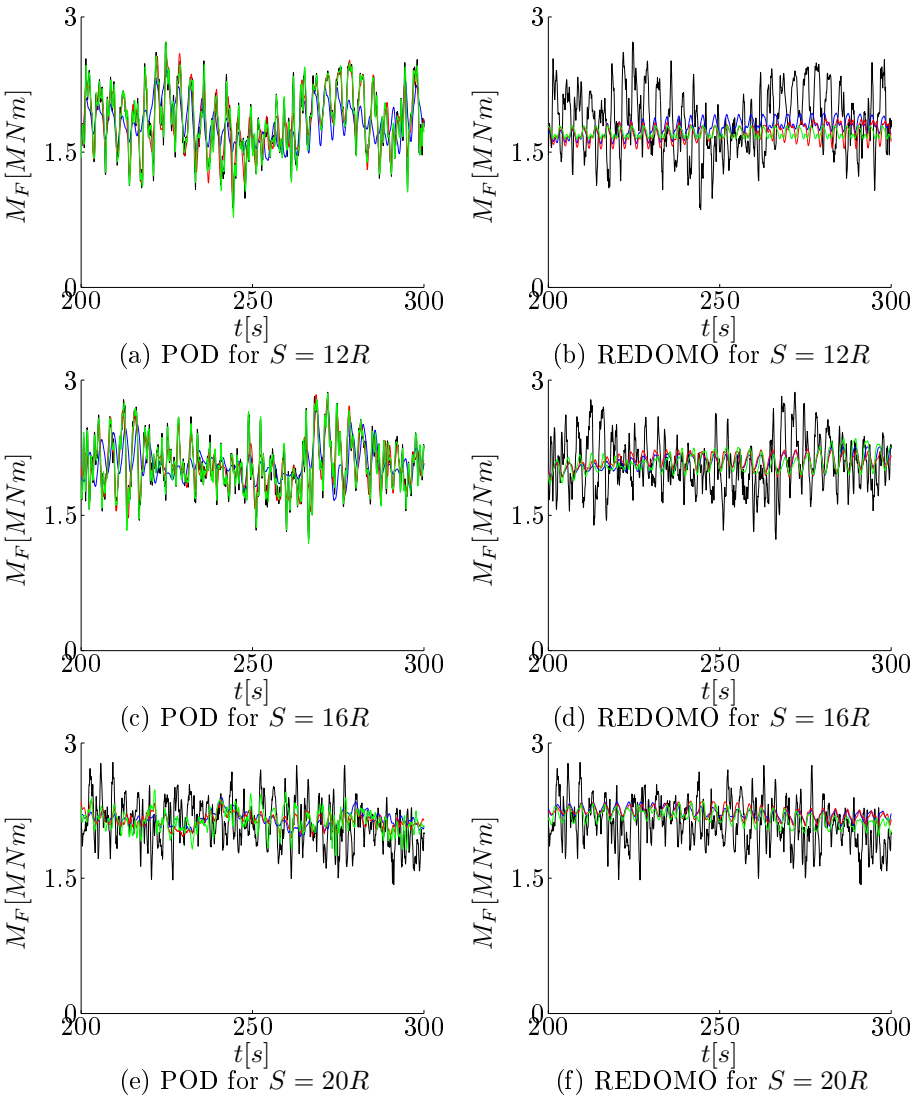

(a) POD for $S = 12R$ (b) REDOMO for $S = 12R$

(c) POD for $S = 16R$ (d) REDOMO for $S = 16R$

(e) POD for $S = 20R$ (f) REDOMO for $S = 20R$

Figure 6.13: Flapwise moment for full and reconstructed flows.
Legend: —— : Full flow. —— : POD: $K = 2$. REDOMO: $K = 2$ and $M = 1$.
—— : POD: $K = 12$. REDOMO: $K = 20$ and $M = 1$. —— : POD: $K = 100$.
REDOMO: $K = 20$ and $M_{HG} = 6$.

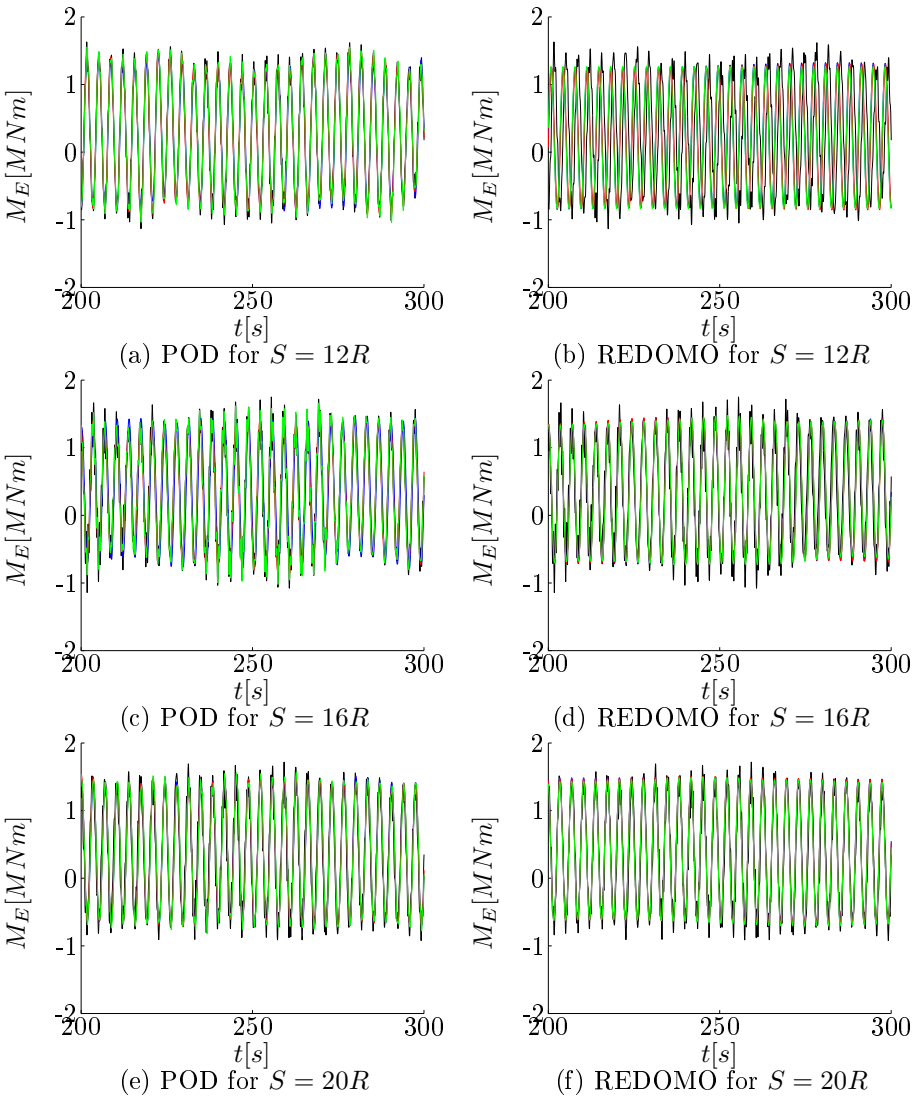

(a) POD for $S = 12R$ (b) REDOMO for $S = 12R$

(c) POD for $S = 16R$ (d) REDOMO for $S = 16R$

(e) POD for $S = 20R$ (f) REDOMO for $S = 20R$

Figure 6.14: Edgewise moment for full and reconstructed flows.
Legend: —— : Full flow. —— : POD: $K = 2$. REDOMO: $K = 2$ and $M = 1$. —— : POD: $K = 12$. REDOMO: $K = 20$ and $M = 1$. —— : POD: $K = 100$. REDOMO: $K = 20$ and $M_{HG} = 6$.

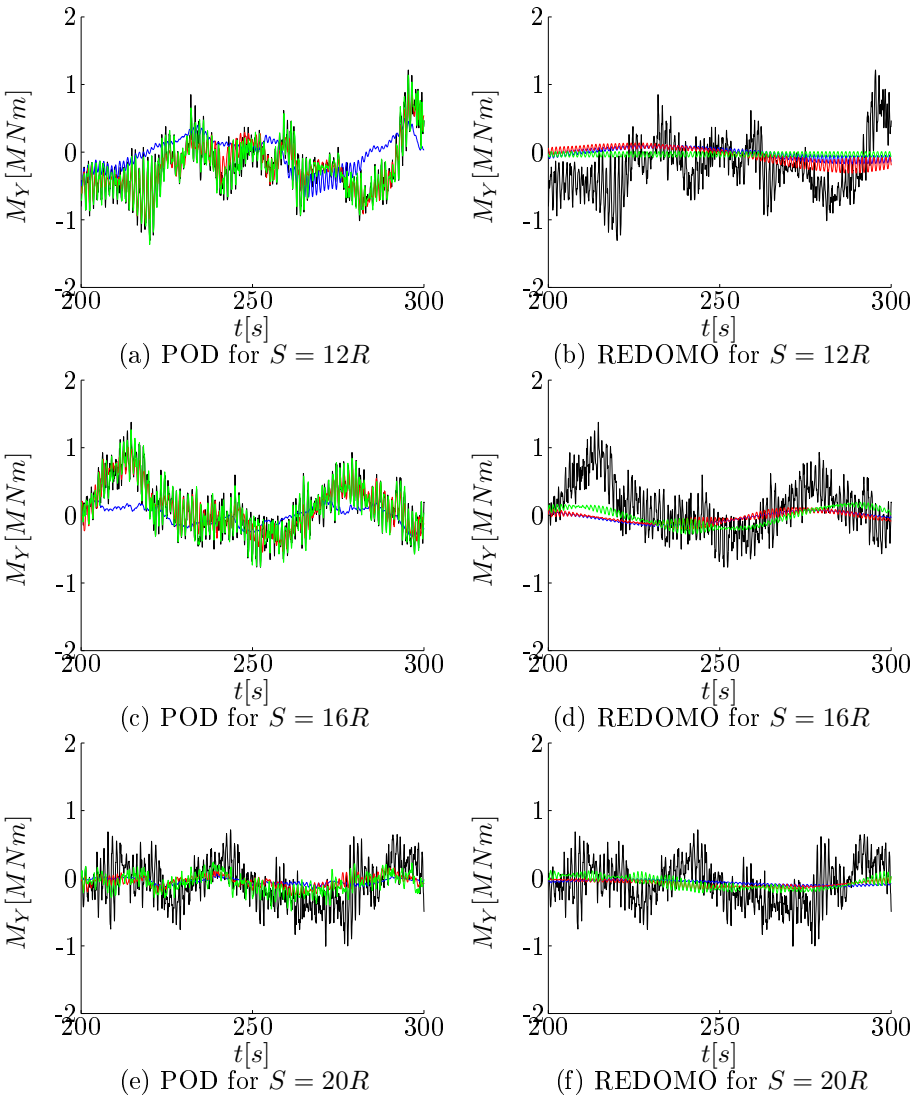

(a) POD for $S = 12R$ (b) REDOMO for $S = 12R$

(c) POD for $S = 16R$ (d) REDOMO for $S = 16R$

(e) POD for $S = 20R$ (f) REDOMO for $S = 20R$

Figure 6.15: Yaw moment for full and reconstructed flows.
Legend: —— : Full flow. —— : POD: $K = 2$. REDOMO: $K = 2$ and $M = 1$.
—— : POD: $K = 12$. REDOMO: $K = 20$ and $M = 1$. —— : POD: $K = 100$.
REDOMO: $K = 20$ and $M_{HG} = 6$.

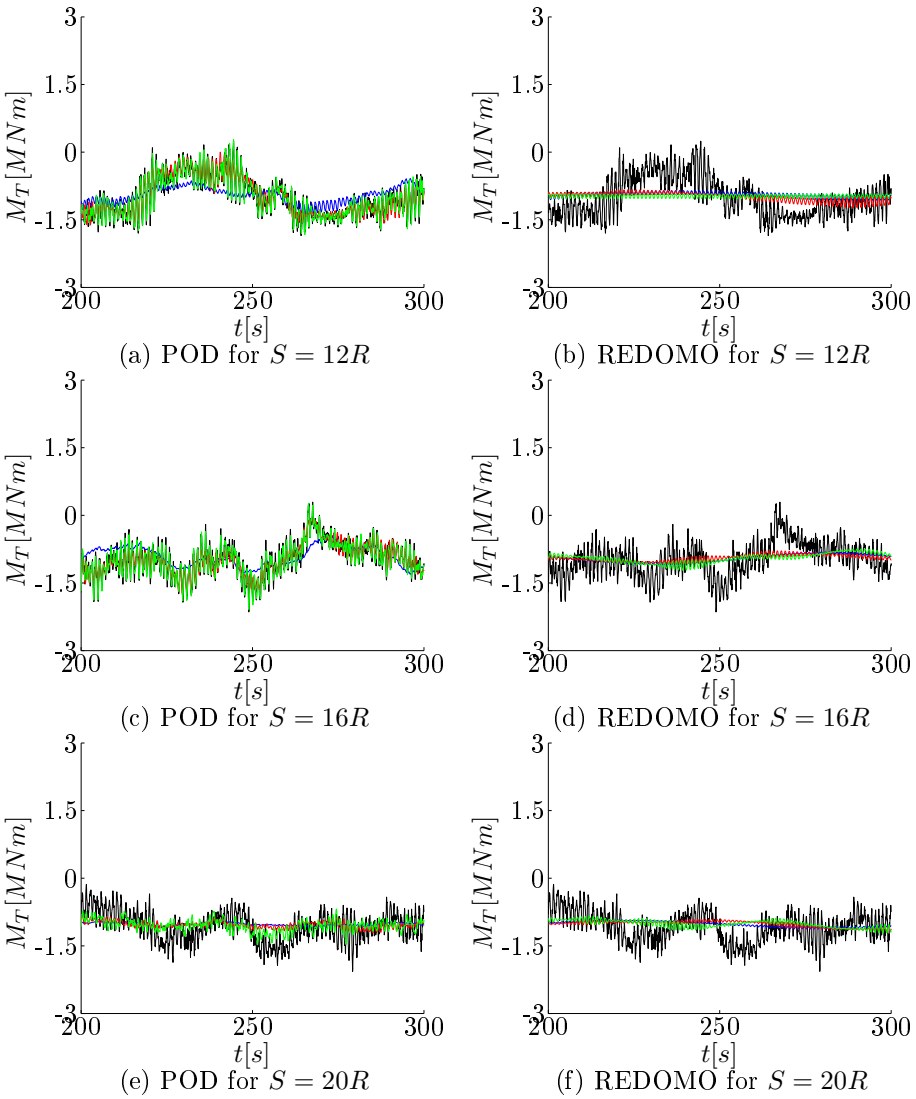

(a) POD for $S = 12R$ (b) REDOMO for $S = 12R$

(c) POD for $S = 16R$ (d) REDOMO for $S = 16R$

(e) POD for $S = 20R$ (f) REDOMO for $S = 20R$

Figure 6.16: Tilt moment for full and reconstructed flows.
Legend: —— : Full flow. —— : POD: $K = 2$. REDOMO: $K = 2$ and $M = 1$. —— : POD: $K = 12$. REDOMO: $K = 20$ and $M = 1$. —— : POD: $K = 100$. REDOMO: $K = 20$ and $M_{HG} = 3$.

is a natural consequence of the energy filtering. Mann turbulence captures this slightly better as there is no filtering of the small scales. POD for $S = 20R$ also give a very good agreement, although it is shifted in magnitude, i.e. fails to reproduce the correct energy level. Mann turbulence also gives a very good agreement with the full flow, but it does not match the levels correctly despite being scaled to the full flow statistics. This difference presumably arise from the difference in vertical shear.

The edgewise moment spectrum reveal similar tendencies in Figure 6.18. The dominating frequency previously seen in Figure 6.14 clearly coincides with a very narrow band around the blade passing frequency $1P$. $3P$ and particular $6P$ are also very distinct. Several POD modes are required to reach the correct levels for $6P$. Mann turbulence once again yield a comparable spectrum, but at a smaller level.

The spectrums for yaw and tilt moments portrait similar trends in Figures 6.19 and 6.20. The dominant frequency is now located at $f \approx 3P$, because the yaw and tilt are moments affecting the entire turbine, not just the individual blades. Therefore, the turbine is exerted by yaw and tilting moment each time any of the three blade passes through a large coherent structure, which occurs at a rate of $3P$.

The spectral analysis shows very good agreement between the full flow and the POD reconstructed flows for small and intermediate spacings. The filtering nature of both POD and REDOMO naturally reconstructs less energy on the higher frequencies, but dominant peaks and most energetic frequencies are matched excellently. Despite its crudeness, REDOMO still capture the peak frequencies in the load spectrums. However, the dynamic response of the turbine is not resolved correctly as the associated peaks are very narrow. Hence, it does not give rise to the correct damping response of the turbine, as the spectral width is related to the damping ratio. Stochastically generated Mann turbulence generally gives a good agreement with the full spectrum, although with smaller level, so an alternative scaling is potentially possible, but will still depend on simulated or measured target values.

6.3.3 Statistical Comparison

The turbine performance in terms of power production is governed by the streamwise inflow velocity at hub height. The different flow cases are in the following figures referenced according to the following list:

1. O: Full flow, reference case.
2. $P1$: POD with $K = 2$.
3. $P2$: POD with $K = 4$.
4. $P3$: POD with $K = 8$.
5. $P4$: POD with $K = 12$.
6. $P5$: POD with $K = 20$.
7. $P6$: POD with $K = 100$.
8. $R1$: REDOMO with $K = 2$ and $M = 1$.

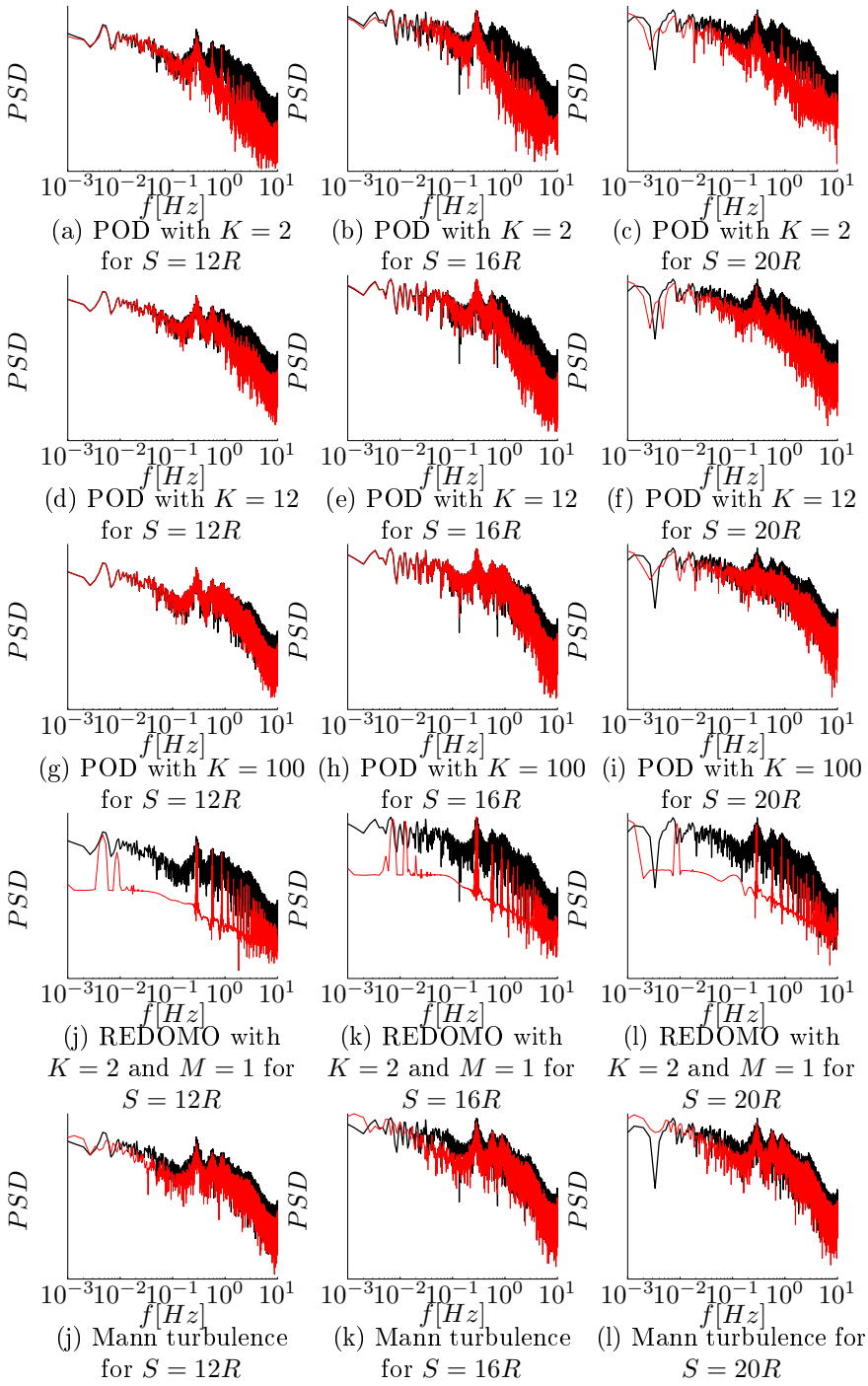

(a) POD with $K = 2$ for $S = 12R$ (b) POD with $K = 2$ for $S = 16R$ (c) POD with $K = 2$ for $S = 20R$

(d) POD with $K = 12$ for $S = 12R$ (e) POD with $K = 12$ for $S = 16R$ (f) POD with $K = 12$ for $S = 20R$

(g) POD with $K = 100$ for $S = 12R$ (h) POD with $K = 100$ for $S = 16R$ (i) POD with $K = 100$ for $S = 20R$

(j) REDOMO with $K = 2$ and $M = 1$ for $S = 12R$ (k) REDOMO with $K = 2$ and $M = 1$ for $S = 16R$ (l) REDOMO with $K = 2$ and $M = 1$ for $S = 20R$

(j) Mann turbulence for $S = 12R$ (k) Mann turbulence for $S = 16R$ (l) Mann turbulence for $S = 20R$

Figure 6.17: PSD of flapwise moments for full and reconstructed flows for all three simulations with PBL. Legend: —— : Full flow. —— : Reconstructed flow.

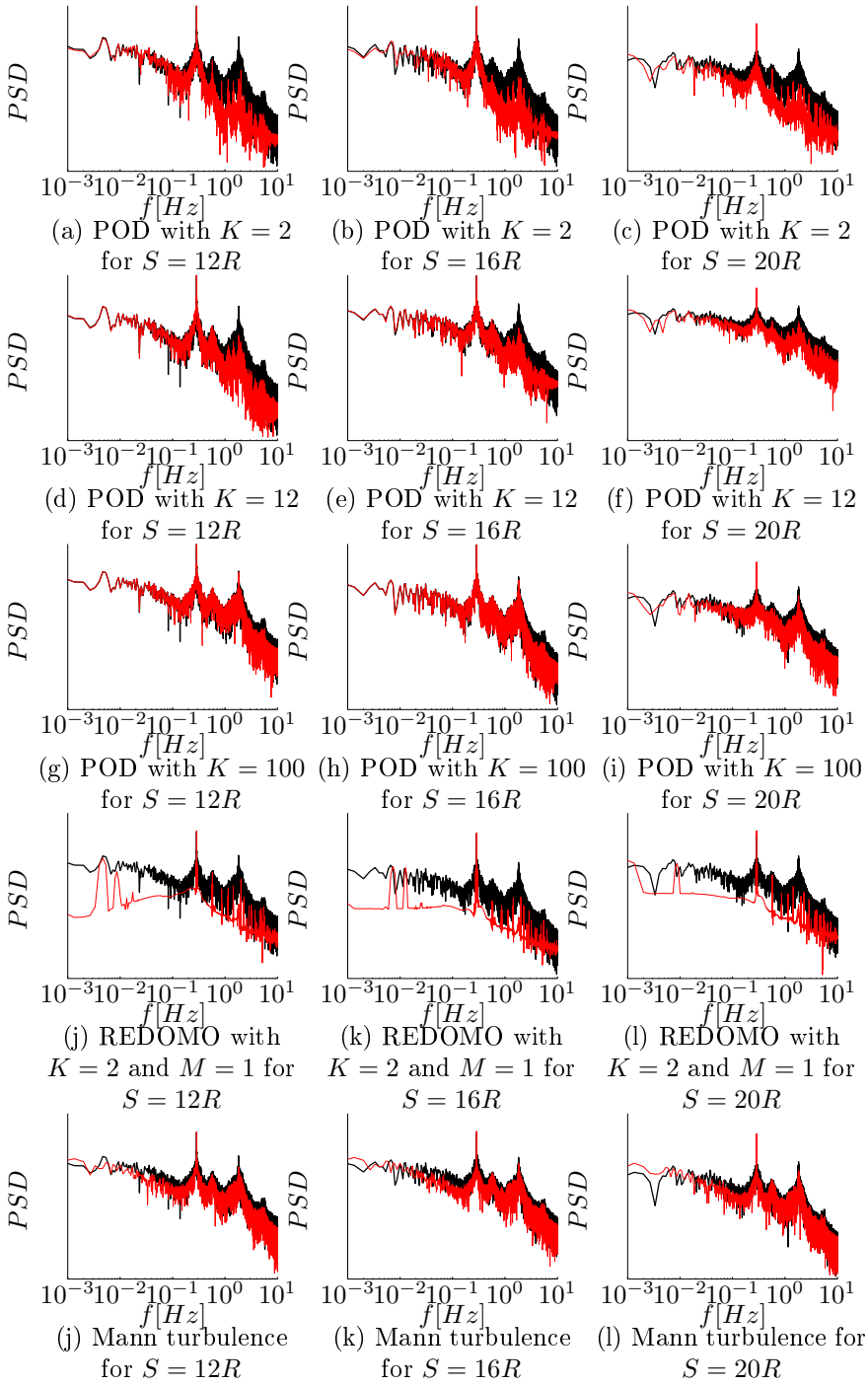

(a) POD with $K = 2$ for $S = 12R$ (b) POD with $K = 2$ for $S = 16R$ (c) POD with $K = 2$ for $S = 20R$

(d) POD with $K = 12$ for $S = 12R$ (e) POD with $K = 12$ for $S = 16R$ (f) POD with $K = 12$ for $S = 20R$

(g) POD with $K = 100$ for $S = 12R$ (h) POD with $K = 100$ for $S = 16R$ (i) POD with $K = 100$ for $S = 20R$

(j) REDOMO with $K = 2$ and $M = 1$ for $S = 12R$ (k) REDOMO with $K = 2$ and $M = 1$ for $S = 16R$ (l) REDOMO with $K = 2$ and $M = 1$ for $S = 20R$

(j) Mann turbulence for $S = 12R$ (k) Mann turbulence for $S = 16R$ (l) Mann turbulence for $S = 20R$

Figure 6.18: PSD of edgewise moments for full and reconstructed flows for all three simulations with PBL. Legend: —— : Full flow. —— : Reconstructed flow or Mann turbulence.

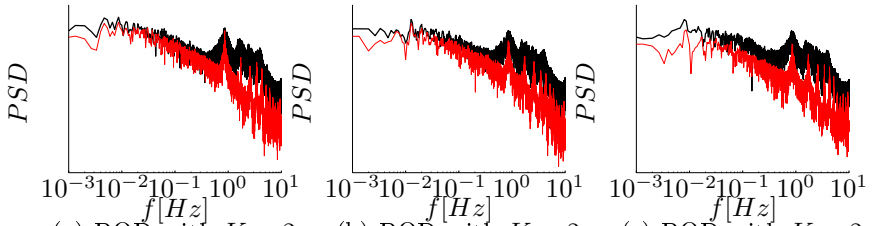

(a) POD with $K = 2$ for $S = 12R$ (b) POD with $K = 2$ for $S = 16R$ (c) POD with $K = 2$ for $S = 20R$

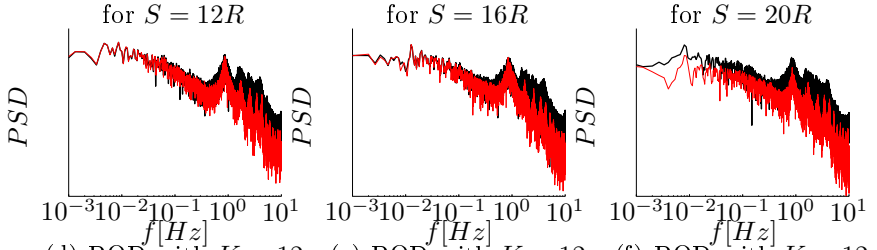

(d) POD with $K = 12$ for $S = 12R$ (e) POD with $K = 12$ for $S = 16R$ (f) POD with $K = 12$ for $S = 20R$

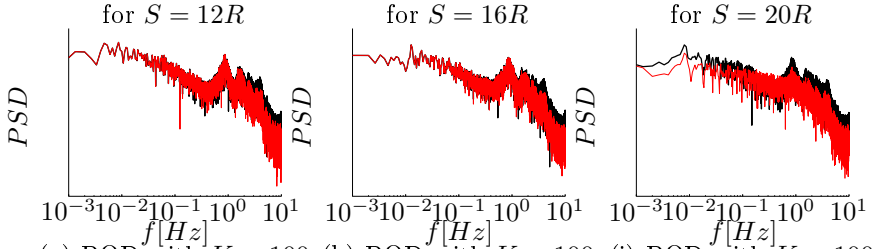

(g) POD with $K = 100$ for $S = 12R$ (h) POD with $K = 100$ for $S = 16R$ (i) POD with $K = 100$ for $S = 20R$

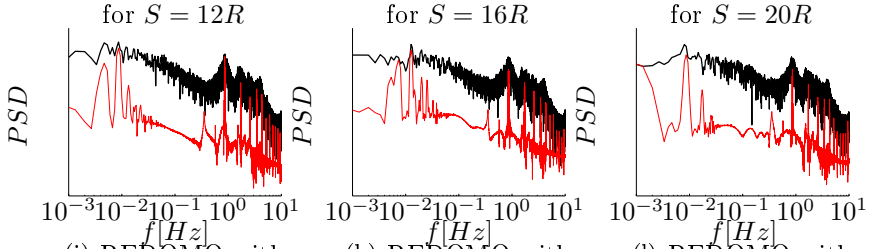

(j) REDOMO with $K = 2$ and $M = 1$ for $S = 12R$ (k) REDOMO with $K = 2$ and $M = 1$ for $S = 16R$ (l) REDOMO with $K = 2$ and $M = 1$ for $S = 20R$

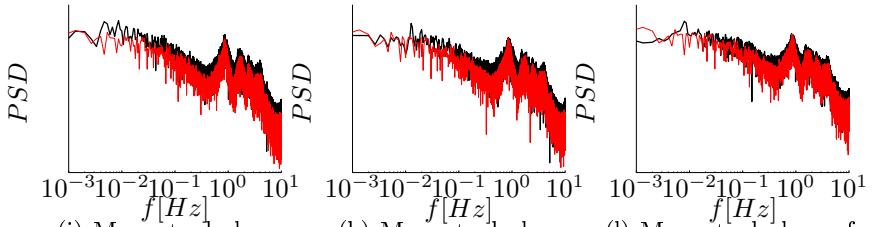

(j) Mann turbulence for $S = 12R$ (k) Mann turbulence for $S = 16R$ (l) Mann turbulence for $S = 20R$

Figure 6.19: PSD of yaw moments for full and reconstructed flows for all three simulations with PBL. Legend: —— : Full flow. —— : Reconstructed flow.

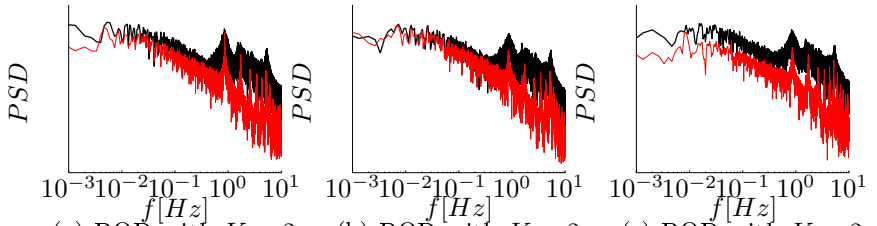

(a) POD with $K = 2$ for $S = 12R$ (b) POD with $K = 2$ for $S = 16R$ (c) POD with $K = 2$ for $S = 20R$

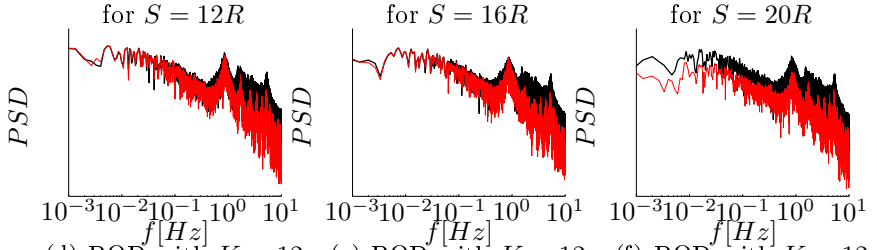

(d) POD with $K = 12$ for $S = 12R$ (e) POD with $K = 12$ for $S = 16R$ (f) POD with $K = 12$ for $S = 20R$

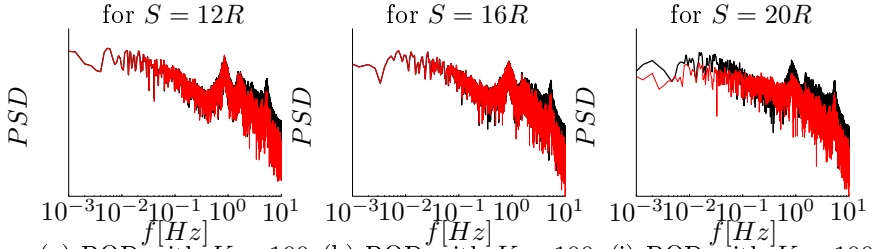

(g) POD with $K = 100$ for $S = 12R$ (h) POD with $K = 100$ for $S = 16R$ (i) POD with $K = 100$ for $S = 20R$

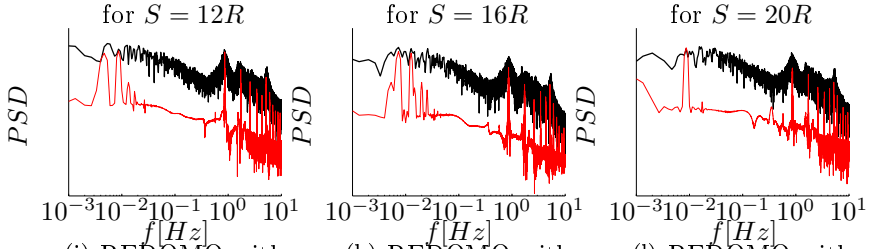

(j) REDOMO with $K = 2$ and $M = 1$ for $S = 12R$ (k) REDOMO with $K = 2$ and $M = 1$ for $S = 16R$ (l) REDOMO with $K = 2$ and $M = 1$ for $S = 20R$

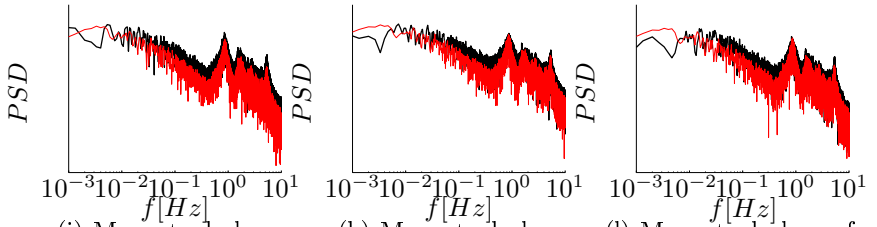

(j) Mann turbulence for $S = 12R$ (k) Mann turbulence for $S = 16R$ (l) Mann turbulence for $S = 20R$

Figure 6.20: PSD of tilt moments for full and reconstructed flows for all three simulations with PBL. Legend: —— : Full flow. —— : Reconstructed flow.

9. $R2$: REDOMO with $K = 20$ and $M = 1$.

10. $R3$: REDOMO with $K = 20$ and $M_{HG} = 6$.

11. $M1$: Mann turbulence.

Figure 6.21 shows the mean and standard deviation of the power production for each simulation. POD underpredicts the mean power production by less than 4% for $S = 12R$, while the three REDOMO examples underpredicts by 7%. The power production is modelled very well($< 1\%$ discrepancy) for all cases with $S = 16R$, while the larger spacing gives rise to a minor overprediction of power, but still less than 2% for both POD and REDOMO. POD also match the standard deviations using $K > 2$ for $S = 12R$ and $S = 16R$, while it is underpredicted for $S = 20R$. REDOMO yields increasing standard deviation for increasing spacing, but does not capture the full variability. Neither does the Mann turbulence, although it is closer for larger spacing.

The higher order statistics in terms of skewness and kurtosis are compared. The third moment or skewness s is computed as

$$s = \frac{E(X-\mu)^3}{\sigma^3} \tag{6.1}$$

where μ is the mean of the signal X and σ is the standard deviation. E represents the expected value of $X - \mu$. Similarly, the fourth moment or kurtosis is computed as

$$\kappa = \frac{E(X-\mu)^4}{\sigma^4} \tag{6.2}$$

The skewness and kurtosis express the shape of the probability density function(PDF) of a given signal. REDOMO cases are disregarded, since the higher order statistics are poor and hence distort the scale for direct comparison between the statistics of the full flow, POD, and Mann turbulence. Figure 6.22 portrait an example of a PDF for the tilting moment for $S = 16R$. The first POD reconstructions show a narrower and more peaked distribution, while POD quickly adapts towards the PDF of the full flow when including more modes. Mann turbulence also yields a narrower and more peaked PDF. The skewness is slightly higher for the reconstructed flow indicating how the full flow has a slightly stronger tendency towards larger negative moments. Kurtosis is a measure of the outlying points and how peaked the distribution is. The kurtosis of the tilting moments are close to 3 for the full flow and the reconstructed flows for $K \geq 8$. As reference, a normal distribution has kurtosis of 3. The similarity(or differences) of the higher order statistics are hence expressed by the skewness and kurtosis in Figures 6.23 and 6.24.

Generally, the skewness are matched well for the small($S = 12R$) and intermediate($S = 16R$) spacings for $K > 4$, while the corresponding skewness for the large spacing($S = 20R$) is further from the target. It appears the small spacing is skewed positive towards higher power, flap-wise, and tilt moments as opposed to the skewness of larger spacings. Conversely, the large spacing is skewed positively towards larger edgewise moments. The intermediate spacing portraits no or very little skewness for power, flap-, edge-wise, and yaw moments. Mann turbulence is more inconsistent with both good and bad agreement for both small and large spacings.

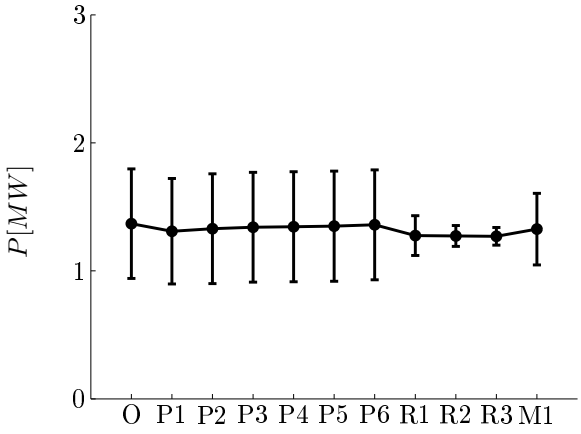

(a) $S = 12R$

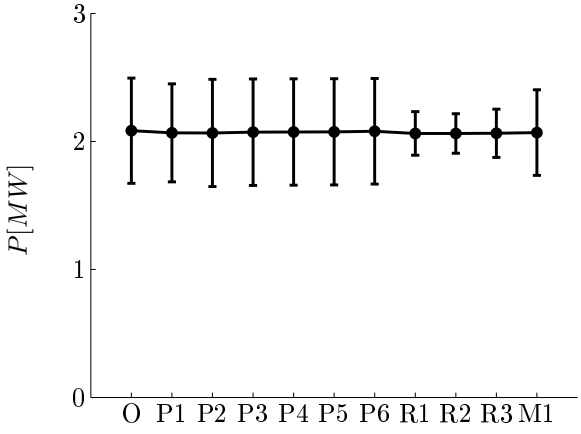

(b) $S = 16R$

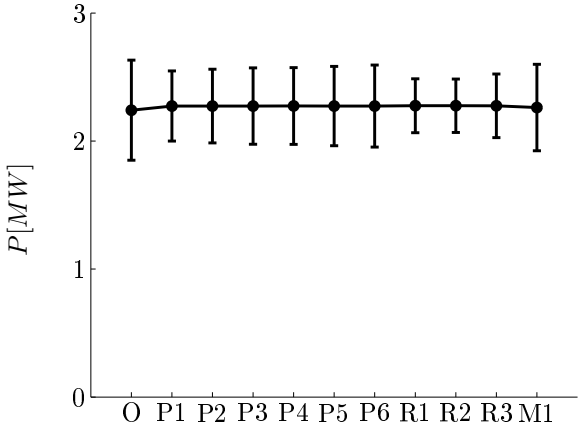

(c) $S = 20R$

Figure 6.21: Mean and standard deviations of power production for various reconstructed flows for all three spacings.

The kurtosis mostly shows good agreement, except for the power and flapwise moment for $S = 20R$ and particular for lower number of POD modes. The remaining distributions yield kurtosis comparable to a normal distribution, i.e. $\kappa = 3$. The edgewise moment is the exception, but it is constant around $\kappa \approx 1.6$ for all cases. Mann turbulence also gives good agreement.

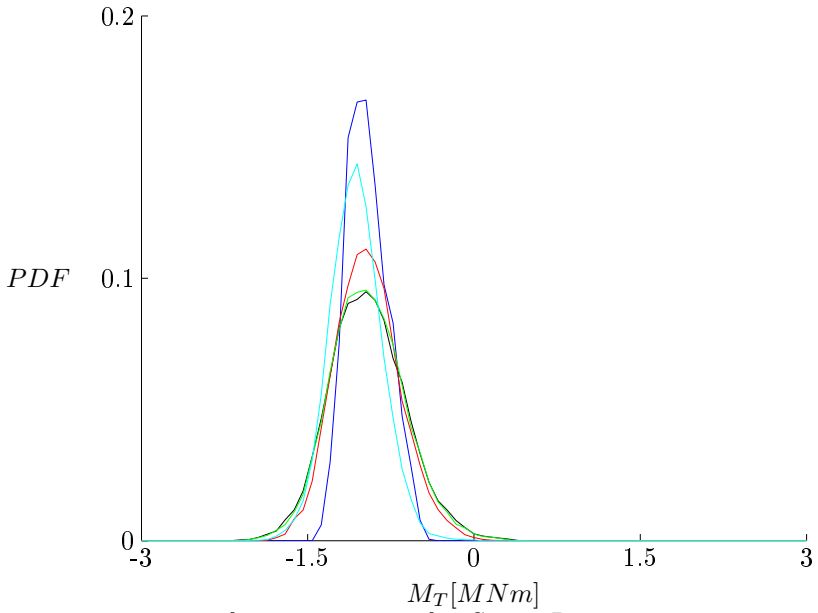

Figure 6.22: PDF of tilting moment for $S = 16R$. Legend: ——— : Full flow. ——— : POD: $K = 2$. ——— : POD: $K = 12$. ——— : POD: $K = 100$. ——— : Mann turbulence.

The reconstructed flows are capable of capturing both the low and high order statistics very well. The high order statistics naturally require more POD modes, but the statistics are generally preserved for $K \geq 8$ for the small and intermediate spacings. The comparison with Mann turbulence is more mixed with both good and poor agreements, which is to be expected as the method does not guarentee that higher order statistics are preserved.

6.3.4 Equivalent Loads Verification

Equivalent load calculations are performed using the reconstructed flow fields and Mann turbulence, and subsequently compared to the equivalent loads for the full flow. Calculating equivalent loads enable a direct comparison between different load situations, where the full flow simulations are assumed represent the correct loads. The formula for calculating the equivalent loads are described in Section 2.5.1. Three different material parameters of $m = 3$, $m = 6$, and $m = 10$ are examined, which corresponds to steel, high quality steel and composite materials, such as fiberglas, see Larsen et al. [35].

The equivalent loads are presented in Figures 6.25, 6.26, and 6.28 for $S = 12R$, $S = 16R$, and $S = 20R$, respectively. The equivalent loads are normalised by the reference equivalent load derived from the full flow to describe how much of the total load is captured by the wake models. The equivalent loads for the

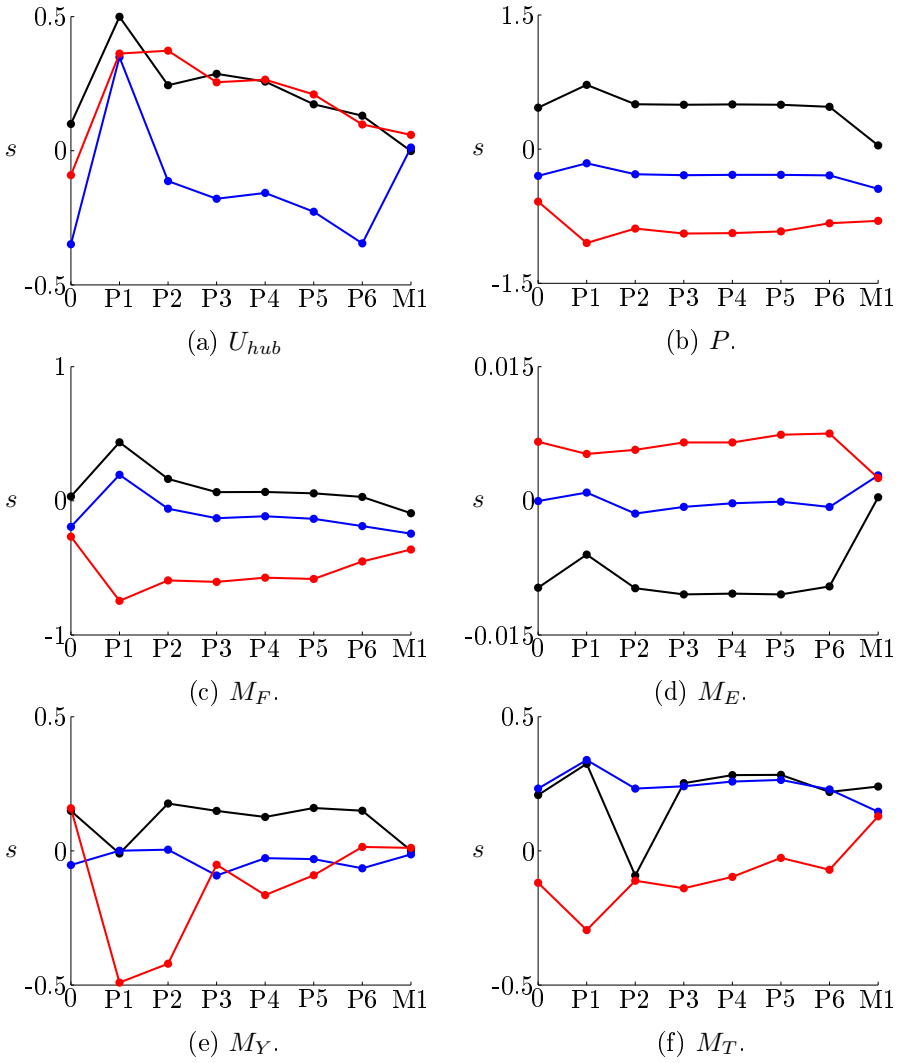

(a) U_{hub} (b) P. (c) M_F. (d) M_E. (e) M_Y. (f) M_T.

Figure 6.23: Skewness for the principal components exerted by the different flows. Legend: —— : $S = 12R$. —— : $S = 16R$. —— : $S = 20R$.

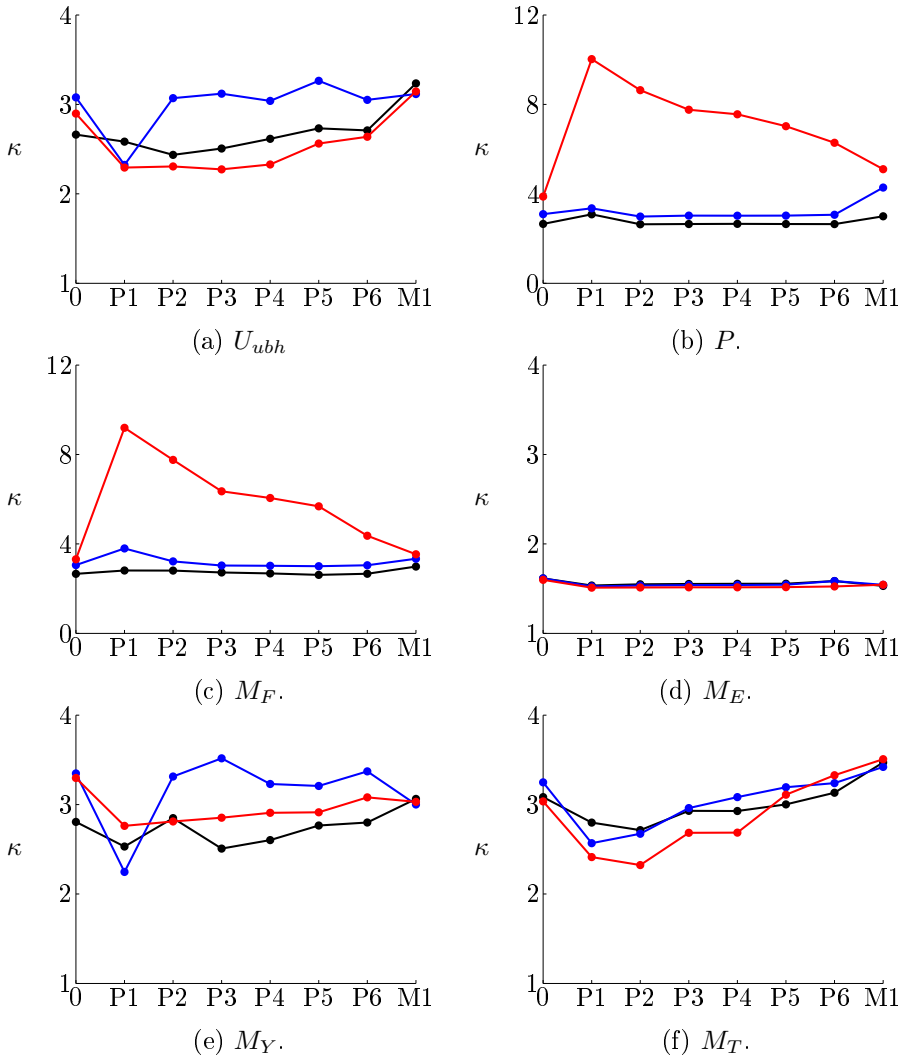

(a) U_{ubh} (b) P. (c) M_F. (d) M_E. (e) M_Y. (f) M_T.

Figure 6.24: Kurtosis for the principal components exerted by the different flows. Legend: —— : $S = 12R$. —— : $S = 16R$. —— : $S = 20R$.

edgewise moments are omitted, since all reconstructions result in more than 90% of the equivalent loads. There is a clear increase in the equivalent loads as more POD modes are included in the reconstructed flow. The equivalent flapwise moments increase from 42% to 96% for $m = 3$ and from 57% to 98% for $m = 10$ as K increases from 2 to 100. This also reveal how the same inflow conditions affect various materials differently. The equivalent loads indicate how the low frequent loads affect the composite materials more, i.e. the materials with higher m-values. This adds complexity to the demands in the attempts to develop a dynamic and detailed wake model, which incorporate all the necessary frequencies. Similar trends are seen for the yaw and tilting moments, although the captured percentage of the equivalent loads are lower than for the flapwise moments. However, POD still results in capturing $62 - 77\%$ of the equivalent loads for $K = 12$ and more than 88% for $K = 100$. REDOMO yields very poor agreement for the equivalent loads as it only corresponds to $5\% - 28\%$ of the full equivalent loads. Mann turbulence results in loads comparable in size to those captured by the first $2 - 4$ POD modes as it accounts for $49 - 61\%$ of the equivalent loads.

The equivalent loads for $S = 16R$ show similar trends while resulting in even better agreement with the equivalent loads from the full flow. The flapwise moments are described by 45% for $m = 3$ and 71% for $m = 10$ using only 2 POD modes. This also reveals a pivotal part of the wake model verification. The proposed wake models are based on an optimal energy filtering of the flow field. But the wind turbine also acts as a filter as it responds and adapts to the highly dynamic flow. The controller includes a temporal filter due to the physical response time and it filters out high frequencies. Moreover, the spatial extend of the wind turbine acts as a spatial filter as the controller essentially reacts to the integrated loads over the entire rotor. This additional filtering explains how 36% of the turbulent kinetic energy gives rise to $45 - 71\%$ of the equivalent flapwise loads. This is seen by comparing the equivalent loads with energy content summarised in Table 5.5. Figure 6.27 shows the cumulative energy content of the POD modes and the regions enclosed by the equivalent loads of the three material parameters for $S = 16R$, i.e. the upper bound is governed by the equivalent loads arising for $m = 10$ and the lower bound from $m = 3$. The horizontal lines represent the equivalent loads from the Mann turbulence. The equivalent flapwise moment is always larger than the energy content for all three material parameter. The POD model is on par with Mann turbulence when including $4 - 8$ modes, but the POD model outperforms Mann for the flapwise moments when including $K \geq 12$. The reconstructed yaw and tilt moments initially yield less of the equivalent loads than the included energy would otherwise presuppose. However, the reconstructed equivalent loads are once again on par with the energy content for $K \geq 12$ and exceeds the energy content for $K \geq 20$. The stochastic Mann turbulence gives rise to loads equivalent of including up to $4-8$ POD modes. This validates how some of the finer scales of the turbulence are superfluous due the various filtering effects, but also that global loads such as yaw and tilt require detailed wake models to predict the loads accurately.

Finally, the equivalent loads for $S = 20R$ is shown in Figure 6.28. The equivalent loads yield a poor comparison, at least compared to the previous cases. No more than 56% of the edgewise loads are recreated, and only a minor improvement is obtained by including more modes for $m = 6$ and $m = 10$. Yaw and tilt show a more linear increase and REDOMO actually performs

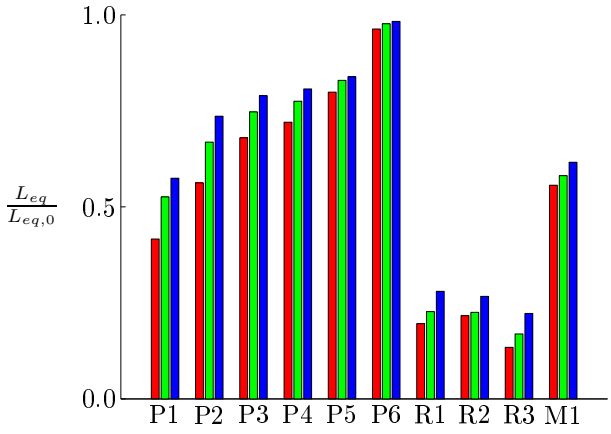

(a) Flapwise moment.

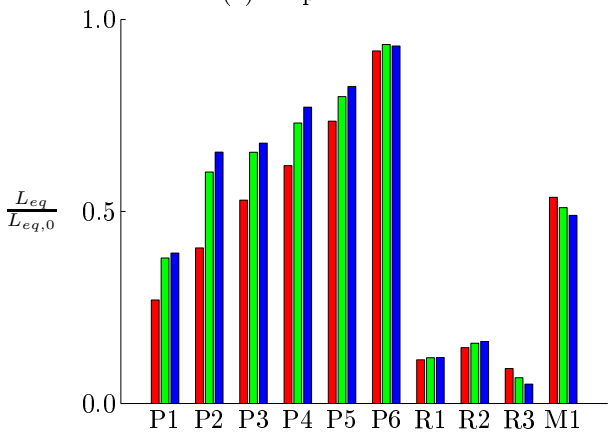

(b) Nacelle yaw.

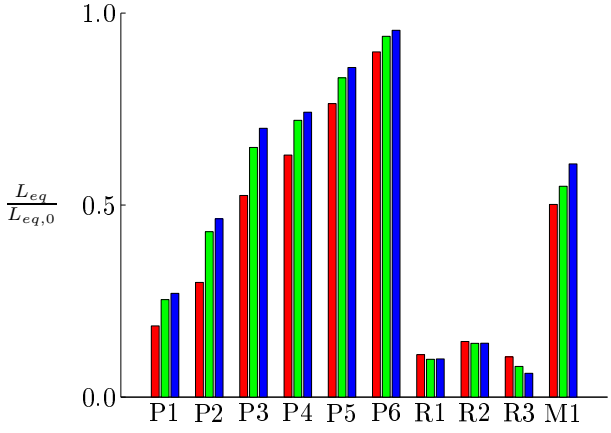

(c) Nacelle tilt.

Figure 6.25: Normalised equivalent loads for various reconstructions for $S = 12R$ with PBL. Legend: : $m = 3$. : $m = 6$. : $m = 10$.

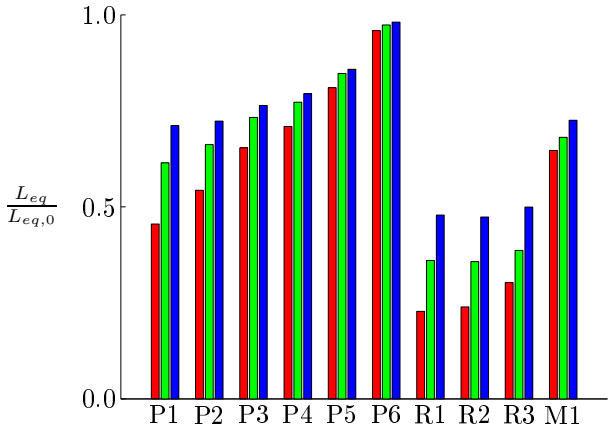

(a) Flapwise moment.

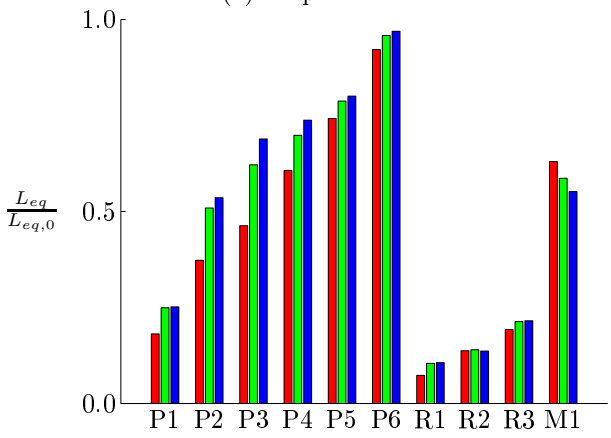

(b) Nacelle yaw.

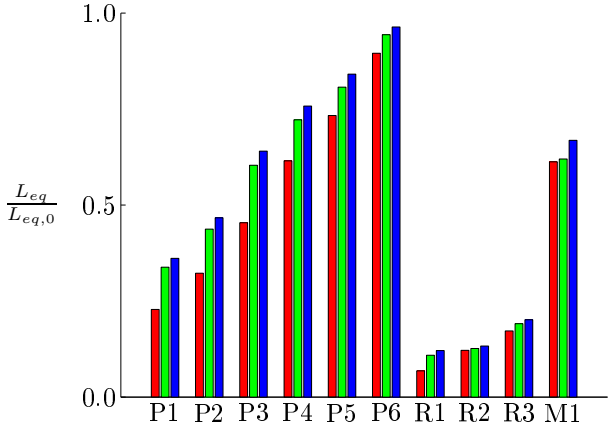

(c) Nacelle tilt.

Figure 6.26: Normalised equivalent loads for various reconstructions for $S = 16R$ with PBL. Legend: : $m = 3$. : $m = 6$. : $m = 10$.

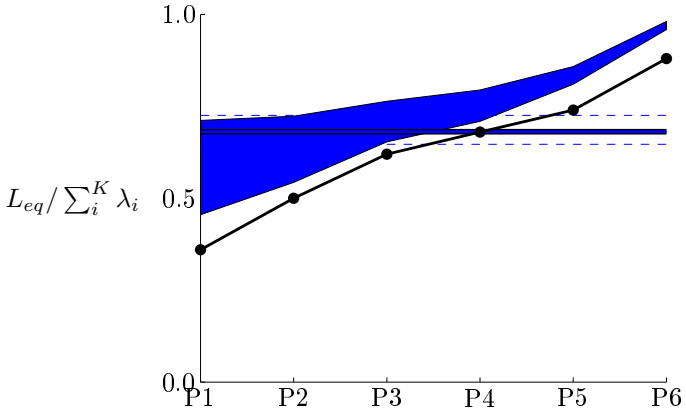

(a) Flapwise moment.

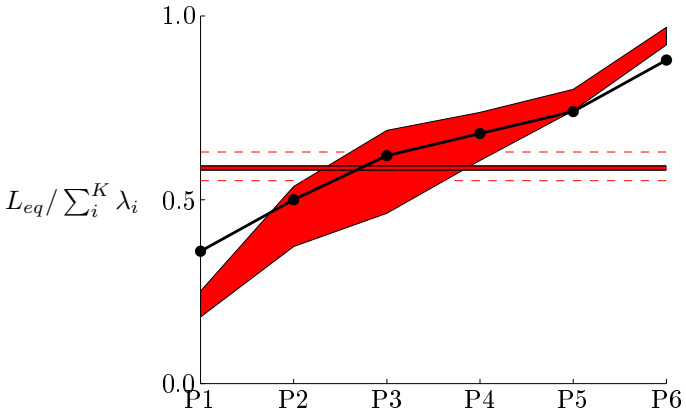

(b) Nacelle yaw.

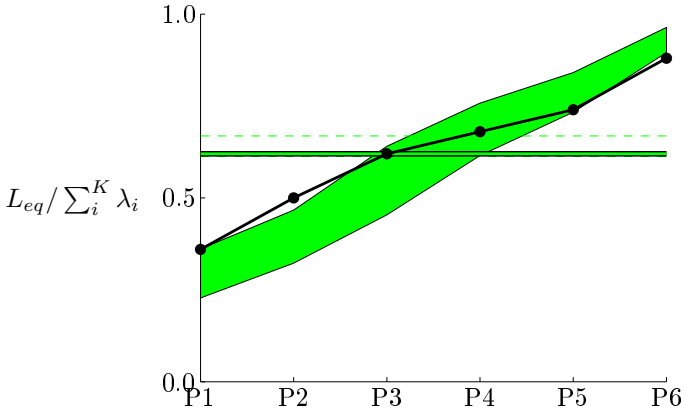

(c) Nacelle tilt.

Figure 6.27: Comparison of equivalent loads and reconstructed energy content for $S = 16R$. Legend: ——: POD coefficients. ■: Flapwise moment. ■: Yaw moment. ■: Tilt moment. The horizontal lines show the corresponding equivalent loads using Mann turbulence.

comparable to the full POD reconstructions when only using a few POD modes. Conversely, the Mann turbulence accounts for $65-77\%$ of the equivalent loads. This naturally suggest that the spacing between the turbines are large enough for the turbulence to approach homogeneous turbulence.

The equivalent loads are captured excellently by the POD reconstructions for $S = 12R$ and $S = 16R$ as more modes are included in the reconstruction. The stochastically generated Mann turbulence accounts for equivalent loads corresponding to the first few POD modes$(2-8)$, as it gives rise to $49-73\%$ of the equivalent loads compared to the full flow situation. Therefore, $K \geq 12$ should be used to reap the benefits of the POD model and gain better agreement in terms of equivalent loads compared to simply employing homogeneous turbulence. Furthermore, the POD modes $K > 100$ are basically redundant for the small and intermediate turbine spacings$(S = 12R-16R)$. Only half of the equivalent loads are accounted for by the reconstructions for larger spacings, whereas Mann turbulence accounts for up to 77%, indicating that the flow is closer to the upscaled homogeneous turbulence.

6.3.5 Verification Summary

The main conclusions from the previous sections with different verifications are briefly summarised in Table 6.2 for the two proposed wake models and the generated Mann turbulence. The summary clearly shows that the POD wake model generally yields excellent comparisons with the full flow for small and intermediate spacings$(S = 12R-16R)$. REDOMO performs poorly in the majority of the verification analyses, while the Mann turbulence generally performs well, particular for large spacings.

6.4 Outlook and Model Application

The previous sections demonstrate how the POD wake models capture all the main features of the flow, which subsequently results in comparable time series, spectrums, statistics, and loads. Conversely, REDOMO fails to capture the dynamics and is insufficient in reproducing inflows, which leads to comparable turbine loads. Despite the excellent agreement between the POD wake models and the full flow, it is important to stress that POD models are not generic and are incapable of predicting additional inflow fields, e.g. for $S = 18R$. Therefore, a comprehensive database containing a range of simulations is necessary, where design situations could be extracted from. The present work includes a parametric investigation of three different spacings, but it is necessary to examine the dependency of other parameters.

Spacing has a clear influence on the ability for the wake models to accurately describe the flow as seen in the previous sections, where the wake models struggled to capture the more spurious events of the large spacing$(S = 20R)$. Therefore, additional spacings could be examined to test the limits of the model applications. The current simulations are also based on wind farms with the same lateral and streamwise separation, which appeared to confine the flow and hence mixing for the small and intermediate spacings, see Section 5.4. Therefore, alternative array layouts could be of interest, e.g. an infinite wind farm separated by $12R$ in the lateral and $20R$ in the streamwise. Investigating partly

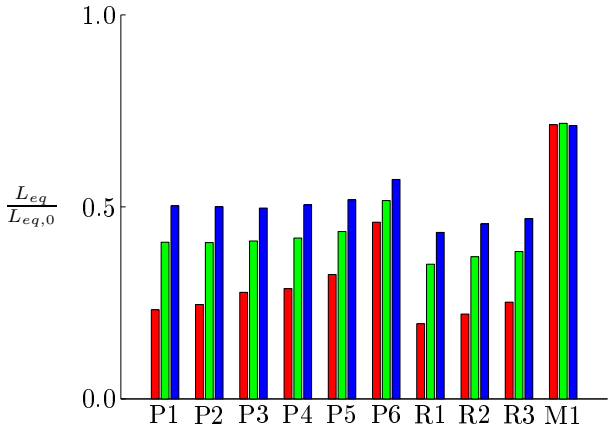

(a) Flapwise moment.

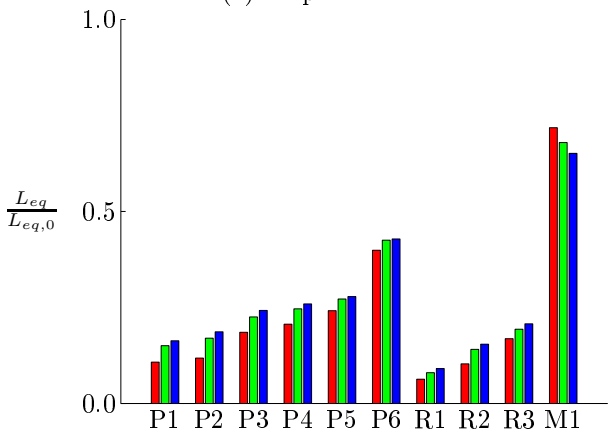

(b) Nacelle yaw.

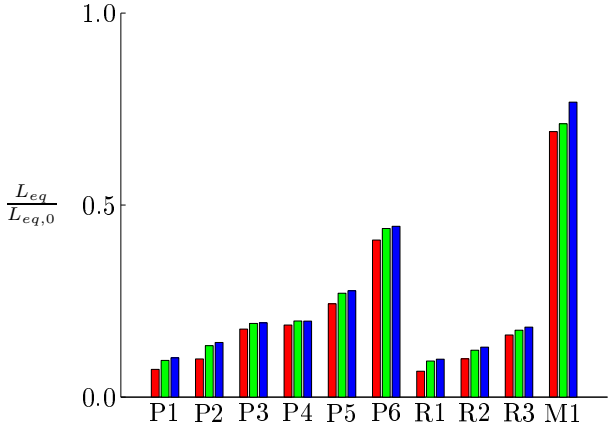

(c) Nacelle tilt.

Figure 6.28: Normalised equivalent loads for various reconstructions for $S = 20R$ with PBL. Legend: : $m = 3$. : $m = 6$. : $m = 10$.

Verification	POD	REDOMO	Mann
Temporal	Excellent fit for the small and intermediate spacings for $K \geq 12$. Poor fit for the large spacing.	Generally poor fit for all spacings, although it captures the correct frequencies for the flap- and edgewise moments.	Not comparable.
Spectral	Excellent fit for the small and intermediate spacings for $K \geq 12$, but the spectral energy is low on the higher frequencies. Mediocre fit for the large spacing, because it captures the correct peak frequencies, but the spectral content is too low.	Captures the correct peak frequencies, but the peaks are too narrow and energy content too low.	Very good fit, although the spectral energy is generally too low.
Statistics	Very good agreement for small and intermediate spacings for $K \geq 8$.	Not comparable.	Mixed results, since higher statistics are not preserved.
Equivalent Loads	Excellent agreement for the small and intermediate spacings for $K \geq 12$. Poor or mediocre agreement for the large spacing.	Poor agreement.	Good agreement for small and intermediate spacings, comparable to POD for $K < 8$. Very good agreement for large spacing.

Table 6.2: Summary of the main conclusions from the preceeding verification.

aligned turbine (sometimes referred to as staggered turbines) are of less interest due to the dynamic nature of the flow deep inside the infinite wind farm, where the turbines are constantly experiencing partial wake situations.

The vertical shear is affected by the atmospheric stability, so different prescribed boundary layers should be investigated and a vertical veer might also be necessary as the size of wind turbines continue to increase, extending further into the atmospheric boundary layer. However, the similarity between several of the dominant spatial POD modes described in Section 4.8 and 5.5 suggest that the main effect of the vertical shear is captured by the mean velocity profile.

Finally, the reported simulations have all been run for one initial inflow velocity of $15m/s$ and other velocity ranges should be explored. However, the present simulations are expected to be somewhat scalable with the freestream velocity. The expected scalability stems from the full coupling of the non-dimensionalised Navier-Stokes solver and the turbines, which are governed by the controller. The time histories and statistics showed how the turbine predominantly operated below rated wind speed ($15m/s$), and hence the active controller ensured that the turbine was operating in the same regime of $P \propto U_{hub}^3$. The variability of the inflow results in a mean wake, which is the combined effect of merging numerous wakes arising from different instanteneous load distributions and different tip-speed ratios. The effect of tip-speed ratio on the far wake was examined in Chapter 3, which showed that the near wake is different for different tip-speed ratios, but also how the far wake velocity profiles approach self-similar gaussian velocity profiles. Self-similarity is also assumed by Frandsen et al. [20], and self-similarity implies that the wake is scalable with λ_{TS} or C_T. Frandsen et al. [20] scaled the asymptotic velocity to C_T, see Section 4.6. Figure 6.29 shows the local C_T distribution for a range of tip-speed ratios from $\lambda_{TS} = 3.6$ to $\lambda_{TS} = 12.7$, i.e. an analysis similar to the sweep curve in Figure 2.2 with uniform inflow. The figure reveals three discernible regimes. The first regime of high tip-speed ratios($\lambda_{TS} = 12.7$) leads to a radially increasing C_T distribution, which peaks near the blade tip. The second regime yields a nearly uniform load distribution for $\lambda_{TS} = 6 - 9$, which is usually the preferred operational range for a wind turbine. C_T has maximum closer to the root and decrease radially in the third regime for tip-speed ratios of 5 or less. The mean streamwise velocities at hub height(Table 5.2) all corresponds to tip-speed ratios in the second regime($\lambda_{TS} = 6 - 9$), where the load distributions are comparable and almost uniformly distributed. Furthermore, the increased turbulence between the turbines will assist in breaking down any instanteneous differences and remnants of the near wake before the wake reaches the following turbine. Hence, it is conjectured that the POD wake models are scalable within the second regime. Shifting the results presented in Figure 6.21 indicates that the POD wake model can be employed for $U_0 \in [8 - 15]m/s$ for $S = 16R$, which then yields average velocities at hub height $U_{hub} \in [6 - 12]m/s$. An additional number of simulations could be run to cover the above rated regime, where the power production is kept constant by pitching the blades.

6.5 Summary

Two different wake models denoted POD and REDOMO were examined and compared to the full flow and stochastically generated Mann turbulence. The

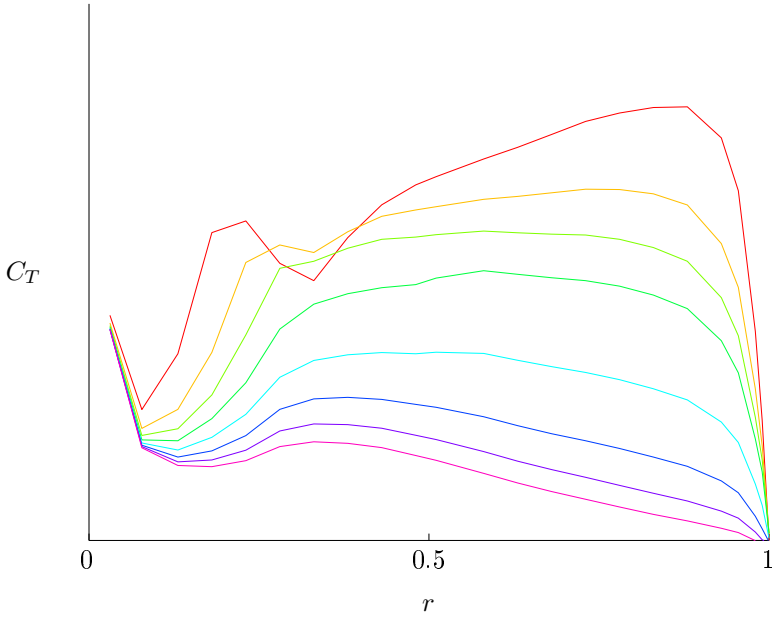

Figure 6.29: Local C_T distribution for range of constant inflow velocities. Legend: —— : $\lambda_{TS} = 12.68$. —— : $\lambda_{TS} = 8.89$. —— : $\lambda_{TS} = 7.23$. —— : $\lambda_{TS} = 6.02$. —— : $\lambda_{TS} = 5.16$. —— : $\lambda_{TS} = 4.52$. —— : $\lambda_{TS} = 4.02$. —— : $\lambda_{TS} = 3.61$.

instanteneous flow characterics were captured excellently by the POD model, while REDOMO resulted in a poor representation of the flow field. POD also gave good agreement with the full flow on a global level in terms of the instanteneous TKE. The performance of the models were assessed by using the wake models as input to full aeroelastic calculations performed in Flex5. REDOMO generally gave poor agreement and appeared less applicable despite its appealing simplicity. The applied filtering is too strong and dominant dynamics are discarded. Conversely, POD yields excellent agreement with the full flow, particular for small and intermediate spacing($S = 12R - 16R$) when using $K \geq 12$ POD modes. Stochastic Mann turbulence gave rise to equivalent loads comparable to the POD reconstructions using $K \in [2 - 8]$. POD resulted in mediocre comparison for large spacing($S = 20R$), which was attributed to the presence of spurious burst of energy, which appear as discontinuities. Homogeneous Mann turbulence gave better comparison for large spacings($S = 20R$).

The overall agreement was excellent for POD in term of time series, spectrums, higher order statistics, and most importantly the loads exerted on the turbine. Therefore, the proposed POD model was verified to meet all three criterias outlined by Sanderse [55] in the Introduction. The proposed POD model is not composed of several submodels dealing with each performance criteria, but inherently fulfill the criterias by retaining the dominant dynamics of the flow.

Chapter 7

Conclusions

Several numerical simulations of wakes and wake interaction between numerous wind turbines have been conducted and the results have been presented. The general Navier-Stokes solver, EllipSys3D, and LES have been employed for the numerical simulations, and the wind turbines are modelled using the Actuator Line method. The overall aim of the present work has been to analyse the turbulent flow deep inside large wind farms in order to derive a dynamic wake model based on the simulated physics.

The wake development behind a single turbine was initially examined in Chapter 3. Two simulations were presented for different tip-speed ratios and C_T-values, i.e. a highly loaded rotor and a rotor operating on or close to its optimal tip-speed ratio. The wake development was shown to be governed by the tip-speed ratio and the analysis highlighted the downstream development and differences between the two cases. The wake exhibited large scale motions and the wake centre was determined by a centre of mass approach, which indicated that the wake centre moved up to $1.6R$ from the centerline. Proper Orthogonal Decomposition(POD) was applied to extracted slices of the three velocity components, and the convergence of the POD modes was examined to determine the necessary number of slices. The spatial POD modes revealed large coherent structures in the wake and several portraited clear symmetric patterns, e.g. dipole, quadrupole, and hexapole structures.

Three idealised cases of infinitely long rows of turbines were simulated and investigated in Chapter 4. The turbulent quantities were deemed statistically converged across all the presented simulations for a temporal window of $1,500s$. The statistics proved a clear dependency on spacing, e.g. increased mean velocity for increased spacing due to enhanced mixing and wake recovery. The mean velocities were compared to the analytical models by N. O. Jensen [28] and Frandsen et al. [20]. The former showed very good agreement, while the latter was essentially calibrated to fit the CFD results. The turbulent flow quantities revealed how the turbulent kinetic energy production is associated with the tip vortices and occurs in an annular band around the turbine. The turbulent kinetic energy was conversely shown to be extracted within the rotor area. The basic hypothesis of the Dynamic Wake Meandering model, that the large wake motions are governed by the large atmospheric scales, was investigated. Large scales were demonstrated to be inherent to the wake interaction deep inside large wind farms as the simulations excluded the influence of atmospheric

turbulence. Furthermore, the analysis highlighted difficulties involved with describing the wake as a passive tracer in a moving frame of reference, which is another fundamental part of the Dynamic Wake Meandering model. The cross correlations were computed as a measure of the integral length scales and to assess the impact of the cyclic boundary conditions, which was deemed minor. POD was applied to velocity components extracted from these simulations as well, and the corresponding POD modes also revealed large coherent structures and symmetric patterns.

The infinite wind farm scenario was simulated in Chapter 5 with a prescribed boundary layer for three different lateral and streamwise spacings. The vertical shear amplified the findings from the idealised rows, i.e. wake recovery was enhanced for large turbine spacings and reduced for small spacings. The turbine spacing was shown to have a significant impact on confining the flow, as the flow was confined between the rows of turbines for small and intermediate spacings($S = 12R - 16R$). The effect was reversed for the large spacing($S = 20R$) as the flow between the turbines was even accelerated, leading to a further increase in wake recovery. The ability of high altitude turbulence to penetrate the boundary layer over the wind farm was investigated qualitatively, which resulted in a minor increase in turbulent mixing and wake recovery. The derived POD modes were often comparable to those derived from the idealised row scenarios, which suggest that the inplane spatial extend of the large coherent structures are comparable for the two scenarios, irrespective of the vertical shear in the streamwise velocity profile.

POD formed the basis for two proposed wake models, which were constructed in Chapter 6. A direct reconstruction using the first POD modes and a simplified model(REDOMO), where the dominant frequencies were identified from the temporal eigenfunctions and scaled to fit the full flow in a least squares sense. The instanteneous flow dynamics and the global turbulent kinetic energy were reconstructed excellently by the POD models, while REDOMO generally struggled to capture the dynamics. The model verification was conducted using flow fields derived from the wake models as input to aeroelastic computations followed by comparing the turbine performance and response with those corresponding to the full flow extracted from the CFD simulations. The models were also compared to stochastically generated Mann turbulence with the same turbulent properties. The spectral analysis generally gave rise to the correct shape of the spectrums derived from the Mann turbulence, although the spectral densities were too low, suggesting the possibility of deriving a different scaling for the stochastic turbulence. The stochastic turbulence was also shown to account for $49-77\%$ of the equivalent loads. The Mann turbulence gave particularly good agreement for the large spacing($S = 20R$), which indicates that the turbulence eventually approach homogeneous turbulence, if the turbines are far enough apart. REDOMO could seldomly capture the dynamics of the flow, which gave rise to poor agreement with the full flow. The POD wake model was verified to give excellent agreement in terms of time series, spectrums, higher order statistics, and equivalent loads for small and intermediate turbine spacing. POD only resulted in a mediocre comparison for large turbine spacings due to the presence of more spurious events. These bursts were more discontinuous for larger spacings, since the flow above and between the turbines was less confined. The verification revealed that the POD wake model should be constructed using 12 or more POD modes to consistently reap the benefits for

small and intermediate turbine spacings compared to merely employing stochastic and homogeneous turbulence. For large turbine spacings, the homogeneous turbulence outperforms the POD models.

The present work has verified the applicability of POD based wake models, which enables fast and reliable computations of the highly complex and dynamic turbulent flow deep inside large wind farms. The dynamics of the proposed wake model delivers a key component in terms of fulfilling all three criterias outlined in the Introduction by a single wake model, where the kinematic models fail to predict the dynamic power production and loads. The derived dynamic inflows broadens the potential applications of the wake model to include both individual turbine design as well as optimizing wind farm layout and wind farm control. However, extending the proposed wake model to other scenarios demands a comprehensive database, where the appropriate model components can be extracted from in order to quickly generate detailed inflow conditions.

Bibliography

[1] Aagaard Madsen, H., Bak, C., Schmidt Paulsen, U., Gaunaa, M., Fuglsang, P., Romblad, J., Olesen, N., Enevoldsen, P., Laursen, J., and Jensen, L. *The DAN-AERO MW Experiments*. Denmark. Forskningscenter Risø. Risø-R. Danmarks Tekniske Universitet, Risø Nationallaboratoriet for Bæredygtig Energi, 2010.

[2] Ainslie, J. F. Development of an eddy viscosity model for wind turbine wakes. *EWEA* (1985).

[3] Ainslie, J. F. Calculating the flowfield in the wake of wind turbines. *Journal of Wind Engineering and Industrial 27* (1988), 213–224.

[4] Amendment 1 to IEC 61400-1 Ed. 3. Wind turbines - part 1: Design requirements., 2009.

[5] Andersen, S. J., Sørensen, J. N., and Mikkelsen, R. Simulation of the inherent turbulence and wake interaction inside an infinitely long row of wind turbines. *Journal of Turbulence 14*, 4 (2013), 1–24.

[6] Andersen, S. J., Sørensen, J. N., and Mikkelsen, R. Reduced order model of the inherent turbulence of wind turbine wakes inside an infinitely long row of turbines. *Journal of Physics: Conference Series. The Science of Making Torque from Wind 2012. Under review.* (201X).

[7] Association., E. W. E. Deep water - the next step for offshore wind energy., 2013.

[8] ASTM E1049-85 (Reapproved 1997). Standard practices for cycle counting in fatigue analysis. Tech. rep., Philadelphia, 1999.

[9] Aubry, N. On the hidden beauty of the proper orthogonal decomposition. *Theoretical and Computational Fluid Dynamics 2* (1991), 339–352.

[10] Aubry, N., Holmes, P., Lumley, J. L., and Stone, E. The Dynamics of Coherent Structures in the Wall Region of a Turbulent Boundary Layer. *J. Fluid Mech. 192* (1988).

[11] Baetke, F., Werner, H., and Wengle, H. Numerical simulation of turbulent flow over surface-mounted obstacles with sharp edges and corners. *Journal of Wind Engineering and Industrial Aerodynamics 35*, 0 (1990), 129 – 147.

[12] Barthelmie, R., Folkerts, L., Larsen, G., Rados, K., Pryor, S., Frandsen, S., Lange, B., and Schepers, G. Comparison of wake model simulations with offshore wind turbine wake profiles measured by sodar. *J. Atmos. Ocean. Technol. 23* (2006), 888–901.

[13] Barthelmie, R., Pryor, S., Frandsen, S., Hansen, K., Schepers, J., Rados, K., Schlez, W., Neubert, A., Jensen, L., and Neckelmann, S. Quantifying the impact of wind turbine wakes on power output at offshore wind farms. *Journal of Atmospheric and Oceanic Technology 27*, 8 (2010), 1302–1317.

[14] Berkooz, G., Holmes, P., and Lumley, J. L. The proper orthogonal decomposition in the analysis of turbulent flows. *Annual Rev. Fluid Mech* (1993), 539–575.

[15] Bingöl, F., Mann, J., and Larsen, G. Light detection and ranging measurements of wake dynamics part i: One-dimensional scanning. *Wind Energy 13*, 1 (2010), 51–61.

[16] Calaf, M., Meneceau, C., and Meyers, J. Large eddy simulation study of fully developed wind-turbine array boundary layers. *Phys. Fluids 22*, 015110 (2010).

[17] Citriniti, J. H., and George, W. K. Reconstruction of the global velocity field in the axisymmetric mixing layer utilizing the proper orthogonal decomposition. *Journal of Fluid Mechanics 418*, -1 (2000), 137–166.

[18] Fong, D. C.-L., and Saunders, M. A. Lsmr: An iterative algorithm for sparse least-squares problems. *CoRR abs/1006.0758* (2010).

[19] Frandsen, S. *Turbulence and turbulence-generated structural loading in wind turbine clusters.* Denmark. Forskningscenter Risoe. Risoe-R. 2007. Risø-R-1188(EN).

[20] Frandsen, S., Barthelmie, R., Pryor, S., Rathmann, O., Larsen, S., Højstrup, J., and Thøgersen, M. Analytical modelling of wind speed deficit in large offshore wind farms. *Wind Energy 9*, 1-2 (2006), 39–53.

[21] Frandsen, S., and Madsen, P. *Spatially average of turbulence intensity inside large wind turbine arrays.* Univ. of Naples, 2003, pp. 97–106.

[22] Frandsen, S. T. Turbulence and turbulence-generated structural loading in wind turbine clusters, 2007.

[23] Gilling, L., Sørensen, N., and Rethore, P. *Imposing Resolved Turbulence by an Actuator in a Detached Eddy Simulation of an Airfoil.* EWEC, 2009.

[24] Hansen, M. *Aerodynamics of Wind Turbines.* Earthscan, 2008.

[25] Hansen, M. H., Hansen, A., Larsen, T. J., Oye, S., Sorensen, P., and Fuglsang, P. *Control design for a pitch-regulated, variable speed wind turbine.* Denmark. Forskningscenter Risœ. Risœ-R. Danmarks Tekniske Universitet, Risø Nationallaboratoriet for Bæredygtig Energi, 2005.

[26] Hansen, M. O. L., Sørensen, J. N., Voutsinas, S., Sørensen, N., and Madsen. State of the art in wind turbine aerodynamics and aeroelasticity. *Progress in Aerospace Sciences 42*, 4 (jun 2006), 285–330.

[27] Ivanell, S. S. A. *Numerical computations of wind turbine wakes.* PhD thesis, KTH, Mechanics, 2009. QC 20101203.

[28] Jensen, N. O. A note on wind generator interaction, 1983.

[29] Johansen, N. A. Verification of simulated fatigue loads on wind turbines operating in wakes. Master's thesis, DTU Mechanical Engineering, Technical University of Denmark, DTU, DK-2800 Kgs. Lyngby, Denmark, Denmark, 2009.

[30] Johansson, P. B., George, W. K., and Woodward, S. H. Proper orthogonal decomposition of an axisymmetric turbulent wake behind a disk.

[31] Jørgensen, B. H., S. J. N., and Brøns, M. Low-Dimensional Modeling of a Driven Cavity Flow with Two Free Parameters. *Theoret. Comput. Fluid Dynamics 16* (2003), 299–317.

[32] Kelley, N., Jonkman, B. J., Scott, G. N., Bialasiewicz, J. T., and Redmond, L. S. *The Impact of Coherent Turbulence on Wind Turbine Aeroelastic Response and Its Simulation: Preprint.* National Renewable Energy Laboratory (U.S.) and National Wind Technology Center (U.S.) and University of Colorado, Boulder, 2005.

[33] Larsen, G. C., Madsen, H. A., Bingöl, F., Mann, J., Ott, S., Sørensen, J. N., Okulov, V., Troldborg, N., Nielsen, M., Thomsen, K., Larsen, T. J., and Mikkelsen, R. Dynamic wake meandering modeling. Tech. Rep. R-1607(EN), Risø-DTU, Roskilde, Denmark, 2007.

[34] Larsen, G. C., Madsen, H. A., Thomsen, K., and Larsen, T. J. Wake meandering: A pragmatic approach. *Wind Energy 11* (2008), 377–395.

[35] Larsen, T., Aagaard Madsen, H., Larsen, G., and Hansen, K. Validation of the dynamic wake meander model for loads and power production in the egmond aan zee wind farm. *Wind Energy* (2012).

[36] Larsen, T., and Hanson, T. A method to avoid negative damped low frequent tower vibrations for a floating, pitch controlled wind turbine. *J. Phys.: Conf. Ser. 75* (2007), 11.

[37] Larsen, T. J., and Hansen, A. *How to HAWC2, the users manual.* Denmark. Forskningscenter Risoe. Risoe-R. Danmarks Tekniske Universitet, Risø National Laboratory, 2007.

[38] Lindberg, W., Spitler, J., and Naughton, J. Modal structure of surface turbulence using low-order turbulence modeling. *43rd AIAA Aerospace Sciences Meeting and Exhibit - Meeting Papers.* (2005), 5193 – 5203.

[39] Lu, H., and Porte-Agel, F. Large-eddy simulation of a very large wind farm in a stable atmospheric boundary layer. *PHYSICS OF FLUIDS 23*, 6 (JUN 2011).

[40] Lumley, J. L. The structure of inhomogeneous turbulence, 1967.

[41] Madsen, P. H., D. J. W. M. T. S. E. M. K. M. H., and Thresher, R. W. Recommended practices for wind turbine testing and evaluation. 3. fatigue loads., 1990.

[42] Mann, J. The spatial structure of neutral atmospheric surface-layer turbulence. *Journal of Fluid Mechanics 273* (7 1994), 141–168.

[43] Mann, J. Wind field simulation. *Probabilistic Engineering Mechanics 13*, 4 (OCT 1998), 269–282.

[44] Mann, J., Astrup, P., Kristensen, L., Rathmann, O., Madsen, P., and Heathfield, D. *WAsP engineering DK*. Denmark. Forskningscenter Risoe. Risoe-R. 2000.

[45] Medici, D., and Alfredsson, P. H. Measurements on a wind turbine wake: 3d effects and bluff body vortex shedding. *Wind Energy 9*, 3 (2006), 219–236.

[46] Michelsen, J. A. Basis3D-a platform for development of multiblock PDE solvers. *Report AFM* (1992).

[47] Mikkelsen, R. *Actuator Disc Methods Applied to Wind Turbines*. PhD thesis, Technical University of Denmark, Mek dept, 2003.

[48] Mikkelsen, R., Sørensen, J., and Troldborg, N. *Prescribed wind shear modelling with the actuator line technique*. 2007.

[49] Noack, B., Morzyânski, M., and Tadmor, G. *Reduced-Order Modelling for Flow Control*. Courses and lectures. SpringerWienNewYork, 2011.

[50] Noack, B. R., Afanasiev, K., Morzynski, M., Tadmor, G., and Thiele, F. A hierarchy of low-dimensional models for the transient and post-transient cylinder wake. *Journal of Fluid Mechanics 497* (12 2003), 335–363.

[51] Ott, S., Berg, J., and Nielsen, M. *Linearised CFD Models for Wakes*. Denmark. Forskningscenter Risoe. Risoe-R. Danmarks Tekniske Universitet, Risø Nationallaboratoriet for Bæredygtig Energi, 2011.

[52] Øye, S. Flex4 simulation of wind turbine dynamics, 1996.

[53] Pope, S. B. *Turbulent Flows*. Cambridge University Press, 2000, 8th Printing 2011.

[54] Sagaut, P. *Large Eddy Simulation for Incompressible Flows - An Introduction*. Springer, New York, 2005.

[55] Sanderse, B. *Aerodynamics of Wind Turbine Wakes: Literature Review*. ECN.: E-series. ECN, 2009.

[56] Saranyasoontorn, K., and Manuel, L. Low-dimensional representations of inflow turbulence and wind turbine response using proper orthogonal decomposition. *Journal of Solar Energy Engineering 127* (2005), 553–562.

[57] Saranyasoontorn, K., and Manuel, L. Symmetry considerations when using proper orthogonal decomposition for predicting wind turbine yaw loads. *Journal of Solar Energy Engineering 128* (2006), 574–579.

[58] Saranyasoontorn, K., and Manuel, L. On the propagation of uncertainty in inflow turbulence to wind turbine loads. *Journal of Wind Engineering and Industrial Aerodynamics. 96*, 5 (2008).

[59] Schepers, G. *Engineering Models in Wind Energy Aerodynamics: Development, Implementation and Analysis Using Dedicated Aerodynamic Measurements : Proefschrift.* Techische Universiteit Delft, 2012.

[60] Sirovich, L. Turbulence and the dynamics of coherent structures, part I-III. *Quarterly of Appl. Math. XLV* (1987), 583–590.

[61] Solari, G., and Piccardo, G. Probabilistic 3-d turbulence modeling for gust buffeting of structures. *Probabilistic Engineering Mechanics. 16*, 1 (2001), 73 – 86.

[62] Sørensen, J. N., and Myken, A. Unsteady actuator disc model for horizontal axis wind turbines. *J. Wind Eng. Ind. Aerodyn. 39* (1992), 139–149.

[63] Sørensen, J. N., and Shen, W. Z. Numerical modelling of Wind Turbine Wakes. *Journal of Fluids Engineering 124*, 2 (2002), 393–399.

[64] Sørensen, N. N. *General Purpose Flow Solver Applied to Flow over Hills.* PhD thesis, Technical University of Denmark, 1995.

[65] Spitler, J., Morton, S., Naughton, J., and Lindberg, W. Initial studies of low-order turbulence modeling of the wind turbine in-flow environment. *Collection of ASME Wind Energy Symposium Technical Papers AIAA Aerospace Sciences Meeting and Exhibit.* (2004), 442 – 451.

[66] Stankiewicz, W., Morzynski, M., Roszak, R., Noack, B. R., and Tadmor, G. Reduced order modelling of a flow around an airfoil with a changing angle. *Archives of Mechanics 60* (2008), 509–526.

[67] Ta Phuoc, L., Lardat, R., Coutanceau, M., and Pineau, G. Rechereche et analyse de modeles de turbulence de sous maille adaptes aux ecoulements instationnaires decolles., 1994.

[68] Troldborg, N. *Actuator Line Modeling of Wind Turbine Wakes.* PhD thesis, DTU Mechanical Engineering, Technical University of Denmark, DTU, DK-2800 Kgs. Lyngby, Denmark, Denmark, 2008.

[69] Troldborg, N., Sørensen, J., and Mikkelsen, R. *Numerical Simulations of Wakes of Wind Turbines Operating in Sheared and Turbulent Inflow.* EWEC, 2009.

[70] Troldborg, N., Sørensen, J., Mikkelsen, R., and Sørensen, N. A simple atmospheric boundary layer model applied to large eddy simulations of wind turbine wakes. *Wind Energy* (2013).

[71] Trujillo, J., Bingol, F., Larsen, G., Mann, J., and Kuhn, M. Light detection and ranging measurements of wake dynamics. part II: two-dimensional scanning. *Wind Energy 14*, 1 (2011), 61–75.

[72] Veers, P. S. Three-dimensional wind simulation. Tech. Rep. SAND88-0152 UC-261, Sandia National Laboratories, 1988.

[73] Zahle, F., and Sørensen, N. *Overset Grid Flow Simulation on a Modern Wind Turbine*. Conference Proceeding Series. American Institute of Aeronautics and Astronautics, 2008.

DTU Wind Energy is a department of the Technical University of Denmark with a unique integration of research, education, innovation and public/private sector consulting in the field of wind energy. Our activities develop new opportunities and technology for the global and Danish exploitation of wind energy. Research focuses on key technical-scientific fields, which are central for the development, innovation and use of wind energy and provides the basis for advanced education at the education.

We have more than 230 staff members of which approximately 60 are PhD students. Research is conducted within 9 research programmes organized into three main topics: Wind energy systems, Wind turbine technology and Basics for wind energy.

Technical University of Denmark
DTU Vindenergi
Frederiksborgvej 399
Building 118
4000 Roskilde
Denmark
Telefon 46 77 50 85
info@vindenergi.dtu.dk
www.vindenergi.dtu.dk